ENERGY DISSIPATION OF COMPOSITE MULTIFILAMENTARY SUPERCONDUCTORS FOR HIGH-CURRENT RAMP-FIELD MAGNET APPLICATIONS

by

CHEN-YU GUNG

Submitted to the Department of Nuclear Engineering
in Partial Fulfillment of the Requirements
for the Degree of

DOCTOR OF PHILOSOPHY

at the

MASSACHUSETTS INSTITUTE OF TECHNOLOGY

January 1993

Signature of Author _____
Department of Nuclear Engineering
January 11, 1993

Certified by ___
_____
Joseph V. Minervini, Ph.D.
Thesis Supervisor

Certified by ___
_____
Makoto Takayasu, Ph.D.
Thesis Co-supervisor

Certified by ___
_____
Professor Ronald G. Ballinger
Thesis Reader

Accepted by _____
Professor Allan F. Henry
Chairman, Department Committee on Graduate Students

ENERGY DISSIPATION OF COMPOSITE MULTIFILAMENTARY SUPERCONDUCTORS FOR HIGH-CURRENT RAMP-FIELD MAGNET APPLICATIONS

by

Chen-yu Gung

Submitted to the Department of Nuclear Engineering
on January 11, 1993
in Partial Fulfillment of the Requirements for the Degree of
Doctor of Philosophy in Nuclear Engineering

ABSTRACT

Energy dissipation, which is also called AC loss, of a composite multifilamentary superconducting wire is one of the most fundamental concerns in building a stable superconducting magnet. Characterization and reduction of AC losses are especially important in designing a superconducting magnet for generating transient magnetic fields. The goal of this thesis is to improve the understanding of AC-loss properties of superconducting wires developed for high-current ramp-field magnet applications. The major tasks include: (1) building an advanced AC-loss measurement system, (2) measuring AC losses of superconducting wires under simulated pulse magnet operations, (3) developing an analytical model for explaining the new AC-loss properties found in the experiment, and (4) developing a computational methodology for comparing AC losses of a superconducting wire with those of a cable for a superconducting pulse magnet.

A new experimental system using an isothermal calorimetric method was designed and constructed to measure the absolute AC losses in a composite superconductor. This unique experimental setup is capable of measuring AC losses of a brittle Nb_3Sn wire carrying high AC current in-phase with a large-amplitude pulse magnetic field. Improvements of the accuracy and the efficiency of this method are discussed.

Three different types of composite wire have been measured: a Nb_3Sn modified jelly-roll (MJR) internal-tin wire used in a prototype ohmic heating coil, a Nb_3Sn internal-tin wire developed for a fusion reactor ohmic heating coil, and a NbTi wire developed for the magnets in a particle accelerator. The cross sectional constructions of these wires represent typical commercial wires manufactured for pulse magnet applications.

Two types of field variation were of interest to this research: (1) a large peak-to-peak triangular cyclic field, and (2) a small sinusoidal wave-form (ripple) field superimposed on various large DC bias fields. The first field condition was used to simulate the ramp field operation of a pulse magnet. Superconducting wires were tested with and without transport current. The ripple field condition was adopted for approaching the ideal, constant critical current condition assumed in the existing AC-loss models. Only current-free wires were tested in this field condition.

In both test conditions, the AC losses must be calculated with a field-dependent critical current density profile which has not been explicitly included in the existing AC-loss models. The formulae of the existing hysteresis-loss and coupling-loss analyses were extended for the field conditions and the test wire cross sectional structures used in this work.

Single-strand AC loss test results were compared with analytical results using these modified loss models. Most calculated results agreed with the experimental data in two of the test wires. Existing AC-loss models were insufficient to explain the occurrence of a local maximum loss in a very low frequency regime in the ramp-rate dependent loss profile of the Nb_3Sn MJR wire.

An inter-bundle coupling loss model has been developed as the first analytical AC-loss model attempting to understand the loss mechanism of this newly found phenomenon. The proposed model has succeeded in explaining the occurrence of the local maximum loss at a slow ramp rate and simulating the trend of the loss profile as a function of the ramp rate. This was achieved by accounting for the collective coupling current effects caused by non-uniform cross sectional construction of the MJR wire.

The measured AC losses of single-strand carrying transport current are not consistent with the predictions by existing loss models, even when a field-dependent critical current density is applied in the calculation. The experimental results show that when a DC or an AC current is applied to a composite superconductor under ramp field condition, the additional AC losses caused by transport current are similar if $I_{DC} = I_{AC,max}$. The test results also reveal that the total loss of a composite wire carrying large transport current may have a higher loss in a slowly ramped field than that in a fast one. This conclusion is just opposite to the general concept that high time-rate of field variation generates high AC losses. These new AC-loss properties of a current-carrying composite wire have been experimentally identified in all three types of test wire. These general phenomena may lead to a new area for future analytical work.

The United State Demonstration Poloidal Coil (US-DPC) is a prototype ohmic heating coil designed as a development step in pulsed superconducting magnet technology. One of the major goals of the US-DPC experiment was evaluating AC losses of the coil at ramp field operation up to 10 T at 10 T/s. AC losses measured in the large-scale US-DPC test were compared with those of constituent US-DPC wires tested in the laboratory-scale experiment. Due to the distinctly different field conditions of these two experiments, the comparison was mainly performed on the calculated AC-loss parameters. Good agreement in these AC-loss parameters was found. A prediction method for AC losses in a full-size cable has been developed out of the loss comparison process. The practical scheme uses the formulae applied in this work combined with the required parameters evaluated from the laboratory-scale single-strand experiments. This prediction method is one of the most important application of this thesis work.

Thesis Supervisor: Dr. Joseph V. Minervini
Thesis Supervisor: Dr. Makoto Takayasu

ACKNOWLEDGEMENTS

This work is supported by the U.S. Department of Energy under Grant No. DE-FG02-91ER-54110.

I am very indebted to my former thesis supervisor Dr. Mitchell O. Hoenig who offered me the opportunity to work on this thesis research. I am also very grateful to my thesis supervisor Dr. Joseph V. Minervini for his continuing support and valuable comments on this thesis work. Special thanks go to my thesis co-supervisor Dr. Makoto Takayasu from whom I learned to be an experimentalist. I would also like to express my gratitude to the members of my thesis committee, Dr. D. Bruce Montgomery, Professors John Meyer and Ian Hutchinson, and particularly Professor Ronald Ballinger for his kindly reading this thesis.

I would like to thank Dr. Michael Steeves for his advices and helpful discussions during my thesis work. Many thanks go to Mr. Bruce Oliver and Mr. Daniel Reisner for their work on the apparatus and their help during the experiment.

I am grateful to the staff of the Francis Bitter National Magnet Laboratory for their technical support. I would like to express my thanks to Dr. David Smathers of Teledyne Wah Chang Albany, Dr. Eric Gregory of Intermagnetics General Co., and Dr. Robert Randall of Supercon for providing me the test wires.

Finally, the whole thesis work would not be possible without the long term support and encouragement of my wife Dinah and the understanding of my daughter Jennifer.

CONTENTS

LIST OF FIGURES

LIST OF TABLES

CHAPTER I

INTRODUCTION

I.1 BACKGROUND

I.1.1 Introduction

The application of superconductors in building large-scale high-current and high-field superconducting magnets has gained increasing prominence in various areas such as magnetic-confined nuclear fusion (Refs. 1.1 to 1.6), particle acceleration (Refs. 1.7 to 1.11), magnetic levitation (Refs. 1.12 to 1.16), etc. AC loss is one of the most fundamental concerns in superconducting magnet design (Refs. 1.5, 1.6, 1.11, and 1.17). AC loss relates to the heat dissipation in a superconducting wire subject to a time-varying (AC) field (Refs. 1.1 to 1.11, 1.17, and 1.24). AC losses, although a very small fraction of the total stored energy in the magnet, are not desirable especially at liquid helium temperature. The reason for this is that any heat added to the superconductor tends to increase its temperature and degrade its superconducting properties (Refs. 1.17 and 1.24). If the heat is not properly removed, the stability of the superconducting magnet will be jeopardized. From an economic viewpoint, the energy required to remove one unit of heat from a cryogenic system at 4 K can be hundreds to a thousand times as large (Refs. 1.2 and 1.17). A carefully designed, low AC-loss, superconducting magnet can greatly reduce the required operating power for the entire magnet system. Since any superconducting magnet must experience a transient charging stage, AC losses occur in both AC and DC superconducting magnets. Pre-estimation of the AC losses during the design stage are important to any type of superconducting magnet (Ref. 1.5).

In order to provide a background for discussing the subject of this thesis, a general introductory survey of bulk superconductor, composite superconducting wire, and their important macroscopic properties including some simple qualitative description of the AC-loss mechanisms is briefly presented in this section.

I.1.2 Type-I and Type-II Superconductors

The superconducting properties of mercury at liquid helium temperature was first discovered by Heike Kamerlingh Onnes and his colleagues in the Netherlands in 1911 (Ref. 1.18). In their experiment, the electric resistivity of a high-purity mercury thread was measured in a liquid helium bath. As shown in Fig. 1.1, when the temperature was reduced to ~4.2 K, a sudden drop of the electric resistance of mercury by a factor of ~10,000 was found within a temperature variation of 0.02 K. After repeating the experiment many times with different mercury samples, Kamerlingh Onnes reported that "Mercury has passed into a new state, which on account of its extraordinary electrical properties may be called the superconducting state." (Ref. 1.18). The threshold temperature at which the electric resistance of a conductor drops suddenly is now known as the 'critical temperature', T_c. In early 1913, the threshold values of the current densities of a mercury thread at temperatures below 4.18 K were reported to be dependent on the temperature by Kamerlingh Onnes (Ref. 1.18). The threshold current density is now called the 'critical current density', $J_c(T)$, which is the most important superconducting property in the area of applied superconductivity. In the same year, the superconducting states of pure tin and lead were found by the same laboratory at critical temperatures of 3.8 K and 6 K, respectively (Ref. 1.18). The resistances of tin and lead were measured in different magnetic fields, and threshold values of the fields were reported to be temperature dependent by Kamerlingh Onnes in 1914 (Ref. 1.18). This threshold field is now known as the 'critical field', $H_c(T)$. Thus, by 1914, Kamerlingh Onnes' laboratory had not only discovered the superconducting state of the materials, but also found the most important characteristics of a superconductor: critical temperatures, critical current densities, and critical fields.

During the early stage of searching for superconductors, major efforts were concentrated on testing superconducting properties of highly-purified metals. The only alloy that had been used was the amalgam of tin and mercury which was found to have superconducting properties similar to pure mercury. No further attention to alloys had been paid before 1920 (Ref. 1.18). Between 1920 and 1930, researchers studied various metals and alloys for the purpose of seeking superconducting materials with higher critical temperatures for high field and high current applications (Ref. 1.18). NbTi was discovered during that period and remains one of the most important superconductors for electromagnet applications due to its favorable metallurgy (Ref. 1.17). The family of

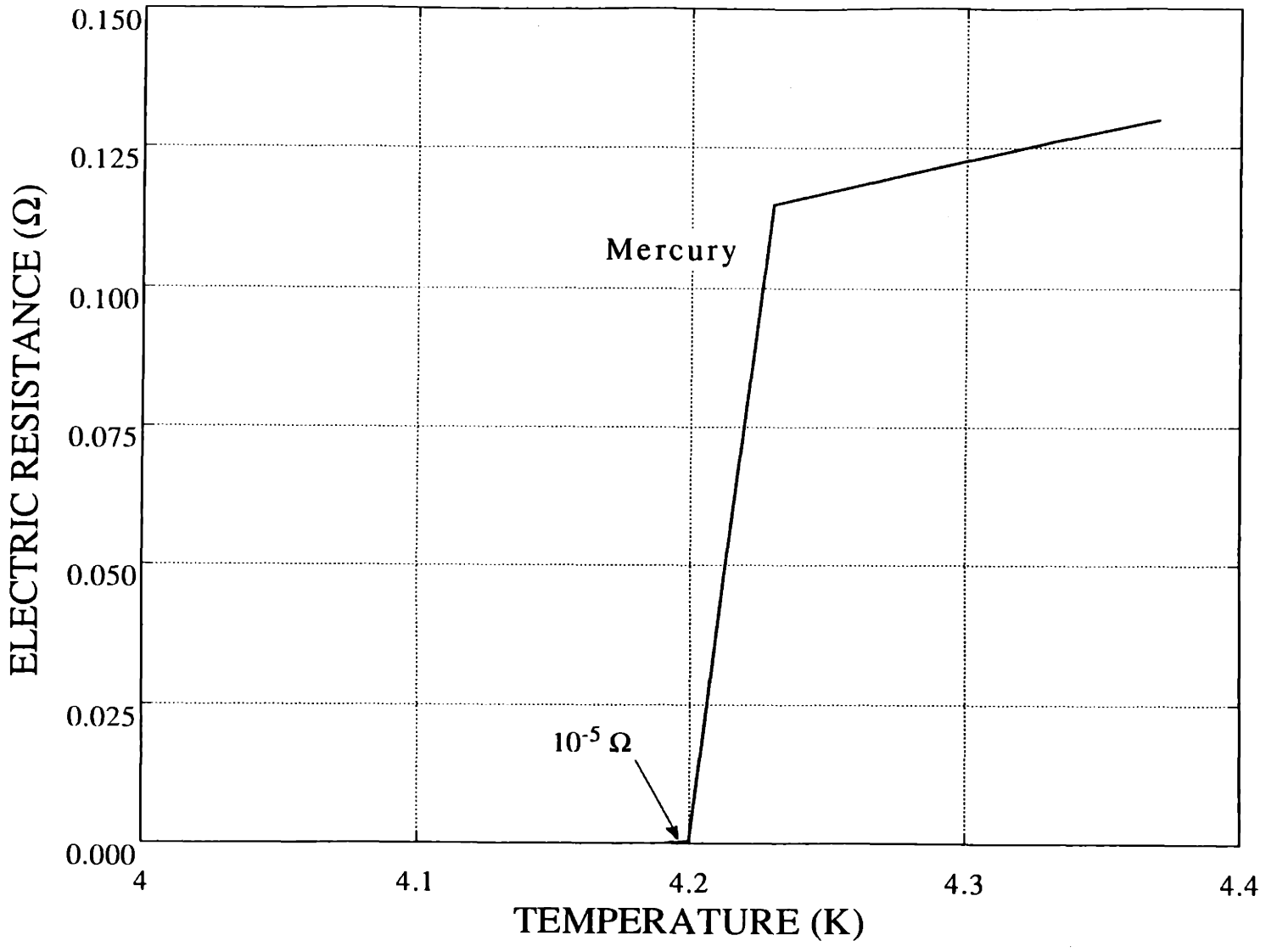

Fig. 1.1 The step-down of the DC electric resistance of mercury at temperature near 4.2 K, the first superconducting material discovered by Kamerlingh Onnes in 1911.

superconductors with the A15 crystal structure, such as V_3Si, V_3Ga, Nb_3Sn, Nb_3Ge, etc., were found in the 1950's (Ref. 1.19). As illustrated in Fig. 1.2, the intermetallic A_3B compound with A15 structure is formed by a body-centered cubic arrangement of B atoms with two A atoms centered in every face yielding orthogonal chain structures running through the crystal (Refs. 1.19 and 20). The A15 crystal structure is responsible for not only the higher critical temperatures (~ 16 - 23 K), but also the inherently brittle and strain-sensitive natures of these compounds. The family of high-T_c superconductors ($T_c \geq 25$ K) discovered in late 1986 and early 1987 also has a similar crystal structure (Ref. 1.19).

The single property of zero DC electric resistance is not sufficient to describe a superconductor since a perfect conductor possesses the same characteristics. In 1933, Meissner and Ochsenfeld found that in low external magnetic fields ($\leq H_c$), the magnetic flux density inside a large single crystal of tin was zero (Ref. 1.18). The finding shows that the superconductor expels the magnetic flux instead of conserving the flux as the perfect conductor does. This perfect diamagnetic property of a superconductor is known as Meissner effect (Refs. 1.17, and 1.21 to 1.27). The zero DC electrical resistance and perfect diamagnetism are the two indispensable phenomenon characterizing a superconductor (Refs. 1.18, 1.21 to 1.23, 1.26 and 1.27). After the phenomenon of the superconductor were characterized, theoretical works attempting to explain the source of superconductivity were developed extensively, which are not within the scope of the present research. Important review articles can be found in Refs. 1.21 to 1.27.

According to their magnetic properties, superconductors are categorized into type-I and type-II conductors, which can be distinguished from the H-T phase diagrams as shown in Fig. 1.3 (Refs. 1.26 and 1.27). As seen in Fig. 1.3(a), at a temperature below T_c, a type-I superconductor has a single critical field, H_c. The superconductor is in the Meissner state when the applied field strengths are less than $H_c(T)$, and becomes a resistive conductor (or a normal conductor, in contrast to the superconductor) when the $H_c(T)$ is exceeded. Fig. 1.3(b) shows that a type-II superconductor has two critical fields, the lower critical field, $H_{c1}(T)$, and the upper critical field, $H_{c2}(T)$. With an applied field strength below $H_{c1}(T)$, the type-II superconductor is in the Meissner state similar to the type-I superconductor. The type-II superconductor becomes normal as the applied field strength exceeds $H_{c2}(T)$. When the applied field strength is between the lower and upper critical fields, a type-II superconductor is able to carry some current without resistance but is no longer perfectly diamagnetic. The phenomenon is known as the mixed state (Refs. 1.26 and 1.27). The existence of the mixed state can be roughly pictured as follows.

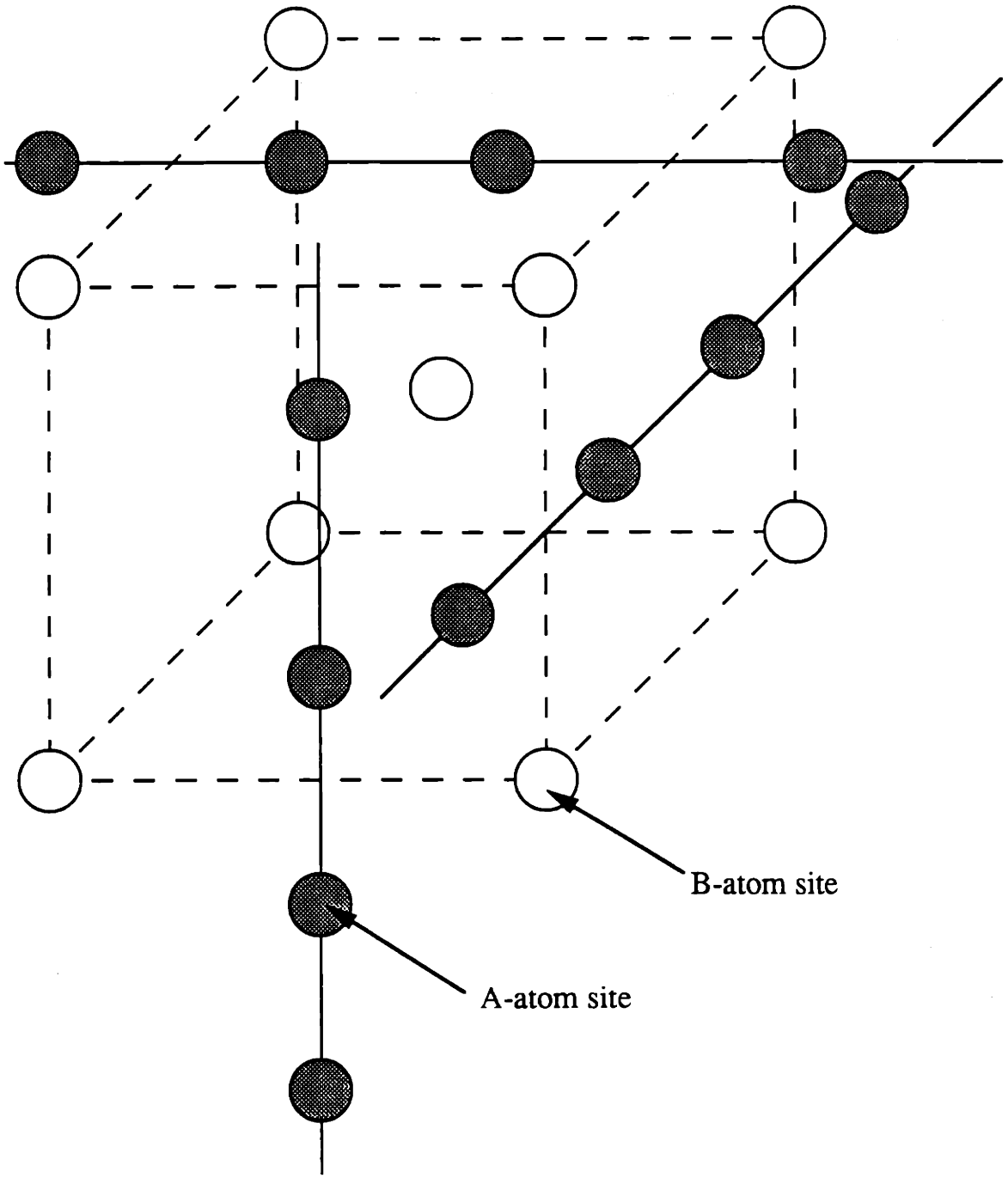

Fig. 1.2 A15 crystal structure with chains of transition atom. Shaded circles denote A-atome site; open circles denote B-atom sites.

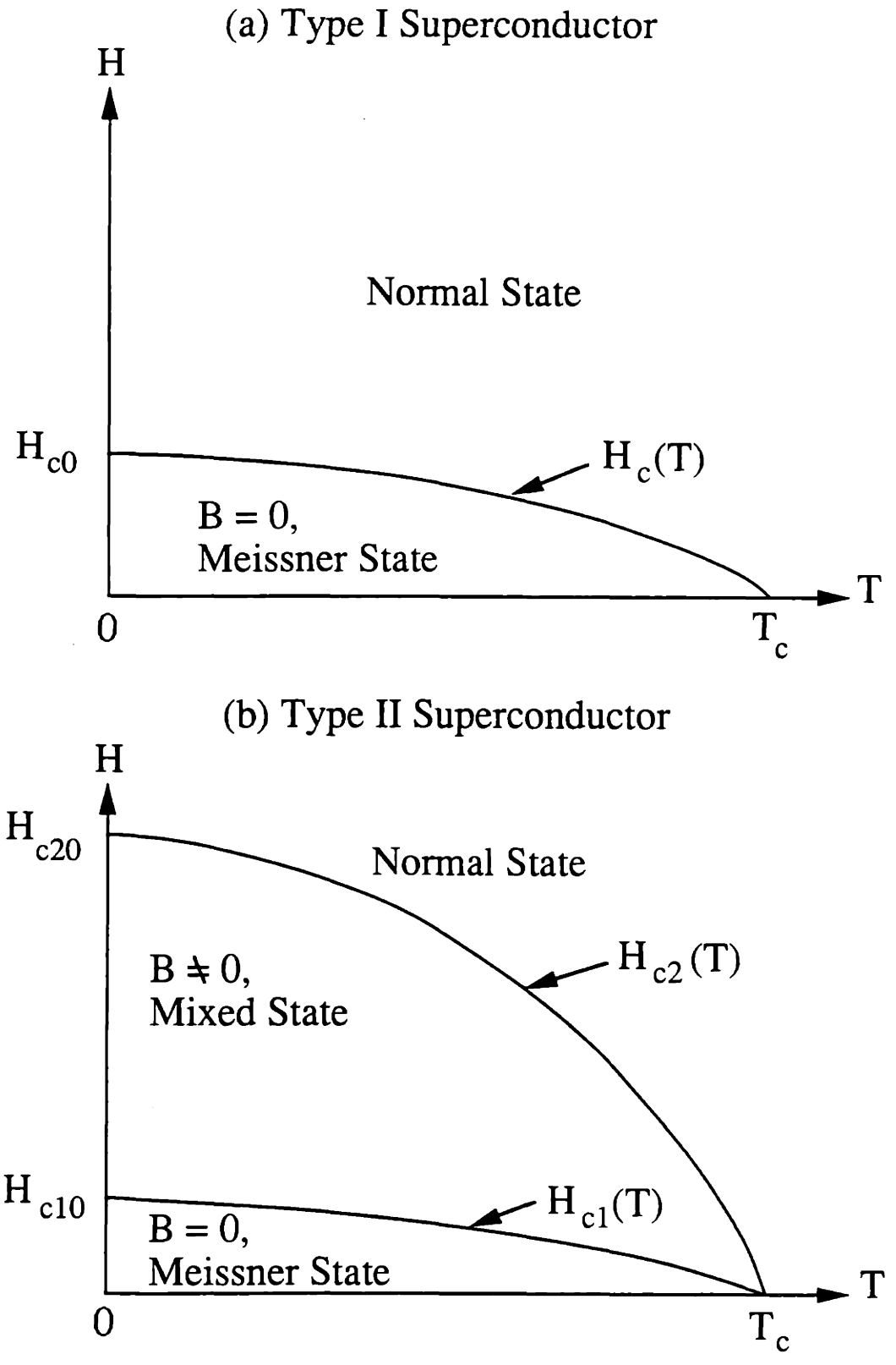

Fig. 1.3 H-T phase diagrams of (a) type-I superconductor and (b) type-II superconductor.

When a small external field strength ($\leq H_{c1}$) is applied to a type-II superconductor, a circulating current is induced on the surface of the superconductor (Ref. 1.26). The surface current generates a field opposing the external field, and the bulk of the superconductor is perfectly diamagnetic which is the same as the type-I superconductor. In the mixed state, when the applied field strength exceeds the lower critical field of a type-II superconductor, Fig. 1.4 shows that the diamagnetic surface current remains circulating, but the material is threaded by resistive (or normal) cores. The superconductor is magnetized when a part of the volume is penetrated by the normal cores. The normal cores along with the vortices form at the surface and move into the material which are in parallel to the applied field. Each normal core contains a single flux quantum in the same direction as the applied field, which is shielded by a vortex of supercurrent. The normal cores have small radii which can be imagined as an array of filaments embedded in a bulk superconductor. When an external current ($< I_c$) is applied to a superconductor containing normal cores, the currents are flowing without resistance in some continuous superconducting paths in the bulk material. The bulk superconductor is now considered as a mixture of superconducting state and normal state, or briefly, in a mixed state. As the applied field strength increases, an increasing region is covered by the normal cores. When the normal cores are overlapped, the so called upper critical field is reached, and the whole superconductor becomes normal (Ref. 1.26).

I.1.3 Flux Pinning and Hard Superconductors

In general, the ranges of the critical fields for type-I superconductors or the lower critical field of the type-II superconductors are on the order of a few hundred Gauss (Ref. 1.27). The order of magnitude of the upper critical field is about 10 T. The usable field range of a type-II superconductor in the mixed state is much larger than that in the Meissner state. However, when a current is applied to a type-II superconductor, the vortices tend to be moved by the Lorentz force. In a perfect type-II superconductor, the movement of the vortices causes an electric resistance called flux flow resistance which is proportional to the normal state resistance of the superconductor (Ref. 1.23). The interaction of the current and the flux flow resistance results in energy dissipation. Fig. 1.5 shows that only a small amount of currents are allowed to flow without resistance in a perfect type-II superconductor in the mixed state. Fortunately, it is found that in the mixed state, the movement of the vortices can be stopped (or pinned) by introducing imperfections and impurities to the type-II conductor (Refs. 1.23, 1.24, and 1.26). As seen in Fig. 1.5, the

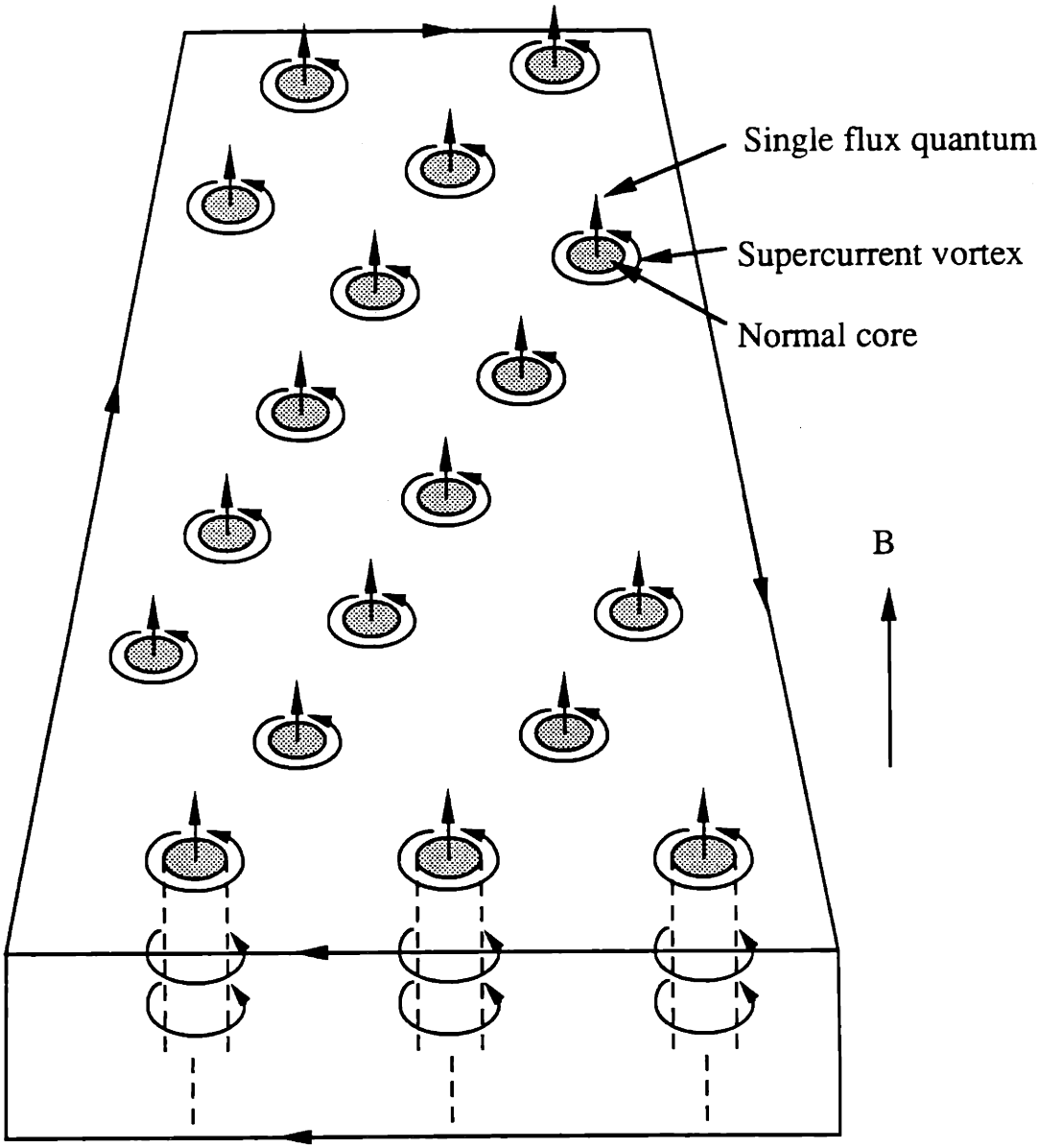

Fig. 1.4 The mixed state of a superconductor slab transverse to the external field with normal cores and encircling supercurrent vortices. The vertical lines represent one flux quantum threading the cores. The surface current maintains the bulk diamagnetism.

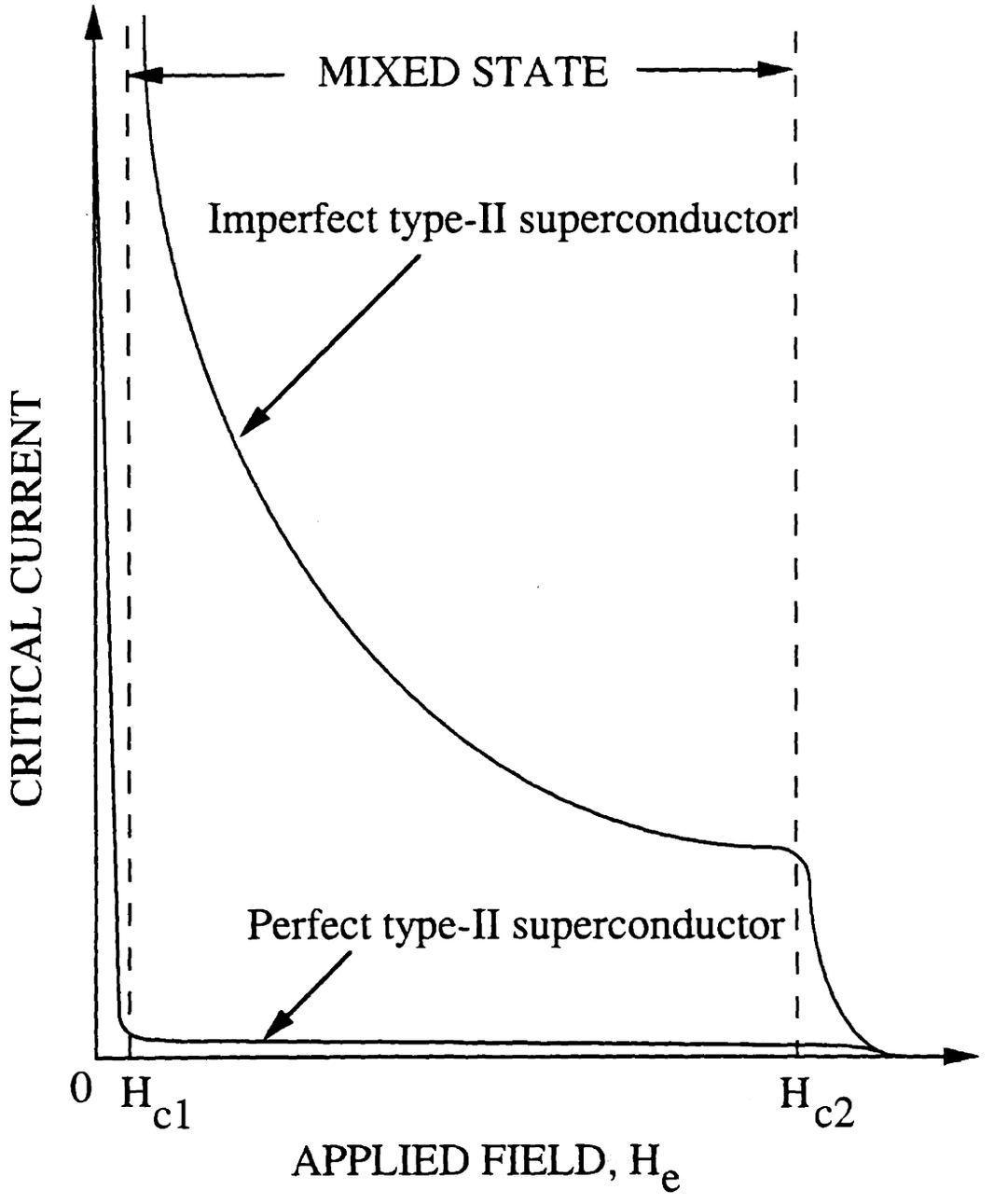

Fig. 1.5 Variation of critical currents of a highly perfect and an imperfect type-II superconductor in a transverse applied field.

critical currents of an imperfect superconductor are considerably improved both above and below H_{c1}. It is important to note that the critical current of a type-II conductor is the current which creates just enough Lorentz force to detach the vortices from the pinning centers (Ref. 1.23).

The magnetization of a perfect type-II superconductor is reversible. However, an imperfect type-II conductor shows some irreversibility in its magnetic properties because of the pinning of the vortices in the conductor (Ref. 1.26). As the external field increases and passes the H_{c1}, the normal cores generated on the surface of the material can not move freely into the interior. Similarly, as the external field drops from above H_{c1}, some of the vortices are pinned in the material and part of the flux is trapped. Thus, if the magnetization of an imperfect type-II superconductor is plotted against the external field, a hysteresis loop as seen in Fig. 1.6 will be found. The area covered by the hysteresis loop is the unrecoverable energy loss during each field cycle, which increases with the pinning force in the material.

In general, a perfect type-II superconductor is difficult to produce unless great care is taken during fabrication. A type-II superconductor with imperfections and impurities, known as a dirty type-II superconductor or hard superconductor, is of great importance in the construction of superconducting electromagnets (Ref. 1.23). The hard superconductor is the superconducting material of interest to the present research, since such a conductor is capable of carrying high DC currents in its mixed state in a wide usable field range. Except for Nb, most hard superconductors are in alloys or compounds, among which NbTi and Nb_3Sn are the most well-known commercialized superconducting materials (Ref. 1.17).

I.1.4 Technical Superconducting Wires

A practical superconducting wire for high field superconducting electromagnet applications must be capable of carrying a high current flowing without resistance in a high field. This can only be accomplished with low-T_c type-II superconductors at the present time. The superconductors in a magnet may be degraded due to various factors such as inappropriate manufacturing process, external disturbance, etc. (Ref. 1.17). The worst case of the degradation is caused by a sudden heating of the superconductor which exceeds the local heat removal capability. Under such conditions, the superconductor may become resistive which will result in further temperature increase due to self-heating. If the power

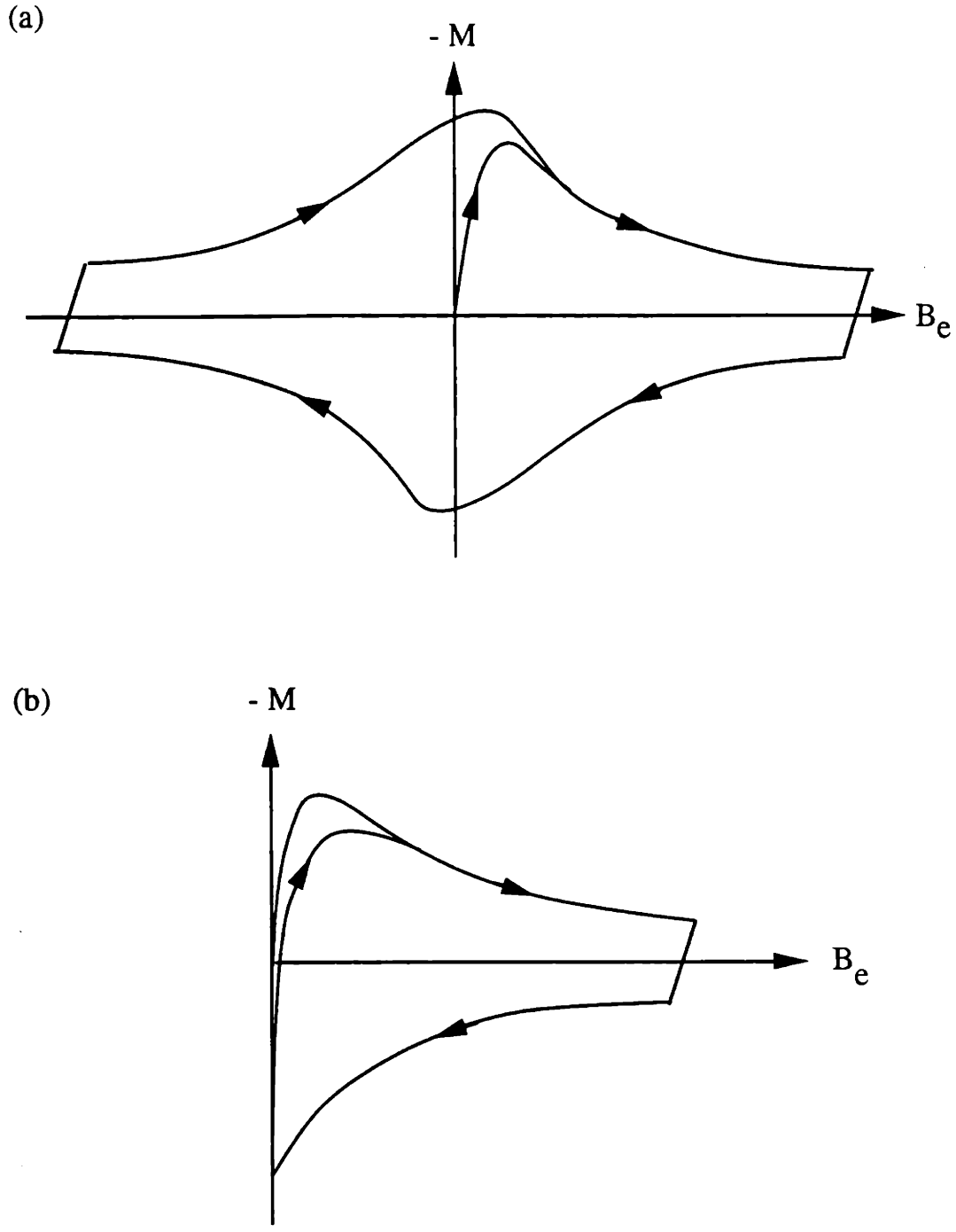

Fig. 1.6 Magnetization loops; (a) full cycle, (b) half cycle

supply to the magnet is not properly shut off in a short time, a local heating process may propagate to a larger region. Eventually, the energy stored in the magnet may be released in the superconductor in the form of heat. The above process is called a quench (Ref. 1.17). A useful superconducting magnet must be designed to operate in a quench-free condition.

In order to prevent the occurrence of large scale quench and provide quench protection to the superconductor, it is necessary to reduce the possibility of sudden heating of the superconductor and improve the efficiency of heat removal. In most cases, the heating of the superconductor comes from the effect of the Lorentz force, both internal and external, to the conductor. Externally, Lorentz forces cause wire movement. The energy is converted into heat due to friction. This type of heat source is not a subject of this research. Internally, as the applied field increases, the critical current density of the superconductor decreases, which implies that the Lorentz force dominates the pinning force. As more flux is able to enter the superconductor from the surface, the flux starts to move and dissipate energy. If the dissipated energy is not properly removed, the pinning centers will be thermally activated, and the critical current density will be further decreased. The cascade effect of flux motion and energy dissipation is called a flux jump (Ref. 1.17). In order to eliminate the flux jump, one may reduce the distance available for flux motion and reduce the temperature effect on the critical current density by efficiently conducting the dissipated energy from the superconductor. Both methods in preventing a flux jump require fine division of the superconductor (Refs. 1.17 and 1.24).

When the hard superconductor becomes resistive (or normal), the electric resistivity is much higher than that of a good normal conductor such as Cu or Al. In order to reduce the self-heating of a normal superconductor, the fine superconductor filaments are embedded in a resistive matrix material with high thermal and electric conductivities. The matrix material, also called a stabilizer, not only increases the heat removal efficiency but also provides an electric bypass of lower Joule heating for the superconductor in the event of a quench. Therefore, the stabilizer serves to prevent a quench and to protect the superconductor during a quench. This composite structure of many filaments in a matrix material is called a multifilamentary zone. In order to enhance the function of the stabilizer, an additional normal material cladding is usually added around the multifilamentary zone (Ref. 1.17).

With the improvement of the stability of superconducting wire, the superconductor filaments are electrically connected by the matrix material. Some currents flowing in the superconductor filaments may link through the normal matrix due to the electric field induced by an AC or transient magnetic field (Refs. 1.17 and 1.24). Based on consideration of AC losses, which will be explained in the next subsection, the composite wire is twisted at the final stage of wire drawing. Fig. 1.7 illustrates the cut-away view of the structure of a practical superconducting wire which is pictured as a twisted composite wire with a multifilamentary zone and a normal cladding. The appearance of a twisted superconducting wire is similar to a solder-filled small-scale twisted electric cable, therefore, a superconducting wire is sometimes also called a superconducting strand.

I.1.5 AC Losses in Technical Superconducting Wires

The major mechanisms of AC losses are: (1) hysteresis losses, (2) coupling current losses, (3) penetration losses, (4) transport-current losses, and (5) self-field losses.

Hysteresis loss is the most fundamental loss mechanism in a hard superconductor affected by a time-varying field (Refs. 1.17, 1.24, and 1.27). Hysteresis loss is initiated once the superconductor is in the mixed state. This type of loss results from irreversible magnetic flux motion in the imperfect type-II superconductor driven by the external changing field at any frequency. Since hysteresis loss corresponds to flux pinning and flux motion, one can imagine that it is related to the critical current density as well as the size of the superconductor.

As mentioned above, the superconductor filaments in a composite wire are electrically connected by the resistive matrix material. The electric potential, induced by the time-varying magnetic field, drives the currents flowing among superconducting filaments. The induced currents flowing across the resistive material, link the shielding currents in the filaments and form closed current loops transverse to the applied field (Refs. 1.28 to 1.31). The electric potential is proportional to the area, enclosed by these current loops, transverse to the changing field. These special kinds of eddy currents are called coupling currents. At some higher frequency, the coupling current may link all the superconductor filaments together. When this occurs the whole multifilamentary zone behaves like a bulk superconductor. The consequence of this is that a flux jump in a single filament may result in a flux jump in all filaments, which is highly undesirable. Twisting a multifilamentary wire is equivalent to segmenting the area available for induced potential. Due to the twist,

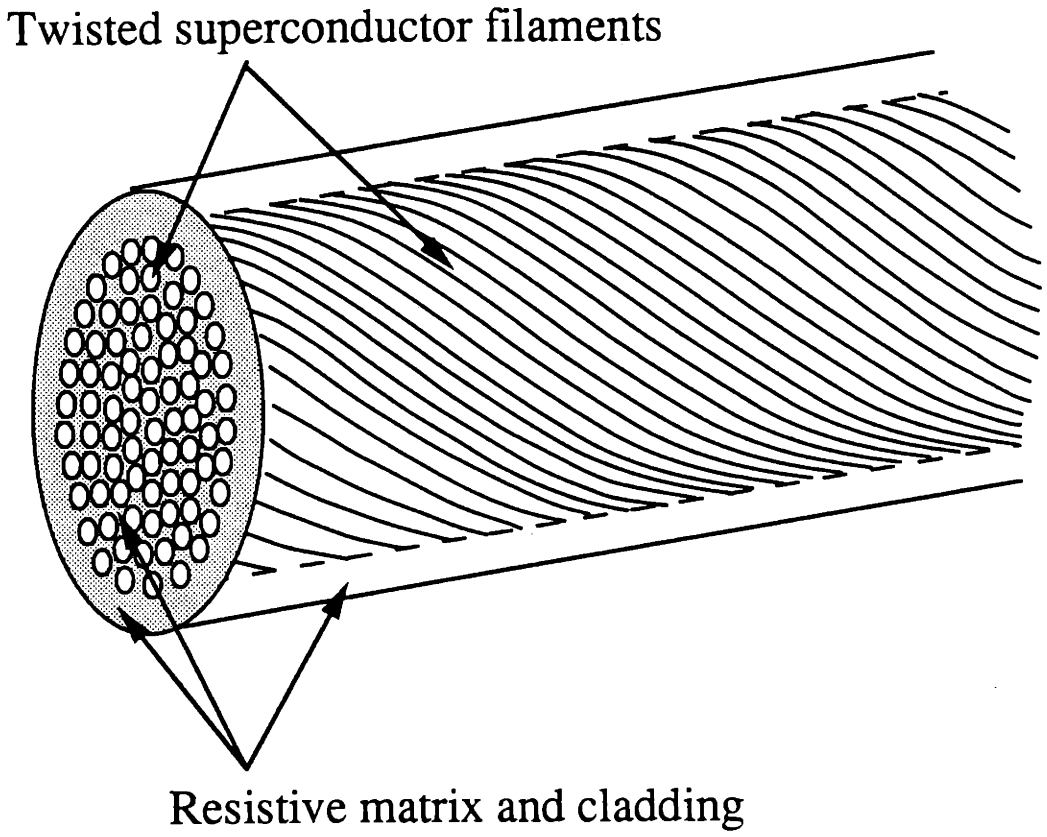

Fig. 1.7 Cut-away view of a twisted multifilamentary superconducting wire.

the electric field between filaments generated by the changing field reverses every half twist pitch. If the twist pitch is short enough, the electric field and thus the coupling currents are kept low, and the filaments are effectively de-coupled. Therefore, a technical superconducting wire is always twisted. The joule heating due to the induced coupling currents flowing in the resistive matrix materials is called coupling (current) loss.

The net electric field in the matrix and the cladding drives the coupling currents to the outer boundary of the multifilament zone. When the current density in the outer-most filament is larger than the critical value of the superconductor, the outer-most filament layer is saturated. The coupling currents will be collected by the next outer-most layer, and so forth. At a certain high frequency, depending on the characteristics of the wire, the whole multifilamentary zone can be saturated (Refs. 1.28, 1.30, 1.32, and 1.33). Theses currents flowing in the saturated layer create a secondary magnetic field trying to screening the whole composite wire from the external field variation. A composite conductor with a saturated layer is like a bulk superconductor penetrated by external field. The loss due to the magnetization caused by the coupling currents flowing in the superconducting filaments in the saturated region is sometimes called penetration loss (Ref. 1.30).

When the current flowing in the superconductor is driven by an external power supply, it is conventionally called transport current as opposed to the induced shielding current. Due to flux pinning, the current flows in the inner region of each superconductor filament, which changes the symmetry of the spatial distribution of the shielding current in the superconducting filament (Refs. 1.17, 1.24, and 1.33). As the external field increases, the area required for the shielding current to flow is also increased, and the region allowable for transport current is reduced. When the transport current density becomes higher than what the superconductor can take in the inner region, the transport current starts to fill in the outer region where the shielding current flows in the opposite direction. The filament is saturated when all the currents are flowing in the same direction. Additional hysteresis type losses due to transport currents is small before the filament is fully penetrated by the external field, but is not negligible after full penetration.

Self-field losses are caused by the interaction of the transport currents and the transverse field induced by the transport currents themselves (Ref. 1.17). For a strand in a superconducting magnet environment, the self-field is usually much smaller than the total applied field generated by all other conductors. Unless the self-field is as significant as the

applied field, the self-field loss of a single strand is usually negligible compared with other types of losses.

Of the loss mechanisms discussed above, hysteresis and transport current losses occur in the superconducting filaments, while coupling current losses take place in the resistive material. The penetration losses are related to the interaction of the coupling currents and the superconductor filaments. The importance of the interactions between different types of losses depend on the external field, the applied current, and the property of the wire (Refs. 1.17, 1.31, 1.33). Since the properties of the wire are affected by the wire design, manufacturing processes, etc., some of the parameters important to the prediction of the AC loss can not be obtained analytically. This is especially true when the wire construction becomes complicated.

I.2 PROBLEM STATEMENT

I.2.1 Introduction

The subject of this thesis was developed out of research on the United State Demonstration Poloidal Coil (US-DPC) (Ref. 1.34). The US-DPC is a prototype ohmic heating coil designed as a development step in pulsed superconducting magnet technology. It was designed and built by the Superconducting Magnet Development Group at MIT and tested at the Japan Atomic Energy Research Institute (JAERI) in late 1990. One of the major goals of the US-DPC experiment was evaluating the AC losses in this large-scale coil at ramp field operation up to 10 T at 10 T/s (Ref. 1.34).

During the design stage, existing AC-loss models were used to pre-estimate the loss behavior of the US-DPC cable. It was found that the existing AC-loss models were mostly developed for analyzing the loss of a composite superconductor affected by a time-changing field with a small field variation. Existing loss models are not totally adequate for simulating large field variation conditions such as those to be generated by an ohmic heating coil in a fusion reactor. It was necessary to extend the existing models to all the expected operating conditions of a pulse coil to provide adequate AC-loss information for designing a stable magnet system.

A single composite superconducting wire may contain thousands of fine superconducting filaments embedded in a matrix. The filaments may be uniformly distributed or clustered in several local regions. The distribution of the electric resistivity of the matrix material may be uniform or may vary by orders of magnitude in different regions. Two key parameters affecting the accuracy of AC-loss calculations are the effective values of the filament size and the resistivity of the matrix along the paths of the coupling current loops. These two parameters depend heavily on the wire design and manufacturing process, and, in practice, may be dramatically different from the design value. The most reliable knowledge of these two key parameters must be obtained experimentally. Single-strand AC-loss measurement is thus indispensable in characterizing AC losses in a single strand as well as a full-size cable.

During the investigation of the existing experimental methods, it was determined that absolute values of the AC losses are required to evaluate those two AC-loss parameters as well as justify the calculated AC losses. Calorimetric measurement is the primary method satisfying such requirements (Ref. 1.35). However, calorimetric measurements have never been performed on a current-carrying Nb_3Sn wire for the current and field conditions relevant to the operation of a ramp field magnet such as the US-DPC. A new apparatus based on the isothermal calorimetric method must be developed by taking into account the Lorentz force effect on the brittle Nb_3Sn single strand. A preliminary experimental apparatus was originally constructed by Takayasu, et al. (Ref. 1.36) who improved the efficiency of this method by coupling an electronic feedback control circuit to the calorimetric system. From the experiences of using this apparatus, it was found that the efficiency of the measurement could be enhanced by improving the stability of the feedback control circuit. Furthermore, the accuracy of AC-loss measurement of a current-free test wire was challenged by field-dependent noise as well as significant noise-to-signal ratio. This thesis work thus includes re-design and construction of a reliable experimental system for characterizing AC losses of current-carrying wires under the current and field conditions simulating the operation of the US-DPC experiment.

An additional two types of wire designed for ramp field applications were also examined using this new apparatus under similar current and field conditions. The cross sectional constructions of these three different composite superconductors are general enough to represent most typical commercial superconducting wires manufactured for ramp field magnet applications. Thus, this thesis research was generalized to investigate the AC losses of composite superconductors for high-current ramp-field applications.

I.2.2 Thesis Scope and Goals

The goal of this thesis is to improve the understanding of AC losses in superconducting magnets for ramp field applications such as the ohmic heating coils in a nuclear fusion reactor and the dipole magnets in a particle accelerator. More specific goals are to develop an experimental method for measuring AC losses under simulated operating conditions, to understand single-strand AC-loss characteristics, and to apply single-strand test results to the cable for a large-scale ramp field superconducting magnet. In order to accomplish these goals, this thesis contains five major tasks:

(1) extension of existing hysteresis-loss and coupling-loss models,
(2) design and construction of an AC-loss measurement system,
(3) measurement of AC losses of composite superconducting strands,
(4) development of analytical models for newly found loss behavior, and
(5) development of a computational methodology for comparing the AC losses of a single-strand with those of a cable for a pulse magnet.

Chapter II contains a general review of existing analytical AC-loss models relevant to this thesis work, which provides a background for further discussions of AC-loss analyses. The review includes hysteresis loss, coupling current loss, penetration loss, and additional losses due to both DC and AC transport currents. In Chapter II the formulae calculating coupling current loss of a single-strand with a multi-layer cross sectional construction are extended to adopt the configurations of all three wires tested.

Two types of field variation are of interest to the present research: (1) a large peak-to-peak triangular cyclic field, and (2) a small sinusoidal wave-form (ripple) field superimposed on various large DC bias fields. The first field condition is used to simulate the ramp field operation of a pulse magnet. The ripple field condition is adopted to approach the ideal condition applied in the existing AC-loss models. In both cases, the AC losses must be calculated with a field-dependent critical current density profile which has not been explicitly included in the existing hysteresis models. In Chapter III, the field-dependent semi-empirical critical current density expressions are first examined, followed by a revision of the existing 2-D hysteresis-loss analysis.

One of the most fundamental contribution of this thesis work is the development of an experimental method for laboratory-scale single-strand AC-loss measurement with the field

and current conditions simulating ramp field operation of a superconducting pulse magnet. The new experimental system developed in this thesis work, is based on an improved isothermal calorimetric method. This was the first experimental setup which evaluates absolute AC losses of a current-carrying Nb_3Sn single-strand under simulated pulse magnet operating conditions. Without any modification, this apparatus can be used not only to estimate different types of single-strand AC loss but also to reliably measure the critical currents of the AC-loss test wire. Such a multi-functional AC-loss measurement system has never been described in the literature. Chapter IV includes a brief review of existing AC-loss experimental techniques, followed by a detailed discussion of the design and fabrication of this improved isothermal calorimetric measurement system.

Chapter V contains AC-loss test results of three different types of wire developed for ramp field magnet applications. Analytical AC losses, calculated with the coupling-loss and the hysteresis-loss models modified in Chapters II and III, are compared with the experimental results. Good agreement between the analytical AC losses and the test results was found in two types of wire without carrying transport current. The US-DPC wire shows a local maximum loss in the ramp rate dependent loss profile in a very low frequency regime, which has never been experimentally observed or analytically predicted. The measured additional AC losses in all three current-carrying wires affected by an AC field are also compared with the model predictions.

A new model is proposed in Chapter VI to provide a possible explanation for the local maximum loss in the low ramp rate regime which was found experimentally in the US-DPC wire. This chapter presents the full derivation of this new model which accounts for the collective coupling current effects in a wire construction similar to that of a US-DPC wire. The proposed model is the first analytical model attempting to understand the special AC-loss characteristics in a US-DPC wire.

A large amount of laboratory-scale single-strand AC-loss measurements have been performed within the US-DPC program. In Chapter VII a methodology for comparing the AC losses of US-DPC wire with US-DPC cable is given. A prediction scheme for the AC losses in a full-size cable is developed out of the loss comparison process. The practical scheme uses the formulae applied in this thesis. AC-loss parameters, required in the calculation, can be evaluated from the laboratory-scale single-strand measurements as demonstrated in the experimental work. The prediction scheme for the AC losses of a full-

size cable, similar to that of US-DPC, is one of the most important applications of this thesis work.

In Chapter VIII a general review of this thesis work is made and conclusions are given. Possible future developments on the basis of the present work are recommended.

I.3 REFERENCES

1.1 Haubenreich, P.N., et al., 'Superconducting magnets for fusion,' Nuclear Fusion, Vol. 22, 1982, p. 1209.

1.2 FED-INTOR, Chapter IX, 1982.

1.3 Brianti, G., and Komarek, P., 'Demands on advanced superconductors by large projects in fusion and particle accelerators,' Cryogenics, Vol. 27, 1987, p. 115.

1.4 Summers, L.T., and Miller, J.R., 'The developments of superconductors for applications in high-field, high-current-density magnets for fusion research,' IEEE Trans. Magnetics, MAG-23, No. 2, 1987, p.1552.

1.5 *ITER MAGNET SYSTEM*-Concept and Design Activity, International Atomic Energy Agency, Vienna 1990.

1.6 Duchateau, J.L., Ciazynski, D., and Vallier, J.C., 'Nb3Sn superconductor for fusion application: facing NET-ITER specifications, evaluation of industrial capability,' presented in ASC'92, Chicago, August 1992.

1.7 Gilbert, W.S., et al., 'magnetic field decay in model SSC dipoles,' IEEE Trans. Magnetics, MAG-25, 1989, p. 1459.

1.8 Herrup, D.A., et al., 'Time variations of fields in superconducting magnets and their effects on accelerators,' IEEE Trans. Magnetics, MAG-25, 1989, p. 1643.

1.9 Hanft, R.W., et al., 'Studies of time dependence of fields in Tevatron superconducting dipole magnets,' IEEE Trans. Magnetics, MAG-25, 1989, p. 1647.

1.10 Goldfarb, R.B., and Spomer, R.L., 'magnetic characteristics and measurements of filamentary Nb-Ti wire for the Superconducting Super Collider,' Adv. Cryog. Eng., Vol. 36, 1990, p. 215.

1.11 Minervini, J.V., et al., 'Cable-in-conduit conductor concept for the GEM detector magnet,' presented in ASC'92, Chicago, August 1992.

1.12 Iwasa, Y., 'High speed magnetically levitated and propelled mass ground transportation,' Chapter 6 of *Superconducting Machines and Devices*, ed. Foner, S. and Schwartz, B.B., Plenum, New York, 1974.

1.13 Kyotani, Y., 'Recent progress by JNR on maglev,' IEEE, MAG-24, 1988, p. 804.

1.14 Klimenko, E.Y., et al., 'Superconducting magnet for high speed ground transportation,' Cryogenics, 30, 1990, p. 41.

1.15 Gamble, B., Cope, D., and Leung, E., 'Optimization of superconducting magnet systems for maglev applications,' presented in ASC'92, Chicago, August 1992.

1.16 Saitoh, T., et al. 'electromagnetic force and eddy current loss in dynamic behavior of a superconducting magnetically levitated vehicle,' presented in ASC'92, Chicago, August 1992.

1.17 Wilson, M.N., *Superconducting Magnets*, Oxford Science Publications, 1983.

1.18 Deaver, B.S., 'H.Kamerlingh Onnes symposium on the origins of applied superconductivity,' IEEE Trans. Magnetics, MAG-23, No. 2, 1987, p. 354.

1.19 Smathers, D.B., 'A15 Superconductors', in Metals Handbook, Vol. 2, 10th Ed.: Properties and Selection, ASM International, 1990.

1.20 Hulm, J.K. and Matthias, B.T., 'Overview of superconducting materials development,' Chpater 1 in *Superconductor materials Science*, Ed. Foner S., and Schwartz, B.B., Plenum Press, 1981.

1.21 Schrieffer, J.R., *Theory of Superconductivity*, W.A. Benjamin, Inc.,1964.

1.22 De Gennes, P.G., *Superconductivity of Metals and Alloys*, translated by P.A. Pincus, 1965.

1.23 Saint-James, D., Sarma, G., and Thomas, E.J., *Type II Superconductivity*, Pergamon Press, 1969.

1.24 Brechna, H., *Superconducting Magnet Systems*, Springer-Verlag, 1973.

1.25 Tinkham, M., *Introduction to Superconductivity*, R.E. Krieger Publishing Co., Inc., 1975.

1.26 Rose-Innes, A.C., and Rhoderick, E.H., *Introduction to Superconductivity*, Pergamon press, 1978.

1.27 Orlando, T.P., and Delin, K.A., *Foundations of Applied Superconductivity*, Addison-Wesley, 1991.

1.28 Morgan, G.H., 'Theoretical behavior of twisted multicore superconducting wire in a time-varying uniform magnetic field,' J. Appl. Phys., Vol. 41, No. 9, 1970, p. 3673.

1.29 Carr, W.J., 'AC loss in a twisted filamentary superconducting wire, I,' J. Appl Phys., Vol. 45, No. 2, 1974, p. 929.

1.30 Ries, G., 'AC-losses in multifilamentary superconductors at technical frequencies,' IEEE Trans. Magnetics, Vol. MAG-13, No. 1, 1977, p. 524.

1.31 Turck, B., 'Coupling losses in various outer normal layers surrounding the filament bundle of a superconducting composite,' J. Appl. Phys., Vol. 50, No. 8, 1979, p. 5397.

1.32 Zenkevitch, V.B., Romanyuk, A.S., Zheltov, V.V., 'Losses in composite Superconductors at high levels of magnetic field excitation: part 1,' Cryogenics, 1980, p. 703.

1.33 Ogasawara, T., et al., 'Transient field losses in multifilamentary composite conductors carrying dc transport currents,' Cryogenics, 1980, p. 216.

1.34 Painter, T.A., et al. 'Test Data from the US-Demonstration Poloidal Coil Experiment', PFC/RR-92-1, also DOE/ER/54110-1, Plasma Fusion Center, Massachusetts Institute of Technology, January 1992.

1.35 Ekin,J.W., 'Superconductors,' Ch. 13 in *Materials at Low Temperatures*, ed. by Reed, R.P. and Clark, A.F., American Society for Materials, 1983.

1.36 Takayasu, M., et al. 'Calorimetric measurement of AC loss in Nb_3Sn superconductor,' Proceedings of MT-11, Tsukuba, Japan, August 1989, p.1033.

CHAPTER II

EXISTING AC-LOSS MODELS FOR TWISTED MULTIFILAMENTARY SUPERCONDUCTING WIRES

II.1 INTRODUCTION

Hysteresis loss, coupling current loss, penetration loss, and additional loss due to transport currents are the four major types of AC losses to be considered for a twisted multifilamentary superconducting wire in an environment simulating the field and current conditions of a high-current high-field pulse magnet. Existing analytical models regarding these AC losses are reviewed in this chapter. The existing analyses of the hysteresis and penetration losses which are important to the development of new models in the present work, are examined in better detail. The existing coupling loss model is slightly modified to include the constructions of all the composite wire of interest to the present work.

II.2 HYSTERESIS LOSSES

II.2.1 Introduction

Analyses of magnetization and hysteresis loss in a type-II superconductor were not available until the development of an important model by Bean and London in early 1960 (Refs. 2.1 to 2.3) which is conventionally called Bean model. The Bean model is a macroscopic model which describes the magnetization of a type-II superconductor using spatially averaged electromagnetic properties of the superconductor. The spatial distribution of the current density in a superconductor is assumed to be either of the critical value or zero in this model. Therefore, the Bean model is also called the critical state model (Refs. 2.4 and 2.5). The Bean model in 1-D slab geometry, although highly simplifying the microscopic superconductivity theories, was surprisingly accurate in predicting the experimental results. Since the Bean model was developed, hysteresis-loss analyses have been performed extensively, both analytically and numerically, in 1-D slab and 2-D cylindrical geometries by many other authors (Ref. 2.6 to 2.14).

In this section, the assumptions and the limitations in making the Bean model are first reviewed, followed by the 1-D and 2-D analytical hysteresis-loss expressions developed by other authors based on this model. All the equations are expressed in the MKS unit system.

II.2.2 Critical State Models

The critical state model developed by C.P. Bean, is the most important analysis of the hysteresis loss in a type-II superconductor (Ref. 2.1 to 2.3). The phenomenological model describes a succession of quasi-static vortex motion in the superconductor by using a macroscopic internal magnetic field intensity, $\mathbf{B}_i$, which is characterized by a bulk critical current density, $\mathbf{J}_c$. When the transport current is zero, the assumptions and limitations applied in the critical state model are (Ref. 2.4)

(1) The magnetic property of the superconductor can be described by a bulk J_c;
(2) The superconductor in the applied changing field is in the mixed state;
(3) The superconductor has no flux jump during the applied field variation;
(4) The J_c remains constant in the region of field penetration;
(5) The superconductor is in isothermal condition, and no temperature change affects J_c;
(6) The dynamic and static critical current densities are the same;
(7) The responding time of the current and field re-distribution to a changing field is short.

In a strongly pinned type-II superconductor, as the external changing field is increased, an induced current will flow in a thin sheath on the surface of the material at a current density higher than the $|J_c|$. The sheath current will decay resistively and the magnetic field will start to penetrate the interior of the material. As the current density reduces to $|J_c|$, the penetration will stop and the current density remains constant. The region which has not been penetrated by the flux has zero current. Thus, a superconductor is said to be in the critical state if the current density is either J_c or zero in any region of the material (Ref. 2.7). In the Bean model, the assumption of a sharp boundary between neighboring regions of different current densities, also called sharp penetration front, is one of the key step in simplifying the magnetization and hysteresis loss calculation (Ref. 2.4). For simplicity, Bean further assumed that the critical current density remains constant during the change of the external field, i.e. J_c is not a function of B. Combining the above assumptions with the volume-averaged macroscopic Ampere's law, the Bean's critical state model for a type-II superconductor without carrying a transport current is simply written as (Ref. 2.4)

$$\nabla \times \mathbf{B}_i = \mu_0 \mathbf{J}, \quad \text{with } |\mathbf{J}| = J_c \text{ or } 0 \tag{2.1}$$

where $\mathbf{B}_i$ is the internal field of the superconductor. The critical current density is a known constant once the applied field is fixed, which is the only empirical parameter in the model. The magnetization and the hysteresis loss can be calculated when the internal field in Eq. (2.1) is solved. Although the properties of the superconductor was highly simplified in the Bean model, the calculated magnetization was consistent with the experimental results of V_3Ga in a lower field region (< 1 T) (Ref. 2.3).

Two important comments on the assumption of a sharp penetration front were discussed in Ref. 2.3. The first concern was about the instantaneous spatial distribution of the current densities. The sharp boundary assumption of the current density distribution, that is $|J| = J_c$ in the flux penetrated region and $J = 0$ in the non-penetrated region, is never completely valid (Ref. 2.3). Since the current density decays exponentially into the non-penetrated region, the decaying distance which is also called the London penetration depth, was estimated on the order of 0.1 μm (Refs. 2.3 and 2.5). However, as long as the size of the superconductor is much greater than the decaying distance, this assumption is approximately true. The second comment was about the temporal variation of the penetration front. Since the flux pinning may be thermally weakened, the flux may cross the sharp boundaries which introduces a discrepancy in the critical state model (Ref. 2.3). However, from experimental evidence, the modification of the sharp boundary due to the temporal decay of the critical current density has been found to be negligible (Ref. 2.6).

The Bean model was generalized by Kim et al. (Ref. 2.6) who modified the above mentioned assumptions (1) and (4) in Bean's approach. In the Bean model the critical current in the superconductor is the prime factor in determining the magnetization. Kim et al. assumed that every macroscopic region of a type-II superconductor in the mixed state carries a critical current determined by the local magnetic field in that region. Thus, the critical current density in Kim's model varies both spatially in the superconductor and temporally by the external changing field. Also, from their measurement, an empirical field-dependent critical current density fitting equation was postulated as (Ref. 2.6)

$$J_c(B_e) = \frac{J_0 \cdot B_0}{B_0 + B_e} \tag{2.2}$$

with two fitting parameters J_0 and B_0 obtained from experiment, where the J_0 is the extrapolated $J_c(0)$, and B_0 is the magnitude of the field at which $J_c(B_0) = 0.5\ J_0$. Eq. (2.2) has been widely applied to approximate the critical current density and field relation of various superconductors due to its simplicity. However, it has also been found that Eq. (2.2) can not simultaneously fit both low and high field critical current densities for some technical superconducting wires such as Nb_3Sn and NbTi (Ref. 2.16). A better expression for the $J_c(B_e)$ will be discussed later.

II.2.3 1-D Slab Geometry

As seen in Fig. 2.1, when a uniform external field B_e is in parallel to the surface of an infinite superconducting slab with a thickness of 2a, by 1-D Ampere's law the critical state model simply states that (Ref. 2.12)

$$\frac{dB_i}{dx} = \mu_0 J_c \tag{2.3}$$

where B_i is the internal field in a superconductor. With the boundary condition of $B_i = B$ at $x = a$, where the applied field, B, is the field applied directly to the surface of the superconductor, the internal field is solved as

$$B_i = B + \mu_0 J_c\,(x - a), \quad \text{for } x > 0. \tag{2.4}$$

For a bulk superconductor in an external field B_e, the applied field is simply $B = B_e$. However, in a composite superconducting wire, the 'applied field' can be quite different from the 'external field' (Ref. 2.11), which will be reviewed in better detailed in Section II.3.2.

The relation between the changes of the internal field and the current density distributions in a slab are shown in Fig. 2.2 (Refs. 2.12 and 2.16). As seen in Fig. 2.2(a), starting from the virgin (flux-free) state, the slab is first partially penetrated by the applied field. The boundary of flux penetration before it reaches the center of the slab can be located by setting $B_i = 0$ in Eq. (2.4). Thus,

$$x_p = a - \frac{B}{\mu_0 J_c} \tag{2.5}$$

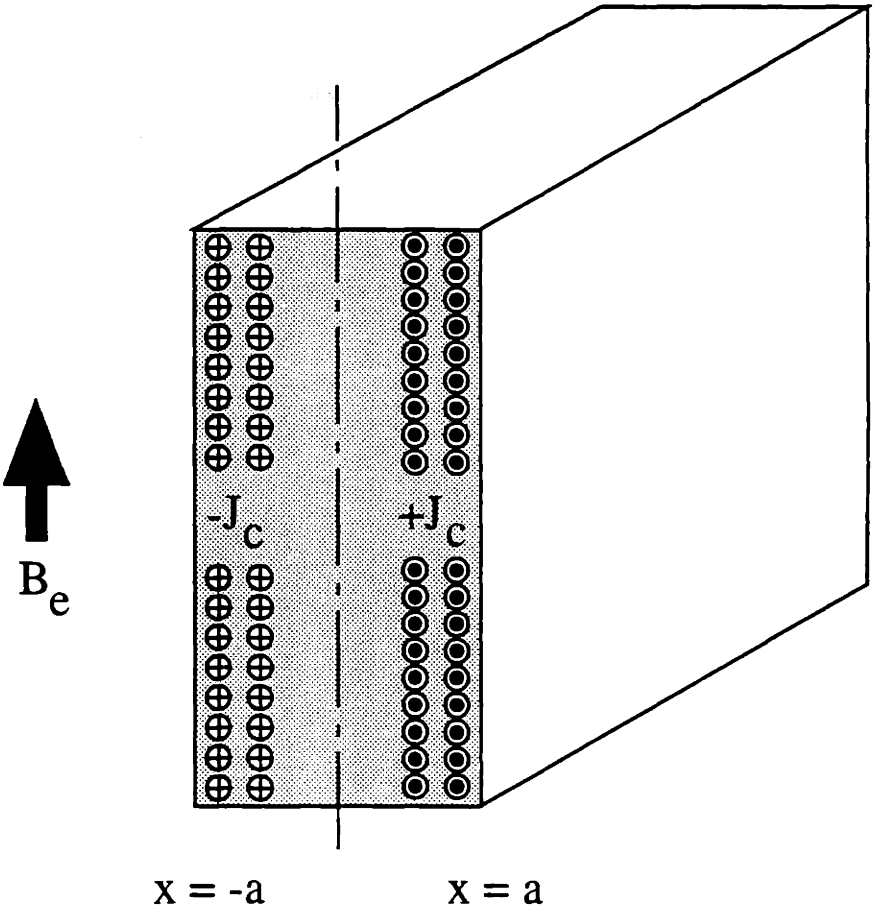

Fig. 2.1 An infinite superconducting slab with a thickness of 2a in a uniform changing field B_e

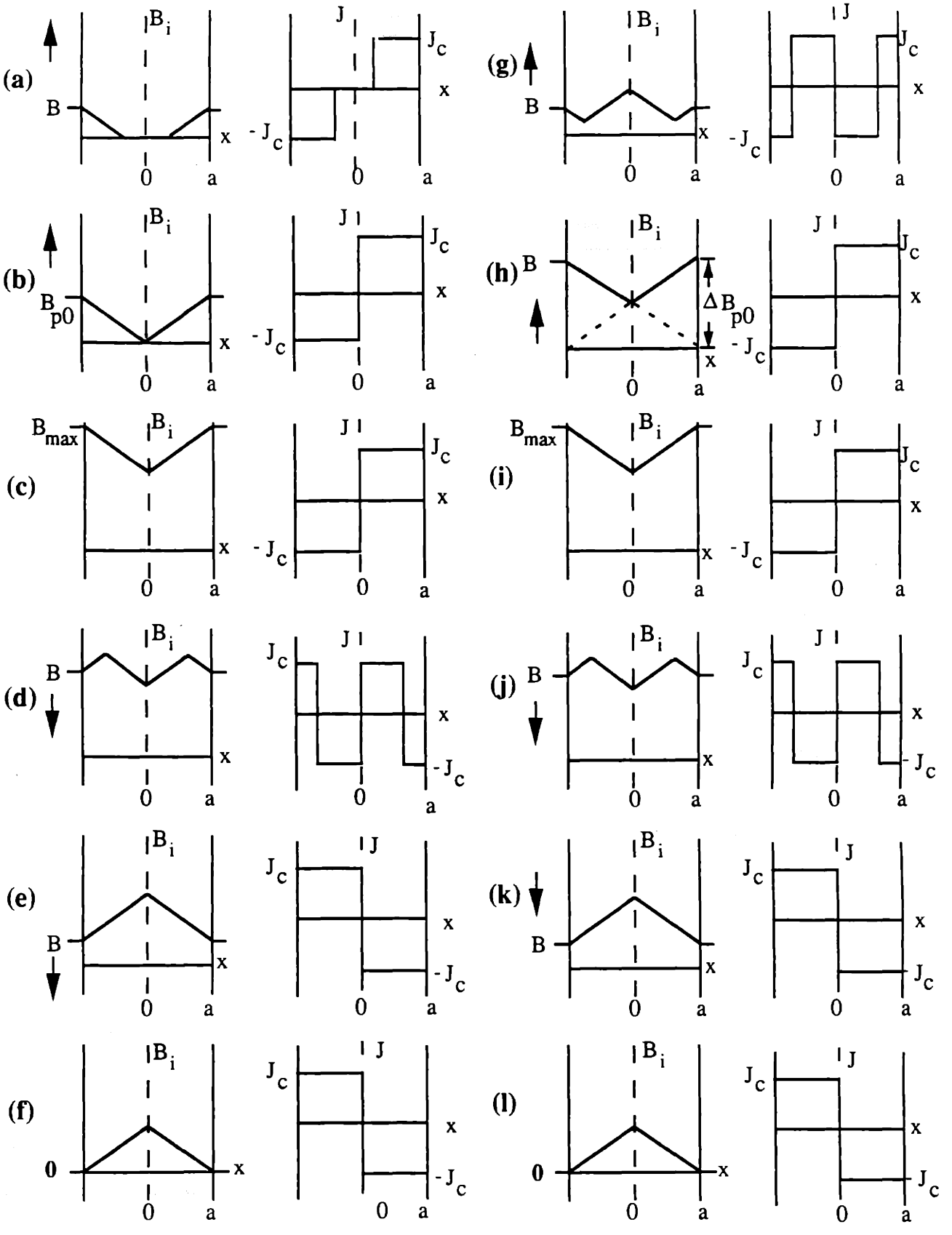

Fig. 2.2 Field and current distributions in a type II superconducting slab based on Bean's critical state model; B_i = internal field, B = applied field, ΔB = peak-to-peak field, B_{p0} = penetration field from virgin state, ΔB_{p0} = penetration field in non-virgin state (Refs. 2.12 and 2.16).

The slab is said to be fully penetrated as the penetration boundary reaches the center of the slab as shown in Fig. 2.2(b), and is filled with critical currents everywhere. Thus, a penetration field for virgin state, B_{p0}, is defined as the applied field at which the first full penetration occurs, which is obtained from Eq. (2.5) by letting $x_p = 0$ (Ref. 2.12). Then

$$B_{p0} = \mu_0 J_c a \tag{2.6}$$

Fig 2.2(f) shows that when the applied field returns to zero from its maximum, B_{max}, part of the flux is trapped in the superconductor. Figs. 2.2(f) to 2.2(l) represent a second field cycle with B starting from zero and the superconductor in a non-virgin state. As shown in Fig. 2.2(h), the flux does not penetrate the slab until the external field reaches ΔB_{p0} which is the first penetration field for the non-virgin state starting from the zero field. In the critical state model, J_c = constant and ΔB_{p0} is simply equal to $2B_{p0}$ (Ref. 2.7), i.e.

$$\Delta B_{p0} = 2\mu_0 J_c a \tag{2.7}$$

In a cyclic changing field with a given B_{max} kept constant, the field and current variations after the first cycle are the same as those in the second cycle.

The magnetization of the superconductor $\mu_0 M(B)$ is expressed as (Ref. 2.12)

$$-\mu_0 M(B) = B - \frac{1}{V}\int_V B_i \, dV \tag{2.8}$$

where V is the volume of the superconductor. In an infinite slab, the magnetization is given by (Ref. 2.12)

$$-\mu_0 M(B) = B - \frac{1}{a}\int_0^a B_i(x) \, dx \tag{2.9}$$

The hysteresis loss per unit volume per cycle, Q_h, is simply the area covered by the magnetization curve, that is (Ref. 2.12)

$$Q_h = -\oint_{\text{cycle}} M(B)\, dB \qquad (2.10)$$

When the applied field is smaller than ΔB_{p0}, the magnetization of each half cycle is expressed as (Ref. 2.7)

$$-\mu_0 M = B - \frac{1}{4}\frac{B^2}{B_{p0}} \qquad \text{for } B \le \Delta B_{p0},\ \dot{B} > 0 \qquad (2.11)$$

and

$$-\mu_0 M = B - \left[\frac{1}{2}\frac{B \cdot B_{max}}{B_{p0}} - \frac{1}{4}\frac{B^2}{B_{p0}}\right] \qquad \text{for } B \le \Delta B_{p0},\ \dot{B} < 0 \qquad (2.12)$$

If the applied field is cycled between 0 and B_{max}, with the range of the field variation $\Delta B = B_{max}$ less than ΔB_{p0}, the loss integration for each half cycle are expressed as

$$Q\uparrow = \frac{1}{\mu_0}\left[\frac{1}{2}B_{max}^2 - \frac{1}{12}\frac{B_{max}^3}{B_{p0}}\right] \qquad \text{for } B_{max} \le \Delta B_{p0},\ \dot{B} > 0 \qquad (2.13)$$

and

$$Q\downarrow = \frac{1}{\mu_0}\left[-\frac{1}{2}B_{max}^2 + \frac{1}{6}\frac{B_{max}^3}{B_{p0}}\right] \qquad \text{for } B_{max} \le \Delta B_{p0},\ \dot{B} < 0 \qquad (2.14)$$

The hysteresis loss per cycle per unit volume is the sum of the integrations in two half cycles which is given as (Refs. 2.7, 2.12, and 2.16)

$$Q_h = \frac{B_{max}^2}{2\mu_0}\frac{B_{max}}{3\,\Delta B_{p0}} \qquad \text{for } B_{max} \le \Delta B_{p0} \qquad (2.15)$$

The hysteresis loss $Q_{h,p0}$ at $B_{max} = \Delta B_{p0}$ becomes

$$Q_{h,p0} = \frac{1}{3}\frac{\Delta B_{p0}^2}{2\mu_0} \qquad (2.16)$$

When the applied field is larger than the penetration field, the magnetization is simply

$$- \mu_0 M = \pm \frac{1}{2} B_{p0} \qquad \text{for } B \geq \Delta B_{p0} \tag{2.17}$$

The positive sign is used when the applied field is increased. The hysteresis loss is the sum of the loss integration beyond the ΔB_{p0} in an up-sweep and that below the B_{max} - ΔB_{pm} in a down-sweep. Therefore,

$$\Delta Q_h = - \int_{\Delta B_{p0}}^{B_{max}} M(B)\, dB - \int_{B_{max} - \Delta B_{pm}}^{0} M(B)\, dB \tag{2.18}$$

where ΔB_{pm} is the first penetration field as the field reduced from B_{max}. Since J_c = constant in the Bean model, ΔB_{pm} is the same as ΔB_{p0}. From Eqs. (2.17) and (2.18), the loss expression in this region is reduced to

$$\Delta Q_h = - 2 \int_{\Delta B_{p0}}^{B_{max}} M(B)\, dB = \frac{1}{2\mu_0} \Delta B_{p0} \left(B_{max} - \Delta B_{p0} \right) \tag{2.19}$$

Similarly, the hysteresis loss in the region of 0 to ΔB_{p0} during the up-sweep and in the region of B_{max} to B_{max} - ΔB_{p0} during the down-sweep can be reduced to

$$- \int_{0}^{\Delta B_{p0}} M(B)\, dB - \int_{B_{max}}^{B_{max} - \Delta B_{pm}} M(B)\, dB = Q_{h,p0} \tag{2.20}$$

where $Q_{h,p0}$ is the penetration field at $B_{max} = \Delta B_{p0}$ as evaluated in Eq. (2.16).

The hysteresis loss per cycle per unit volume is thus the sum of ΔQ_h and $Q_{h,p0}$ which is also written as (Refs. 2.7, 2.12, and 2.16)

$$Q_h = \frac{B_{max}^2}{2\mu_0} \left\{ \frac{\Delta B_{p0}}{B_{max}} - \frac{2}{3} \left(\frac{\Delta B_{p0}}{B_{max}} \right)^2 \right\} \qquad \text{for } B_{max} \geq \Delta B_{p0} \tag{2.21}$$

As a summary, when a field is applied in parallel to the surface of an infinite superconductor slab, with the applied field cycled between 0 and B_{max}, the hysteresis losses per cycle per unit volume, based on Bean model, are given as

$$Q_h = \frac{B_{max}^2}{2\mu_0} \frac{1}{3} \frac{B_{max}}{\Delta B_{p0}} \qquad \text{for } B_{max} \le \Delta B_{p0} \qquad (2.15)$$

and

$$Q_h = \frac{B_{max}^2}{2\mu_0} \left\{ \frac{\Delta B_{p0}}{B_{max}} - \frac{2}{3} \left(\frac{\Delta B_{p0}}{B_{max}} \right)^2 \right\} \qquad \text{for } B_{max} \ge \Delta B_{p0} \qquad (2.21)$$

Both expressions are in the units of Joule / cycle / m^3 - superconductor.

II.2.4 2-D Cylindrical Geometry

II.2.4.1 Introduction

Two dimensional AC-loss analysis of a cylindrical superconductor in a transverse changing field has been done by a few authors (Refs. 2.7 to 2.12). In general, most of the models or computations were developed on the basis of Bean model with J_c = constant, and all required numerical calculations. Due to the complexity of the numerical processes which is not of interest to this thesis work, only the principle of the analysis will be roughly reviewed. Simple analytical formulae deduced from either the numerical or the experimental results in the references are summarized in this section as the foundation for more general expressions derived in Chapter III.

The major difficulty in 2-D modeling is found in determining the location and the shape of the flux penetration front (Refs. 2.8, 2.9, 2.11 to 2.13). Mathematically, this is a two dimensional quasi-static moving boundary problem which can not be solved analytically. All the authors used a preset function such as ellipse, polynomial, or a set of polygonal functions with undetermined parameters or coefficients for the contour (Refs. 2.7 to 2.12). The region outside the contour is filled with critical screening currents induced by the transverse changing field. The external field inside the contour should be cancelled by the field due to the screening current. The parameters for the contour of flux penetration front were then determined numerically by optimizing the position and the shape of the contour till the field generated by the screening current matches the external field at some locations.

The optimization schemes and the number of matching points depended on the individual preferences.

Good comparisons among the calculated contours or between the calculated and measured magnetization curves have been reported in Refs. 2.7 to 2.12. It is interesting to identify the sensitivity of the calculated hysteresis losses to different contour shapes. Wilson (Ref. 2.7) used a rather crude elliptical contour with a single optimization parameter: ratio of the major axis to minor axis. The field matching condition was simply selected at the center of the cylinder (Ref. 2.7). Both Ashkin and Zenkevitch, et al. used more complex polygonal functions with undetermined coefficients to calculate the contour. The contour was determined when the screening current generated field on the contour becomes constant (Refs. 2.8 and 2.11). For $\Delta B < \Delta B_{p0}$, loss expression in integral form was given by Wilson. Fig. 2.3 shows normalized hysteresis losses based on these two very different contour representations for this lower field region. The largest deviation is estimated about 6.5% at $\Delta B / \Delta B_{p0} \approx 1$. In the region of $\Delta B > \Delta B_{p0}$, the difference between the crude and complex approaches decreases as the ΔB becomes larger. The comparison indicates that the hysteresis loss is not sensitive to the contour representations for the flux penetration boundaries.

Zenkevitch, et al. (Ref. 2.11) deduced very simple magnetization formulae for transverse field conditions from their numerical calculations. The calculated results from these formulae have been verified by their measurements (Ref. 2.13). Pang, et al. (Ref. 2.10) derived a set of semi-empirical formulae from the magnetization measurements. These semi-empirical formulae are applicable to both NbZr and NbTi samples tested in their experiments. The formulae by Zenkevitch, et al. and by Pang, et al. are in the same forms. The magnetization and hysteresis-loss formulae given by Zenkevitch, et al., based on the Bean model, are summarized here.

II.2.4.2 Existing Expressions Based on Bean Model

When a cylindrical superconductor of radius r_f is affected by a transverse time-varying applied field B, the magnetization and hysteresis-loss equations given by Zenkevitch et al. in Ref. 2.11 are transformed and summarized in the followings.

(i) For an initial rising field:

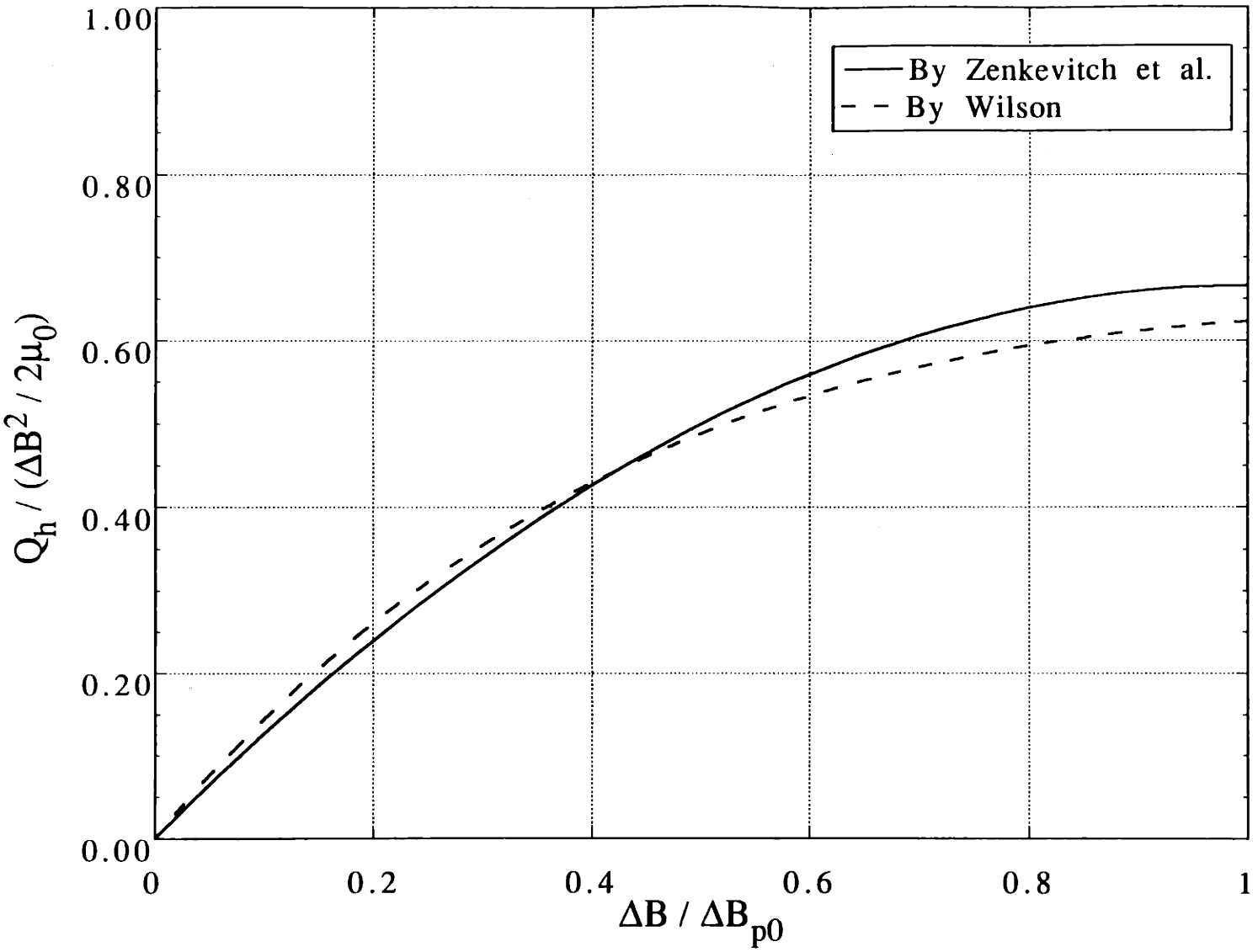

Fig. 2.3 Comparisons of normalized hysteresis losses due to different contour representations for the flux penetration boundaries.

The penetration field in an initial virgin state is

$$B_p = \frac{2}{\pi} \mu_0 J_c r_f \tag{2.22}$$

and the empirical magnetization equations are expressed as

$$\mu_0 M = \left[-\frac{2}{3} \frac{B^3}{B_p^2} + 2 \frac{B^2}{B_p} - 2B \right] \cdot \text{sign}(B); \quad \text{for } B \le B_p \tag{2.23}$$

$$\mu_0 M = -\frac{2}{3} B_p \cdot \text{sign}(B); \quad \text{for } B \ge B_p \tag{2.24}$$

(ii) For a cyclic field

The penetration field of a superconductor in a cyclic applied field is given as $\Delta B_p = 2B_p$, or

$$\Delta B_p = \frac{4}{\pi} \mu_0 J_c r_f \tag{2.25}$$

With B_m representing the field at the end of the preceding cycle which can be B_{max} or B_{min}, the magnetizations in cyclic field conditions are

$$\mu_0 (M - M_m) = \left[-\frac{2}{3} \frac{(B - B_m)^3}{4B_p^2} + 2 \frac{(B - B_m)^2}{2B_p} - 2(B - B_m) \right] \cdot \text{sign}(B - B_m); \quad \text{for } |B - B_m| \le \Delta B_p \tag{2.26}$$

$$\mu_0 (M - M_m) = -\frac{4}{3} B_p \cdot \text{sign}(B - B_m); \quad \text{for } |B - B_m| \ge \Delta B_p \tag{2.27}$$

The expressions for the irreversible magnetization, $\mu_0 M_m$, are distinguished by comparing the peak-to-peak field change, $\Delta B = B_{max} - B_{min}$, with the ΔB_p. Thus,

$$\mu_0 M_m = \frac{2}{3} B_p \left[1 + \left(\frac{\Delta B}{2B_p} - 1 \right)^3 \right] \cdot \text{sign}(B - B_m); \quad \text{for } \Delta B \le \Delta B_p \tag{2.28}$$

$$\mu_0 M_m = \frac{2}{3} B_p \cdot \text{sign}(B - B_m); \quad \text{for } \Delta B \ge \Delta B_p \tag{2.29}$$

After integrating the magnetization over the applied field as was done in the 1-D case, the hysteresis losses of a cylindrical superconductor wire in a transverse cyclic field are given as

$$Q_h = \frac{\Delta B^2}{2\mu_0}\left[\frac{4}{3}\frac{\Delta B}{\Delta B_p} - \frac{2}{3}\left(\frac{\Delta B}{\Delta B_p}\right)^2\right] \qquad \text{for } \Delta B \le \Delta B_p \qquad (2.30)$$

$$Q_{h,p} = \frac{\Delta B_p^2}{3\mu_0} \qquad \text{at } \Delta B = \Delta B_p \qquad (2.31)$$

and

$$Q_h = \frac{2\Delta B_p^2}{3\mu_0}\left[\frac{\Delta B}{\Delta B_p} - \frac{1}{2}\right] \qquad \text{for } \Delta B \ge \Delta B_p \qquad (2.32)$$

Again, all the hysteresis losses are in the units of Joule / cycle / m^3 - superconductor.

II.3 COUPLING-CURRENT LOSSES

II.3.1 Introduction

Analysis of coupling-current losses in a multifilamentary zone with uniformly distributed filaments has been studied by several authors using different approaches (Refs. 2.14 to 2.23). All the models give very similar results and have been compared with experimental results. In general, the dissipated power due to the coupling currents correspond to the twist pitch and the overall transverse conductivity of the composite. For the purpose of improving the stability of a composite superconducting wire, the multifilamentary zone as seen in Fig. 2.4, is usually enclosed with a high thermally and electrically conductive material which provides an additional resistive path for the coupling currents (Ref. 2.19). The coupling current loss is thus increased. From the manufacturing viewpoint, it is advantageous to include a ductile normal core as shown in Fig. 2.4, to reduce the frequency of wire breakage during the wire extrusion and drawing processes. Similar to the outer cladding, the normal core increases the coupling current loss.

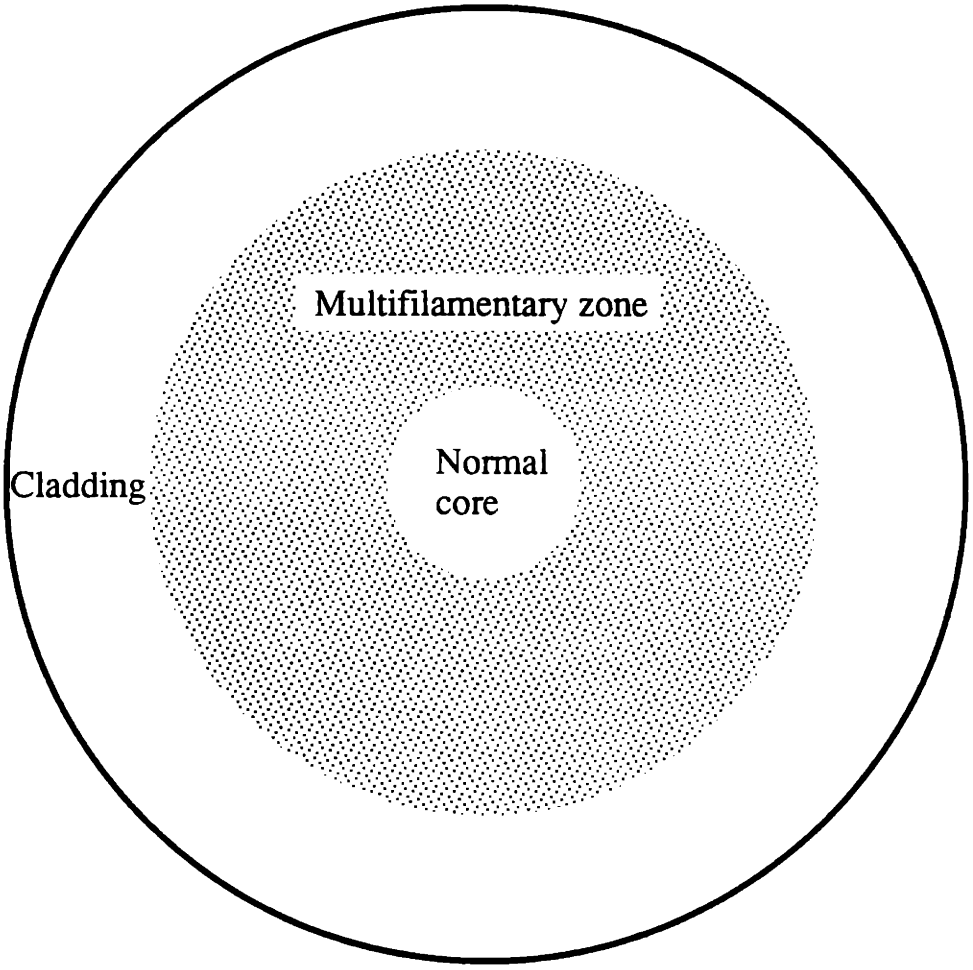

Fig. 2.4 Schematic of the cross sectional view of a multifilamentary superconducting strand with cladding and normal core. The multifilamentary zone contains superconductor filaments and resistive matrix material. Both cladding and normal core are usually made of high conductive material.

In Section II.3.2, the existing analyses of the coupling-current losses will be briefly reviewed beginning with the cause of the coupling currents and the reduction of the loss due to twisting of a uniformly distributed multifilamentary zone. Figs. 2.4 and 2.5 show the typical constructions of a NbTi and two Nb_3Sn wires, respectively. It is common for a wire to have a multi-layer structure in the cross sectional direction. Coupling loss analysis considering multi-layer construction in a composite wire provides more information than those calculated with averaged matrix material properties. In order to calculate the coupling loss of the wire constructions applied in this work, the existing 4-layer model (Refs. 2.37 to 2.39) is generalized into a 5-layer model in Section II.3.3.

II.3.2 Uniform Multifilamentary Zone

II.3.2.1 Coupling Current and Time Constant

Fig. 2.6(a) shows a transverse changing field applied to a non-twisted multifilamentary zone with a length of L. By Faraday's law the induced electric field, transverse to the applied magnetic field, tends to drive the currents across the inter-filamentary matrix material. Due to the cancellation effect in the middle part of the wire, the transverse current loop crosses the filaments at the ends of the wire. As seen in Fig. 2.6(a), when a pair of filaments are separated by a distance of d on the projected plane perpendicular to the applied field, the induced electric potential is simply $V = -\Phi = -\dot{B}Ld$. With the induced transverse electric field $E_t = \dot{B}L$, the induced transverse current density is (Refs. 2.16 and 2.21)

$$J_t = \frac{E_t}{\rho_t} = \frac{\dot{B}\,L}{\rho_t} \tag{2.33}$$

and the dissipated power density is given as

$$P_c = \frac{E_t^2}{\rho_t} = \dot{B}^2 \frac{L^2}{\rho_t} \tag{2.34}$$

where ρ_t is the effective transverse resistivity of the wire including the effects due to the superconductor filaments which will be described later. As seen in the above equations, the induced current density flowing in both the filaments and the matrix is proportional to the length of the wire, and the loss of a non-twisted wire is proportional to the square of the

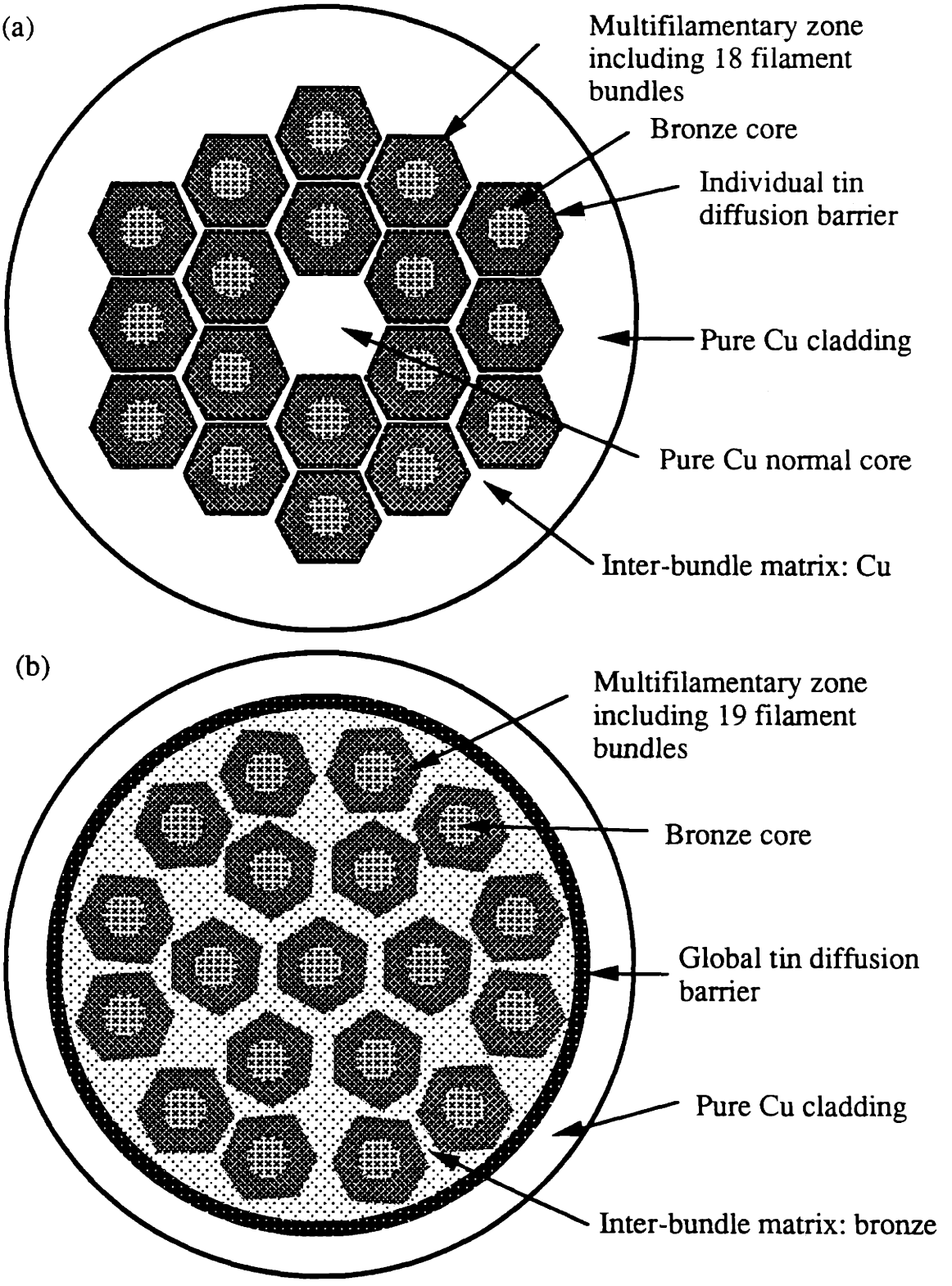

Fig. 2.5 Schematic of the cross sectional view of two typical types of internal-tin Nb3Sn wires; (a) internal-tin modified jelly roll wire with individual tin diffusion barrier; (b) internal-tin wire with global tin diffusion barrier.

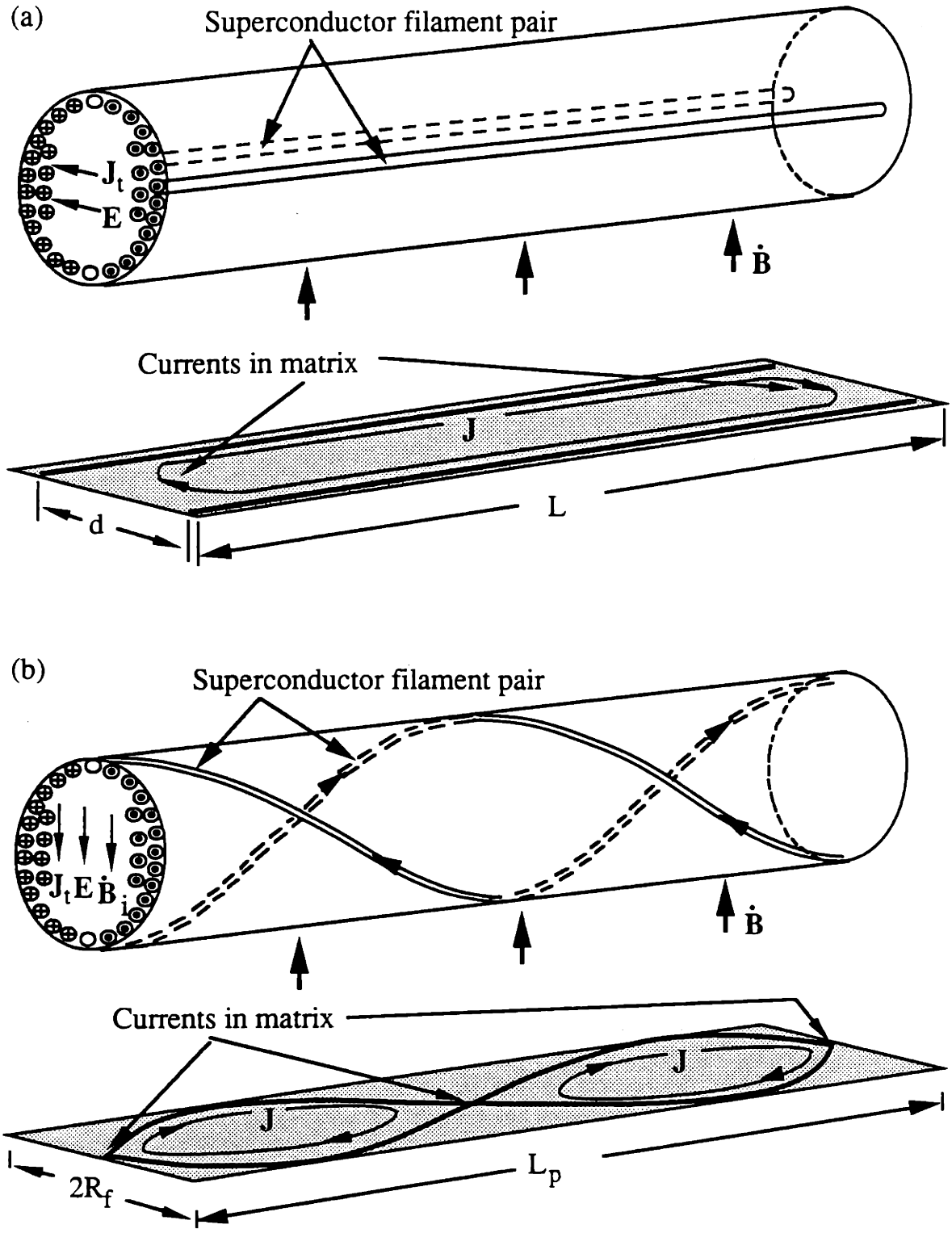

Fig. 2.6 Coupling currents in (a) a non-twisted and (b) a twisted superconducting wire in a uniform transverse changing field. Filaments in the inner region of the wire are not shown. The locations of currents flowing in the matrix materials are indicated on the projected (shaded) planes.

wire length. A long non-twisted wire may have coupling current density as high as the superconductor critical current density even with a very small $\dot{B}$.

As shown in Fig. 2.6(b), upon periodically twisting the multifilamentary zone at a twist pitch of L_p, the coupling currents flow across the matrix material between a pair of filaments at every cross-over point on the projected plane. As seen by the coupling currents, twisting the wire is equivalent to electrically segmenting the wire into small pieces, each with a length of $L_p/2$ (Refs. 2.16 and 2.21). Thus, the coupling current density and the loss are determined by the twist pitch instead of the length of the wire.

Analysis of the coupling current losses of a twisted cylindrical filamentary zone can be found in Refs. 2.14 to 2.23. The analysis was performed on the basis of the following assumptions: (1) uniformly distributed filaments, (2) thin or no cladding to the multifilamentary zone, and (3) long twist pitch compared with the circumference of the multifilamentary zone, i.e. $L_p \gg 2\pi R_{MF}$, where R_{MF} is the radius of the multifilamentary zone. By Faraday's law,

$$\oint_C \mathbf{E}\cdot d\mathbf{l} = -\int_S \dot{\mathbf{B}}\cdot d\mathbf{s} \tag{2.35}$$

Considering the contour PQR shown in Fig. 2.7(a), because of the twisting the E fields are generated in the -X and -Z directions. By the assumption of $L_p \gg 2\pi R_{MF}$, the path along the twisted filament is nearly parallel to the axis of the cylinder which implies that

$$E_z \approx E_{//} \approx 0$$

where $E_{//}$ is the electric field parallel to the superconductor filament, which is zero since the currents are flowing without resistance in the filament. Therefore, the contribution to the contour integration of the E field is only from QR which is the path passing through the matrix material. As seen in Fig. 2.7(b), the differential area projected on the XY-plane and encircled by the contour is $ds = dy\,dz = R_{MF}\sin\theta\,dz$. Letting $\dot{\mathbf{B}} = \dot{B}\,\mathbf{e}_x$ and $E_x = E$, Eq. (2.35) becomes (Ref. 2.16)

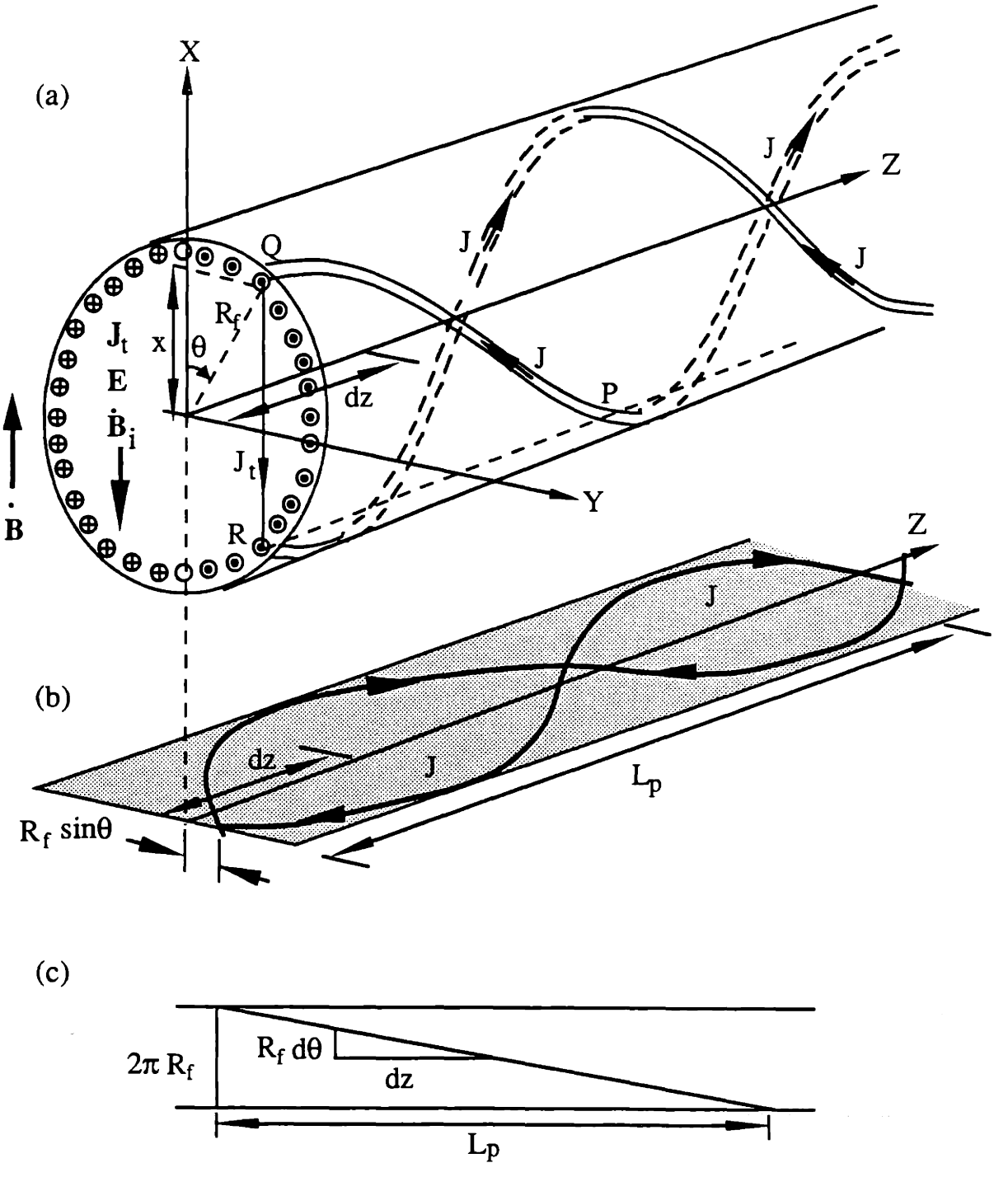

Fig. 2.7 Coupling currents of a pair of superconductor filaments in a twisted composite wire affected by a uniform transverse changing field. The filaments are uniformly distributed over the whole cross sectional area, and the inner filaments are not shown. The coupling currents flowing in the filaments are projected to a plane transverse to the field and the returning currents pass through the matrix at each cross over point.

$$\int_Q^R E\,dl = \int_P^Q \dot{B}\, R_{MF} \sin\theta\, dz \tag{2.36}$$

As shown in Figs. 2.7(a) and (c), dl = -dx and

$$dz = \frac{L_p\, d\theta}{2\pi} \tag{2.37}$$

Then the induced electric field is calculated as (Refs. 2.7, 2.16, and 2.19)

$$E = -\dot{B}\frac{L_p}{2\pi} \tag{2.38}$$

which is independent from R_{MF} and the distance between the filaments. With effective transverse resistivity of the multifilamentary zone ρ_t, the transverse coupling current density is given as

$$J_t = -\dot{B}\frac{L_p}{2\pi}\frac{1}{\rho_t} \tag{2.39}$$

The transverse currents in the multifilamentary zone are collected by the outer-most layer of the filaments, and turning into supercurrents to shield the filaments in the inner region from the applied transverse AC field. Assuming that the field changing rate is low enough that the shielding currents are flowing in a thin filament sheath, the relationship between the linear shield current density, $K_s(\theta)$, and the transverse current density, J_t, is

$$\frac{dK_s(\theta)}{dz} = J_t \cos\theta$$

Solving the differential equation by applying Eqs. (2.37) and (2.39),

$$K_s(\theta) = \frac{1}{\rho_t}\left(\frac{L_p}{2\pi}\right)^2 \dot{B} \sin\theta \tag{2.40}$$

where $K_s(\theta)$ has the units of current per peripheral length. If $K_s(\theta)$ in the outer-most layer of the multifilamentary zone (with a thickness of $2r_f$) is greater than $f_{SC\ in\ MF}J_c$, a region

of the multifilamentary zone will be saturated by the shielding currents, where $f_{SC\ in\ MF}$ is the local volume fraction of the superconductor in a multifilamentary zone. This region is called the saturated region, which will be reviewed in Section II.4. For now, only the thin sheath is considered.

From Ampere's law, the shielding currents produce a secondary uniform field against the external field, which has a magnitude of (Ref. 2.19)

$$B_s = \frac{\mu'}{2} K_s\left(\frac{\pi}{2}\right) \tag{2.41}$$

with $\mu' = \mu_0 ((1 - f_{SC\ in\ MF}) / (1 + f_{SC\ in\ MF}))$ for $B \rightarrow 0$, and $\mu' = \mu_0$ for B large. In the present work, during a large fraction of the cycling time the applied AC field is much greater than the penetration field, the $\mu' = \mu_0$ will be used as a good approximation throughout the work. The coefficient of 1/2 in Eq. (2.41) results from the demagnetization factor of a cylinder (Ref. 2.19). The applied field which is the difference between the external field and the field induced by the shielding currents, is written as

$$\begin{aligned} B &= B_e - B_s \\ &= B_e - \frac{\mu_0}{2}\left(\frac{L_p}{2\pi}\right)^2 \frac{1}{\rho_t} \dot{B} \\ &= B_e - \tau \dot{B} \end{aligned} \tag{2.42}$$

where the natural decay time constant of the coupling current (or simply coupling time constant) of a cylindrical conductor, τ, is defined as (Ref. 2.19)

$$\tau \equiv \frac{\mu_0}{2\rho_t}\left(\frac{L_p}{2\pi}\right)^2 \tag{2.43}$$

which is the most important parameter in the coupling-loss analysis. As seen in Eq. (2.43), the τ is determined by the twist pitch and the transverse resistivity. The transverse resistivity is determined by the matrix materials, the volume fraction of the superconductor, and the clustering of the filaments if they are not uniformly distributed. Thus, the coupling time constant contains all the information besides the superconductor of a twisted multifilamentary zone. In Section II.3.3, the effective transverse resistivity will be further

extended to include the information of the normal core and the cladding of a practical composite wire.

II.3.2.2 Effective Transverse Resistivity

For a multifilamentary zone in a transverse AC field, Eq. (2.38) shows that the induced electric field is uniformly distributed and opposite to the applied field. Thus, calculation of the effective transverse resistivity ρ_t depends heavily on the cross sectional structure of the wire. If more than one matrix material exists in the filamentary zone (Fig. 2.5(a), for example), the effective electric resistivity ρ_e of this region would be the homogenized resistivity averaged over the coupling current paths. In general, the multifilamentary zone can be categorized into the filament clustering region (or filament bundle) and the inter-bundle matrix region which does not contain superconductor.

In the filament bundle, defining $f_{SC\ in\ bundle}$ as the local volume fraction of the superconductor, the effective resistivity ρ_e for the case of no contact resistance between the superconductor and the matrix material, can be estimated as (Ref. 2.25)

$$\rho_e = \frac{1 - f_{SC\ in\ bundle}}{1 + f_{SC\ in\ bundle}} \rho \qquad (2.44a)$$

and, if the contact resistance between filament and the matrix is high,

$$\rho_e = \frac{1 + f_{SC\ in\ bundle}}{1 - f_{SC\ in\ bundle}} \rho \qquad (2.44b)$$

For Nb_3Sn composite wire, the matrix material is considered to be tightly joined with the superconductor, and the superconductor is equivalent to a short circuit to the matrix (Refs. 2.17 and 2.24). The effective resistivity becomes smaller as shown in Eq. (2.44a). During manufacturing of a composite NbTi wire, a high resistance layer at the interface of NbTi and matrix material (copper) is formed, and Eq. (2.44b) is applied to estimate the effective transverse resistivity in the multifilamentary zone (Refs. 2.17 and 2.24).

By electric circuit theory, in a heterogeneous multifilamentary zone, the resistivity along each current path is the length-weighted sum of the resistivities in regions with different materials including the clustering of the superconducting filaments. Since all the transverse

current paths are in parallel, the effective transverse resistivity ρ_t is the inverse sum of the resistivities of all the current paths.

Turck (Ref. 2.24) sliced the cross sectional area of a single hexagonal multifilamentary bundle within a double-stacked wire into 11 parallel strips. The effective transverse resistivity was calculated as the averaged resistivity of these parallel strips. The calculated effective transverse resistivity had the same order of magnitude as the measurement. Nevertheless, this principle can hardly be applied to a real wire which contains a highly distorted internal structure caused by the wire drawing. Another difficulty in evaluating the effective transverse resistivity comes from the uncertainty in the spatial distribution of the matrix resistivity in the multifilamentary zone. This is especially true for a composite Nb_3Sn wire made of tin diffusion process.

The resistivity of the matrix material is affected by the purity of the material, the operation temperature and the applied magnetic field. For the present work, the resistivities of Cu and CuSn alloy matrix at 4.2 K are of major interest. For a better stability margin, sometimes a pure Cu is selected as the matrix material at the price of increasing the coupling loss. When a pure copper is used at 4.2 K in an AC field, two material properties can affect the wire performance: residual resistivity ratio and magnetoresistivity. Both are affected by the purity of the Cu which is discussed below.

II.3.2.2.1 Low Temperature Resistivity and Residual Resistivity Ratio

The purity of the matrix material can be judged from the residual resistivity ratio (RRR), which is defined as (Ref. 2.27)

$$\text{RRR} \equiv \frac{\text{Resistance at 300 K}}{\text{Resistance at 4.2 K}} \tag{2.45}$$

The RRR is obtained by measuring the resistances of the same wire at both 300 K and 4.2 K without a background field. However, the above definition is good only for a solid resistive wire. For a composite superconducting wire, the RRR has to be tested at the final stage of the wire fabrication (including heat treatment in the case of Nb_3Sn). Unlike the type-I superconductor which has a sharp step-down of the resistance at a well-defined critical temperature, the type-II superconductor has a wider temperature range in the normal-to-superconductive transition. In the case of a composite wire, as the temperature

is reduced to an upper current sharing temperature $T_{CS,upper}$, part of the current in the matrix starts to flow without resistance in the superconductor. Thus, from the experience in this thesis work, the cryogenic resistance of the matrix in a composite wire should be taken at a temperature slightly higher than the $T_{CS,\,upper}$, and the RRR becomes

$$RRR \approx \frac{\text{Resistance at 300 K}}{\text{Resistance at } T \approx T_{CS,upper} \text{ of the composite wire}} \qquad (2.46)$$

The $T_{CS,upper}$'s of most low-T_c type-II superconductors are lower than 20 K. As seen in Fig. 2.8 (Ref. 2.26), the difference in the resistances between 4.2 K and 20 K can be large for an annealed high-purity Cu with an RRR > 1000. Considering all the possible cold work during the magnet windings (NbTi composites) or contamination to the Cu due to the heat treatment (Nb_3Sn composites), the RRR of Cu matrix in a commercial composite wire is about 300 or less. Eq. (2.46) can be used as a reasonable approximation to Eq. (2.45).

In a Nb_3Sn composite wire, a large fraction of the cross sectional area is covered by CuSn bronze. As mentioned before, the Sn content in the filamentary zone is not uniform, which is especially true for internal-tin process. The resistivity of CuSn, which varies with the Sn alloying and the background temperature, is important in the coupling-loss calculation. The top curve in Fig. 2.8 is the temperature dependence of resistivity of a bronze with 5 at.% of Sn. At a temperature below 20 K, the alloyed Cu has a resistivity more than two orders of magnitude higher than a pure Cu, and a much smaller RRR compared with pure Cu. Fig. 2.9 shows the variations of the resistivity and the RRR of CuSn plotted against the atomic fraction of Sn in Cu (Ref. 2.26). When the Sn content in the Cu is above about 3 at.%, the resistivity tends to saturate at 10^{-7} Ω-m, and the RRR approaches unity. The resistivities and the RRR's of the CuSn alloys at room temperature and 4.2 K are summarized in Table 2.1 (Refs. 2.26 and 2.27) for future use. Considering the relatively small contribution to the coupling loss due to the high resistivity of the CuSn bronze and other possible errors in the loss estimation, the RRR of all the CuSn will be taken as unity for simplicity.

For an internal-tin composite wire, the resistive materials commonly used as tin diffusion barrier are V, Nb, and Ta. All these materials are superconductors at 4.2 K in zero background field and become resistive at a field above ~ 0.5 T. The resistive property is more relevant to the coupling loss analysis. Only very limited information on the electric resistivities of these materials, especially at low temperature, is available. The resistivities

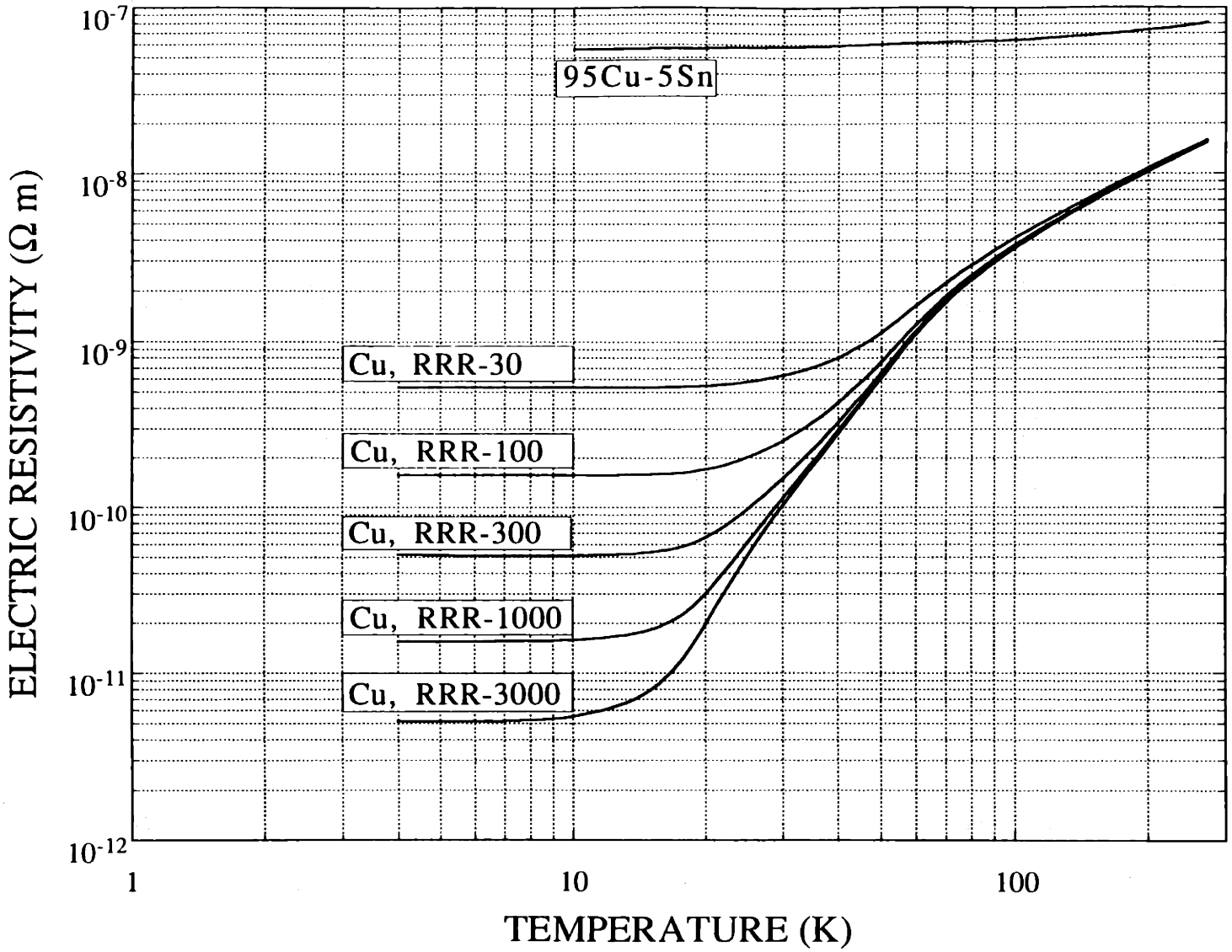

Fig. 2.8 Electrical resistivity versus temperature for annealed copper and CuSn alloy (Ref. 2.26).

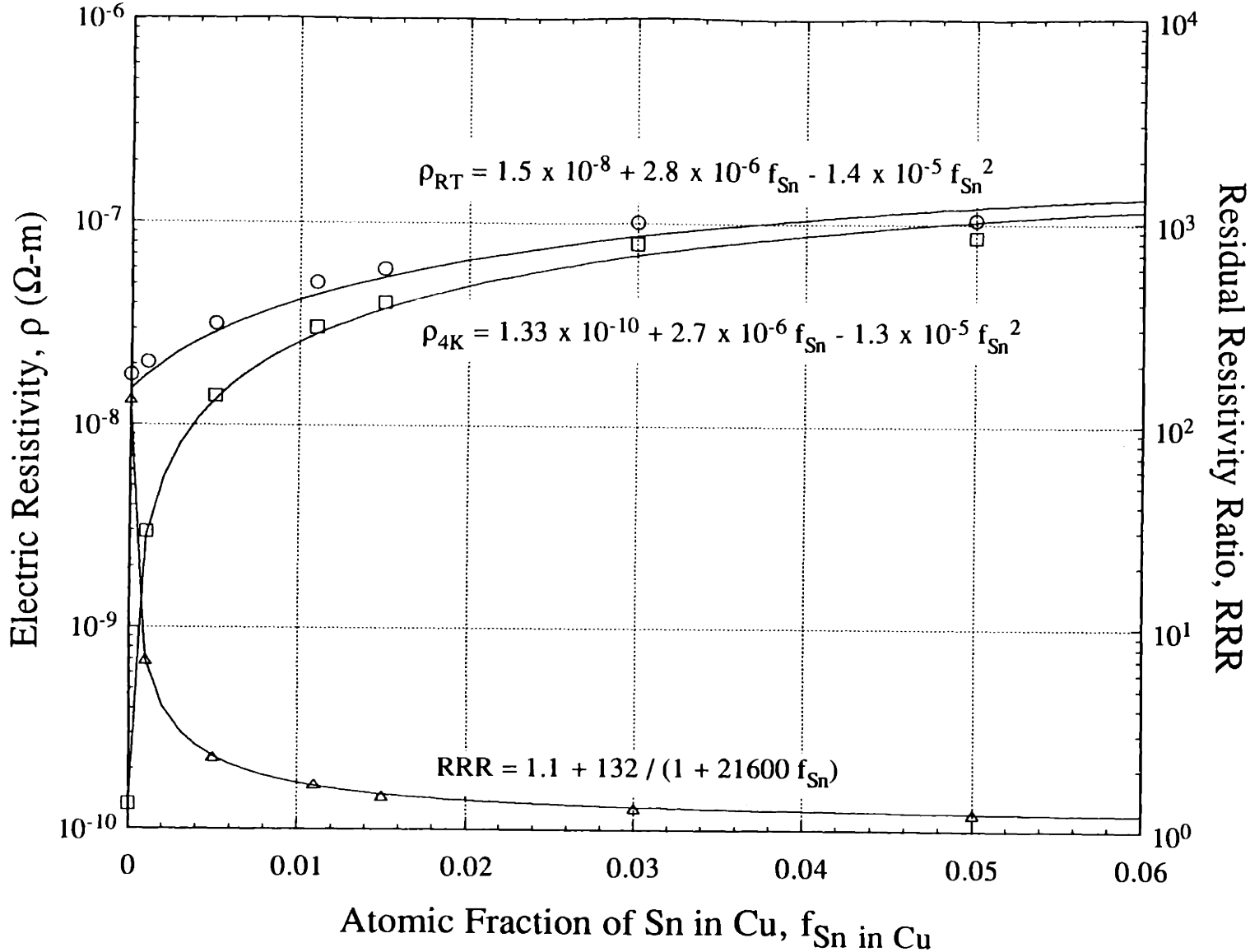

Fig. 2.9 Electric resistivity and residual resistivity ratio of CuSn bronze as a function of atomic fraction of Sn in Cu. The symbols are the data extracted from Ref. 2.26; the solid lines are the best-fit curves.

of these tin diffusion barrier materials are listed in Table 2.2 (Refs. 2.26, 2.28 and 2.29). Some of them are roughly estimated from the figures in the references. Since the volumetric fraction of the diffusion barrier in a composite wire is small, the uncertainty of the low temperature resistivities of these materials has a small effect to the overall coupling loss estimation.

Table 2.1 Resistivity and RRR of CuSn alloy (Refs. 2.26 and 2.27)

Atomic% Sn	$\rho_{300\ K}$ (Ω m)	$\rho_{4.2\ K}$ (Ω m)	RRR
Stock Cu	1.77×10^{-8}	0.0133×10^{-8}	133
0.1% Sn	2.06×10^{-8}	0.30×10^{-8}	6.94
0.5% Sn	3.17×10^{-8}	1.39×10^{-8}	2.28
1.1% Sn	5.10×10^{-8}	3.04×10^{-8}	1.68
1.5% Sn	5.95×10^{-8}	4.05×10^{-8}	1.47
3.0% Sn	10.12×10^{-8}	7.91×10^{-8}	1.28
5.0% Sn	10.48×10^{-8}	8.59×10^{-8}	N.A.

Table 2.2 Resistivity of tin diffusion barrier material (Refs. 2.26, 2.28, and 2.29)

Material	$\rho_{300\ K}$ (Ω m)	$\rho_{cryogenic}$ (Ω m)
V	19.68×10^{-8}	N.A.
Nb	$\sim 26 \times 10^{-8}$	$\sim 3 \times 10^{-8}$ (77 K)
Ta	13.15×10^{-8}	$\sim 0.34 \times 10^{-8}$ (4.2 K, > 10 mT)

II.3.2.2.2 Magnetoresistivity

Similar to the residual resistivity ratio, the magnetoresistivity depends on the purity of the material. The magnetoresistivity of Cu wire at 4.2 K in an externally applied field has been evaluated experimentally by several authors (Refs. 2.29 to 2.36). A general expression is given as

$$\rho(B) = \frac{\rho(B = 0, T = 300\ K)}{RRR} + \beta_M \cdot B \quad (\Omega\ m) \tag{2.47}$$

where $\rho(B=0, T=300K) = 2.0 \times 10^{-8}$ (Ω m) for room temperature resistivity of Cu and the multiplication factor $\beta_M = 4.8 \times 10^{-11}$ (Ω m/T) for magnetoresistivity effect will be used in this work.

The magnetoresistivity of the tin diffusion barrier material can hardly be found. Only Ta has been measured by Ando, et al. (Ref. 2.29). The experimental results showed that the resistivity of Ta at 4.2 K saturated at 0.34×10^{-8} (Ω m) for a background field greater than about 10 mT. For a high field condition which is of interest to the present research, it would be a reasonable approximation to use a constant value for the resistivity of the Ta (as listed in Table 2.2) in various background fields.

II.3.2.3 Critical Field Changing-rate

As discussed in section II.3.2.1, Eq. (2.40) shows that at a large field ramp rate the outer layer of the multifilamentary zone will be saturated by the induced transverse coupling currents. By Eq. (2.42), the magnetization caused by the coupling currents (Eq. 2.41) shields the multifilamentary zone from the external field by $\tau\dot{B}$. Eq. (2.42) is valid only when the slow field variation requirement, or equivalently the thin saturation layer condition is satisfied. In this subsection, quantification of the applicable range of Eq. (2.42) will be examined.

Analogous to a solid superconductor, the difference between the external field and the field in the center of a multifilamentary zone is not greater than the magnitude of the penetration field of the multifilamentary zone $B_{p,MF}$, which is expressed as

$$B_e - B \leq B_{p,MF} \tag{2.48}$$

$$B_{p,MF}(B_e) = \frac{2}{\pi} \mu_0 J_{c,MF}(B_e) R_{MF} \tag{2.49}$$

where $J_{c,MF}(B_e)$ and R_{MF} are the critical current density and the radius of the multifilamentary zone, respectively. If a large external field $B_e >> B_{p,MF}$ is applied, $B \approx B_e$. For a uniformly distributed multifilamentary zone,

$$J_{c,MF}(B_e) = f_{SC \text{ in } MF} J_{c,SC}(B_e) \tag{2.50}$$

where $f_{SC\ in\ MF}$ is the local volume fraction of superconductor. From Eq. (2.42) the difference between the external field and the field in the center of the multifilamentary zone is

$$B_e - B = \tau \dot{B} \tag{2.51}$$

The thin saturation layer condition is satisfied as long as the changing-rate of the applied field is slow enough such that $\tau \dot{B} << B_{p,MF}(B_e)$. Also, if the field changing-rate is slow or if the external field has a constant field changing-rate, the phase-shift between B_e and B would be small or zero, then $\dot{B} \approx \dot{B}_e$. Eq. (2.51) is linearized as

$$B_e - B \approx \tau \dot{B}_e, \qquad \text{if } \tau \dot{B}_e << B_{p,MF}(B_e) << B_e \tag{2.52}$$

Eq. (2.52) gives a more quantitative condition for a slowly changing-field at which the field shielding effect due to the magnetization by the saturation layer can be neglected.

A similar argument can be reached from the analysis of the critical twist pitch or critical field changing-rate of a twisted composite wire in an early article by Morgan (Ref. 2.15). The author showed that a multifilamentary zone with a radius of R_{MF}, a twist pitch of L_p, and an effective transverse resistivity of ρ_t, can carry a maximum circulating current of I_{max} at a critical transverse changing field $\dot{B}_c$, which is given as (Ref. 2.15)

$$I_{max} = \left(\frac{L_p}{2\pi}\right)^2 \frac{\dot{B}_c}{\rho_t}\, 2R_{MF} \tag{2.53}$$

where I_{max} can not exceed the critical current I_c of a multifilamentary zone. If the field changing rate is higher than $\dot{B}_c$, the transverse coupling currents tend to cross the filaments at a current density of $J_{c,SC}$. At an even higher field changing rate, the multifilamentary zone behaves like a bulk superconductor with a size the same as that of the multifilamentary zone. The above description can also be interpreted as that at a critical field changing rate $\dot{B}_c$ the whole multifilamentary zone is saturated with I_c. With the definition of $J_{c,MF}$ in Eq. (2.50), $I_{max} = \pi R_{MF}^2 J_{c,MF}$, Eq. (2.53) can be re-written as

$$B_{p,MF} = \frac{8}{\pi^2} \tau \dot{B}_c \approx \tau \dot{B}_c \tag{2.54}$$

at which the critical shielding field $\tau\dot{B}_c$ is as large as the penetration field of the multifilamentary zone. The multifilamentary zone is now similar to a fully penetrated bulk superconductor. The condition of thin saturated layer is valid only if $\dot{B}_e << \dot{B}_c$ or $\tau\dot{B}_e << B_{p,MF}$ is satisfied, which re-confirms the criteria applied in Eq. (2.52).

The following coupling current loss expressions are valid under the assumption of slow field changing-rate. At a higher field changing-rate, the so-called penetration loss caused by the saturation layer becomes dominant which will be reviewed in Section II.4.

II.3.2.4 Coupling Current Loss

The dissipated power density due to the transverse coupling currents flowing in the resistive matrix material in the multifilamentary zone is similar to that in Eq. (2.34) or alternatively $P = J_t E$. The expressions of E and J_t have been given in Eqs. (2.38) and (2.39), respectively. Thus, at slow field changing-rate the power density of coupling current loss in the multifilamentary zone becomes

$$P_c = \frac{\dot{B}_e^2}{\rho_t(B_e)}\left(\frac{L_p}{2\pi}\right)^2 \quad (W / m^3 \text{ of matrix in multifilamentary zone})$$

In this equation, external field instead of applied field is used for both field changing-rate and the field-dependent effective transverse resistivity. Applying the coupling time constant defined in Eq. (2.43), the coupling loss power density is simplified as

$$P_c = \frac{2\,\tau(B_e)\,\dot{B}_e^2}{\mu_0} \quad (W / m^3 \text{ matrix in multifilamentary zone}) \tag{2.55}$$

where the field-dependent coupling time constant of the multifilamentary zone is thus

$$\tau(B_e) \equiv \frac{\mu_0}{2\rho_t(B_e)}\left(\frac{L_p}{2\pi}\right)^2 \tag{2.56}$$

In a cyclic transverse field, the coupling current loss per unit volume of wire per cycle is obtained by integrating Eq. (2.55) over a period of field variation. Different from the hysteresis losses, the final expressions of the coupling losses depends heavily on the wave-form of the applied field. A good summary of the coupling-loss equations for different

transverse AC fields can be found in Ref. 2.7. However, only field-independent matrix resistivities are applied in those formulae. Magnetoresistivity effect to the coupling loss, which is important in pure metal matrix, is not included.

II.3.3 Composite Strand With Multi-layer Construction

For various reasons as mentioned above, it has become very usual to have multiple layers of resistive materials in addition to the multifilamentary zone in a practical superconducting strand. The coupling current loss equations for different multi-layer cross sectional constructions have been derived by Turck (Refs. 2.37 and 2.38). Ito, et al. (Ref. 2.39) generalized Turck's expressions for a composite multifilamentary strand containing both resistive center-core and two resistive outer layers, and verified these expressions experimentally. In this sub-section, the principle in making Turck's model will be briefly reviewed. The expressions given by Ito, et al. will be extended to include three outer layers with various resistivities.

Considering a composite multifilamentary strand with multiple layers of cladding affected by a transverse time-varying field, in addition to the coupling currents flowing in the multifilamentary zone parallel but opposite to the external field direction, the azimuthal coupling currents are flowing in these outer layers. If a normal center-core is enclosed by the multifilamentary zone, the coupling loss of the core region should be calculated independently due to its different effective resistivity.

Fig. 2.10 shows a composite wire containing a normal center-core with a radius of R_{MFi} enclosed by a concentric multifilamentary zone with an OD of R_{MFo}, and three concentric resistive outer layers with the outer radii of R_1, R_2, and R_3. The corresponding resistivities of these multiple layers are ρ_i, ρ_t, ρ_1, ρ_2, and ρ_3, respectively. In the cylindrical coordinates (r, φ, z), the Laplace equation for the voltage induced by the AC field in each of the resistive layer i is written as (Refs. 2.37 and 2.38)

$$\frac{\partial^2 V_i}{\partial r^2} + \frac{\partial V_i}{r\,\partial r} + \frac{1}{r^2}\frac{\partial^2 V_i}{\partial \varphi^2} = 0 \qquad \text{for } i = 1 \text{ to } 3 \qquad (2.57)$$

where the induced voltage is assumed to be zero in the axial direction since the axial component of the E field is neglected under the assumption that $L_p >> 2\pi R_{MF}$.

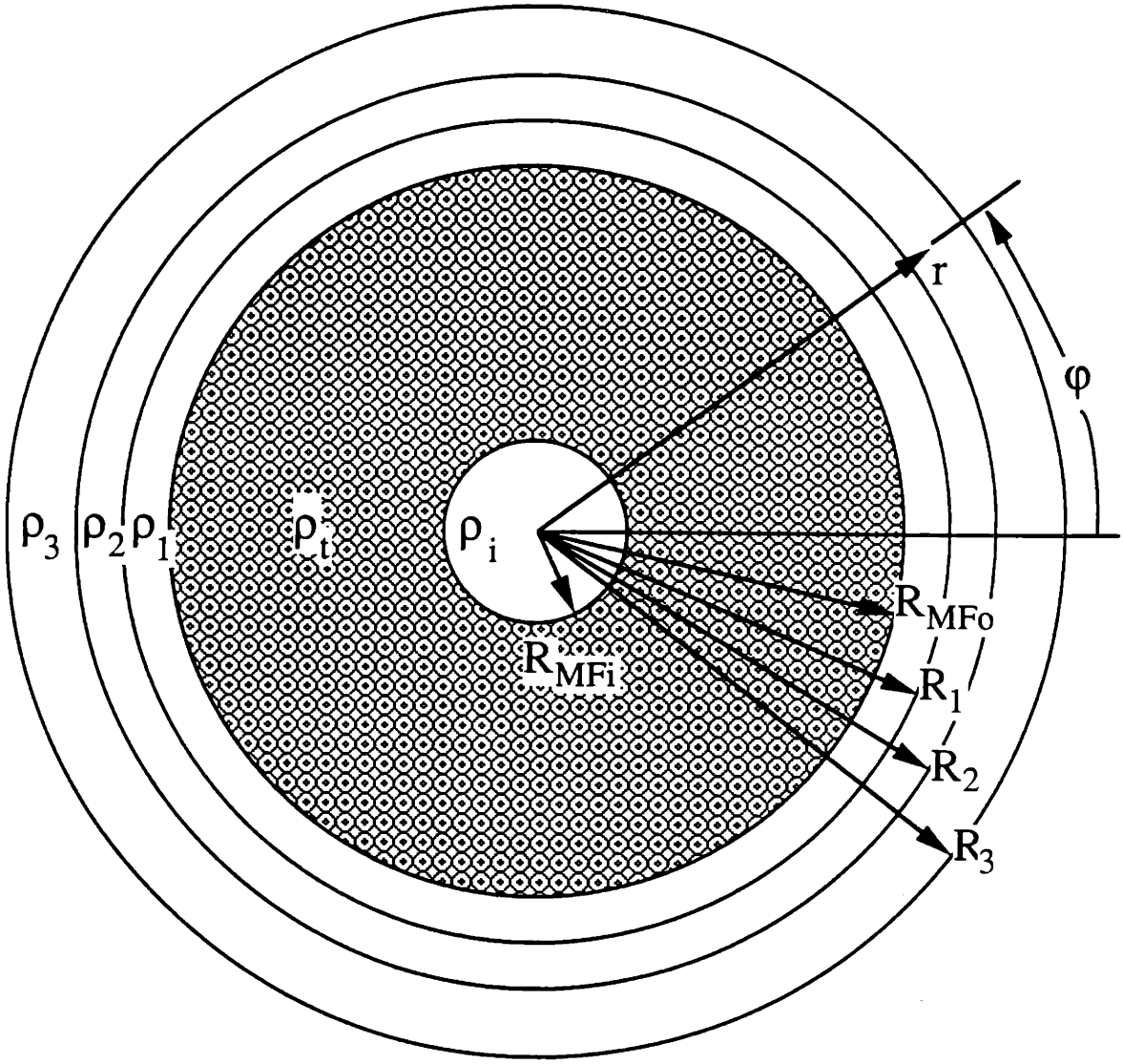

Fig. 2.10 Schematic of the cross sectional construction of a composite strand containing five concentric layers.

The voltages at the inner and outer boundaries are obtained by integrating the induced electric field in the multifilamentary zone (Eq. 2.38), which are expressed as (Refs. 2.37 and 2.38)

$$V(R_{MFi}, \varphi) = \frac{\dot{B} L_p}{2\pi} R_{MFi} \cos\varphi, \tag{2.58}$$

and

$$V(R_{MFo}, \varphi) = \frac{\dot{B} L_p}{2\pi} R_{MFo} \cos\varphi, \tag{2.59}$$

The third boundary condition is simply the zero electric field in the radial direction at the outermost surface of the composite wire, which is given as

$$E_{r,3}(R_3) = 0, \tag{2.60}$$

The interface conditions are the continuity of the azimuthal component of the electric field and the continuity of the radial component of the current density at each interface of two neighboring resistive layers which are written as (Refs. 2.37 and 2.38)

$$E_{\varphi,i}(R_i) = E_{\varphi,(i+1)}(R_i), \qquad \text{for } i = 1 \text{ and } 2, \tag{2.61}$$

$$\frac{E_{r,i}(R_i)}{\rho_i} = \frac{E_{r,(i+1)}(R_i)}{\rho_{i+1}}, \qquad \text{for } i = 1 \text{ and } 2. \tag{2.62}$$

The electric fields in the resistive layers can be calculated once Eq. (2.57) is solved for each layer by using the boundary and interface conditions expressed in Eqs. (2.58) to (2.62). When the applied field is changed slowly such that $B \approx B_e$, the coupling current loss of this 5-zone composite wire is given as

$$P_c = \frac{\dot{B}_e^2 L_p^2}{(2\pi)^2} \left(\frac{R_{MFo}}{R_3}\right)^2 \left\{ \frac{k}{\rho_t(B_e)} + \frac{l}{\rho_i(B_e)} + \frac{m(B_e)}{\rho_1(B_e)} + \frac{n(B_e)}{\rho_2(B_e)} + \frac{s(B_e)}{\rho_3(B_e)} \right\} \quad (W / m^3 \text{ wire}) \tag{2.63}$$

where the expression of field-dependent resistivity takes the magnetoresistivity into account, and

$$k = \frac{R_{MFo}^2 - R_{MFi}^2}{R_{MFo}^2}, \qquad l = \frac{R_{MFi}^2}{R_{MFo}^2}, \qquad m = \frac{R_1^2 - R_{MFo}^2}{R_{MFo}^2}\left(R_{MFo}^2 + \delta R_1^2\right) a_1^2,$$

$$n = \frac{R_2^2 - R_1^2}{R_1^2}\left(R_1^2 + \gamma R_2^2\right) a_2^2, \qquad s = \frac{R_3^2 - R_2^2}{R_2^2}\left(R_2^2 + R_3^2\right) a_3^2,$$

with

$$a_1 = \frac{R_{MFo}}{R_{MFo}^2 + \delta R_1^2}, \qquad a_2 = a_1 \frac{R_1^2(\delta + 1)}{R_1^2 + \gamma R_2^2}, \qquad a_3 = a_2 \frac{R_2^2(\gamma + 1)}{R_3^2 + R_2^2},$$

and

$$\gamma = \frac{\rho_3(B_e)\left(R_3^2 + R_2^2\right) + \rho_2(B_e)\left(R_3^2 - R_2^2\right)}{\rho_3(B_e)\left(R_3^2 + R_2^2\right) - \rho_2(B_e)\left(R_3^2 - R_2^2\right)}, \qquad \delta = \frac{\rho_2(B_e)\left(\gamma R_2^2 + R_1^2\right) + \rho_1(B_e)\left(\gamma R_2^2 - R_1^2\right)}{\rho_2(B_e)\left(\gamma R_2^2 + R_1^2\right) - \rho_1(B_e)\left(\gamma R_2^2 - R_1^2\right)}$$

The effective transverse resistivity of a composite wire with multi-layer construction can be defined as

$$\frac{1}{\rho_{wt}(B_e)} = \left(\frac{R_{MFo}}{R_3}\right)^2 \left| \frac{k}{\rho_t(B_e)} + \frac{l}{\rho_i(B_e)} + \frac{m(B_e)}{\rho_1(B_e)} + \frac{n(B_e)}{\rho_2(B_e)} + \frac{s(B_e)}{\rho_3(B_e)} \right| \quad (1 / \Omega\text{-m}) \tag{2.64}$$

Similar to the τ for the multifilamentary zone defined in Eq. (2.43), the instantaneous field-dependent coupling time constant of the composite wire τ_w, is given as

$$\tau_w(B_e) = \frac{\mu_0}{2\,\rho_{wt}(B_e)} \left(\frac{L_p}{2\pi}\right)^2 \quad (s) \tag{2.65}$$

The AC-loss power density Eq. (2.63) becomes

$$P_c = 2\,\frac{\tau_w(B_e)\,\dot{B}_e^{\,2}}{\mu_0} \quad (W / m^3 \text{ resitive material in the wire}) \tag{2.66}$$

which has a similar form as Eq. (2.55).

II.4 PENETRATION LOSSES

II.4.1 Introduction

As discussed in Section II.3, the net electric field in the matrix and the cladding drives the coupling currents to the outer boundary of the multifilament zone. If the coupling current is larger than the critical current of the filaments in the outer-most layer of the multifilamentary zone. The outer-most filaments are saturated, and the coupling currents will be collected by the next outer-most layer, and so forth. A secondary field induced by the saturated layer tends to against the applied field which creates a field shielding effect to the filaments in the inner region. Thus, the multifilamentary zone behaves like a solid superconductor penetrated by the magnetic field. The loss due to this type of magnetization caused by the coupling currents flowing in the saturated region is sometimes called penetration loss (Ref. 2.19).

Ries (Ref. 2.19) calculated the penetration loss in the saturated layer of a multifilamentary zone in a manner analogous to the hysteresis loss in a single bulk cylindrical superconductor for the reason that both have an outer layer flowing at critical current density with a similar elliptical or cosine current distribution and both have $E = 0$ at the penetration front. Analysis of penetration loss can also be found in several other articles (Refs. 2.11, 2.40 to 2.45).

For the purpose of the present research, all the applied field changing-rates are so low that $\tau_w \dot{B}_e << B_{p,MF}$, the conventional penetration loss can be neglected without introducing significant error to the analytical results. This will be verified in Section V.3. However, as will be shown in Chapter VI, the penetration loss due to the saturation layer may occur at a very low field changing-rate for some types of superconducting strand. Only the 1-D slab geometry is used to prove this phenomenon in the new model. The article by Ogasawara, et al. (Ref. 2.42) will be reviewed here as the basis for the future model development. The procedure of their analysis is more important than the final loss expression.

II.4.2 1-D Multifilamentary Slab

II.4.2.1 Penetration Depth

Considering an infinite multifilamentary slab affected by a time-varying external field applied in the direction parallel to the slab surface, at a slow field variation the relation between the external field B_e and the applied field B has been given in Eq. (2.51) as

$$B_e - B = \tau \dot{B}$$

where the coupling time constant for the multifilamentary slab with twist pitch of L_p and effective transverse resistivity of ρ_t, is expressed as

$$\tau \equiv \frac{\mu_0}{\rho_t}\left(\frac{L_p}{2\pi}\right)^2 \tag{2.67}$$

The penetration field for the multifilamentary slab is

$$B_{p,MF} = \mu_0 J_{c,MF} a_{MF} \tag{2.68}$$

where a_{MF} is the half width of the multifilamentary slab, and

$$J_{c,MF} = f_{SC \text{ in } MF} J_{c,SC} \tag{2.50}$$

For simplicity, the Bean model and the field-independent effective transverse resistivity are used here.

At a higher field changing-rate, the outer region of the multifilamentary slab is saturated by the transverse coupling currents which are generated in the non-saturated region with a current density of

$$J_t = \frac{1}{\rho_t}\left(\frac{L_p}{2\pi}\right)\dot{B} \tag{2.69}$$

The coupling currents are collected by the outer layer of filaments at a thickness of δ and become a shielding current with a linear current density (current per peripheral length) of K_s. By continuity of current,

$$K_s = \left(\frac{L_p}{2\pi}\right) J_t \left(1 - \frac{\delta}{a_{MF}}\right) = \frac{\tau \dot{B}}{\mu_0}\left(1 - \frac{\delta}{a_{MF}}\right) \tag{2.70}$$

Since by definition $K_S = \delta J_{c,MF}$, the penetration thickness is obtained from Eq. (2.70) as

$$\frac{\delta}{a_{MF}} \approx \frac{\tau \dot{B}}{B_{p,MF}} \left(1 + \frac{\tau \dot{B}}{B_{p,MF}}\right)^{-1} \tag{2.71}$$

II.4.2.2 Linearized Shielding Field

As discussed in II.2.2.1, the shielding current generates a shielding field B_S such that $B_e - B = B_S = \mu_0 K_S$. Substituting K_S with Eq. (2.70),

$$B_e - B \approx \tau \dot{B} \left(1 - \frac{\delta}{a_{MF}}\right) \tag{2.72}$$

Applying Eq. (2.71) in Eq. (2.72),

$$B_e - B \approx \tau \dot{B} \left(1 + \frac{\tau \dot{B}}{B_{p,MF}}\right)^{-1} \tag{2.73}$$

Since Eq. (2.73) can not be solved analytically, Ogasawara, et al. linearized the equation by taking the slow and fast field changing-rates as

$$B_e - B \approx \tau \dot{B}_e, \quad \text{for } \tau \dot{B}_e << B_{p,MF} \tag{2.74a}$$

$$B_e - B \approx B_{p,MF}, \quad \text{for } \tau \dot{B}_e >> B_{p,MF} \tag{2.74b}$$

which were further relaxed to

$$B_e - B \approx \tau \dot{B}_e, \quad \text{for } \tau \dot{B}_e < B_{p,MF} \tag{2.75a}$$

$$B_e - B \approx B_{p,MF}, \quad \text{for } \tau \dot{B}_e > B_{p,MF} \tag{2.75b}$$

II.4.2.3 Penetration Losses

Analogous to the hysteresis loss analysis for a superconductor slab, the magnetization of the multifilamentary slab due to the shielding field was given as (Ref. 2.42)

$$- \mu_0 M_{c1} \approx \tau \dot{B}_e - \frac{1}{2} \frac{(\tau \dot{B}_e)^2}{B_{p,MF}}, \qquad \text{for } \tau \dot{B}_e \le B_{p,MF} \tag{2.76a}$$

$$- \mu_0 M_{c2} \approx \frac{1}{2} B_{p,MF}, \qquad \text{for } \tau \dot{B}_e > B_{p,MF} \tag{2.76b}$$

Ogasawara, et al. considered a trapezoidal field with the same rise-time and down-time of T_m, and a constant $\dot{B}_e = \Delta B_e / T_m$. The solution to Eq. (2.52) gives

$$B = \dot{B}_e \left[t - \tau \left(1 - e^{-t/\tau} \right) \right], \qquad \text{for } 0 \le t \le T_m \tag{2.77}$$

and

$$\dot{B} = \dot{B}_e \left(1 - e^{-t/\tau} \right), \qquad \text{for } 0 \le t \le T_m \tag{2.78}$$

The fast or slow field changing-rate was distinguished by

$$\tau \dot{B} = B_{p,MF} \tag{2.79}$$

Substitute Eq. (2.78) into Eq. (2.79), a $t = t_1$ was solved at which the field changing-rate switches from slow to fast as the field is raised from 0 to a maximum. The penetration loss integration is written as

$$Q_s \approx - 2 \left[\int_0^T M_{c1} \dot{B}_e \, dt + \int_T^{T_m} M_{c2} \dot{B}_e \, dt \right] \tag{2.80}$$

where T is the smaller of t_1 and T_m.

II.4.3 Total AC Loss

In addition to the penetration losses in the saturated region, the hysteresis loss of the superconductor filaments and the coupling current loss of the matrix material in the non-saturated region, as have been reviewed in this chapter, must also be taken into account for the total loss (Ref. 2.42). In a uniformly distributed multifilamentary zone, the saturation layer is always initiated from the outer-most region. At a low field changing rate, the fraction of the inner non-saturated region is approximated as

$$f = 1 - \left(\frac{\delta}{a_{MF}}\right) = 1 - \frac{\tau \dot{B}_e}{B_{p,MF}} \qquad (2.81)$$

for a multifilamentary slab. The volume fraction of the non-saturated region must be used to weigh the hysteresis-loss and coupling-loss integrations. The total loss of a current-free conductor is estimated as the weighted sum of the above three types of loss.

II.5 ADDITIONAL LOSS DUE TO TRANSPORT CURRENTS

When a composite type-II superconducting wire is used to build a high current AC magnet, it is important to identify the change of the AC losses due to the externally applied transport currents. Although a few articles regarding the additional loss due to transport current have been published (Refs. 2.7, 2.12, and 2.40 to 2.57), all the analysis were based on the Bean model with the assumption of J_c = constant. Analytical loss formulae are only available in 1-D slab geometry. In this section, attention is focused on the transport current effect on the AC losses of a composite slab.

II.5.1 DC Transport Current in a Multifilamentary Slab

II.5.1.1 Magnetization

Similar to what has been described in section II.2.3, an infinite multifilamentary superconducting slab with a thickness of 2a is assumed to be affected by a cyclic uniform external field B_e in the parallel direction. As seen in Fig. 2.11(a), the filaments in the slab are further assumed to be in the critical state: both halves of the slab are filled with critical currents in the opposite directions. When a DC transport current I_t is applied to the slab, the shift of the electric center line is determined as

$$\Delta x = \frac{I_t}{2J_{c,MF}} = \frac{I_t}{I_c}\frac{I_c}{2J_{c,MF}} = i\, a_{MF}$$

where $i \equiv I_t / I_c$, a_{MF} is the half width of the multifilamentary slab, and $I_c = 2a_{MF}J_{c,MF}$ is evaluated at $B_{mean} = (B_{max} + B_{min}) / 2$. Fig. 2.11(b) shows that in the critical state model, the penetration field at some bias field is modified from $B_{p,MF} = \mu_0 J_{c,MF}\, a_{MF}$ (Eq. (2.68)) into

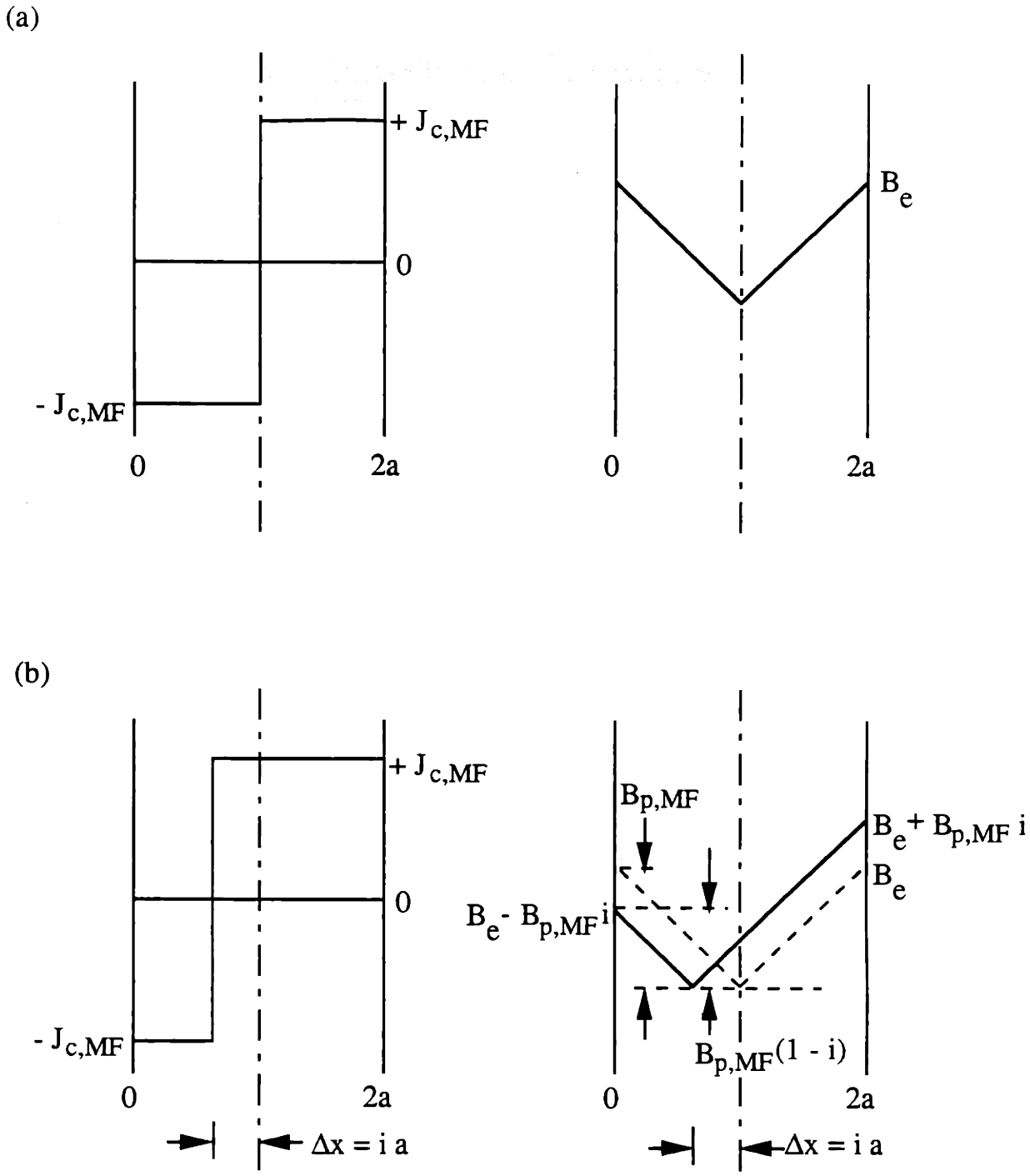

Fig. 2.11 Current and flux distribution of a composite superconducting slab in a parallel field; (a) without transport current, (b) with DC transport current. $i = I_t / I_c$.

$$B'_{p,MF} = \mu_0 J_{c,MF} a_{MF} (1 - i) = B_{p,MF} (1 - i), \tag{2.82}$$

and the penetration field for a cyclic changing field becomes

$$\Delta B'_{p,MF} = 2 \mu_0 J_{c,MF} a_{MF} (1 - i) = \Delta B_{p,MF} (1 - i). \tag{2.83}$$

Similar expressions can be found in Refs. 2.7 and 2.12.

In the case of a composite wire in a transverse changing field, the transport current is carried by the inner non-saturated region of thickness 2 (a_{MF} - δ), where δ is the thickness of the saturation layer as described in Eq. (2.71). The reduced transport current is expressed as (Ref. 2.42)

$$i^* = \frac{I_t}{2 (a_{MF} - \delta) J_{c,MF}} = \frac{I_t}{2 a_{MF} J_{c,MF}} \frac{a_{MF}}{(a_{MF} - \delta)} = \frac{I_t}{I_c} \frac{a_{MF}}{(a_{MF} - \delta)} = i \frac{a_{MF}}{(a_{MF} - \delta)} \tag{2.84}$$

Substituting Eq. (2.71) for δ into Eq. (2.84) to have

$$i^* = \frac{i}{\left(1 - \frac{\tau \dot{B}}{B_{p,MF}}\right)} \approx \frac{i}{\left(1 - \frac{\tau \dot{B}_e}{B_{p,MF}}\right)} \tag{2.85}$$

Due to the increment of the $\dot{B}_e$, the inner region at a given I_t becomes saturated when i^* = 1. From Eq. (2.85), one obtains the saturation criteria for a composite carrying transport current as

$$\frac{\tau \dot{B}_e}{B_{p,MF}} \approx \frac{\tau \dot{B}}{B_{p,MF}} = 1 - i, \qquad \text{at } i^* = 1, \text{ composite slab saturated} \tag{2.86}$$

Similar to what has been reviewed in subsection II.4.2, when the multifilamentary slab carries a transport current, the relationships between the external field and the applied field are extended from Eq. (2.75) as

$$B_e - B \approx \tau \dot{B}_e, \qquad \text{for } \tau \dot{B}_e \le B_{p,MF} (1 - i) \tag{2.87a}$$

$$B_e - B \approx B_{p,MF} (1 - i), \qquad \text{for } \tau \dot{B}_e > B_{p,MF} (1 - i) \tag{2.87b}$$

When the variation of the applied field ΔB_e is smaller than the $\Delta B'_{p,MF}$, the composite slab is partially penetrated (Fig. 2.12(a) and (b)). Since the field affects only the saturated region, the hysteresis loss pattern is the same as that with $I_t = 0$ (Ref. 2.7). The magnetization of the multifilamentary slab due to the shielding currents is the same as that of Eq. (2.76a),

$$- \mu_0 M_{c1} \approx \tau \dot{B}_e - \frac{1}{2} \frac{(\tau \dot{B}_e)^2}{B_{p,MF}}, \qquad \text{for } \tau \dot{B}_e \le B_{p,MF}(1 - i) \qquad (2.76a)$$

At a very slow field variation, the thickness of the saturation layer and thus the penetration loss approaches zero,

$$Q_{s1} \approx 0 \qquad \text{for } \tau \dot{B}_e << B_{p,MF}(1 - i) \qquad (2.88)$$

Assuming that the variation of the external field is much larger than the penetration field of the filament ΔB_p, the hysteresis magnetization of the filaments is

$$- \mu_0 M_{h1} = \frac{1}{2} B_p (1 - i^{*2}) \left(1 - \frac{\tau \dot{B}_e}{B_p}\right), \qquad \text{for } \tau \dot{B}_e \le B_{p,MF}(1 - i) \qquad (2.89)$$

In a slowly changing field, with J_c independent from the external field variation, the hysteresis loss is approximated as

$$Q_{h1} \approx \frac{\Delta B_e^2}{2\mu_0} \frac{\Delta B_p}{\Delta B_e} (1 - i^2) \qquad \text{for } \tau \dot{B}_e << B_{p,MF}(1 - i) \qquad (2.90)$$

If at any instant the field variation from the mean value is beyond the $B_{p,MF}(1 - i)$, as seen in Figs. 2.12(c), and (d), the magnetization of the multifilamentary slab due to the shielding currents is affected by the transport current as

$$- \mu_0 M_{c2} = \frac{1}{2} B_{p,MF} (1 - i^2) \qquad \text{for } \tau \dot{B}_e > B_{p,MF}(1 - i) \qquad (2.91)$$

Based on the Bean model, J_c = constant, the penetration loss becomes

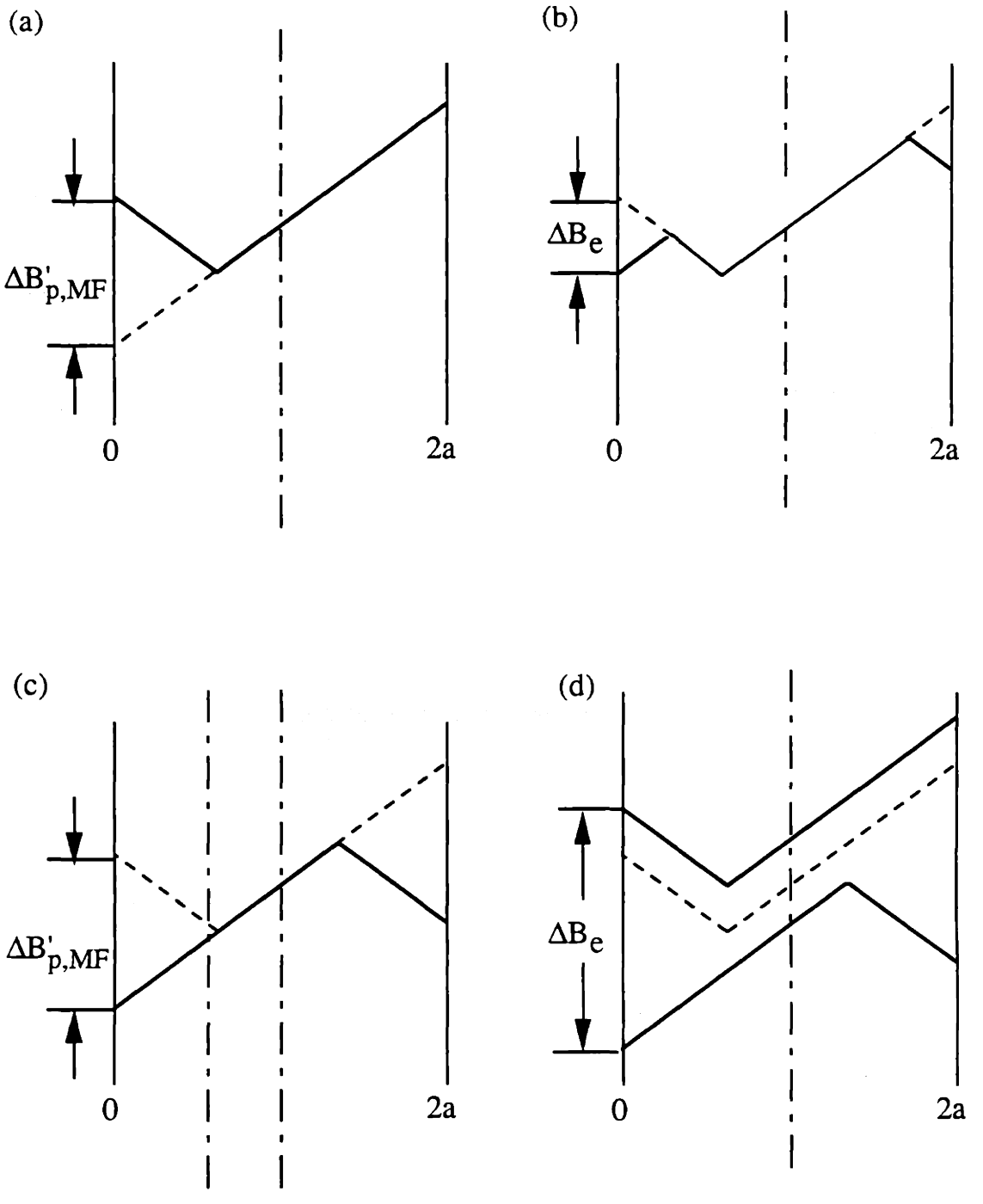

Fig. 2.12 (a) A superconducting slab carrying DC transport current in a parallel AC field; (b) $\Delta B_e < \Delta B'_{p,MF}$; (c) $\Delta B_e = \Delta B'_{p,MF}$; (d) $\Delta B_e > \Delta B'_{p,MF}$.

$$Q_{s2} = \frac{\Delta B_e^2}{2\mu_0} \frac{\Delta B_{p,MF}}{\Delta B_e}(1 - i^2) \qquad \text{for } \tau \dot{B}_e > B_{p,MF}(1 - i) \qquad (2.92)$$

In a fast changing field, all the filaments in the multifilamentary slab are saturated by either the transport currents or the coupling currents, the magnetization current in the filaments against the external field variation can no longer exist. Thus,

$$- \mu_0 M_{h2} = 0 \qquad \text{for } \tau \dot{B}_e > B_{p,MF}(1 - i) \qquad (2.93)$$

and

$$Q_{h2} = 0 \qquad \text{for } \tau \dot{B}_e > B_{p,MF}(1 - i) \qquad (2.94)$$

II.5.1.2 Dynamic Resistivity

According to Ogasawara, et al. (Refs. 2.41 to 2.44 and 2.48), when a current-carrying composite superconducting wire is affected by a changing field, the current source delivers a real power to the superconducting filaments and a resistive voltage appears across the wire. By Faraday's law, a voltage builds up due to the change of the total flux enclosed in the non-saturated region. For a superconducting filament with a radius of r_f in a multifilamentary slab with a half width of a_{MF}, the loss voltage per length of the filament can be expressed as

$$V_t = \frac{d}{dt}\left(\frac{1}{2} B_e \Delta x\right) = \frac{1}{2} \dot{B}_e \frac{I_t}{I_c} 2r_f = \frac{1}{2} \dot{B}_e \, i \, 2r_f \qquad \text{for } \delta \rightarrow 0 \qquad (2.95)$$

where δ is the thickness of the saturation layer in the multifilamentary zone. As the field changing rate increases, the growth of the saturation layer tends to decrease the area that the transport currents can flow without additional loss. Therefore, the loss voltage V_t is modified by substituting i with i^*. From Eq. (2.85),

$$V_t = \frac{1}{2} \dot{B}_e \, i^* \, 2r_f = \frac{1}{2} \dot{B}_e \, 2r_f \frac{i}{\left(1 - \frac{\tau \dot{B}_e}{B_{p,MF}}\right)} \qquad \text{for } \tau \dot{B}_e \leq B_{p,MF}(1 - i) \qquad (2.96)$$

The dynamic loss per unit volume of the multifilamentary zone is simply

$$Q_d = \frac{2}{A_{MF}} \int_0^t V_t I_t \, dt \tag{2.97}$$

where A_{MF} is the cross sectional area of the multifilamentary zone. At a low field changing rate, the loss is approximated as

$$Q_d \approx \frac{\Delta B_e^2}{\mu_0} \frac{\Delta B_{p,MF}}{\Delta B_e} i^2 \qquad \text{for } \tau \dot{B}_e << B_{p,MF}(1 - i) \tag{2.98}$$

When the whole composite is fully saturated in a high field changing-rate, the inner region is saturated by the transport current, that is $i^* = 1$. By Eq. (2.96), the loss voltage in the inner region is simplified to

$$V_{t,inner} = \frac{1}{2} \dot{B}_e \, 2r_f \tag{2.99}$$

Due to the twisting, the saturated region shields the inner region by $\mu_0 K_s = B_e - B$. The field penetrating the saturated region is thus $B_e - B$. In the outer saturated region, the loss voltage is

$$V_{t,outer} = \frac{1}{2}(\dot{B}_e - \dot{B}) \, i \, 2a_{MF} \tag{2.100}$$

From Eq. (2.86), the changing-rate of the applied field is related to the external field and the transport current by

$$\dot{B} = (1 - i)\frac{B_{p,MF}}{\tau} = (1 - i)\dot{B}_e \frac{B_{p,MF}}{\tau \dot{B}_e} \tag{2.101}$$

Substituting Eq. (2.101) into Eq. (2.100),

$$V_{t,outer} = \frac{1}{2} \dot{B}_e \, i \, 2a_{MF} \left(1 - (1 - i)\frac{B_{p,MF}}{\tau \dot{B}_e}\right) \tag{2.102}$$

The total loss voltage at a higher field changing-rate is the summation of Eqs. (2.99) and (2.102) which is given as

$$V_t = \frac{1}{2}\dot{B}_e\, 2r_f + \frac{1}{2}\dot{B}_e\, i\, 2a_{MF}\left(1 - (1 - i)\frac{B_{p,MF}}{\tau \dot{B}_e}\right) \qquad \text{for } \tau \dot{B}_e > B_{p,MF}(1 - i) \quad (2.103)$$

Since $B_e - B \approx B_{p,MF}$ at a high field changing-rate, the loss due to the dynamic resistivity is approximated as

$$Q_d \approx \frac{\Delta B_e^{\,2}}{\mu_0} i^2 \frac{\Delta B_{p,MF}}{\Delta B_e} \qquad \text{for } \tau \dot{B}_e > B_{p,MF}(1 - i) \quad (2.104)$$

II.5.1.3 Additional Loss Due to DC Transport Current

The total loss of a composite superconducting slab is taken as the linear sum of the coupling loss, the hysteresis loss, and the loss due to dynamic resistivity as a DC transport current is applied. As summarized by Ogasawara, et al. (Ref. 2.42), for slow field variation, $\tau \dot{B}_e << B_{p,MF}(1 - i)$:

$$Q_{s1} \approx 0 \quad (2.88)$$

$$Q_{h1} \approx \frac{\Delta B_e^2}{2\mu_0} \frac{\Delta B_{p,MF}}{\Delta B_e}(1 - i^2) \quad (2.90)$$

$$Q_d \approx \frac{\Delta B_e^2}{\mu_0} \frac{\Delta B_{p,MF}}{\Delta B_e} i^2 \quad (2.98)$$

the total loss is given as

$$Q_t(i) \approx \frac{\Delta B_e^2}{2\mu_0} \frac{\Delta B_{p,MF}}{\Delta B_e}(1 + i^2) \quad (2.105)$$

At $I_t = 0$, the total loss contains only the hysteresis loss of the filaments in the composite. The form of $Q_t(0)$ is consistent with that of Eq. (2.21) if $B_{max} >> \Delta B_{p0,MF}$ is applied. The relationship of the losses between with and without a DC transport current is simply

$$Q_t(i) \approx Q_t(0)\,(1 + i^2) \tag{2.106}$$

The additional loss due to the DC transport current is $i^2Q_t(0)$. The same conclusion can be found in other previous publications (Refs. 2.12, 2.41 to 2.45).

For high field changing-rate, $\tau \dot{B}_e > B_{p,MF}\,(1 - i)$:

$$Q_{s2} = \frac{\Delta B_e^2}{2\mu_0}\,\frac{\Delta B_{p,MF}}{\Delta B_e}\left(1 - i^2\right) \tag{2.92}$$

$$Q_{h2} = 0 \tag{2.94}$$

$$Q_d \approx \frac{\Delta B_e^{\,2}}{\mu_0}\,i^2\,\frac{\Delta B_{p,MF}}{\Delta B_e} \tag{2.104}$$

the total loss is given as

$$Q_t(i) \approx \frac{\Delta B_e^2}{2\mu_0}\,\frac{\Delta B_{p,MF}}{\Delta B_e}\left(1 + i^2\right) \tag{2.107}$$

The similar conclusion of $Q_t(i) \approx Q_t(0)\,(1 + i^2)$ is reached.

II.5.2 AC Transport Current in a Multifilamentary Slab

The same formulations for the magnetization and the loss voltage of dynamic resistivity applied in Section II.5.1 were used to analyze the loss of a multifilamentary slab carrying a time-varying (AC) transport current by Ogasawara, et al. (Ref. 2.44). In their analysis, the critical current was fixed as a constant and was evaluated at $B_{mean} = (B_{max} + B_{min}) / 2$. The AC transport current was assumed to be in-phase with the external AC field and varied between 0 and I_m. By including the time-dependent transport current in the loss integrations, with $i_m \equiv I_m/I_c$, the relation of

$$Q_t(i) \approx Q_t(0)\,(1 + \frac{1}{3}\,i_m^2) \tag{2.108}$$

was concluded for a composite slab carrying AC transport current in both slow and fast field variations. The same conclusion was reached for the case of slow field variation in another article (Ref. 2.53).

II.6 SUMMARY

Hysteresis loss analyses for 1-D slab and 2-D cylindrical geometries, based on the Bean critical state model, have been reviewed. Hysteresis loss is the most fundamental loss of a superconductor in a time-varying field, which occurs at any time-rate of field variation. Critical current density and the filament size are the most important parameters in calculating hysteresis loss.

Coupling loss is strongly affected by the coupling time constant which contains all the physical properties of a twisted composite wire other than the superconducting filaments. The coupling loss is an increasing function of the field changing rate. Depending on the coupling time constant, when the frequency of the AC field increases, the coupling loss may become larger than the hysteresis loss. In this chapter, the existing coupling loss model for a composite wire with 4-layer structure has been generalized into a 5-layer structure to include all the wire constructions encountered in the present work.

At a high field changing rate, the coupling currents saturate the outer-most layer of the superconductor filaments. The thickness of the saturation layer grows as the frequency increases. The penetration loss due to the magnetization of the saturated layer becomes important. Meanwhile, the fraction of filaments producing hysteresis loss as well as coupling loss is reduced. At a critical field changing rate, the total loss reaches a maximum value then decreases monotonically with the increase of the frequency of the field variation. For the field conditions applied in the present work, the saturation layer in a single strand is always negligible. The mechanism of penetration loss is more important than the final loss expressions in the existing analysis, which will be applied to develop a new AC-loss model in Chapter VI.

When a transport current is applied to a composite superconductor, the hysteresis loss is reduced due to the saturation of the filaments by the transport current. However, the increase of the loss due to the dynamic resistance is more than the decrease of the hysteresis loss. The net loss of a current-carrying composite superconductor is always larger than

that of a current-free conductor. In the existing analysis based on the Bean critical state model, the additional loss caused by the transport current is of hysteresis type of loss which is independent from the field changing rate. The loss becomes significant when the applied DC or synchronized AC current approaches the critical current at a given field.

The existing hysteresis-loss models were developed on the basis of critical state model which assumes $|J_c|$ = constant. These models are best applied for a superconductor affected by a small changing field superposed on a large DC bias field. In this thesis work, two types of field variation are of interest: (1) a small sinusoidal wave-form field superimposed on various large DC bias fields, and (2) a large peak-to-peak unidirectional triangular cyclic field. The first field condition is a good approach to the critical state model. However, the critical current changes with the DC bias field. In the second field condition, the critical current in the superconductor changes instantaneously with the large amplitude AC field. The variation of the critical current with the applied field is large enough that the Bean model is no longer valid. Modifications of the existing hysteresis-loss model in 2-D cylindrical geometry for the field conditions of interest to this thesis work will be performed in Chapter III.

II.7 REFERENCES

2.1 Bean, C.P., 'Magnetization of Hard Superconductors,' Phys. Rev. Letters, Vol. 8, 1962, p. 250.

2.2 Bean, C.P. and Doyle, M.V., 'Superconductors as Permanent Magnets,' J. Appl. Phys., Vol 33, 1962, p. 3334; and Vol 34, 1963, p. 1364.

2.3 Bean, C.P., 'The Magnetization of High Field Superconductors,' Revs. of Mod. Phys., Vol 36, 1964, p. 31.

2.4 Bean,C.P., et al. 'A Research Investigation of the Factors That Affect the Superconducting Properties of Materials,' AFML-TR-65-431, 1966.

2.5 Orlando, T.P., and Delin, K.A., *Foundations of Applied Superconductivity*, Addison-Wesley, 1991.

2.6 Kim, Y.B., Hempstead, C.F., and Strand, A.R., 'Magnetization and Critical Supercurrents,' Phys. Rev., Vol. 129, 1963, p. 528.

2.7 Wilson, M.N., *Superconducting Magnets*, Oxford Science Publications, 1983.

2.8 Kato, Y., Hanawaka, M., and Yamafuji, K., 'Flux Penetration into a Wire of a Nonideal Type II Superconductor in a Transverse Magnetic Field,' Jpn. J. Appl. Phys., Vol. 15, No. 4, 1976,

2.9 Ashkin, M., 'Flux distribution and hysteresis loss in a round superconducting wire for the complete range of flux penetration,' J. Appl. Phys., Vol. 50, No. 11, 1979, p. 7060.

2.10 Pang, C.Y., McLaren, P.G., Campbell, A.M., 'Losses in Superconducting Cylinders in Transverse Fields,' Proceedings of the 1980 International Cryogenic Engineering conference, Genova, Italy, 1980, p. 739.

2.11 Zenkevitch, V.B., Romanyuk, A.S., Zheltov, V.V., 'Losses in composite Superconductors at high levels of magnetic field excitation: part 1,' Cryogenics, 1980, p. 703.

2.12 Minervini, J.V., "Analysis of Loss Mechanisms in Superconducting Windings for Rotating Electric Generators," MIT thesis, 1981.

2.13 Zenkevitch, V.B., Romanyuk, A.S., Zheltov, V.V., 'Losses in composite Superconductors at high levels of magnetic field excitation: part 2,' Cryogenics, 1981, p. 13.

2.14 Rutherford Laboratory, 'Experimental and theoretical studies of filamentary superconducting composites,' J. Physics D, Vol. 3, 1970, p. 1517.

2.15 Morgan, G.H., 'Theoretical behavior of twisted multicore superconducting wire in a time-varying uniform magnetic field,' J. Appl. Phys., Vol. 41, No. 9, 1970, p. 3673.

2.16 Brechna, H., *Superconducting Magnet Systems*, Springer-Verlag, 1973.

2.17 Carr, W.J., 'AC loss in a twisted filamentary superconducting wire, I,' J. Appl Phys., Vol. 45, No. 2, 1974, p. 929.

2.18 Kwasnitza, K., and Horvath, I., 'AC loses of superconducting composites with 8 μm NbTi filaments in a DC magnetic field with a superimposed AC component at $1 \leq f \leq 500$ Hz,' Cryogenics Vol 15, 1975, p. 723.

2.19 Ries, G., 'AC-losses in multifilamentary superconductors at technical frequencies,' IEEE Trans. Magnetics, Vol. MAG-13, No. 1, 1977, p. 524.

2.20 Kwasnitza, K., 'Scaling law for the AC losses of multifilaments superconductors,' Cryogenics, 1977, p. 616.

2.21 Wilson, M.N., *Superconducting Magnets*, Oxford Science Publications, 1983.

2.22 Zenkevitch V.B., Romaniuk, A.S., 'Losses in multifilamentary superconductors at low levels of excitation,' IEEE Trans. Magnetics, Vol. MAG-13, No. 1, 1977, p. 567.

2.23 Zenkevitch V.B., Romaniuk, A.S., 'The effect of magnetic properties of a composite superconductor on the losses in variable magnetic field: part 1 theory,' Cryogenics Vol. 19, 1979, p. 725.

2.24 Turck, B., 'Effective transverse resistivity in multifilamentary superconducting composite,' ICEC 9 - ICMC, Kobe, Japan, May 11-14, 1982.

2.25 Carr, W.J.Jr., IEEE Trans. Magnetics, Vol. 13, No. 1, 1977, p. 192.

2.26 *Handbook on Materials for Superconducting Machinery*, MCIC-HB-04, 1977, updated March 1985.

2.27 Fickett, F.R., 'Electric and magnetic properties of CuSn and CuNi alloys at 4 K,' Cryogenics, 1982, p 135.

2.28 *CRC Handbook of Chemistry and Physics*, 70th Ed., 1989-1990.

2.29 Ando, T., Takahashi, Y., Nishi, M., and Shimamoto, S., 'AC losses in a Ta barrier Nb_3(SnIn) strand in demo poloidal coil,' Adv. Cryo. Eng., Vol. 34, 1988, p. 879.

2.30 Hall, L.A., 'Survey of electrical resistivity measurements on 16 pure metals in the temperature range from 0 to 273 K,' NBS Technical Note 365, 1968.

2.31 Benz, M.G., 'Magnetoresistance of copper at 4.2 K in transverse fields up to 100 KG,' J. Appl. Phys., Vol. 40, No. 5, 1969, p. 2003.

2.32 Fickett, F.R., 'A preliminary investigation of the behavior of high purity copper in high magnetic fields,' International Copper Research Report, No. 186, 1972.

2.33 Nick, W., and Schnidt, C., 'Thermal magnetoresistance of copper matrix in compound superconductors, a new measuring method,' IEEE Trans. on Magnetics, MAG-17, No. 1, 1981, p. 217.

2.34 Fickett, F.R, 'The effect of mill temper on the mechanical and magnetoresistive properties of oxygen-free copper in liquid helium,' Adv. Cryo. Eng., Vol. 30, 1984, p. 453.

2.35 Fickett, F.R., and Capobianco, T.E, ' Relationship between mechanical and magnetoelectric properties of oxygen-free copper at 4 K,' Adv. Cryo. Eng., Vol. 32, 1986, p. 421.

2.36 Fickett, F.R., 'Transverse magnetoresistance of oxygen-free copper,' IEEE Trans. on Magnetics, Vol. 24, No. 1, 1988, p. 1156.

2.37 Turck, B., 'Coupling losses in various outer normal layers surrounding the filament bundle of a superconducting composite,' J. Appl. Phys., Vol. 50, No. 8, 1979, p. 5397.

2.38 Turck, B., 'Effect of the respective positions of filament bundles and stabilizing copper on coupling losses in superconducting composites,' Cryogenics, 1982, p. 466.

2.39 Ito, D., Koisumi, M., Hamajima, T., Nakane, F., 'The influence of filament bundle location on coupling losses in superconducting composites. Part I: mixed matrix conductor,' Cryogenics, 1983, p. 643.

2.40 Soubeyrand, J.P., and Truck, B., 'Losses in superconducting composites under high rate pulsed transverse field,' IEEE Trans. on Magnetics, MAG-15, No. 1, 1979, p. 248.

2.41 Ogasawara, T., et al., 'Alternating field losses in superconducting wires carrying dc transport currents: part 1 single core conductors,' cryogenics, 1979, p. 736.

2.42 Ogasawara, T., et al., 'Transient field losses in multifilamentary composite conductors carrying dc transport currents,' Cryogenics, 1980, p. 216.

2.43 Ogasawara, T., et al., 'Alternating field losses in superconducting wires carrying dc transport currents: part 2: multifilamentary composite conductors,' cryogenics, 1981, p. 97.

2.44 Ogasawara, T., et al., 'Transient field losses in multifilamentary composite conductors carrying transport currents,' IEEE Trans. on Magnetics, MAG-17, No. 1, 1981, p. 967.

2.45 Campbell, A.M., 'The effect of transport current and saturation on the losses of multifilamentary superconducting wires,' Cryogenics, 1981, p. 107.

2.46 London, H., 'Alternating current losses in superconductors of the second kind,' Phys. Letters, Vol. 6, No. 2, 1963, p. 162.

2.47 Hancox, R., 'Calculation of a.c. losses in a type II superconductor,' Proc. IEE, Vol. 113, No. 7, 1966, p. 1221.

2.48 Ogasawara, T., et al., 'Effective resistance of superconducting winding in oscillating magnetic fields,' IEEE Trans. on Magnetics, MAG-11, No. 2, 1975, p. 362.

2.49 Duchateau, J.L., Turck, B., Krempasky, L., and Polak, M., 'The self-field effect in twisted superconducting composites', Cryogenics, 1976, p. 97.

2.50 Turck, B., Krempasky, L., and Polak, M., ' Self field and external field effects on the current distribution in superconducting wires,' MT-6, Aug. 1977, Bratislava, Czechoslovakia.

2.51 Murphy, J.H., 'Skin effect alternating current losses in multifilamentary superconductors,' IEEE Trans. on Magnetics, MAG-13, No. 1, 1977, p. 564.

2.52 Shen, S.S., and Schwall, R.E., 'Interaction of transport current and transient external field in composite conductors,' IEEE Trans. on Magnetics, MAG-15, No. 1, 1979, p. 232.

2.53 Carr, W.J., 'AC loss from the combined action of transport current and applied field,' IEEE Trans. on Magnetics, MAG-15, No. 1, 1979, p. 240.

2.54 Sumiyoshi, F., Hori, H., Irie, F., and Kawashima, T., 'Using magnetic field pulses with a slow sweep rate to produce uniform current distribution in multifilamentary superconducting wire,' Cryogenics, 1983, p. 373.

2.55 Sumiyoshi, F., et al., 'On the distribution of a transport current inside a multifilamentary superconducting wire in a rapidly changing transverse magnetic field,' Cryogenics, 1983, p. 619.

2.56 Kawashima, T., Sumiyoshi, F., Irie, F., and Yamafuji, K., 'Losses in a multifilamentary superconducting wire caused by a simultaneous sweep of current and magnetic field,' Cryogenics, 1984, p. 313.

2.57 Kanbara, K., 'Hysteresis loss of a round superconductor carrying a d.c. transport current in an alternating transverse field,' Cryogenics, 1987, Vol. 27, p. 621.

CHAPTER III

HYSTERESIS LOSSES WITH FIELD-DEPENDENT CRITICAL CURRENT DENSITY

III.1 INTRODUCTION

The existing hysteresis-loss models, as have been reviewed in Chapter II, were developed on the basis of critical state model which assumes $|J_c|$ = constant. These models are best applied for a superconductor affected by a small changing field superimposed on a large DC bias field. In this thesis work, two types of field variation are of interest: (1) a small sinusoidal wave-form field superimposed on various large DC bias fields, and (2) a large peak-to-peak unidirectional triangular cyclic field. The first field condition is a good approach to the critical state model. However, the critical current changes with the DC bias field. The existing 2-D analytical approximations based on the Bean model will be modified by expressing the critical current density as a function of the DC bias field. The second field condition is applied to simulate the field condition of a superconducting magnet for ramp-field application. The critical current in the superconductor changes instantaneously with the large amplitude AC field. The variation of critical current with field is large enough that the Bean model is no longer valid. Modifications of the existing hysteresis-loss model in 2-D cylindrical geometry for the field conditions mentioned above will be performed in this chapter. Assumptions and simplifications in modifying the existing hysteresis-loss models will be discussed. The expression of the effective filament diameter, which is an important index to the extent of the filament bridging, will be shown.

As shown in Chapter II, the hysteresis loss depends heavily on the critical current density. The field-dependent critical current density profile is an important parameter affecting the hysteresis loss of a superconductor in a large field variation. Expressions of the field-dependent critical current profiles for Nb_3Sn and NbTi superconductor will be discussed before modifying existing hysteresis loss models.

III.2 CRITICAL CURRENT DENSITIES

III.2.1 Multifilamentary Composite

In some superconducting magnet application such as the ohmic heating coil in a fusion reactor, the range of the field variation can be as large as ± 14 T. When calculating the hysteresis losses of a superconductor in a transverse field with such a large variation, it is necessary to have a good estimation of the profile of the axial critical current density throughout the range of the field variation. The first field dependent critical current density applied to the hysteresis-loss analysis was the one shown in Eq. (2.2) which was postulated by Kim, et al. (Ref. 2.6). The expression was obtained empirically from the measured critical current density of superconductor tubes.

The critical current density of a bulk superconductor is determined by the flux pinning force in the conductor, which can be modified by grain-boundary pinning, alloying additives, radiation damage, etc. (Refs. 3.1 to 3.5). All the methods tend to increase the room temperature resistivity of the superconducting material. Since a technical superconductor is always in multifilamentary composite form, the critical current density is thus determined by not only the flux pinning behavior of the superconductor itself but also the additional factors, such as longitudinal compressive stress imposed by the stabilizer (Refs. 3.1, 3.6, and 3.7), the completeness of the heat treatment for A15 compounds, etc. For high current and high field applications, the superconducting wires are further twisted into cables and may be enclosed in conduit material (Refs. 3.8 and 3.9). Depending on the need, the superconducting cable may be operated at a temperature different from 4.2 K. The critical current density of a superconducting wire is further affected by the operation temperature (Refs. 3.10 and 3.11), the thermal compatibility with the conduit material (Ref. 3.12), the longitudinal hoop stress (Refs. 3.5 to 3.7) and the lateral compressive stress from other wires in the cable (Ref. 3.13) due to Lorentz force, etc.

Discussions of the critical current densities will be focused on Nb_3Sn composite wires. Existing general expressions of the critical current density partly based on flux pinning behavior and partly from empirical formulae are included for self-sufficient purposes. For the purpose of hysteresis-loss calculation relevant to this thesis work, only the magnetic field effect on the superconductor will be considered. In general, a superconductor can carry very high current when the external field approaches to zero. The field-dependent critical current profile decreases almost exponentially as the field increases. External effects

as mentioned above will be taken as constant and lumped into some fitting parameters. In order to improve the critical current and/or critical field, NbTi superconductor is usually optimized by adding a third element. The field-dependent critical current density expression of an optimized NbTi composite, which is less complicated compared with that of a Nb_3Sn composite, will be simply extracted from published articles for future computation.

III.2.2 Existing General Expression for Nb_3Sn

Summers, et al. combined the field, temperature, longitudinal strain and radiation damage dependence of the critical current density of a multifilamentary Nb_3Sn superconducting wire into a single functional form (Ref. 3.10). Excluding the radiation damage dependence, the expression is written as

$$J_c(b, t, \varepsilon) = C(\varepsilon) \{B_{c2}(t,\varepsilon)\}^{-1/2} (1 - t^2)^2 b^{-1/2} (1 - b)^2 \qquad (3.1)$$

where

ε = intrinsic strain of the multifilaments

$C(\varepsilon) = C_0 (1 - a |\varepsilon|^u)^{1/2}$

C_0 = a coefficient independent of field, temperature, and strain

$B_{c2}(t, \varepsilon) = B_{c20}(\varepsilon) (1 - t^2) \{1 - 0.31 t^2 (1 - 1.77 \ln t)\}$

$B_{c20}(\varepsilon) = B_{c20m} (1 - a |\varepsilon|^u)$

$t = T / T_{c0}(\varepsilon)$

$b = B / B_{c2}(T, \varepsilon)$

$T_{c0}(\varepsilon) = T_{c0m} (1-a |\varepsilon|^u)^{1/w}$

$a = 900$ for $\varepsilon < 0$, 1200 for $\varepsilon > 0$

$u = 1.7$

$w = 3$

Four parameters, ε, C_0, B_{c20m}, and T_{c0m}, in the expression need to be found by the best fit to the experimental data. The expression is general enough to fit all the experimental critical current density profiles of binary Nb_3Sn wires as mentioned in the same reference. Good agreement was found in the high field region (> 10 T) when the formula was applied to a Ti-alloyed Nb_3Sn wire.

As shown by Summers et al., when the above formula was applied to fit the field-dependent critical current of a ternary alloyed Nb_3Sn, it failed to satisfy the experimental data in both high-field and low-field regions simultaneously. The low-field critical currents were over-estimated while the high-field end fitted well. This is because the field-dependent part of the formula was originally developed for binary Nb_3Sn in Kramer's flux-line-shearing model (Ref. 3.2). For high field applications, the purpose of adding a third alloying element is usually to raise the high field critical currents at the price of reduced low field performance. Therefore, the decrease of the field-dependent critical current profiles of some ternary alloyed Nb_3Sn superconductors become less steep in the low-field region. In some cases only a single end of the critical current profile can be fitted well by applying the above formula (Ref. 3.10). However, the discrepancy depends on the degree of the alloying which will be discussed in the next subsection. Successful fitting to both wires and cable made of the same ternary Nb_3Sn has also been reported (Ref. 3.11).

III.2.3 Field-Dependent J_c's for Nb_3Sn and NbTi

Once the superconducting system and the operating condition have been fixed, assuming the temperature does not change throughout the cycle, the critical current and therefore the hysteresis loss depend only on the external field. Thus, all the parameters other than the applied field can be lumped into a few constants. As mentioned above, the superconductor filaments are affected by complicated manufacturing processes. The best way to find out these lumped constants is by data fitting to the measured critical current profile. It is important to know that for some superconducting wires even with the same structure and made by the same manufacturer, their critical current profiles may be different by more than 20%. If an averaged critical current profile is used without careful examination, this can be one of the sources causing error in the hysteresis-loss calculation .

III.2.3.1 Nb_3Sn

From flux pinning theories of Nb_3Sn (Ref. 3.1), the effect of the field on the pinning force, F(B), has the following relationship:

$$F(B) \propto \left(\frac{B}{B_{c2}(T,\varepsilon)}\right)^p \left(1 - \frac{B}{B_{c2}(T,\varepsilon)}\right)^q$$

Theoretically, critical current density is reached once the Lorentz force due to the transport current and the fluxoid exceeds the pinning force in the superconductor. The pinned vortices begin to move and cause power dissipation. The relationship between the pinning force and the Lorentz force may be described as (Ref. 3.1)

$$F(B) \propto J_c(B) \cdot B$$

Thus, the shape of $J_c(B)$ affected by the field is in the form of (Ref. 3.1)

$$J_c(B) \propto \left(\frac{B}{B_{c2}(T,\varepsilon)}\right)^{-(1-p)} \left(1 - \frac{B}{B_{c2}(T,\varepsilon)}\right)^{q} \tag{3.2}$$

Table 3.1 shows a list of the experimental values of p and q for Nb_3Sn with different alloying additives for high field applications (Ref. 3.5). The p value is less sensitive to the alloying additives, which remains at about 0.5. The binary Nb_3Sn has a q value of 2, larger than those of ternary conductors, which represents a steeper decrease of the $J_c(B)$ distribution in the low-field region. The q value depends on not only the alloying element and its content but also the extent of heat treatment for reacting the Nb and Sn.

Table 3.1 $J_c(B)$ of binary and some ternary Nb_3Sn (Ref. 3.5)

Compound	**p**	**q**
Nb_3Sn	0.5	2.0
Nb - 5%† Hf/Cn - 5% Sn - 4% Ga	0.4	1.1
Nb_3Sn + 0.6% Ti	0.6	1.7
Nb_3Sn + 1.85% Ti	0.5	1.5
Nb_3Sn + 0.6% Ta	0.5	1.4
Nb_3Sn + 2.2% Ta	0.5	1.7

† in at.%

The semi-empirical critical current formula to be used in the present work is written as

$$I_c(B) = C^* B^{-(1-p)} \left(B_{c2}^* - B\right)^q \tag{3.2a}$$

where the fitting parameters are C^*, B_{c2}^*, p and q. Compared with Eq. (3.1), C^* is a lumped constant independent from the field effect, B_{c2}^* is an equivalent upper critical field

extrapolated from the critical current distribution, and the exponents p and q are the parameters containing the metallurgic information. Eq. (3.2a) contains four degrees of freedom, similar to that of Eq. (3.1). However, Eq. (3.2a) concentrates on the material property instead of environmental effects such as temperature and stresses which are lumped into C^* and $B_{c2}{}^*$ as constants. Expressions of critical current density are similar to that of Eq. (3.2a) with some change to the leading constant coefficient.

For non-copper J_c of a Nb_3Sn composite,

$$J_{c,nonCu}(B) = C^*_{nonCu}\, B^{-(1-p)} \left(B^*_{c2} - B\right)^q, \tag{3.2b}$$

$$C^*_{nonCu} = \frac{C^*}{\pi R_w^2 f_{nonCu}}$$

where R_w is the radius of the composite wire, and f_{nonCu} is the volume fraction of non-copper materials in the composite. In the case of Nb_3Sn, the non-Cu materials are the constituent materials for making the superconductor filaments before the heat treatment, which include Nb, Sn, alloying additives, and diffusion barriers.

For superconductor J_c of a Nb_3Sn composite,

$$J_{c,SC}(B) = C^*_{SC}\, B^{-(1-p)} \left(B^*_{c2} - B\right)^q \tag{3.2c}$$

$$C^*_{SC} = \frac{C^*}{\pi R_w^2 f_{nonCu} f_{SC\ in\ nonCu} (1 + f_{HT})}$$

where $f_{SC\ in\ nonCu}$ is the volume fraction of niobium in the non-Cu material before the heat treatment, and f_{HT} is the fraction of the volume increment of niobium filament after forming Nb_3Sn by the heat treatment. The typical value for f_{HT} is about 35% (Refs. 3.14 and 3.15).

As shown in Table 3.1, the binary Nb_3Sn has a p value of 0.5 and a q value of 2. Physically, the ternary Nb_3Sn compound is a correction of the binary compound. The correction effect, mathematically shown in the expression of the critical current densities, perturbs both of the p and q values. For the convenience of future hysteresis-loss

integration, the correction part of the $J_{c,SC}(B)$ due to the perturbation of the q is separated as

$$J_{c,SC}(B) = C^*_{SC}\left(B^*_{c2} - B\right)^2 B^{-(1-p)}\left(B^*_{c2} - B\right)^{q-2} \quad \text{for } Nb_3Sn \tag{3.3a}$$

The last term on the right-hand-side is considered as a correction term due to alloying additives, which can be linearized by taking a Taylor expansion as follows

$$\left(B^*_{c2} - B\right)^{q-2} \approx B^{*\,q-2}_{c2}\left[1 + (2-q)\frac{B}{B^*_{c2}} + (\text{higher order terms})\right] \quad \text{for } 1 < q \le 2 \tag{3.3b}$$

The above series converges since $q \le 2$ and $B \le B^*_{c2}$. Substituting Eq. (3.3b) into Eq. (3.3a), the $J_{c,SC}(B)$ is approximated as

$$J_{c,SC}(B) \approx C^*_{SC}\left(B^*_{c2} - B\right)^2 B^{-(1-p)}\left(B^{*\,q-2}_{c2} + (2-q)\,B^{*\,q-3}_{c2}B\right) \quad \text{for } 1 < q \le 2 \tag{3.3c}$$

As q = 2, the expression in Eq. (3.3c) is exactly the same as that in Eq. (3.3a). By using the linearized expression for $J_{c,SC}(B)$ a general analytical hysteresis loss integration for the family of Nb_3Sn will be performed in Section III.4.

III.2.3.2 NbTi

NbTi is the most popular metallic superconductor in alloy form. Compared with Nb_3Sn, the superconductor material in a NbTi composite is thermomechanically more compatible with the stabilizing matrix. The critical field of an optimized ternary NbTi can be raised to about 10 T. The pinning force for an optimized NbTi composite has the following relationship with the applied field (Refs. 3.4, 3.16, and 3.17):

$$F(B) \propto B\,(1-B) \tag{3.4}$$

The critical current and the critical current density of the superconductor have a linear relationship with the applied field which has also been observed by Hampshire and Larbalestier (Ref. 3.17). The field-dependent critical current is thus written as

$$I_c(B) = C^*\,(B^*_{c2} - B) \tag{3.6a}$$

where the C^* and $B_{c2}{}^*$ are the field independent fitting parameters as discussed before. With much better defined volume fraction of superconductor in a NbTi composite, the formula for the superconductor critical current density is given as

$$J_{c,SC}(B) = C^*_{SC} (B^*_{c2} - B) \qquad (3.6b)$$

With f_{SC} = volume fraction of the superconductor in the wire, the leading coefficient becomes

$$C^*_{SC} = \frac{C^*}{\pi r_w^2 f_{SC}}$$

Although the physical explanation to the field-dependent critical current densities of Nb_3Sn and NbTi are dramatically different from material science viewpoint (Ref. 3.4), the expression of Eqs. (3.6a) and (3.6b) can be seen as special case of Eqs. (3.2a) and (3.2c) by letting p = 1 and q = 1. Thus, Eqs. (3.2a) to (3.2c) can be taken as general expressions for a binary Nb_3Sn and an optimized NbTi superconductor, respectively.

III.2.4 Low-Field Critical Current Densities

The slope of the critical current distribution plotted against applied field is usually large in the low field region and small in the high field region. In practice, critical currents are usually measured in the higher field region (eg. > 8 T), and extrapolated to the lower field region. If an arbitrary function such as a polynomial, is applied for data fitting in the high field region, the extrapolated low field critical currents can be underestimated. Since the magnetization curve strongly depends on the field-dependent critical current, the low field magnetization is usually much higher than that at high field. The hysteresis loss is calculated as the area covered by the magnetization curve. The area in a low field region sometimes can dominate that in a high field region. The error in the hysteresis-loss calculation introduced by the extrapolation of the low field critical current density may become significant.

With some measured high field critical current data, instead of randomly choosing an extrapolation scheme, the semi-empirical functions listed above for Nb_3Sn and NbTi provide a better approach. As discussed, the exponents p and q in Eq. (3.2a) determine the

shape of the I_c distribution. With similar alloying elements and fractional contents, the exponents are about the same. If the elements and the amounts of the alloying additives are known, a better extrapolation can be obtained by using the exponents based on other experimental results such as those shown in Table 3.1. The multiplication constants are then determined from the high field critical current data.

The above expressions of the critical current are valid at a field beyond the first critical field of a superconductor, B_{c1}, which is typically 10^{-2} T or less. For hysteresis-loss calculation, the critical current density at fields lower than the B_{c1} is not needed since the type-II superconductor is in the Meissner state and the flux does not penetrate the superconductor.

III.3 HYSTERESIS LOSSES WITH A SMALL CYCLIC FIELD ON A LARGE DC BIAS FIELD

As a small amplitude time-varying field is superimposed on a large DC bias field, B_{DC}, the DC bias field affects the J_c and therefore the penetration field. With some minor modifications on the definitions of the variables, the expressions for the penetration field, magnetization, and the hysteresis losses are expressed as explicit functions of both the variation of the changing field and the magnitude of the DC bias field.

III.3.1 1-D Slab Geometry

Consider that both the small time-varying field and the B_{DC} field are parallel to the surface of an infinite slab with a width of 2a. The peak-to-peak value of the applied AC field is $\Delta B = B_{max} - B_{min}$, and the time-varying field is changed symmetrically with respect to the DC bias field. For a small ΔB, the penetration field at B_{DC} for a cyclic changing field is written as

$$\Delta B_p(B_{DC}) = 2\mu_0 J_{c,SC}(B_{DC})\, a \qquad \text{for } \Delta B << B_{DC} \qquad (3.7)$$

It is important to notice that the above relation of $\Delta B_p(B_{DC}) = 2B_p(B_{DC})$ holds only if the changing field is small compared with the DC bias field.

The hysteresis losses per cycle per unit volume, as modified from Eqs. (2.15) and (2.21) based on the Bean model for 1-D slab geometry, become

$$Q_h = \frac{\Delta B^2}{2\mu_0}\,\frac{1}{3}\,\frac{\Delta B}{\Delta B_p(B_{DC})} \qquad \text{for } \Delta B \le \Delta B_p(B_{DC}) \qquad (3.8)$$

and

$$Q_h = \frac{\Delta B^2}{2\mu_0}\left\{\frac{\Delta B_p(B_{DC})}{\Delta B} - \frac{2}{3}\left(\frac{\Delta B_p(B_{DC})}{\Delta B}\right)^2\right\} \qquad \text{for } \Delta B > \Delta B_p(B_{DC}) \qquad (3.9)$$

Since the J_c is a decreasing function of the applied field, the $\Delta B_p(B_{DC})$ decreases as the B_{DC} increases (Eq. (3.7)). As seen from Eq. (3.8), if the variation of the applied field is less than the penetration field at B_{DC}, the hysteresis loss increases with both the ΔB and the B_{DC}. However, when the ΔB is greater than the $\Delta B_p(B_{DC})$ at B_{DC}, the dependences of the loss on both the ΔB and the B_{DC} are reversed (Eq. (3.9)). Thus, by perturbing either ΔB or B_{DC}, a maximum hysteresis loss always occurs at $\Delta B = \Delta B_p(B_{DC})$.

III.3.2 2-D Cylindrical Geometry

When a small cyclic field superposed on a large DC bias field is applied transverse to a cylindrical superconductor of radius r_f, the magnetization and hysteresis-loss equations given by Zenkevitch et al. in Ref. 3.18 are modified by including the DC bias field effect, and listed in the following.

The penetration field of a cylindrical superconductor in a cyclic applied field is given as $\Delta B_p(B_{DC}) = 2B_p(B_{DC})$, or

$$\Delta B_p(B_{DC}) = \frac{4}{\pi}\mu_0 J_{c,SC}(B_{DC})\, r_f \qquad \text{for } \Delta B << B_{DC} \qquad (3.10)$$

where the penetration field in an initial virgin state $B_p(B_{DC})$ is given as

$$B_p(B_{DC}) = \frac{2}{\pi}\mu_0 J_{c,SC}(B_{DC})\, r_f \qquad (3.11)$$

With a symmetric $\Delta B = B_{max} - B_{min}$ with respect to the B_{DC}, the hysteresis losses in a cyclic field condition are given as

$$Q_h = \frac{\Delta B^2}{2\mu_0}\left[\frac{4}{3}\frac{\Delta B}{\Delta B_p(B_{DC})} - \frac{2}{3}\left(\frac{\Delta B}{\Delta B_p(B_{DC})}\right)^2\right] \qquad \text{for } \Delta B \le \Delta B_p(B_{DC}) \qquad (3.12)$$

and

$$Q_h = \frac{2\Delta B_p^2(B_{DC})}{3\mu_0}\left[\frac{\Delta B}{\Delta B_p(B_{DC})} - \frac{1}{2}\right] \qquad \text{for } \Delta B > \Delta B_p(B_{DC}) \qquad (3.13)$$

The hysteresis loss at $\Delta B = \Delta B_p(B_{DC})$ is written as

$$Q_{h,p} = \frac{\Delta B_p^2(B_{DC})}{3\mu_0} \qquad \text{at } \Delta B = \Delta B_p(B_{DC}) \qquad (3.14)$$

III.4 HYSTERESIS LOSSES WITH A LARGE CYCLIC FIELD

III.4.1 Basic Assumptions

In a typical type-II superconductor, the J_c reduces almost exponentially as the applied field is increased from zero. The assumption of J_c = constant in the critical state model is best applied to a technical superconducting wire in the high field region where the variation of the $J_c(B)$ is slow. Thus, if the change of the applied field covers a large range, the instantaneous J_c dependence on the time-varying applied field should be considered.

The largest difference in the internal field distribution throughout a filament is about ΔB_{p0} or $\Delta B_p(B_{DC})$ which depends on the size of the superconductor. Considering the small size of the filamentary superconductors in a technical superconducting wire (sub-micron to few microns), the ΔB_p is on the order of 10^{-2} to 10^{-1} T which is small compared with $\Delta B = B_{max} - B_{min}$ (1 ~ 10 T). Thus, the assumption of spatially uniform $|J_c|$ in the penetrated regions is generally acceptable for a filamentary superconductor in a large cyclic field.

The above assumptions for the J_c, applied-field dependent and spatially uniform in the penetrated regions, lead to more realistic hysteresis-loss expressions compared with the original Bean's critical state model. Compared with the Kim model, the field-dependent non-uniform spatial distribution of J_c in a superconductors is relaxed due to the small

filament size. This highly reduces the complexity in the analytical form of hysteresis loss without introducing a significant error.

In the case of $\Delta B >> \Delta B_{p0}$, the losses in the partially penetrated regions are much smaller than the overall hysteresis losses, which can be proved by comparing Eqs. (2.16) with (2.21) for 1-D slab geometry or comparing Eqs. (2.31) with (2.32) for the cylindrical case. Thus, the hysteresis-loss calculations in this regime are simplified by neglecting the small contributions due to the losses in the partially penetrated regions. The hysteresis loss expressions are further generalized by using a B_{min}, instead of zero, for the lower bound in the magnetization integrations. The penetration field ΔB_{p0} is then generalized as $\Delta B_{p0}(B_{min})$ which is the first penetration field for a applied field starting from B_{min}.

The hysteresis-loss expressions derived in the following subsections are valid if the applied field condition satisfies $B_{max} - B_{min} >> \Delta B_{p0}$. The form of the ΔB_{p0} is changed due to the field dependency of the critical current density, which will be derived for different geometries. The hysteresis loss is obtained by integrating the magnetization over the applied field in the fully penetrated regions. Since the magnetization can be expressed explicitly as a function of field, the loss integrations will be carried out for Nb_3Sn and NbTi, respectively.

III.4.2 1-D Slab Geometry

Fig. 3.1 (a) shows the flux distribution in a 1-D slab in its virgin state. The applied field is increased from zero toward the penetration field. Applying Ampere's Law in 1-D slab geometry,

$$\frac{dB_i(x)}{dx} = \mu_0 J_{c,SC}(B) \tag{3.15}$$

Carrying out the similar derivation for Eq. (3.6) with field dependent critical current density and a lower bound of the field variation B_{min}, the $B_{p0}(B_{min})$ for a slab with a width of 2a becomes

$$B_{p0}(B_{min}) = \mu_0 J_{c,SC}(B_{min} + B_{p0}(B_{min}))\, a \tag{3.16}$$

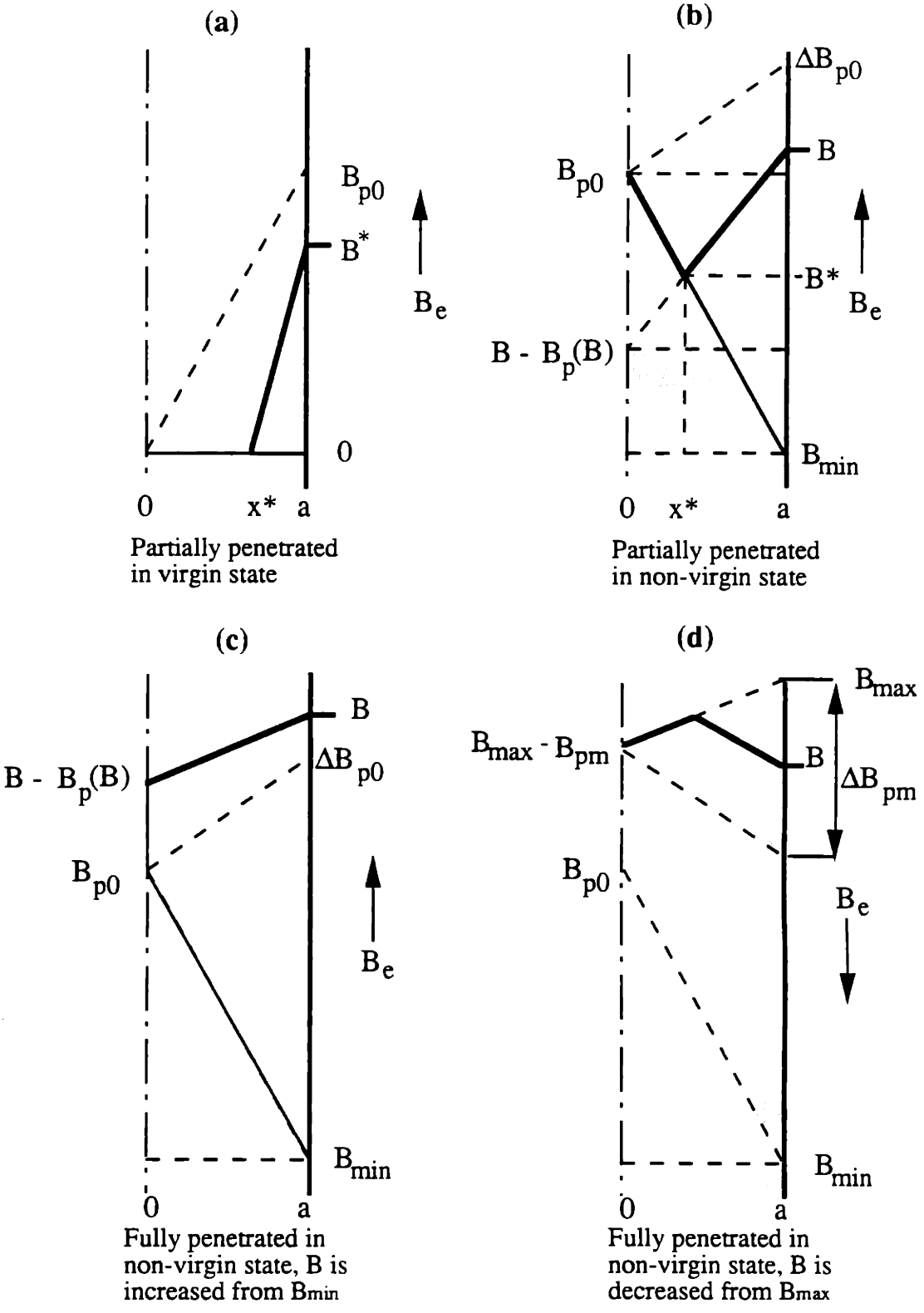

Fig. 3.1 Flux distribution in a slab, with Jc(B) distributed uniformly in penetrated region. Be: external field, B: applied field, B_{p0} and ΔB_{p0}: penetration field in virgin and non-virgin state, $B_p(B)$: penetration field at B, and ΔB_{pm}: penetration field at maximum field.

The penetration field, $\Delta B_{p0}(B_{min})$, in the case of cyclic field change is the summation of two penetration fields as shown in Fig. 3.1 (b), which is given as

$$\begin{aligned} \Delta B_{p0}(B_{min}) &= B_{p0}(B_{min}) + B_p(B_{min} + \Delta B_{p0}(B_{min})) \\ &= B_{p0}(B_{min}) + \mu_0 J_{c,SC}(B_{min} + \Delta B_{p0}(B_{min}))\, a \end{aligned} \tag{3.17}$$

Both $B_{p0}(B_{min})$ and $\Delta B_{p0}(B_{min})$ can be obtained in a few iterations with a computer program. Once the lower bound of the cycling field is fixed, both $B_{p0}(B_{min})$ and $\Delta B_{p0}(B_{min})$ are constants depending on only the properties and metallurgic processes of the superconducting wire.

Fig. 3.1(c) shows that the slab is fully penetrated in a non-virgin state in a rising field. Fig. 3.1(d) shows that the penetration fields B_{pm} and ΔB_{pm} at B_{max} are obtained in the similar way but with much smaller values compared with $B_{p0}(B_{min})$ and $\Delta B_{p0}(B_{min})$. The difference between ΔB_{p0} and ΔB_{pm} is caused by the field-dependent critical current density. In the critical state model, these two variables are the same. For a type-II superconductor, if the B_{min} is close to zero, the ΔB_{p0} is usually not equal to $2B_{p0}$. However, the $\Delta B_{pm} \approx 2B_{pm}$ is a good approximation as long as $\Delta B >> \Delta B_{p0}(B_{min})$.

Based on the basic assumptions and simplifications describe in Section III.4.1, the hysteresis loss for a 1-D superconductor slab in a large transverse cyclic field is approximated as

$$\begin{aligned} Q_h &= -\int_{B_{min}+\Delta B_{p0}}^{B_{max}} M(B)\, dB - \int_{B_{max}-\Delta B_{pm}}^{B_{min}} M(B)\, dB + Q_{h,p} \\ &\approx -2\left[\int_{B_{min}}^{B_{max}} M(B)\, dB\right] \end{aligned} \tag{3.18}$$

where

$$Q_{h,p} = -\int_{B_{min}}^{B_{min}+\Delta B_{p0}} M(B)\, dB - \int_{B_{max}}^{B_{max}-\Delta B_{pm}} M(B)\, dB$$

is the hysteresis loss in the partially penetrated regions. With a large field variation, Eq. (3.18) approximates the hysteresis loss by considering the conductor as fully penetrated in

the whole field range, and the $Q_{h,p}$ is neglected. The instantaneous magnetization at a given applied field in the fully penetrated region is written as

$$- \mu_0 M(B) = \pm \frac{1}{2} B_p(B) \tag{3.19}$$

where

$$B_p(B) = \mu_0 J_{c,SC}(B)\, a \tag{3.20}$$

Substituting Eqs. (3.19) and (3.20) into Eq. (3.18), the hysteresis loss for a superconductor slab with the surface parallel to a large cyclic field is simplified to

$$Q_h \approx a \int_{B_{min}}^{B_{max}} J_{c,SC}(B)\, dB \tag{3.21}$$

The lower bound of the loss integration B_{min} should not be less than the first critical field B_{c1} as discussed above.

III.4.2.1 Nb_3Sn

Substituting Eqs. (3.3a) and (3.3b) into Eq. (3.21), the hysteresis loss of a Nb_3Sn superconductor slab in a large cyclic changing field is estimated as

$$Q_h \approx a\, C^*_{SC} \left[\frac{1}{p} B^{*q}_{c2} B^p - \frac{q}{p+1} B^{*q-1}_{c2} B^{p+1} - \frac{3-2q}{p+2} B^{*q-2}_{c2} B^{p+2} + \frac{2-q}{p+3} B^{*q-3}_{c2} B^{p+3} \right]_{B_{min}}^{B_{max}},$$

for Nb_3Sn with $(B_{max} - B_{min}) \gg \Delta B_{p0}(B_{min})$ and $1 < q \leq 2$. (3.22)

III.4.2.2 NbTi

By applying the $J_c(B)$ for an optimized NbTi as shown in Eq. (3.5b) to the hysteresis loss integration in Eq. (3.21), the hysteresis loss for a slab NbTi superconductor in a large cyclic field variation is given as

$$Q_h \approx a\, C^*_{SC} \left[B^*_{c2} B - \frac{1}{2} B^2 \right]_{B_{min}}^{B_{max}}$$

for NbTi with $(B_{max} - B_{min}) \gg \Delta B_{p0}(B_{min})$ (3.23)

III.4.3 2-D Cylindrical Geometry

Similar to the 1-D case, the penetration fields for a cylindrical superconductor filament with radius of r_f are expressed as

$$B_{p0}(B_{min}) = \frac{2}{\pi} \mu_0 J_{c,SC}(B_{min} + B_{p0}) r_f \tag{3.24}$$

and

$$\Delta B_{p0}(B_{min}) = B_{p0}(B_{min}) + \frac{2}{\pi} \mu_0 J_{c,SC}(B_{min} + \Delta B_{p0}) r_f \tag{3.25}$$

Both $B_{p0}(B_{min})$ and $\Delta B_{p0}(B_{min})$ are obtained iteratively as described before.

By changing the bias field dependent variable into instantaneous applied field dependent variable for the penetration field in Eqs. (3.27) and (3.29), the magnetization function for large field variation becomes

$$\mu_0 M(B) = -\frac{2}{3} B_p(B) \cdot \text{sign}(B - B_m) \tag{3.26}$$

Substituting Eq. (3.26) into Eq. (3.18), with $B_p(B) = (2/\pi)\, \mu_0 J_{c,SC}(B)\, r_f$, the hysteresis loss is approximated as

$$Q_h \approx -2 \int_{B_{min}}^{B_{max}} M(B)\, dB = \frac{8}{3\pi} r_f \int_{B_{min}}^{B_{max}} J_{c,SC}(B)\, dB \quad (J / m^3 \text{ superconductor}) \tag{3.27}$$

Wilson had the same expression in Ref. 3.7 with an intuitive approach. In the case of large field variation, the 1-D and 2-D hysteresis losses, Eqs. (3.21) and (3.27), are different in the forms only by a multiplication constants. Similar relationship has been used to scale 2-D hysteresis loss from 1-D calculated results by Bottura and Minervini (Ref. 3.19).

III.4.3.1 Nb_3Sn

Using Eqs. (3.3a) and (3.3b) for the $J_{c,SC}(B)$, performing the integration in Eq. (3.27), the hysteresis loss of a cylindrical Nb_3Sn superconductor in a large transverse cyclic changing field is approximated as

$$Q_h \approx \frac{8}{3\pi} r_f C^*_{SC} \left[\frac{1}{p} B^{*q}_{c2} B^p - \frac{q}{p+1} B^{*q-1}_{c2} B^{p+1} - \frac{3-2q}{p+2} B^{*q-2}_{c2} B^{p+2} + \frac{2-q}{p+3} B^{*q-3}_{c2} B^{p+3} \right]_{B_{min}}^{B_{max}}$$

for Nb_3Sn with $(B_{max} - B_{min}) \gg \Delta B_{p0}(B_{min})$, and $1 < q \leq 2$. (3.28)

III.4.3.2 NbTi

Substituting Eq. (3.5b) into Eq. (3.27) and integrating the $J_{c,SC}(B)$ of NbTi over a large field variation, the hysteresis loss of a cylindrical NbTi superconductor filament with a radius of r_f, can be estimated as

$$Q_h \approx \frac{8}{3\pi} r_f C^*_{SC} \left[B^*_{c2} B - \frac{1}{2} B^2 \right]_{B_{min}}^{B_{max}}$$

for NbTi with $(B_{max} - B_{min}) \gg \Delta B_{p0}(B_{min})$ (3.29)

III.5 EFFECTIVE FILAMENT DIAMETER

As shown in Eqs. (3.21) and (3.27), hysteresis losses of a superconductor is linearly proportional to the size of the conductor. In a composite single strand, for the purpose of keeping high current carrying capability, the superconducting filaments are sometimes made as compact as possible. Small inter-filamentary spacings increase the possibility of filament coupling (Refs. 3.20 to 3.22) and thus increases the hysteresis losses, which counteracts the original purpose of fine-division of the superconductor. Filament coupling can be categorized into proximity coupling and metallurgical coupling (or bridging) (Refs. 3.14 and 3.15). Filament bridging effect is of major concern to the present research. The phenomenon of the proximity coupling will be briefly described for the purpose of completeness.

Proximity coupling occurs in a pure matrix material such as Cu or Al with inter-filamentary spacing on the order of sub-micrometer. Pure matrix material is usually found in a composite wire with metallic superconductor such as NbTi (Refs. 3.19 to 3.21). Proximity induced superconductivity decays exponentially within a certain characteristic length from the interface with a superconductor. For a pure Cu at 4.2 K, the characteristic length is about 0.45 μm. Due to the proximity coupling, the matrix becomes a weak superconductor between the superconducting filaments. The total hysteresis loss becomes

the sum of the intrinsic filamentary hysteresis loss and the hysteresis loss of a superconductor with the size of the filamentary zone. Proximity coupling can be suppressed by using alloys as matrix. Thus, this type of coupling is usually not found in a composite Nb_3Sn wire because the heat treatment process always alloys the inter-filamentary matrix material.

Filament bridging in a composite wire occurs when the filaments are linked by superconducting paths in the inter-filamentary matrix. The occurrence of bridging depends on variables such as wire design and manufacturing, winding or cabling processes, heat treatment process, etc. All these variables are not deterministic. Filament bridging can be considered as three dimensional random events. Analytical simulation of the degree of bridging can hardly be achieved. The conventionally defined effective filament diameter d_{eff}, resulting from systematic inconsistency between the experimental and the analytical hysteresis losses, provide a way to quantify the bridging effect. The effective filament diameter should be considered as a statistical index to the filament bridging in a composite wire instead of a physical size of the filament. Because of the non-uniform cross sectional area along the filament and the growth of the Nb filaments due to reaction with tin, a local matrix to Nb ratio higher than about 1.2 is usually required for a Nb_3Sn composite (Ref. 3.14). With a too small local matrix to Nb ratio, the effective filament diameter can be an order of magnitude larger than the geometric filament size. Filament bridging is rarely found in NbTi multifilamentary wire even with a local matrix to NbTi ratio as low as 0.5 (Ref. 3.14).

The effective filament diameter is estimated from either magnetization or hysteresis-loss measurements. Considering a composite wire containing cylindrical Nb_3Sn filaments affected by a slowly-varied large-amplitude transverse field, the d_{eff} can be defined from the width of the magnetization loop (Ref. 3.15) as shown in Fig. 1.6 at a field larger than the full penetration field. The width between two magnetization branches, $M_{wire}(B_e\uparrow)$ and $M_{wire}(B_e\downarrow)$, at a given applied field of $B \approx B_e$ is expressed as (Ref. 3.15)

$$2\,\mu_0 M_{wire}(B_e) \equiv \mu_0 M_{wire}(B_e\uparrow) + \mu_0 M_{wire}(B_e\downarrow) \tag{3.30}$$

Applying Eq. (3.26) to a composite superconducting wire with

$$B_p(B_e) \equiv \frac{2}{\pi}\mu_0\, f_{nonCu}\, f_{SC\ in\ nonCu}\, J_{c,SC}(B_e)\, r_f \tag{3.31}$$

the left-hand-side of Eq. (3.30) becomes

$$2\,\mu_0 M_{wire}(B) = 2\mu_0 \frac{4}{3\pi} f_{nonCu}\, f_{SC\ in\ nonCu}\, J_{c,SC}(B)\, r_f \tag{3.32}$$

With a measured width of the magnetization, the effective filament diameter is approximated as

$$d_{eff} = 2\, r_{f,eff} \approx \frac{[2\,\mu_0 M_{wire}(B_e)]_{expt}\, A_{wire}}{2\mu_0 \frac{2}{3\pi} I_c(B_e)} \quad (m) \tag{3.33}$$

where A_{wire} = cross sectional area of the composite wire (m), and the $I_c(B_e)$ is obtained from a separate experiment usually measured at a given high field.

If the absolute value of hysteresis loss is known from measurement, the loss per unit volume of non-Cu materials per cycle is calculated from Eq. (3.27) as

$$Q_{h,nonCu} = \frac{Q_h}{f_{SC\ in\ nonCu}} \approx \frac{8}{3\pi} r_f \int_{B_{min}}^{B_{max}} \frac{J_{c,SC}(B)}{f_{SC\ in\ nonCu}}\, dB = \frac{8}{3\pi} r_f \int_{B_{min}}^{B_{max}} J_{c,nonCu}(B)\, dB \tag{3.34}$$

Since the non-Cu material includes all the constituent materials for making superconductor filaments of which accurate volume fractions can be obtained from the manufacturer, it is convenient to perform the loss calculation on the basis of non-Cu material. The effective filament diameter can be approximated as

$$d_{eff} = 2\, r_{f,eff} \approx \frac{[Q_{h,nonCu}]_{expt}}{\frac{4}{3\pi} \int_{B_{min}}^{B_{max}} \frac{I_c(B)}{A\, f_{nonCu}}\, dB} \quad (m) \tag{3.35}$$

To use Eq. (3.35), the field-dependent critical current distribution in the applied field range is required, and the integration can be performed analytically in the similar way as mentioned in Section III.4.3. To avoid the uncertainty due to the extrapolation of the low field critical current, the B_{min} adopted in the experiment should be kept reasonably high.

III.6 SUMMARY

Two types of field variation are of interest in this thesis work: (1) a small sinusoidal wave-form field superposed on various large DC bias fields, and (2) a large peak-to-peak unidirectional triangular cyclic field. For the first field condition, the existing 2-D analytical approximations based on the Bean model have been modified by expressing the critical current density as a function of the DC bias field. The second field condition is applied to simulate the field condition of a superconducting pulse magnet. For the second field condition, the variation of the field-dependent critical current is large enough that the Bean model is no longer valid. Modifications of the existing hysteresis-loss model in 2-D cylindrical geometry for such field condition have been performed in this chapter. Assumptions and simplifications in modifying the existing hysteresis-loss models have been discussed. Evaluations of the effective filament diameter from magnetization signal or absolute value of AC loss have also been shown.

From the discussions in this chapter and the review in Chapter II, the most important parameters in determining AC losses are filament diameter, field-dependent critical current density profile, and coupling time constant. These three parameters are strongly affected by the wire manufacturing processes, which can not be accurately estimated simply with analytical method. Effective values of these three parameters evaluated from experimental results are usually applied in AC-loss calculations for more realistic prediction. In Chapter IV, design and construction of a cryogenic experimental apparatus performing laboratory-scale measurements of AC losses of a composite superconducting wire will be discussed.

III.7 REFERENCES

3.1 Ekin, J.W., 'Strain scaling law for flux pinning in practical superconductors. Part 1: Basic relationship and application to Nb_3Sn conductors,' Cryogenics, 1980, p. 611.

3.2 Kramer, E.J., 'Flux pinning in high-current-carrying superconductors,' Adv. Cryo. Eng., Vol. 28, 1982, p. 307.

3.3 Welch, D.O., Suenaga, M., and Snead, C.L., 'Flux pinning by grain boundaries in A15 superconductors,' in "International Symposium on Flux Pinning and Electromagnetic Properties of Superconductors," Fukuoka, Japan, 1985, p. 30.

3.4 Larbalestier, et al., 'Flux pinning in NbTi and Nb_3Sn composites,' ibid., p. 58.

3.5 Ekin, J.W., 'High-field flux pinning and stain scaling law,' ibid., p. 267.

3.6 Ekin, J.W., 'Strain effects in Superconducting Compounds,' Adv. Cryo. Eng., Vol. 30, 1984, p. 823.

3.7 Ekin, J.W., 'Mechanical properties and strain effects in superconductors,' in *Superconductor Materials Science*, ed. Foner, S. and Schwartz, B.B., Plenum Press, 1981, p. 455.

3.8 Hoenig, M.O., 'Internally cooled cabled superconductors,' Cryogenics, 1980, p. 373.

3.9 Hoenig, M.O., ''Internally cooled cabled superconductors,' Cryogenics, 1980, p. 427.

3.10 Summers, L.T., 'A model for the prediction of Nb_3Sn critical current as a function of field , temperature, strain, and radiation damage,' Trans. Magnetics, Vol. 27, No. 2, 1991, p. 2041.

3.11 Takayasu, M., et al., 'Critical currents of Nb_3Sn wires of the US-DPC coil,' Adv. Cryo. Eng., Vol. 38, 1992, p. 619.

3.12 Steeves, M.M., Hoenig, M.O., Cyders, C.J., 'Effects of Incoloy 903 and tantalum conduits on critical current in Nb_3Sn cable-in-conduit conductors,' Adv. Cryo. Eng., Vol. 30, 1984, p. 883.

3.13 Ekin, J.W., 'Effect of transverse compressive stress on the critical current and upper critical field of Nb_3Sn,' J. Appl. Phys., Vol. 62, No. 12, 1987, p. 4829.

3.14 Thoner, M., et al.,'Nb_3Sn multifilamentary superconductors: an updated comparison of different manufacturing routes,' IEEE Trans. Magnetics, Vol. MAG-27, No. 2, 1991, p. 2027.

3.15 Ghosh, A.K. and Suenaga, M., 'Magnetization and critical currents of tin-core multifilamentary Nb3Sn conductors,' IEEE Trans. Magnetics, Vol. MAG-27, No. 2, 1991, p. 2407.

3.16 Kahan, A., 'Critical current density and flux shear mechanisms,' Cryogenics, Vol. 30, 1990, p. 678.

3.17 Hampshire, D.P., and Larbalestier, D.C., 'The critical current of NbTi multifilamentary wire ...,' IEEE Trans. Magnetics, Vol. 25, No. 2, 1989, p. 1956.

3.18 Zenkevitch, V.B., Romanyuk, A.S., Zheltov, V.V., 'Losses in composite superconductors at high levels of magnetic field excitation: part 1,' Cryogenics, 1980, p. 703.

3.19 Bottura, L, and Minervini, J.V., 'Calculation of magnetization, hysteresis and power dissipation in a superconductor during bipolar field cycles,' presented at the 1992 Applied Superconductivity Conference, Chicago, IL, Aug. 23-28, 1992.

3.20 Harada, N, et al.,'Excess magnetization due to interfilamentary proximity coupling in NbTi multifilamentary wires,' Cryogenics, Vol. 31, 1991, p. 183.

3.21 Carr, W.J., 'Progress and problems in understanding hysteresis loss,' Adv. Cryo. Eng., Vol. 38, 1992, p. 491.

3.22 Heine, K., et al., 'Fine filament NbTi and Nb_3Sn conductors,' Adv. Cryo. Eng., Vol. 38, 1992, p. 653.

CHAPTER IV

DESIGN OF SINGLE-STRAND AC-LOSS EXPERIMENT

IV.1 INTRODUCTION

In order to reduce AC losses, the cross sectional structure of a commercialized composite superconducting wire for pulse magnet applications may become very complicated (Ref. 4.1). The AC losses predicted by model calculations based on known loss mechanisms, both analytical and numerical, must be verified experimentally. This is especially important for a newly designed wire. Single-strand AC-loss measurements must also be performed on the wires taken from different billets for quality control during mass-production stage. In order to design a stable superconducting pulse magnet, it is required to have a reliable pre-estimation of AC losses in the conductor. As described in Chapters II and III, experimental information for evaluating effective filament diameter and effective coupling time constant of a candidate composite superconducting wire is indispensable for a better prediction of AC losses. Laboratory-scale AC-loss measurement is thus of fundamental important.

A new laboratory-scale isothermal calorimetric system for measuring AC losses of a composite superconducting wire has been designed and constructed as part of this thesis work. The motivations of building this new measurement apparatus were as follows:

(1) to measure the absolute values of total AC losses;
(2) to evaluate specific loss components;
(3) to provide AC-loss characteristics of a current-carrying US-DPC wire affected by a large-amplitude ramp field prior to the US-DPC experiment;
(4) to estimate the d_{eff} and τ_{eff} for analytical AC-loss calculations;
(5) to compare the AC losses between single-strand and US-DPC cable.

This chapter describes the design and construction of a reliable laboratory-scale experimental apparatus which is capable of measuring the AC losses of a brittle Nb_3Sn single-strand composite superconductor carrying high DC or AC currents and affected by a time-changing background magnetic field with a large field variation.

IV.2 REVIEW OF EXPERIMENTAL TECHNIQUES

Magnetization, decay time constant, and calorimetric methods are the major techniques used in measuring AC losses (Refs. 4.1-4.3). The principle of measurement and the advantages and disadvantages of each technique will be briefly reviewed in this section.

IV.2.1 Magnetization Method

Fig. 4.1 shows a simplified experimental set-up for the measurement of AC loss using the magnetization method (Refs. 4.1 and 4.4). In general, two pick-up coils with large inductance are placed in the cryostat together with the test wire. One of the pick-up coils, enclosing the test wire, is installed very near the wire for better sensitivity. A second coil is used as a dummy coil which picks up only the background field signal. The voltage signals from these two coils are negatively coupled and balanced with a potentiometer. Before the test wire is mounted inside the first pick-up coil, the two coils are balanced in the time-varying background field by adjusting the potentiometer. A large error can be introduced if the pick-up coil set is not properly balanced. This is because the background field induced voltage component is usually much larger than the magnetization signal (Ref. 4.1). When the test wire is in place and the background field is changed, a voltage generated by the change of the magnetization of the test wire can be detected in the balanced pick-up coil set. The integrated signal is proportional to the magnetization of the test wire and is plotted against the background field. The AC loss is proportional to the area covered by the magnetization curve.

The advantage of the magnetization method is that only a minimal volume of the test wire is required (Ref. 4.2). The test result provides the instantaneous magnetization of the test wire in a time-varying field which reveals the physical insight concerning phenomena such as penetration field, flux jumps, etc. The cryogenic requirement of this method is relatively simple compared to that of the calorimetric method which will be discussed in Section IV.2.3. The magnetization method is usually applied to measure hysteresis loss in a superconductor without transport current at a nearly static field variation. It is difficult to

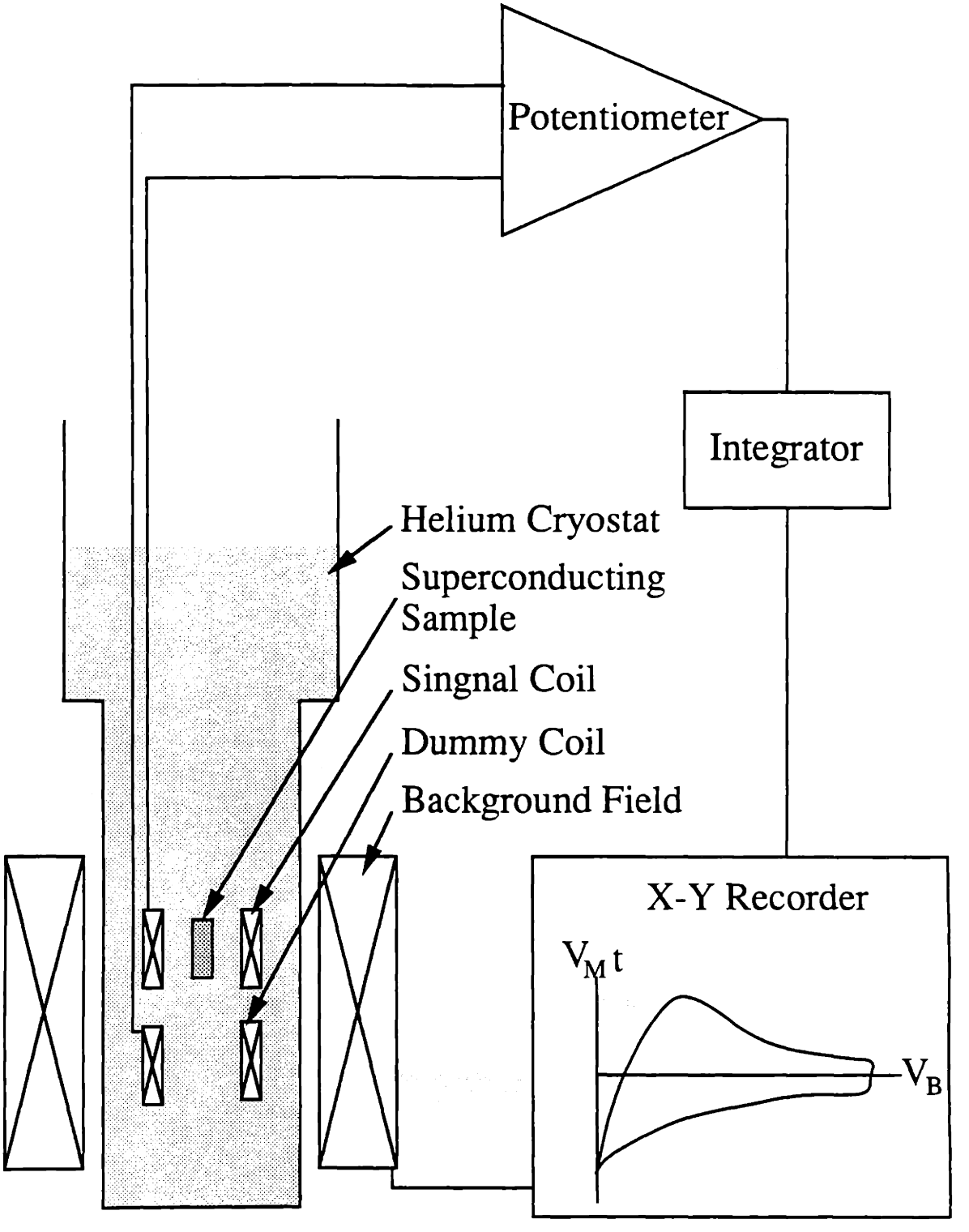

Fig. 4.1 Schematic of the magnetization measurement. The background field is proportional to V_B, and the magnetization is proportional to $V_M t$.

measure the magnetization of a conductor carrying a transport current and affected by an AC field with a higher time-rate of field variation (Ref. 4.2). A few articles regarding magnetization measurement of a composite NbTi wire carrying DC transport currents have been found in the literature survey (Ref. 4.4 to 4.6). Only a single test data was obtained at a higher time-rate of field variation (Ref. 4.6).

The direct results of magnetization measurement are the voltage of the background field (V_B) vs. the time integrated voltage of the pick-up coil ($V_M t$). In order to obtain the absolute loss value, both voltages have to be calibrated. The former can easily be characterized by comparing the field generated by the magnet and the voltage measured from the magnet power supply. The latter has to be calibrated either by a reference sample wire with known magnetization or by another method such as calorimetry. The calibration constant for magnetization also depends on the mutual inductance of the test wire and the pick-up coil, which is affected by the test wire geometry. Calibration is one of the most common sources of error (Ref. 4.3 and 4.7) and the largest disadvantage of this method (Ref. 4.8).

A DC voltage in the amplifier induced by the temperature drift, is usually superimposed on the pick-up coil signal V_M. The DC voltage accumulated by an analog integrator can cause an open hysteresis loop which produces a large uncertainty in the loss calculation. This is especially important when only the hysteresis loss is of interest and a long measuring time is required to limit the error results from coupling loss component. The integration of the differential flux V_M can also be done digitally with a computer data acquisition system. Limited computer memory for data storage is the major concern in using digital integration.

IV.2.2 Decay Time Constant Method

Fig. 4.2(a) shows the schematic of a decay time constant measurement system (Refs. 4.8 and 4.9). Figs. 4.2(b) and 4.2(c) illustrate two different ways to generate a transient field which induces coupling currents in the composite wire. This method uses only one pick-up coil enclosing the test wire, and needs no balancing adjustment as required in the magnetization method. When a composite multifilamentary wire is placed in an external field which is ramped up quickly (~ 10 - 100 ms) then either held constant (Fig. 4.2(b)) or dropped abruptly (~ 10 μs) (Fig. 4.2(c)), the decay time constant of the coupling current in the matrix material of the test wire induced by the up-ramping field can be measured from the decay curve of the pick-up coil signal (Refs. 4.8 and 4.9). The decay time constant is

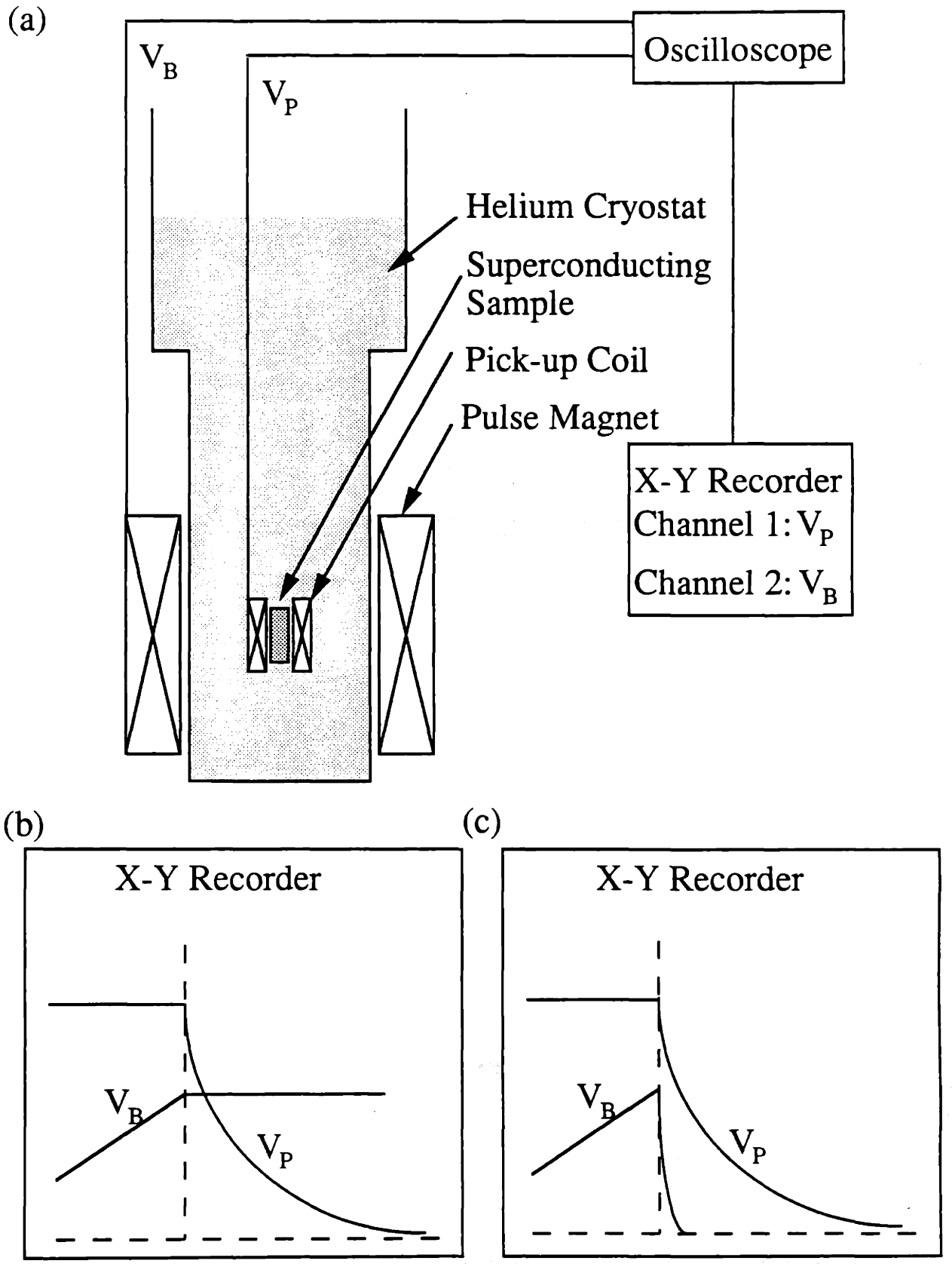

Fig. 4.2 Schematic of the decay time constant measurement.

also affected by the geometry of the test wire. This is usually known for a given standard test wire (Ref. 4.8). The coupling current loss is calculated using Eq. (2.66) with the measured coupling time constant.

The decay time constant measurement can only be used to measure characteristics of the matrix material. These characteristics includes the resistivities and twist pitch information. In general, the twist pitch is a known factor. The effective transverse resistivity is of more interest, especially when a composite wire contains complicated cross sectional construction with multiple heterogeneous matrix regions. The decay time constant changes with the resistivity of the matrix material as reviewed in Eq. (2.43). The resolution of different time constants in multiple matrix regions depends on the mutual inductance between the test wire and the pick-up coil, and the differences of the resistivities of these matrix materials.

IV.2.3 Calorimetric Methods

Calorimetric methods can be categorized as either adiabatic or isothermal. Both methods measure the total AC loss of the test wire.

IV.2.3.1 Adiabatic Calorimetry

Adiabatic calorimetry uses a test sample which is suspended in an evacuated stainless steel calorimeter. The test sample is either a superconducting single-strand or a cable. The leak-tight calorimeter is immersed in a liquid helium bath. When an AC field is applied, the temperature of the test sample rises due to AC losses. From the temperature difference, the heat capacities of the test sample and the sample holder, the dissipated energy can be calculated. The temperature of the test sample is monitored by sensors which must not be sensitive to the magnetic field. Interpretation of the experimental results depends heavily on the type and the positions of the temperature sensors. Different calorimeters designed for various ranges of sensitivity, from micro-Watts to a few hundred watts, have been reported by different authors (Refs. 4.10 to 4.14).

The test sample and the sample holder are suspended in the chamber with strings or wires of low thermal conductivity to reduce the heat transfer between the test sample and the environment. Any contact of the test sample with the chamber or the helium bath may introduce error in the measurement. In order to maintain a good vacuum at cryogenic

temperature, the calorimeter must be made of metallic material, usually stainless steel. In general, all the openings and joints are permanently sealed or welded which causes some difficulty in sample mounting.

Some authors used calorimeter made of a stainless steel with a detachable top cover to alleviate the difficulty in sample handling (Refs. 4.10 and 4.14). However, the O-ring for the joint between the top cover and the canister which is made of soft metallic material such as In or Cu, has very low electric resistivity. The eddy current loss generated by a fast changing field in the low resistive sealing material may affect the accuracy of the measurement.

The most important requirement of this method is to prevent heat from leaking into the liquid helium. Therefore this method can not be used with a sample carrying transport currents in a time-varying field since the connection of the test sample current leads to the bus bars destroys the adiabatic condition of the measurement. Also, the critical current density of the the test sample changes with the temperature rise once the energy is dissipated in the adiabatic system. For these reasons, this method can hardly be applied to characterize AC losses in a current-carrying sample.

IV.2.3.2 Isothermal Calorimetry

IV.2.3.2.1 Gas Flow-rate Measurements

Traditional isothermal calorimetric method measures the gas flow rate boiled off by the heat sources in the liquid helium. This method is the least convenient but the most versatile and reliable technique for measuring AC losses (Ref. 4.2). The greatest advantage of this method is that the averaged absolute values of the AC losses can be obtained even when a DC or AC transport current is applied to the test wire. If the test wire volume is large enough to provide good signal-to-noise ratio and the flow-meter is properly selected, this method can be used to measure the total AC losses at a lower frequency where the hysteresis loss dominates.

In an early designs, isothermal calorimetric method simply measured the liquid helium boil-off rate due to AC losses of the test wire with a helium gas flow-meter (Refs. 4.2, 4.15, and 4.16). The helium gas flowrate is converted to AC-loss power by equating it to the energy required to change the thermodynamic state of the helium. The reading of the

helium gas flow-meter is accurate only if the helium gas flow is in standard temperature and pressure condition. In order to eliminate possible errors resulting from the absolute value of the flow-meter, a calibration heater is sometimes included in the calorimeter. The heater is adjusted to provide power to the liquid helium bath at zero background field, which generates the same helium gas flow-rate as that of the AC losses of the test wire. The absolute AC-loss power is then equal to the heater power (Ref. 4.17).

The isothermal calorimeter is usually a non-metallic bell jar with the bottom-end open for the convenience of automatically refilling the liquid helium. A chimney is installed to connect the top of the calorimeter to a helium gas flow-meter. Earlier test results (Ref. 4.18) showed that a small leakage on a previously made calorimeter, which was located above the test wire coil and in the high AC field region, generated a field-dependent noise to the helium gas flow rate. The diamagnetic property of helium gas is probably the reason for the field-dependent gas leak rate (Ref. 4.18). The noise was in-phase with the AC field which could not be cancelled by the heater calibration at zero field. In the worst case, a low AC-loss signal could be masked by this field dependent noise. This illustrates the importance of eliminating gas leaks in this method. The flow-meter with a small orifice, which is connected to the warm-end of the chimney, may induce spontaneous thermoacoustic oscillations in the chimney (Refs. 4.19 to 4.23). Thermoacoustic oscillations add energy to the calorimeter and reduce the resolution of the flow-meter reading. To obtain a reliable test result with this method, the cryogenic apparatus must be free from thermoacoustic resonance.

The greatest disadvantage of isothermal calorimetric method is the long equilibrium time of the liquid helium bath (Ref. 4.8). Without any improvement to the traditional calorimetric measurement, whenever power deposited into the liquid helium bath is changed by 10 to 10^2 mW, the waiting time for the helium gas flow-rate to reach a new equilibrium state may be as much as 20 to 30 minutes. Since the liquid helium level and therefore the experimental background condition may change with time, a long waiting time is not only a problem for the efficiency of the test but also affects the accuracy of the measurement .

IV.2.3.2.2 Gas Collection-rate Measurements

A few authors have applied an alternative method of isothermal calorimetry to the measurement of AC losses which is fast and is able to measure a very low level of loss

(Refs. 4.24 to 4.26). The basic principle is still based on boiling the liquid helium. The boiled off helium gas, instead of being released through a chimney and a flow-meter, is collected in a glass tube with the top-end sealed. The liquid helium level in the glass tube is pushed down by the helium gas. The rate of change of liquid helium level is measured. The AC-loss power is estimated from the time-rate of the boil-off helium mass multiplied by the theoretical enthalpy of the liquid helium.

Kuroda (Ref. 4.24) visually observed the rate of change through windows on the cryostat. However, radiation losses at cryogenic temperature resulted in a high background reading. Eikelboom (Ref. 4.25) improved Kuroda's method by using two low-intensity light sources separated at a given distance along the glass tube. Each light source was coupled with a sensor across the glass tube. A ball floated on top of the liquid helium in the glass tube. As the helium level was pushed down by the accumulation of boiled off helium, the ball intercepted the upper and lower light to the respective sensor which signaled the start and stop of a timer. The AC-loss power depended on the time interval required for the ball to pass these two sensors. This improved method could be used to measure a wide range of energy dissipation in the calorimeter, between 1 and 100 mW, as claimed by the author.

With the gas collection method, after each loss measurement, the glass tube has to be refilled with liquid helium. Some authors (Refs. 4.24 and 4.26) used a removable plug to cover the top-end of the glass tube. Kuroda kept the plug below the bulk liquid helium level (Ref. 4.24). Gas leaking through the joint between the plug and the glass tube was reported by Niessen et al. (Ref. 4.26). To avoid gas leakage at the plug, Niessen et al. extended the top-end of the tube beyond the top flange of the cryostat, which was at room temperature. Noise due to spontaneous thermoacoustic resonance in the glass tube became a major mechanism in reducing the resolution of the measurement (Ref. 4.26). In Eikelboom's set-up, in order to release the collected gas, an electromagnet was applied to flip a top-end closed glass tube by about 120°. Throughout the whole procedure, the full length of the glass tube remained in the liquid helium which eliminated the error due to either gas leakage or thermoacoustic resonance.

Other major concerns with this method include pressure variation in the cryogenic system and condensation of the boiled off gas collected in the glass tube. Since the boiled off gas in the glass tube is compressible, the rate of gas collection at a fixed volume can be changed by pressure variation. The pressure in the glass tube is affected by the levels of

the bulk liquid helium and the liquid nitrogen in the external reservoir of the cryostat. If the background AC field is generated by a superconducting coil in the same cryostat, the pressure in the glass tube is also affected by the boiled off gas from the background coil.

Condensation of the boil-off gas in the glass tube results from the contact of the gas with the glass wall at 4.2 K and a slightly higher pressure in the tube. Condensation becomes a more serious problem if a test wire is in a low loss condition and a significantly longer measuring time is required. To reduce the measuring time in this case, a heater in the sample housing energized at a fixed power has been suggested (Ref. 4.25). The AC loss of the test wire was obtained by subtracting the heater power from the total loss. From a standard error analysis, the error of the difference between two large values, is the summation of the absolute errors of these two large numbers. Thus, the error of the measurement may not be significantly magnified if the heater power is on the same order as the AC-loss power. However, the efficiency of measuring a small loss can not be significantly improved by using a small heater power. The selection of the optimum heater power is then dependent on the user's experience in this set-up.

IV.3 APPARATUS FOR SINGLE-STRAND AC LOSS MEASUREMENTS

The isothermal calorimetry method with heater calibration and gas flow-rate measurement, which will be called calorimetric measurement from now on for simplicity, was selected to measure AC losses in the single-strand superconducting samples based on the advantages of versatility and reliability. The principles and the detail considerations in designing the experimental apparatus including the cryogenic probe, the calorimeter, the sample holder, the sample winding, the flow-rate control feedback system, and the data acquisition system will be described in this section.

IV.3.1 Design Guidelines

A majority of the test wires of interest in the present research are Nb_3Sn composite multifilamentary wires which must be activated with a heat-treatment at a final temperature above 900 K for more than 150 hrs. After the heat-treatment, the Nb_3Sn filaments are extremely brittle and the matrix materials, copper and/or bronze, are soft due to high temperature annealing. Any stress imposed on the wire is almost totally transferred to the

Nb_3Sn filaments. This may degrade the critical current density of the superconductor. The stresses on the test wire result from: (1) the thermomechanical incompatibility of the sample holder with the test wire in the temperature range of about 1000 K, (2) handling and mounting of the test wire after the heat-treatment, and (3) the Lorentz force on a current-carrying test wire. Preventing the degradation of the superconducting properties of the test wire due to various stress mechanisms was one of the major concerns in designing the test apparatus.

The most important consideration in the cryogenic design is reducing the background noise to a minimum. Noise which depends on the time-varying field, is the most unwanted. Former experience with the calorimetric measurement method (Ref. 4.23) has shown that the metallic materials used to construct the calorimeter should be reduced to a minimum. The reason is that the time-varying field induced eddy currents in the metallic material generates field-dependent Joule heating noise. Any metallic material used in the high field region should have high electric resistivity. Gas leaks, especially in the high field region, are not allowed since the leakage induces a noise to the flow-meter signal which is in-phase with the AC background field. It is also important to prevent the helium gas boiled off by the background cryostat from entering the calorimeter. The time constant of the heat exchange through the calorimeter wall in the radial direction should be long enough compared with the measuring time. The noise due to spontaneous thermoacoustic resonance in the chimney should be either avoided or made negligible compared with the flow-rate signal in the full range of the possible AC losses.

For practical application, it is important to improve the efficiency of the calorimetric measurement. The long waiting time for equilibrium of the liquid helium at different power levels can be reduced by maintaining a constant equilibrium state with a constant heat deposition rate. As observed in earlier experiments (Ref. 4.23), the constant flow-rate control feedback circuit has been proven to be successful in both reducing the measuring time and improving the experimental accuracy. The principle of waiting-time reduction using constant flow-rate feedback control and the design of the feedback circuit modified from the former version will be discussed in Section IV.3.7.

In the present research, the AC loss of the test wire is always measured in a cyclic changing field. The loss per cycle is calculated as the product of the period of a cycle and the loss power averaged over several field cycles. Since the wave-form of the gas flow-rate varies with the changing rate as well as the peak-to-peak value of both the background

field and the transport current, application of a computer data acquisition system not only eliminates the human error in data reading but also improves the precision of the averaging and the efficiency of the measurement.

IV.3.2 Cryogenic Probe

Fig. 4.3 shows the schematic of a cryogenic probe mounted with a calorimeter and coupled with a constant flow-rate control system. The full length of the probe is about 230 cm measured from the top flange of the probe. The cryogenic probe consists of an aluminum top flange with Styrofoam insulation, a pair of 5 kA gas-cooled leads connected to copper bus bars, a pair of stainless steel tubes carrying a G-10 plate, four G-10 rods, the G-10 calorimeter with the chimney, the test wire on a MACOR holder, and the stainless steel heater on a G-10 holder. The G-10 is a laminate composite material consisting of an epoxy resin matrix reinforced with a glass-fiber woven fabric (Ref. 4.27). The thermal expansion coefficient of G-10 in the glass fiber wrap direction is about the same as that of copper, and it is about 2.5 times larger in the direction of the lamination. The MACOR is a machinable glass ceramic (MGC) manufactured by Corning Glass Works (Ref. 4.28). The physical properties of MACOR will be further discussed in Section IV.3.5.2. The probe is loaded into the tail of a stainless steel cryogenic dewar which has an inner diameter (ID) of 13 cm. When no current is applied, the gas-cooled current leads and other openings on the top flange keep the pressure in the liquid helium section less than 0.1 Torr above atmospheric pressure. During experiment, the dewar is inserted into a 15 cm-bore water-cooled Bitter magnet at the Francis Bitter National Magnet Laboratory (FBNML) with the mid-plane of the test wire coil aligned with the mid-plane of the background magnet.

Two 1.8 mm thick stainless steel tubes with outer diameters (OD) of 2.13 cm are bolted to the top flange which carry all but the weight of the gas-cooled leads. The lower ends of the stainless steel tubes are connected with a 2.54 cm thick G-10 plate which holds four 1.9 cm OD G-10 rods extending down into the high field region. As seen in Fig. 4.4, two current leads of the test wire penetrate the top flange of the calorimeter and are soldered to the copper bus bars which are connected with the gas-cooled leads. For the purpose of preventing heat from entering the calorimeter through the current leads, about 6.35 cm of the current leads between the top of the calorimeter and the ends of the bus bars are not attached to any structural material. A shallow U-bend on each current lead is adopted for the purpose of stress relief. Any relative motion between the bus bars and the top of the calorimeter can easily destroy the current leads. Thus, the lower ends of these four G-10

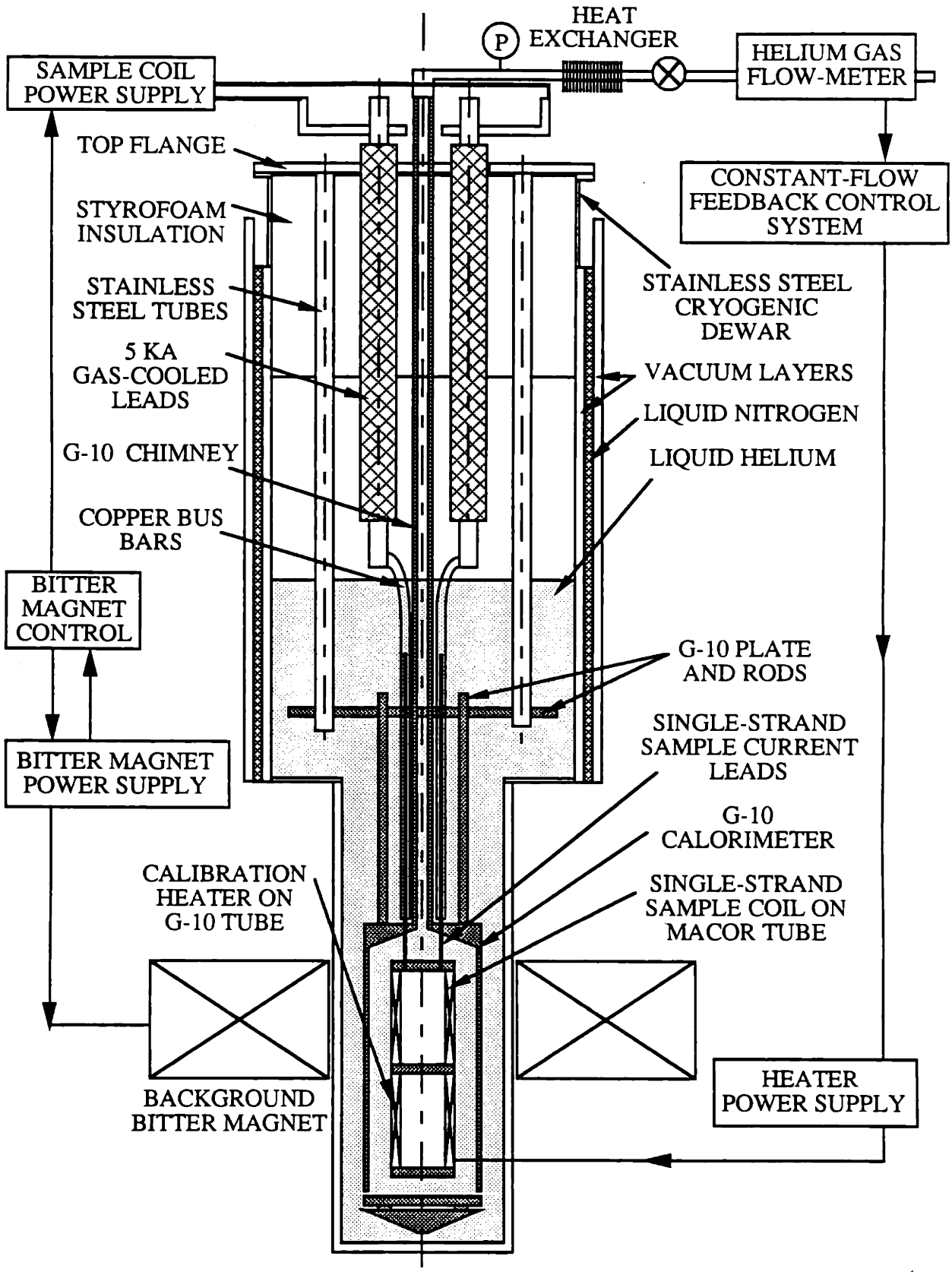

Fig. 4.3 Experimental setup of isothermal calorimetric AC-loss measurement with heater calibration and constant-flow feedback control system

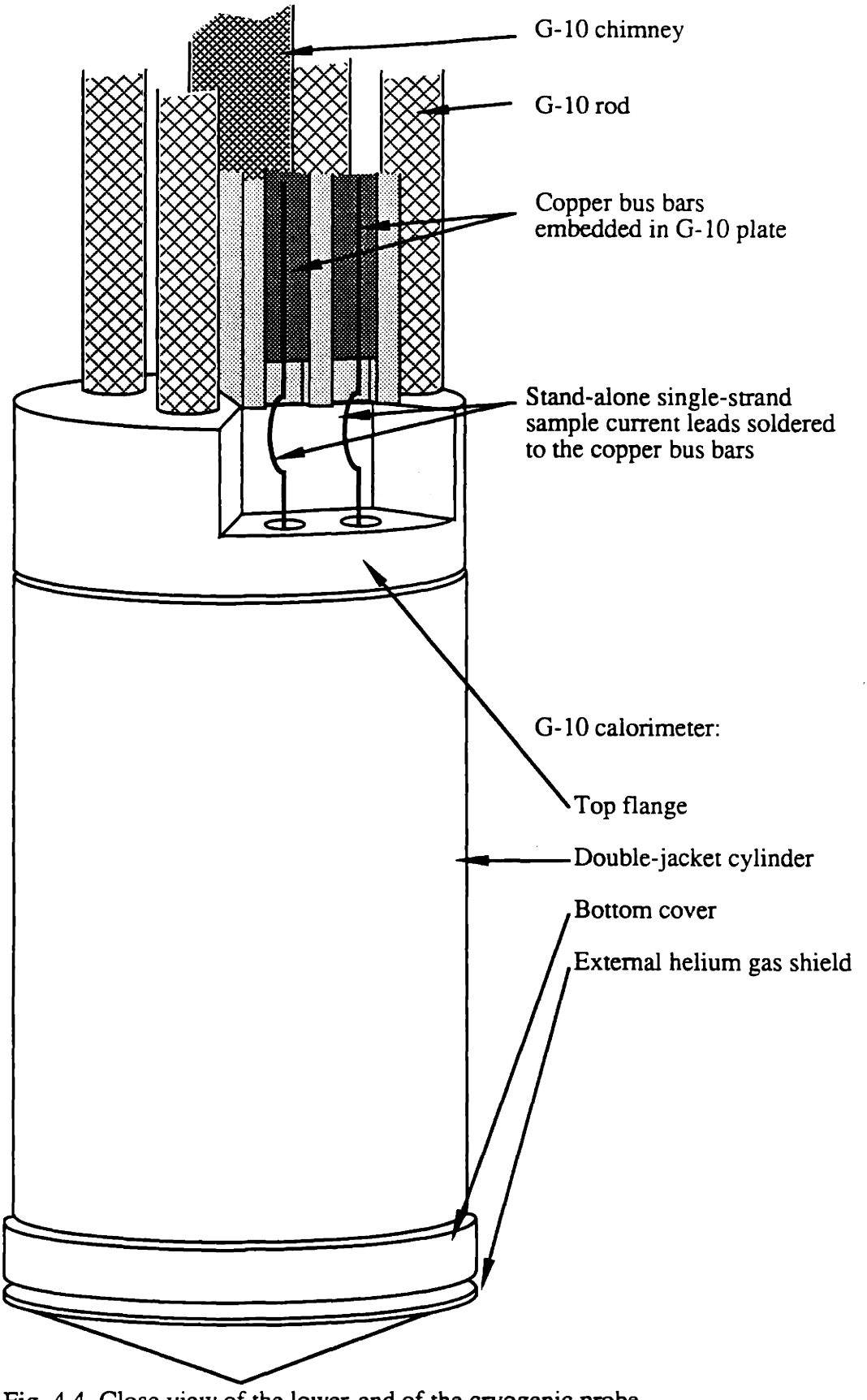

Fig. 4.4 Close view of the lower-end of the cryogenic probe.

rods are screwed into the top flange of the G-10 calorimeter, which insures a rigid connection. The copper bus bars are firmly fixed into the grooves on a piece of 0.64 cm thick G-10 plate by an array of small-size screws. This prevents the degradation of the critical currents of the test wire caused by the difference in thermal contraction between the bus bars and the G-10 structure. The ends of the bus bars and the G-10 plate are bolted to the G-10 rods and the top of the calorimeter.

The total length contraction of the probe when cooled down from room temperature to 4.2 K is estimated about 1 cm. The heat conducted into the cryostat by the stainless steel tubes and the bus bars connected with the gas-cooled leads is estimated to be 10.3 W. Additional Joule heating on the bus bars when carrying a current of 300 A is about 1.2 W. The heat conduction through the G-10 chimney and the heat generated by the eddy currents in the stainless steel parts which are kept in the low field region, are estimated as ~ 0.1 W. As a rough estimation, the total power conducted into the cryostat by the structural materials, the current leads, and the Joule heating of the bus bars at 300 A is about 11.5 W. This is equivalent to a liquid helium consumption rate of about 16 *l* / hr. The measured consumption rate was about 10 *l* / hr when no current was applied. The over-estimation of the helium consumption rate resulted from the conservative evaluation of the heat conduction through the gas-cooled current leads and bus bars.

IV.3.3 Chimney

As shown in Fig. 4.5, the lower-end of the G-10 chimney is screwed into the top flange of the calorimeter as a mechanical support. The joint is permanently sealed by applying Stycast throughout the threads. Stycast is a strong, easily cast epoxy, which is made by Emerson and Cuming Co. The thermal expansion coefficient of Stycast is similar to that of copper. Since the lower-end joint of the chimney is close to the high field region, it is important to have a leak-tight joint at 4.2 K. The upper-end of the chimney is above the top flange of the cryostat, and is connected with a flexible hose sending the boil-off helium gas through the heat exchanger and a gas flow-meter.

In the initial design, in order to reduce heat transfer between the background cryostat and the gas in the chimney, a double-jacket chimney was used to insulate the gas boiled off in the calorimeter. The outer and the inner tubes of the chimney were permanently sealed with Stycast at both ends. Based on the cryopump effect, the chimney wall should become a vacuum layer. Although gas permeation through the G-10 at cryogenic temperature (Ref.

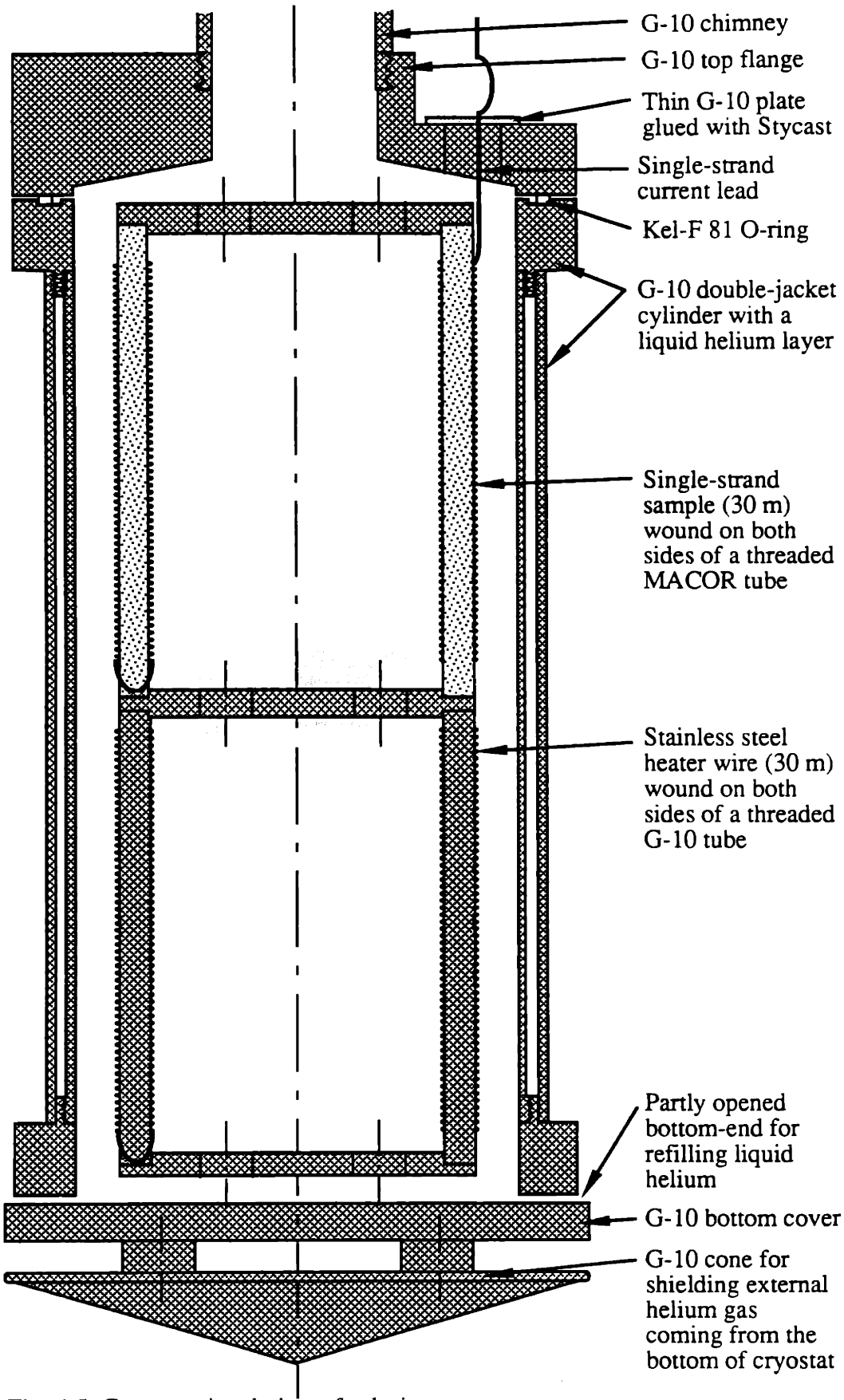

Fig. 4.5 Cross sectional view of calorimeter.

4.29) is likely to raise the pressure in the vacuum layer, the thermal conductivity of a gaseous layer is still much less than that of a single G-10 wall.

Preliminary tests showed that the intensity of spontaneous thermoacoustic resonance in the inner tube of the double-jacket chimney was very strong even when no heat was deposited into the calorimeter. When the heater power was raised to about 60 mW which was equivalent to a gas flow rate of about 1000 SCCM (Standard Cubic Centimeter per Minute), thermoacoustic resonance caused a flow rate fluctuation of about ± 300 SCCM. The intensity of the resonance increased as the deposited power to the calorimeter was raised. Based on one of the experimental results by Bannister (Ref. 4.19), increasing the length of the tube exposed to the 300 K environment consistently increased the oscillation intensity. Compared to a single wall chimney, the heat conducted from the room temperature environment by the inner tube of a double-jacket chimney was able to reach a position closer to the surface of liquid helium since the cooling effect by the bulk liquid helium bath was partly isolated by the vacuum layer. This is an alternative way to increase the warm length of a tube as described by Bannister. Raising the power deposited into the calorimeter raised the gas flow-rate through the flow-meter. The back pressure caused by the small opening of the flow-meter tended to push down the liquid helium level in the chimney, which further increased the warm length of the inner tube and thus the intensity of the resonance.

From another observation by Bannister (Ref. 4.19), the resonance amplitude of a tube was found to increase proportionally to the slenderness ratio, defined as length vs. inner diameter. A single wall G-10 tube with an inner diameter of ~ 2.5 cm is used for the present probe, which has a similar length as the former version (Ref. 4.23) but with the cross sectional area increased by four times. To avoid error caused by heat transfer though the chimney wall, heater calibration immediately after each measurement with AC field must be performed.

In a preliminary test of the present set-up, a small resonance with an amplitude of about 1% of the flow-meter signal was observed at a flow-rate greater than ~ 4000 SCCM which was equivalent to ~ 240 mW. In most of the commercially available composite superconductors, the total losses are typically below ~ 200 mW under the AC field conditions applied in this thesis work. This upper limit of obtaining a low-noise signal is high enough to cover the full range of the AC-loss measurements. For future applications of measuring a lossy single-strand or cable with the same apparatus, reduction of the

resonance in the chimney can be achieved by using a larger orifice for the flow-meter, using the same flow-meter with a calibrated room-temperature gas by-pass, reducing the volume of the test wire, or connecting a buffer tank between the chimney and the flow-meter.

A 30.5 cm liquid helium level sensor made of a calibrated single superconductor filament, manufactured by American Magnetics, Inc., is loaded in the chimney with the lower-end at ~ 2.54 cm above the first turn of the test wire coil. A small heater on the top-end of the superconductor sensor for improving the accuracy of level measurement, perturbed the helium gas flow-rate. The sensor is powered only briefly when the flow-rate reading approaches the 4000 SCCM limit. If the liquid helium level is below the lower-end of the sensor, the reliability of the test result should be examined very carefully.

IV.3.4 Calorimeter

A calorimeter must be able to (1) collect all the gas boiled off by the enclosed test wire and calibration heater, and (2) isolate the disturbance caused by the background liquid helium bath. In order to preserve the test wire during the mounting process, which is especially important for a Nb_3Sn wire with single-strand current leads, the G-10 calorimeter as shown in Fig. 4.5 is composed of three detachable parts: a top flange, a double-jacket cylinder, and a bottom cover.

As seen in Fig. 4.5, the 5.1 cm thick top flange has a funnelled bottom surface for the purpose of gas collection. A tapped hole in the center of the flange was made to provide mechanical support to the chimney. As mentioned before, in order to prevent damage to the single-strand current leads caused by relative displacement between the calorimeter and the bus bars, four 1.9 cm OD G-10 rods and a 0.64 cm thick G-10 plate mounted with copper bus bars are firmly fixed to this top flange. Another two 1.27 cm holes on the flange are for the test wire current leads to pass through. Since the Nb_3Sn is brittle after the final heat treatment, each hole is sufficiently large for the uncertainty in the position of a current lead. After the current leads are passed through these two holes with great care, they are soldered to the copper bus bars. To keep a minimal stress on the current leads imposed by the structural material on the flange, each hole for the current lead is covered with a pair of semi-circular thin G-10 disks, each with a small dent near the center of the straight edge for enclosing the wire, and is sealed with Stycast. Each time after mounting a

new test coil, the calorimeter was closed and pressurized to about 2 atm for checking the leak tightness of these seals at room temperature.

The double-jacket cylindrical wall of the calorimeter is made of G-10 rings and tubes, and joined with Stycast. Ideally, the double-jacket wall was used to provide a vacuum layer as a thermal barrier in the radial direction. However, some small leakage at joints simply glued by the Stycast without mechanical reinforcement, were found in a pressure test at 77 K, which could hardly be detected at room temperature. The leaks through the Stycast joints were very likely caused by the difference in thermal contractions in different directions of the G-10 at cryogenic temperatures. With small leakages, the vacuum layer is thus gradually filled up with liquid helium. The heat transfer condition in the radial direction of the calorimeter and therefore the background flow rate may become time-dependent which is determined by the uncontrollable leakage of the double-jacket wall. In order to prevent a time-dependent background flow rate, the outer wall of the double-jacket cylinder was purposely drilled with several holes. The vacuum layer becomes a liquid helium layer which functions as a convection shield. To verify the effectiveness of the liquid helium layer to the radial-direction heat loads, the full length of the outer wall of the double-jacket cylinder was covered by a heater wire with a turn-to-turn spacing of about 1 cm. No significant change on the background flow rate was observed as the the heater power was varied between 0 and ~ 1.7 W.

The detachable joint of the top flange and the double-jacket cylinder is about 8.9 cm above the mid-plane of the test coil which is in the high field region. A leak-tight seal at cryogenic temperature was made with a press joint and a non-metallic Kel-F 81 O-ring in a groove (Ref. 4.30). The Kel-F 81 plastic, manufactured by the 3M company, is a polymer with a low 'cold flow' characteristics, which has been applied at near 0 K as claimed by the manufacturer. The linear length reduction of the Kel-F 81 is about 3% as the temperature is reduced from 300 K to 4.2 K, which is about ten times greater than that of G-10 in the wrap direction. In order to release the thermomechanical interaction between the G-10 and the O-ring, it is important to have a groove with an ID smaller than that of the O-ring. The top flange and the double-jacket cylinder of the calorimeter are held together by 6 size-6 non-magnetic stainless steel bolts which pre-compress the O-ring at room temperature. The size of the stainless steel bolts were selected as small as possible without jeopardizing the integrity of the calorimeter and located as far as possible away from the test wire. Compared to the strength of a metallic base material for the O-ring, the pre-stress imposed by the G-10 with small size bolts is relatively limited. Small ripples due to the glass fibers

in the G-10 have been found on the base surface in the groove. Vacuum grease was applied to the top and bottom surfaces of the O-ring to fill the small dents between the glass fibers.

To prevent possible gas leaks due to the limited pre-stress and non-uniform surface in contact with the O-ring, a second barrier is included. A narrow Mylar sheath is taped on the inner surface of the double-jacket cylinder with one edge extending above the top of the cylinder. As the top flange and the cylinder are joined together, the upper part of the Mylar sheath covers the top joint with the O-ring. As long as the pressure difference between inside and outside of the calorimeter is not large, the boiled off gas will not be trapped in the corner where the O-ring is located, which greatly reduces the possibility of gas leak.

The bottom-end of the calorimeter must be partly opened in the radial direction for the purpose of automatic refilling and maintaining a near atmospheric pressure. Some spacers glued on one side of the disk provide radial openings (Fig. 4.5) for the above mentioned purposes. The other side of the bottom disk, without spacers, is used to close the calorimeter for gas leak check in a pressure test. In order to prevent helium gas from entering the calorimeter, the bottom G-10 disk is made slightly wider than the outer diameter of the double-jacket cylinder. A 32-pin female connecter penetrates the center of the bottom disk and is sealed with Stycast, which interconnects the electric signals from both sides of the calorimeter.

IV.3.5 Test Wire and Test Wire Coil Winding

IV.3.5.1 Test Wires

Single-strand test wires, of interest to the present study, were those used for high-current AC superconducting magnets which generate large-amplitude (> 5 T) ramp-fields. Three types of wires with different cross sectional structure, including a NbTi, a Nb_3Sn internal-tin, and a Nb_3Sn modified jelly-roll (MJR) internal-tin wire, were available for AC-loss measurements. The NbTi wire as shown in Fig. 4.6(a), was made by Supercon for the inner coils of the dipole magnets of the Superconducting Supercollider (SSC) which has a uniform multifilament zone with a normal core in the center of the wire. The internal-tin Nb_3Sn wire as shown in Fig. 4.6(b), was designed by Intermagnetics General Corporation (IGC) Advanced Superconductors, Inc. for fusion reactor ohmic heating coil application which has 19 multifilament bundles surrounded by a global tin diffusion

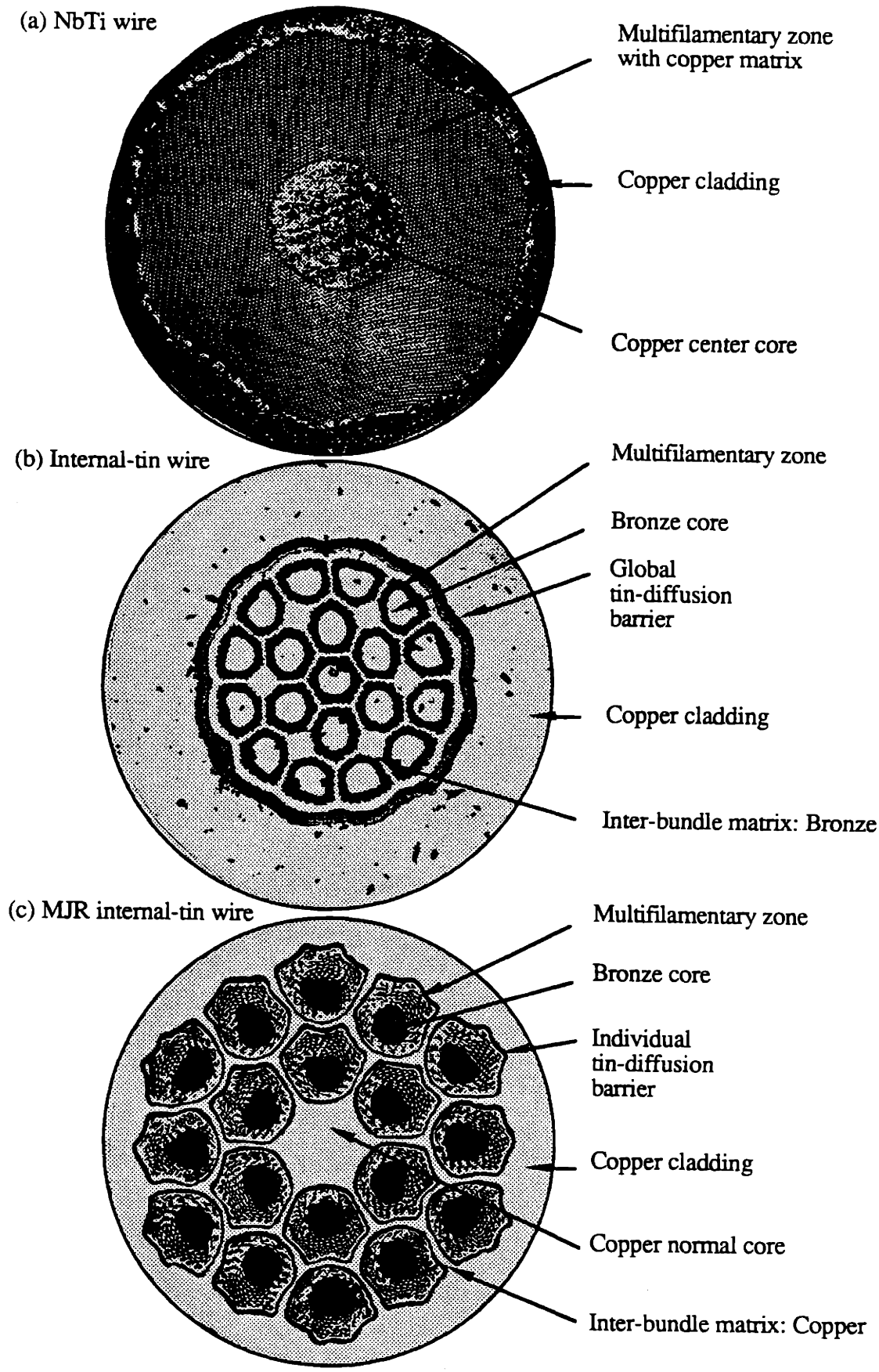

Fig. 4.6 Cross sectional constructions of test wires.

barrier. The MJR wire as shown in Fig. 4.6(c), was made by Teledyne Wah Chang Albany (TWCA) for the US-Demonstration Poloidal Coil (US-DPC) (Ref. 4.31) which has a normal core in the center of the wire, and is surrounded by 18 multifilament bundles with individual diffusion barrier.

To obtain the best performance of a Nb_3Sn conductor, the conductor is usually processed using the wind-and-react method. As mentioned before, after the reaction (heat treatment), the Nb_3Sn wire becomes extremely fragile which introduces one of the major difficulties in test wire preparation. The sample holder has to be carefully designed to reduce the possibility of degrading the superconducting wire due to sample handling, thermal stress, and wire motion caused by the electromagnetic forces.

IV.3.5.2 Sample Holder

Compared with the magnetization or adiabatic calorimetric methods, the isothermal calorimetric method with flow rate measurement needs a large volume of test wire for better signal-to-noise ratio. A continuous long length wire is preferred for testing AC losses with transport currents. Because the critical current density of a composite wire, drawn from a single billet, may not be uniform along the length of the wire, it is best to test the critical current density of the same AC-loss test wire. This implies that the AC-loss test wire must be able to survive a maximum Lorentz force determined by the maximum current that the wire can carry at a given field.

The sample holder was designed mainly for Nb_3Sn wires with the following concerns: (1) The sample holder has to be non-metallic and thermally compatible with Nb_3Sn in the temperature range between 4.2 K and 1000 K; (2) A large fraction of the test wire volume should be in the homogeneous zone ($\pm$ 5% of variation) of the available background field; (3) A multi-layer winding may introduce deviation to the isothermal condition since the temperature of the internal turns may be changed due to the trapped boil-off gas; (4) Epoxy potting for prevention of wire movement may change the surface condition for boiling and heat transfer, and thus should not be used; (5) Possible wire damage due to epoxy cracking at cryogenic temperature is another reason for not using epoxy potting; (6) Low inductive winding is required to avoid distortion of the background field by the transport currents; (7) Test wire with conventional low self-inductance bifilar winding has the potential risk that those turns affected by the outward Lorentz forces can be damaged by wire motion.

Based on these considerations, as shown in Fig. 4.7, the test wire coil is made by winding two solenoids from a single wire, one on the inside and the other on the outside of the sample holder tube. The new design uses a circular MACOR tube with an ID of 6.35 cm and an OD of 7.62 cm. In order to reduce the self-inductance, the test wire coil winding has 74 turns on the inside wall and 63 turns on the outside wall. The self-inductance of the overall winding is estimated to be 0.5 μH. The total wire length is about 30 m. The test wire is held by the groove on both the inner and outer surfaces of the tube. The width of the groove is ~ 0.9 mm and the depth is ~ 0.5 mm. The distance between neighboring turns is ~ 1.9 mm for the outer winding and ~ 1.6 mm for the inner winding. The length of the coil in the axial direction is approximately 12.5 cm. For either side of the winding, the direction of the Lorentz force due to transport current in the test wire and the background field is toward the mandrel and thus firmly pushes the wire into the thread groove. The detailed procedure of this special coil winding method is listed in APPENDIX A.

The test wire and the MACOR mandrel required heat treatments up to a temperature of ~ 1000 K, and tests at a temperature of 4.2 K. The thermal compatibility of the mandrel and the test wires had been considered during the design stage. From 920 K to 4.2 K, the calculated length reduction of the wire was $\Delta L/L = -0.0072$, and the estimated length reduction of the MACOR was $\Delta L/L = -0.0085$, a difference of about 0.13 %. At 4.2 K, the MACOR sample holder was expected to place a compressive stress on the wire in the inner windings. However, it was found that after heat treatment, the superconducting wire wound on the outside was tightly embedded in the threads, and the wire wound on the inside was loose. With a careful examination of the wire and the sample holder, no observable dimensional change was found on the MACOR tube at room temperature, but the inner coil reduced in length by about 1/3 of a turn, a shrinkage of about 0.45 %. In order to keep the inner windings from getting out of the grooves, stainless steel rods were used to support the wire during heat treatment and were replaced by G-10 rods for tests at 4.2 K.

To understand the cause of the unexpected length reduction due to heat treatment, several linear wires including solid copper wires, bronze Nb_3Sn wires, and internal-tin Nb_3Sn wires, were heat treated together in a quartz furnace. Each test wire, with a typical length of about 61 cm, had one end fixed to a quartz rack and the other free-end marked for observation. Shortenings of all internal-tin wires were observed at temperature between

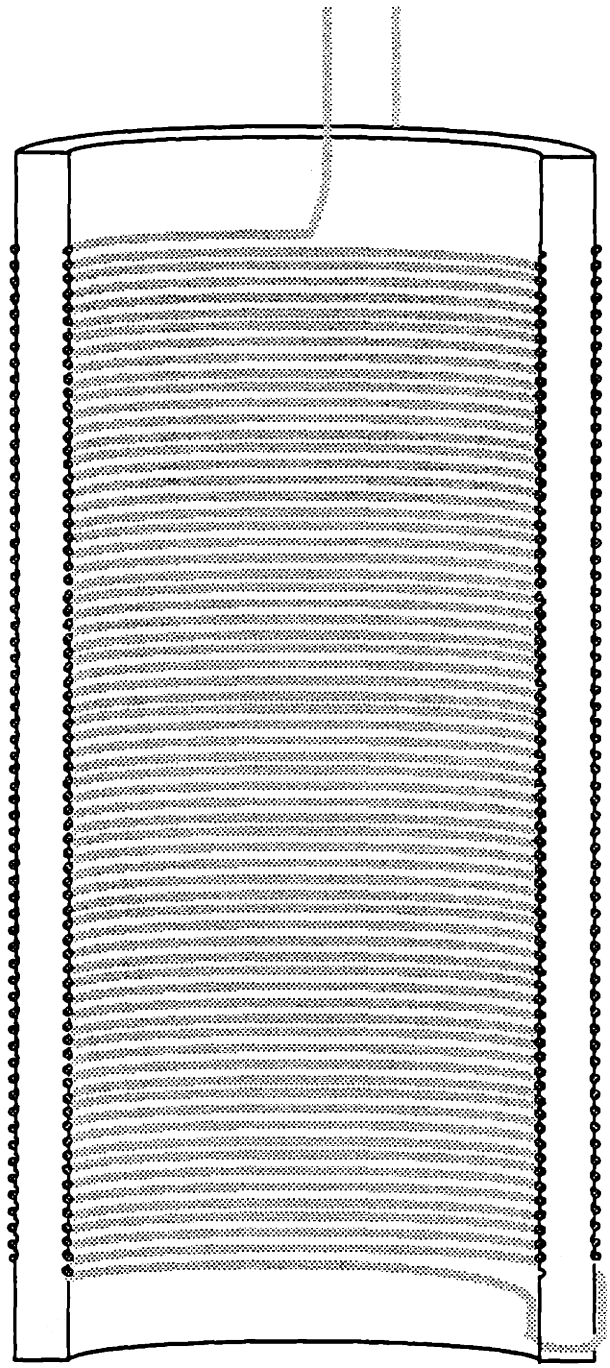

Fig. 4.7 Single-strand superconducting sample wound on the inner and outer threaded surfaces of a MACOR tube; ID = 6.35 cm, OD = 7.62 cm, axial winding length = 12.7 cm, sample length = 30 m.

150 °C and 200 °C. After the heat treatment, the lengths of all the internal-tin wires measured at room temperature were consistently reduced by about 0.4% to 0.45%. No apparent dimensional changes were found on the solid copper wires and the bronze Nb_3Sn wires (Ref. 4.32). The length reduction of the internal-tin type wires occurring at the low-temperature stage of the heat treatment was also noticed by one of the wire manufacturer (Refs. 4.33 and 4.34).

The low temperature annealing of the internal-tin wire is due to the special wire manufacturing process. The composite internal-tin wire can be drawn to the final length without intermediate anneals, which is the unique advantage of this kind of wire. The overall cross sectional area reduction can be as much as 400,000 to 1 (Ref. 4.35) which represents a heavy cold-work to all the constituent metals. When the cold-worked metal is heated, the distorted lattice tends to recover its normal shape, which is the stress relieving process. Copper, with an overall volume fraction usually higher than 60%, is the major constituent material in a composite wire. For a heavily cold-worked copper (93% cold-work), the stress relieving temperature has been reported between 80 °C to 200 °C (Ref. 4.36). This is consistent with the temperature range in which the length reduction of the composite internal-tin wire occurred.

In a large scale superconducting coil, the required continuous conductor length can be of order of kilometer. For a friction-free internal-tin wire or cable, the length reduction after heat treatment would be about 4 m. Prevention of stress concentration due to such conductor length reduction should be considered.

IV.3.6 Background Fields and Applied Transport Currents

Since all the test wires are for AC superconducting magnet applications, it is desirable to characterize the AC losses of the superconducting wires carrying high AC and/or DC transport currents in a time-varying strong AC fields. At the Francis Bitter National Magnet Laboratory (FBNML) a 15.2 cm-bore water-cooled Bitter magnet which can be energized up to 12 T for steady state operation, has been used for uni-directional cyclic ramping. With voltage control of the 10 MW power supply to the magnet, the field can be continuously swept at a peak field up to 9 T (0 - 9 T - 0) with the shortest rise-time of 7 s. At a lower peak field ($\leq$ 4.5 T), a shorter rise-time of 3 s can be used without degrading the peak value.

Three low-noise Hewlett Packard HP 6260B power supplies, each with a maximum current of 100 A, are connected in parallel to provide the transport currents to the AC-loss test wire. Either DC currents or AC currents synchronized with the changing field are available. Before loss measurement of a current-carrying wire in a ramp field condition, it is necessary to measure the critical current densities of the test wire at various DC fields. The 300 A power supply can usually satisfy the DC critical currents for the test wire at a higher DC field (say > 7 T). For critical current measurement at a lower field (between 3 T and 7 T for example), another 1 kA power supply with a higher level of noise is available at FBNML.

The background magnet can also be modulated to generate a small amplitude AC field superposed on a high DC field. Since the AC losses are dominated by the coupling loss at a higher field changing rate, such a background field condition provides another useful alternative to identify the coupling losses.

IV.3.7 Constant Flow-rate Control Circuit

As mentioned before, the conventional isothermal calorimetric method measures AC losses by the helium boil-off rate with a flow-meter. The averaged helium gas flow-rate is recorded when the helium system reaches a new equilibrium state due to the AC losses of the test wire with or without transport currents at a given AC field. After the field and the transport current are turned off and the helium system returns to its background equilibrium state, the previous flowrate is then calibrated by energizing a heater enclosed in the same calorimeter. As the averaged helium gas flow-rate boiled off by the heater matches that by the AC losses, the calibrating heater power is equivalent to the total AC loss power. For convenience, the first measurement with background field is called the magnet shot, and the second one is called the calibration shot. The waiting time for the helium system to reach a new equilibrium state depends on the energy dissipated into the system, and usually takes longer than 20 minutes. To obtain a data point, one has to wait for the new equilibrium state twice for each of the magnet shot and the calibration shot. The waiting time for measuring a single data point would be more than an hour. The conventional method is impractical especially with a limited background magnet time available at FBNML, 200 minutes biweekly.

From the above description, it is clear that all the waiting time comes from the change of the equilibrium state of the helium system. If the equilibrium state of the helium system can

be fixed during the experiment, the waiting time would be eliminated. A constant flow-rate feedback control system which was first discussed by Takayasu, et al. in Ref. 4.23, has been built by this group to approach such a fixed equilibrium state. With a slight improvement on the stability of the feedback loop, the constant flow-rate control system reduced the waiting time by a factor of approximately 5 (Ref. 4.32).

The principle of a fixed equilibrium state is that the variations of different heat sources have no effect on the equilibrium state of the liquid helium in the calorimeter as long as the total dissipated power is kept constant. Throughout the experiment, the heater inside the calorimeter is at all times energized. The flow-meter voltage signal is compared with a preset standard DC voltage in the feedback control system which is greater than all the expected flow-rate caused by AC losses. The block diagram of the constant flow-rate control feedback system in shown Fig. 4.8. The output voltage of the feedback circuit controls the heater power supply and tends to maintain the total helium flow-rate at a constant value determined by the standard DC voltage. Fig. 4.9 shows the operating scenario of the constant flow-rate control feedback system. At zero field and zero transport current, the helium is boiled off solely by the heater (Fig. 4.9(a)). Whenever a loss power is dissipated by the test wire during a magnet shot, the control circuit reduces the heater power by a similar amount, and the total helium flow-rate is perturbed only by a small amplitude near the set point of the DC voltage (Fig. 4.9(b)). In the calibration shot, heater calibration is performed by fine tuning the DC voltage to make up the perturbed part of the flow-rate (Fig. 4.9(c)). AC loss power is the difference of the heater powers in the consecutive magnet shot and calibration shot.

A similar idea was suggested in an early unpublished report (Ref. 4.17) which was found after the present constant flow-rate feedback control circuit had been built and applied. The former author controlled the heater power manually which was only feasible for a very slow field change. In the cyclic ramp field condition, adjustment of the heater power following the field variation can hardly be done manually.

The overall sensitivity of the experimental system is about 0.3 mW (~ 5 SCCM), and the resolution is better than 0.2 mW. The system error resulting from the fluctuation of the heater power due to the perturbation of the cryostat is estimated to be less than ± 1.63 mW which will be further discussed in Section V.4. The typical range of the AC losses of a 30 m long Nb_3Sn composite wire is between 10 and 200 mW.

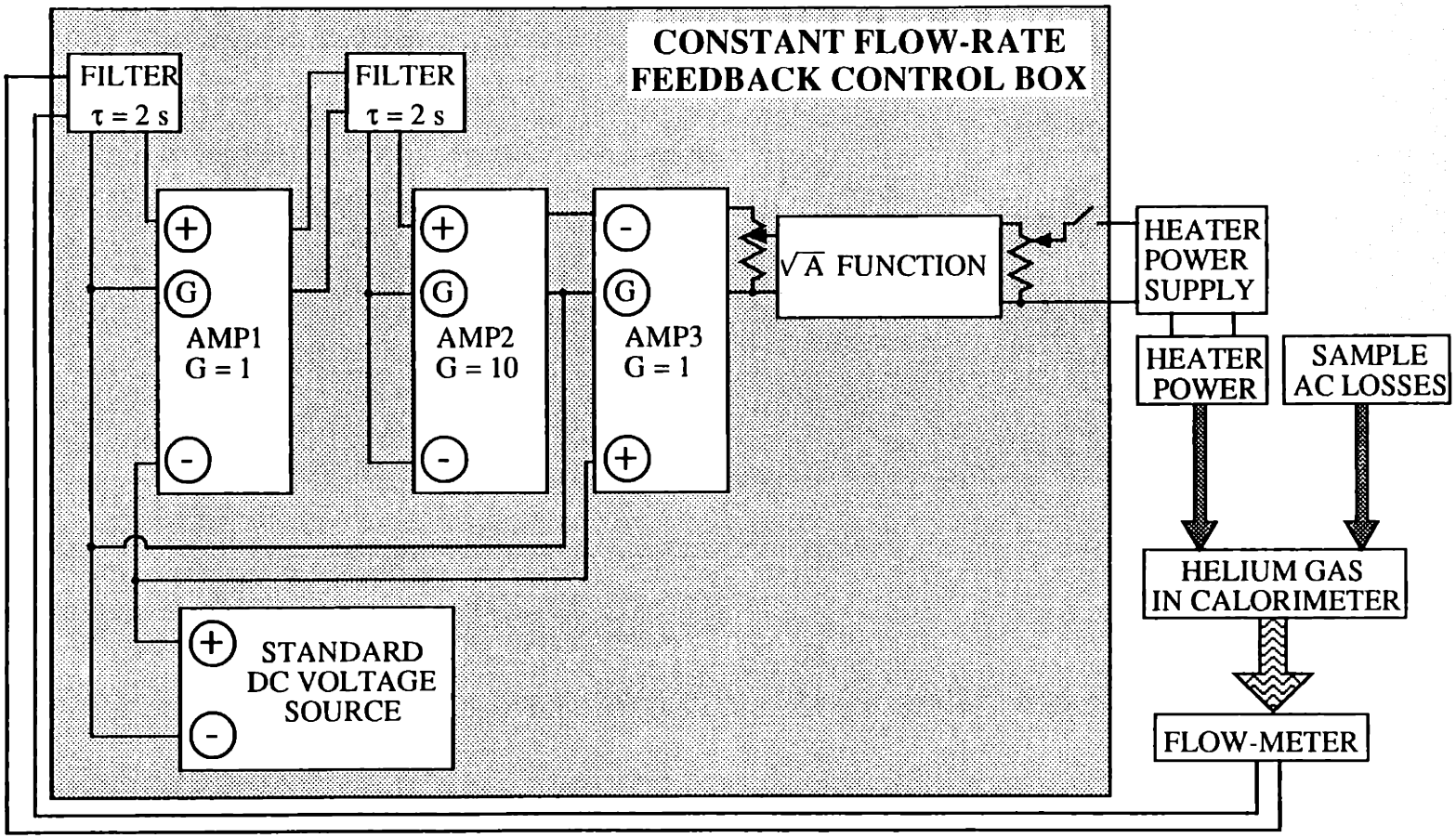

Fig. 4.8 Constant flow-rate feedback control circuit (Ref. 4.19).

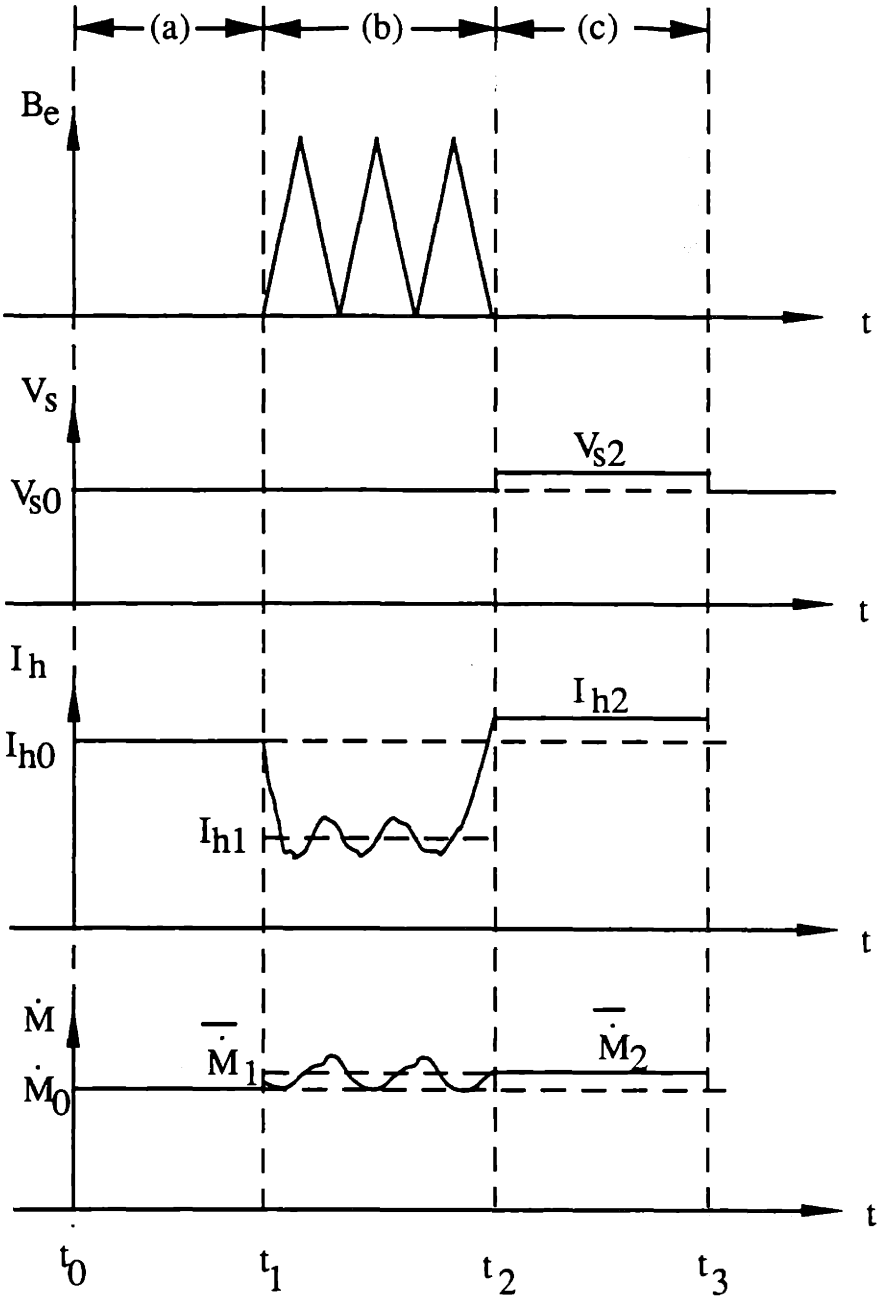

(a) PRESET V_{s0}, I_{h0}, AND $\dot{M}_0$

(b) MAGNET SHOT: record $\bar{I}_{h1}$ and $\bar{\dot{M}}_1$

(c) CALIBRATION SHOT: adjust V_s, match $\bar{\dot{M}}_2$ with $\bar{\dot{M}}_1$, record I_{h2}

(d) AC LOSS = $(I_{h2}^2 - \bar{I}_{h1}^2) \times R_h$

Fig. 4.9 Isothermal calorimetric measurement with constant flow-rate control; relationship between external field B_e, reference standard DC voltage V_s, heater current I_h, and helium gas flow-rate $\dot{M}$.

IV.3.8 Data Acquisition

As seen in Fig. 4.9, the helium gas flow-rate and the heater current are the two major parameters needed for calibration and loss calculations, respectively. After a transient time, each of these two variables is recorded and averaged over the number of data. The resulting loss calculated from the averaged current is thus an averaged total AC losses of the composite superconducting wire at a given background field and current condition. During the data taking time, both signals are perturbed by factors such as the pressure of the cryostat, the background changing field, the transport current, etc. The perturbed signal profile is usually smooth but not a regular sinusoidal or triangular wave-form. Human error due to visual reading and manual averaging can not easily be characterized. Due to this, computer data acquisition has been used to improve the resolution in data reading.

A Macintosh II computer along with an NB-MIO-16X data acquisition (DA) board, an NB-DMA-8-G multifunction interface board, and a Laboratory Virtual Instrument Engineering Workbench 2 (LabVIEW® 2) software package made by National Instruments Co. have been used as standard data acquisition equipment at the FBNML. The DA board, an interface between computer and electronic instruments, has 16 single-ended input channels which can be configured as 8 differential input channels. The acquisition rate of using a single channel is 55.6 Ksample/s. When multiple channels are used, the sampling rate would be the single channel rate divided by the number of channels. For example, if all 8 channels are used, the sampling rate for each channel would be about 7 Ksample/s.

The LabVIEW 2 software package is a library of subroutines expressed in a high level graphic programming language (Ref. 4.38). The application program is written in a form of *block diagram* by selecting the needed *icons* and I/O interface components from the library. Each icon is a subroutine containing implicit input/output (I/O) ports. The data flows among the icons and the I/O components are connected by *wires*. Various built-in DA subroutines in the library have been written for communication between the DA board and the application program. Since a good knowledge of the DA hardware is required to write this type of subroutine, the programmer usually just selects an appropriate DA subroutine for his need. A user has to write an application program for the special need of a specific experiment. A new icon can be assigned to a user created application program and used either independently or as a subroutine. The *control* and *indicator* components, analogous to the read and write commands in conventional programming languages, are

selected and connected in the block diagram screen with related images displayed on a screen of the *front panel*. Fig. 4.10 shows a typical display of the front panel. The images of the controls and indicators in the front panel are expressed graphically as electronic switches and meters, respectively. With proper arrangement, the display of the front panel would be visually like an electronic instrument with desired functions, and thus it is called *virtual instrument* (VI).

Two LabVIEW 2 application programs simulating multi-channel oscilloscopes have been either improved or written for different purposes. The first one, modified from the existing FBNML program by including the averaging and error calculation subroutines, is applied mainly to the slow calorimetric measurement. The second program, with 8-channel input and a minimum sampling time of less than 1 ms, is designed for recording fast signals such as flux jumps in a magnetization measurement.

For the AC-loss test, three to four channels are used to record the gas flow-rate, the heater current, the background field, and the transport current if it is applied. The sampling rate would be greater than 10 Ksample/s. In AC-loss experiment, the frequency range is between 0.01 Hz to 0.1 Hz for ramp field test, and 7.5 Hz for sinusoidal ripple field test. The sampling rate of the DA system is fast enough to take 1000 data points over two to three periods of the field ramping or over few seconds of the field rippling. In a magnet shot, the averaged flow-rate is calculated by the computer after the end of data acquisition. The averaged flow-rate is then applied to the following calibration shot. With the DA system, the data taking time has been reduced by about 80% with less human error.

IV.4 SUMMARY

This chapter presents the design and construction of a new isothermal calorimetric measurement system. The isothermal calorimetric method is selected based on the advantage of providing absolute values of AC losses. To practically apply this method, the disadvantages of mild accuracy and long waiting-time for the equilibrium of the helium system must be overcome. In the new experimental system, which is designed and constructed in this thesis work, the accuracy has been improved by eliminating the field-dependent noise as well as the thermoacoustic resonance at cryogenic temperature. The efficiency of this method has been improved by using a constant flow-rate control feedback system and a data acquisition system. The unique feature of the present set-up is capable of

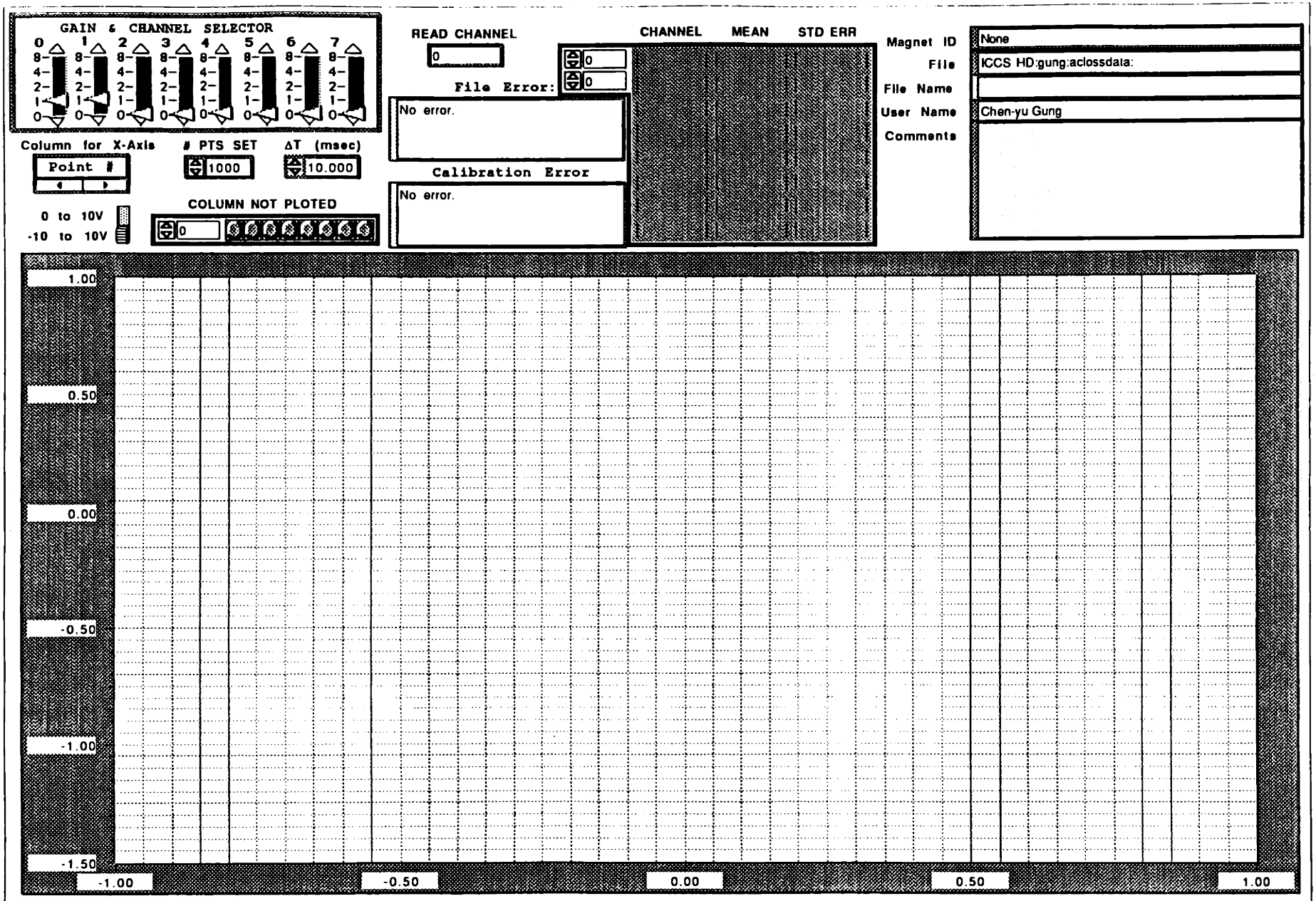

Fig. 4.10 Typical front panel view of virtual instrument applied for data acquisition in AC-loss experiment.

measuring the AC losses of a brittle Nb_3Sn single-strand carrying a high AC current in-phase with the large-amplitude pulse magnetic field.

The system error of this new experimental setup will be evaluated in Chapter V. In order to validate the present apparatus, benchmark comparisons of the hysteresis losses obtained in the present work with those performed independently by other author will also be made in Chapter V.

IV.5 REFERENCES

4.1 Wilson, M.N., *Superconducting Magnets*, Oxford Science Publications, 1983.

4.2 Ekin,J.W., 'Superconductors,' Ch. 13 in *Materials at Low Temperatures*, ed. by Reed, R.P. and Clark, A.F., American Society for Materials, 1983.

4.3 Itoh, K., Wada, H., and Tachikawa, K., 'Results on the First VAMAS Intercomparison of AC Loss Measurements,' Adv. Cryo. Eng., Vol. 38, 1992, p. 459.

4.4 Shen, S.S., and Schwall, R.E., 'Interaction of transport current and transient external field in composite conductors,' IEEE Trans. Magnetics, MAG-15, No. 1, 1979, p. 232.

4.5 Ogasawara, T., et al., 'Transient field losses in multifilamentary composite conductors carrying dc transport currents,' Cryogenics, 1980, p. 216.

4.6 Dragomirecky, M, Minervini, J.V., Ekin, J.W., Goldfarb, R.B., Clark, A.F., 'Losses in a Nb-Ti superconductor as functions of AC field amplitude and DC transport current', ICEC 11, Berlin, Germany, 22-25 April, 1986

4.7 Goldfarb, R.B., Minervini, J.V., 'Calibration of ac susceptometer of cylindrical specimens,' Rev. Sci. Instrum., Vol. 55, No. 5, 1984.

4.8 Bruzzone, P., 'AC losses in high current superconductors for nuclear fusion magnets,' Thesis, Swiss Federal Institute of Technology, Zurich, 1987.

4.9 Ando, T., Takahashi, Y., Nishi, M., and Shimamoto, S., 'Time constant measurement technique for multifilamentary superconductors in parallel field,' in 'Proc. of International symposium on flux pinning and electromagnetic properties in superconductors,' Fukuoka, Japan, 1985.

4.10 Schmidt, C., 'Measuring AC losses of superconductors', Cryogenics, Vol. 25, 1985, p 492.

4.11 Mower, T.M., and Iwasa, Y.,'AC losses in multifilamentary composite superconducting strands and cables,' Adv. Cryo. Eng., No. 32, 1986, p. 771.

4.12 Mower, T.M., Iwasa, Y., 'Experimental investigation of AC losses in cabled superconductors,' Cryogenics, Vol. 26, 1986, p. 281.

4.13 Minervini, J.V., Steeves, M.M., Heonig, M.O., 'Calorimetric measurement of AC loss in ICCS conductors subjected to pulsed magnetic fields,' IEEE Trans. Magnetics, MAG-23, No. 2, 1987, p. 1363.

4.14 Schmidt, C., and Specht, E., 'AC loss measurements on superconductors in the microwatt range', Rev. Sci. Instrum., Vol. 61, No. 3, 1990, p. 988.

4.15 Rhodes, R.G., Rofers, E.C., and Seebold, R.J.A., 'Measurement of 50 c/s losses in superconductors,' Cryogenics, 1964, p. 206.

4.16 Pech, T,. duflot, J.P., and Fournet, G., 'Comparative measurements of 50 c/s losses in superconductors,' Phys. Lett., Vol. 16, No. 3, 1965, p. 201.

4.17 Bean,C.P., et al. 'A Research Investigation of the Factors That Affect the Superconducting Properties of Materials,' AFML-TR-65-431, 1966.

4.18 Takayasu, M., unpublished results, 1987.

4.19 Bannister, J.D., 'Spontaneous pressure oscillations in tubes connecting liquid helium reservoirs to 300 K environments,' in *Pure and Applied Cryogenics*, Vol. 6, 'Liquid Helium Technology', 1966.

4.20 Narahara, Y., et al., 'Thermal effects due to oscillations of gas columns,' Cryogenics, Vol. 28, 1988, p. 177.

4.21 Luck, H., and Trepp, Ch., 'Thermoacoustic oscillations in cryogenics. Part 1: basic theory and experimental verification,' Cryogenics, Vol. 32, No. 8, 1992, p. 690.

4.22 Luck, H., and Trepp, Ch., 'Thermoacoustic oscillations in cryogenics. Part 2: applications,' Cryogenics, Vol. 32, No. 8, 1992, p. 698.

4.23 Takayasu, M., et al. 'Calorimetric measurement of AC loss in Nb_3Sn superconductor,' Proceedings of MT-11, Tsukuba, Japan, August 1989, p.1033.

4.24 Kuroda, K., 'modified boil-off method for measuring AC losses of superconducting composites', Cryogenics, Vol. 26, 1986, p. 566.

4.25 Eikelboom, J.A., 'Apparatus for calorimetric measurement of AC losses in superconductors,' Cryogenics, Vol. 31, 1991, p. 363.

4.26 Niessen, E.M.J., et al., 'Current degradation and coupling losses in ring shaped wires due to applied magnetic field changes,' MT-12, Leningrad, USSR, June 1991.

4.27 Benzinger, J.R., 'Manufacturing capabilities of CR-grade laminates,' Adv. Cryo. Eng., Vol. 26, 1980, p. 252.

4.28 Provided by manufacturer.

4.29 Evans, D., and Morgan, J.T., 'Gas permeability through composite materials,' Cryogenics, Vol. 28, 1988, p. 283.

4.30 Guthrie, A., *Vacuum Technology*, Chapters 10 and 12, John Wiley & Sons, Inc., 1963.

4.31 M.M. Steeves, et al., 'The US demonstration poloidal coil,' IEEE Trans. Magnetics, MAG-27, No. 2, 1991, p.2369 .

4.32 Gung, C.Y., et al., 'AC loss measurements of Nb_3Sn wire carrying transport current,' IEEE Trans. Magnetics, MAG-27, No. 2, 1991, p. 2162.

4.33 Smathers, D.B., private communication.

4.34 Smathers, D.B., and Siddall, M.B., "Reaction mandrel material effect on critical current of Nb_3Sn coiled short samples," presented at the 1989 TMS annual meeting in Las Vegas, Nevada, March 1989.

4.35 Gregory, E., 'Conventional wire and cable technology,' Proc. IEEE, Vol. 77, No. 8, 1989, p. 1110.

4.36 Williams, R.S., and Homerberg, W.O., Principles of Metallography, McGraw-Hill, 1948, p. 69 to 78.

4.37 S.S. Shen, and R.E. Schwall, 'Interaction of Transport Current and Transient External Field in Composite Conductors,' IEEE Trans. Magnetics, MAG-15, No. 1,1979, p. 232.

4.38 *LabVIEW 2 User Manual*, National Instrument Corporation, October 1990.

CHAPTER V

ANALYSIS OF SINGLE-STRAND AC-LOSS TEST RESULTS USING EXISTING MODELS

V.1 INTRODUCTION

The major purpose of this chapter is to provide the experimental results of the field-dependent critical currents as well as measured AC losses for different superconducting wires in various background field and current conditions. Of equal importance, analysis of the measured AC losses using existing models are performed in this chapter to justify either the general knowledge in the AC-loss mechanisms or the feasibility of the existing AC-loss models to some specific strand construction.

Part of the major experimental work performed in the present research is testing the current-carrying brittle Nb_3Sn single-strand wire in an AC background field ramped at a large amplitude. Most of the AC-loss experiments performed by other researchers are limited to test either hysteresis loss or coupling time constant individually with a current-free Nb_3Sn single-strand. In this thesis work, the applied ramp rates are fast enough to include both hysteresis and coupling losses in the total loss. Instead of testing single point data, a loss profile as a function of applied field, field ramp rate, transport current, DC bias field, etc. can be measured with the present experimental setup.

In this chapter, the test condition including the background field and the applied current will be specified, followed by the specifications of different test wires. Cross sectional construction of the superconducting strand in a better detail than the manufacturer's specification are estimated for model calculations.

The measured critical currents at various fields will be shown first. The field-dependent critical current profile, which is required information for the AC-loss modeling, is obtained by fitting the semi-empirical equation to the experimental data as described in Chapter III. Based on the critical current formula and the estimated transverse resistivity, the importance

of the penetration loss will be evaluated for the applied field conditions. Experimental error of the calorimetric measurement system will be estimated before showing the test results.

Benchmark comparisons of the hysteresis losses obtained in the present work with those performed independently by other author are made for a few similar test wires. Effective filament diameter for each wire is obtained from extrapolated hysteresis loss. In the ramp field condition, AC loss of each current-free test wire is shown as a function of ramp rate and applied field, respectively. Loss profile of a composite superconductor carrying DC or synchronized AC current is shown as a function of applied current and field ramp rate, respectively. In the ripple field condition, the loss is plotted against the DC bias field. All the test results are compared with the existing loss models.

V.1.1 Background Field and Applied Transport Current

The ultimate goal of the laboratory-scale experiment is to characterize AC-loss properties of composite superconductor strands in an environment simulating the operation of a superconducting magnet for ramp field applications. The constituent single strand of an AC superconducting coil must carry AC transport current and is affected by the synchronized magnetic field. Since a strong self-field can not be generated by the limited conductor volume applied in the laboratory-scale experiment, it is necessary to obtain the desired field condition from an external magnet. The DC or synchronized AC transport current is supplied to the single-strand with an independent power supply. All the test were performed at the Francis Bitter National Magnet Laboratory (FBNML) with the background field provided by a water-cooled resistive Bitter magnet with a bore size of 15.2 cm.

Fig. 5.1 shows the wave-forms of the applied background field for testing the AC losses. The cyclic ramp field (continuous triangular wave-form field) as shown in Fig. 5.1(a) is applied for the major AC-loss measurements. Available background fields limited by the power supply of the Bitter magnet are: the maximum field must be less than 9 T; the minimum field must be kept positive; the rise-time and the down-time must be slower than 3 s at a smaller amplitude (say < 4.5 T), and slower than 6 s at a larger amplitude. An additional constraint on the slowest rise-time, $T_m \leq 60$ s, is limited by the sensitivity of the isothermal calorimetric system and the loss level of the test wire.

For the purpose of distinguishing various sources of the AC losses, loss measurements are performed on the same conductor without transport current and with DC or

(a) Cyclic Ramp Field:

$B_{max} \leqq 9$ T; $B_{min} = 0$ T; 3 s $\leqq T_m \leqq 60$ s

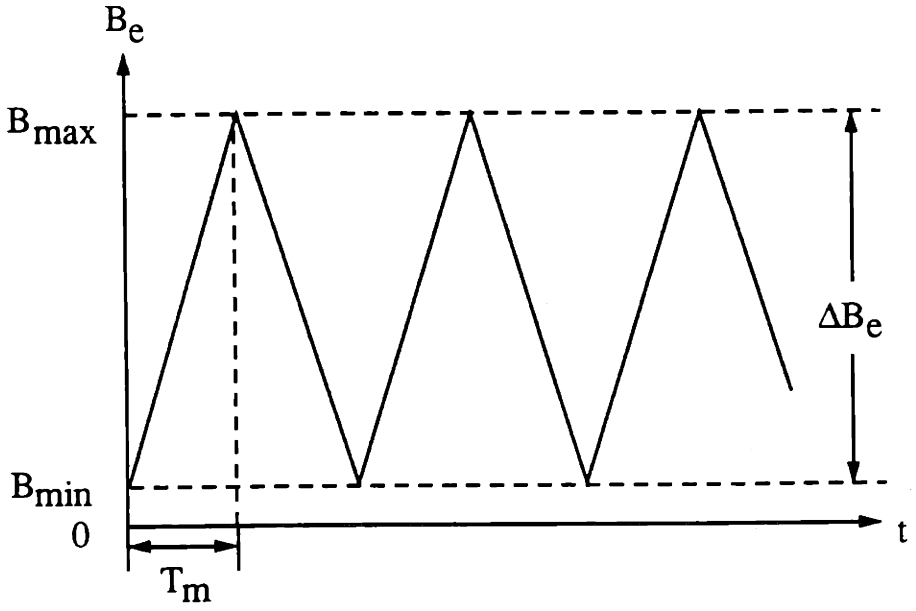

(b) Small Sinusoidal Wave-form Field Superposed to a Large DC Bias Field:

$\Delta B_e = 0.086$ T; $f = 7.5$ Hz; 0.5 T $\leqq B_{DC} \leqq 12$ T

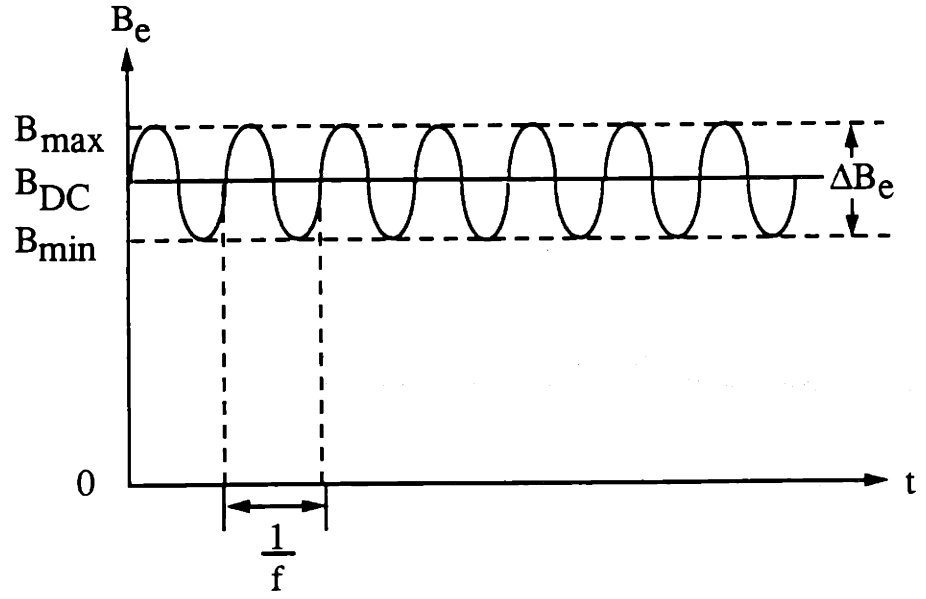

Fig. 5.1 Two types of cyclic background fields applied in the AC-loss measurements.

synchronized AC transport currents in the same cyclic ramp field condition. The most complicated test condition in the laboratory-scale experiment is then a single-strand carrying a transport current in-phase with a large cyclic background ramp field. The DC current and the maximum AC current are varied between 25% and 95% of the critical current value measured at a DC field the same as the peak value of the applied AC field. The DC critical current at 10 μV/m criteria is measured on the same AC-loss test wire during the AC-loss experiment (section IV.4).

Fig. 5.1(b) shows the second field condition. A small ripple field with fixed amplitude and frequency superimposed on various large DC bias fields, is applied to the same wire as tested in the ramp field condition. The peak-to-peak variation of the ripple field is fixed at 0.086 T, and the frequency is set at 7.5 Hz. During the test the DC bias field is varied between 0.5 T and 12 T. No transport current is applied to the test wire for this field condition.

Under ripple field condition, the hysteresis loss of the superconducting wire at a given DC bias field is approximated by the critical state model with $J_c \approx$ constant and a constant effective transverse resistivity. Error in the AC-loss analysis, caused by the uncertainty in the low field critical current density, will be revealed when they are compared with the test results at a low DC bias field.

V.1.2 Specifications of The Test Wires

Three types of wires: a NbTi, an internal-tin, and a modified jelly-roll (MJR) internal-tin wire, with different cross sectional constructions were tested. All three types of strand have been existing and widely applied for a long period. The cross sectional constructions of these three wires have been shown in Fig. 4.6.

Specifications of these wires, mostly given by the manufacturer, are listed in Tables 5.1 to 5.3. The filament diameters were estimated from the microphotographs of the as-received wires (Ref. 5.1). In the case of the Nb_3Sn wires, the physical cross sectional area of the Nb_3Sn filament is about 35% larger than that of the Nb filament after the heat treatment. The volume fractions of the filament and the local Cu to filament ratios in the non-Cu region are also changed.

Table 5.1 Specification of the bare Supercon SSC NbTi wire

Diameter	0.808 mm	Filament alloy	*****
Length	30 m	Filament bundles	1
Twist pitch	≈12.7 mm	NbTi Filament diameter	≈ 6 μm
RRR	≈ 64	Filament number	*****
Chrome plating thickness	none		
Vol % non-Cu	42.2		
Within the filament region:			
Vol % filament	66.67	Vol % Cu	33.33
Local Cu/filament ratio	0.5		

Table 5.2 Specification of the bare ITER-NET IGC 19-subelement wire

Diameter	0.73 mm	Filament alloy	Nb-7.5% Ta
Length	30 m	Filament bundles	19
Twist pitch	≈12.7 mm	Nb Filament diameter	≈ 2.6 μm
RRR	≈ 162 (tested w/ Cr)	Filament number	4902
Chrome plating thickness	none		
Diffusion barrier	Ta /filament zone		
Diffusion barrier thickness	*****		
Vol % non-Cu	40		
Within the non-Cu region (before heat treatment):			
Vol % filament	21	Vol % Cu	*****
Vol % tin	*****	Vol % Ta	7.5
Local Cu/filament ratio	1		

Table 5.3 Specification of the chrome-plated TWCA US-DPC wire

Diameter	0.78 mm	Filament alloy	Ti
Length	30 m	Filament bundles	18
Twist pitch	≈12.7 mm	Nb Filament diameter	≈ 3 μm
RRR	≈ 22	Filament number	*****
Chrome plating thickness	≈ 1 - 2 μm		
Diffusion barrier	V / bundle		
Diffusion barrier thickness	≈2 μm		
Vol % non-Cu	46		
Within the non-Cu region (before heat treatment):			
Vol % filament	22.9	Vol % Cu	48.8
Vol % tin	15.8	Vol % V	12.6
Local Cu/filament ratio	1.69		

In order to calculate the coupling loss of a composite wire with multi-layer construction as described in section II.3.3, more detailed cross-sectional configurations (see Fig. 2.10) of these three types of wire, either estimated from the microphotographs or obtained from

private communications with the manufacturers, are listed in Table 5.4. Some data which may have been listed in the former tables are restated here for self-sufficiency.

Table 5.4 Detail cross sectional construction of the test wires (Fig. 2.10)¶

Parameter	NbTi SSC wire	Nb_3Sn internal-tin ITER-NET wire	Nb_3Sn MJR US-DPC wire
Outer radius of center core, r_{MFi}	1.12×10^{-4}	0.	0.65×10^{-4}
Outer radius of MF zone, r_{MFo}	3.24×10^{-4}	1.95×10^{-4}	3.24×10^{-4}
Outer radius of inner layer, r_1	---	2.05×10^{-4}	---
Outer radius of middle layer, r_2	---	2.25×10^{-4}	---
Outer radius of wire, r_3	4.04×10^{-4}	3.65×10^{-4}	3.9×10^{-4}
Physical radius of filament, r_f	3.0×10^{-6}	1.3×10^{-6}	$\sim 1.2 \times 10^{-6}$
Resistivity of central core†, ρ_i	2.0 / ~40. / 4.8	2.0 / 162. / 4.8	2.0 / 22. / 4.8
Effective transverse resistivity of the matrix in the MF zone†, ρ_t	8.0 / ~40. / 19.2	3.35 / 1.5 / 0.	1.56 / 1.0 / 0.
Resistivity of inner layer†, ρ_1	---	6.0 / 1.5 / 0.	---
Resistivity of middle layer†, ρ_2	---	34.0 / 1.0 / 0.	---
Resistivity of outer layer†, ρ_3	2.0 / ~40. / 4.8	2.0 / 162. / 4.8	2.0 / 22. / 4.8
SC volume fraction, $f_{SC\ in\ wire}$‡	0.422	0.1134	0.142
SC volume fraction, $f_{SC\ in\ MF}$‡	0.667	0.28	0.309

¶ units: r in (m), ρ in (Ω-m).

† a / b / c : for an altered expression of Eq. (2.47) written as

$$\rho(4.2\ K, B_e) = (a \times 10^{-8}) / b + (c \times 10^{-11}) \times B_e,$$

where $a = \rho(B_e = 0, 300\ K) / 10^{-8}$ (Ω-m), b = RRR, $c = \beta_M / 10^{-11}$ (Ω-m/T).

‡ $f_{SC\ in\ wire} = f_{nonCu}\, f_{SC\ in\ nonCu}\, (1 + f_{HT})$ for Nb_3Sn composite;
$f_{SC\ in\ MF} = f_{SC\ in\ nonCu}\, (1 + f_{HT})$ for Nb_3Sn composite.

The outer radius of the outer-most layer is the same as the outer radius of the wire for all three test wires. In the case of internal-tin wire, the Ta tin-diffusion barrier is considered as the middle layer in the model, and the bronze region between the diffusion barrier and the multifilamentary region is taken as the inner layer. The data for resistivities in different regions are either measured or extracted from Tables 2.1 and 2.2. The NbTi and internal-tin wires have a relatively homogeneous resistivity distribution in the multifilamentary region compared with that of a MJR wire. In the case of MJR wire, the effective transverse resistivity in the multifilamentary zone is homogenized over all the bronze regions in the filament bundles and the copper region among the bundles. AC loss in the thin diffusion barriers is neglected.

V.2 CRITICAL CURRENT MEASUREMENT

DC critical currents of the AC-loss test wire were measured with transport current method before performing the AC-loss measurements of a current-carrying wire. The voltage was taken from the middle 3 turns on the outer coil winding which were aligned to the mid-plane of the background magnet. The inductive voltage due to the background field was cancelled by the voltage from a 3-turn pickup coil wound along the above mentioned 3 turns of the test coil. The 10 μV/m criteria was applied to the critical current measurement. Regular examination of the critical currents was also performed to ensure no serious degradation of the AC-loss test wire.

The transport current method examines the critical current at any cross section along the conductor between the voltage taps. The critical current is constrained by the worst part of the conductor. The experimental results and the best-fit semi-empirical critical current formula are shown in Figs. 5.2 to 5.4.

As shown in Fig. 5.2, the critical current profile of the NbTi wire has a linear relationship with the background field. The trend is consistent with the analytical critical current density model for an optimized NbTi conductor as reviewed in Section III.2.3.2. However, the measured critical current seems to rise faster than the linear relationship in the field range of less than ~ 3 T. The critical current at a field less than 3 T was not measured due to the limitation of the current power supply.

The critical current profile of the internal-tin AC-loss test wire was measured in the field range between 7 T and 12 T before it was damaged by wire movement due to the Lorentz force. The experimental results obtained in the present work along with the measurements performed on a similar wire by Suenaga (Ref. 5.2) are shown in Fig. 5.3. The critical currents measured in the present work are consistently 15% lower than those by Suenaga in the overlapping region. The cause of the discrepancy is not clear. In the present work, the voltage taps for measuring the voltage rise due to the critical current were soldered to include three turns of the outer windings near the mid-plane of the mandrel where degradation of the wire property caused by local stress concentration is not likely to occur. In contrast to the stainless steel barrel sample holder used by Suenaga, the MACOR sample holder applied in this work has a similar coefficient of thermal expansion as that of Nb_3Sn. As discussed in Chapter II, the length of the internal-tin wire reduces by about 0.4% after the heat treatment due to the stress relief of the matrix material. The sample holder tends to

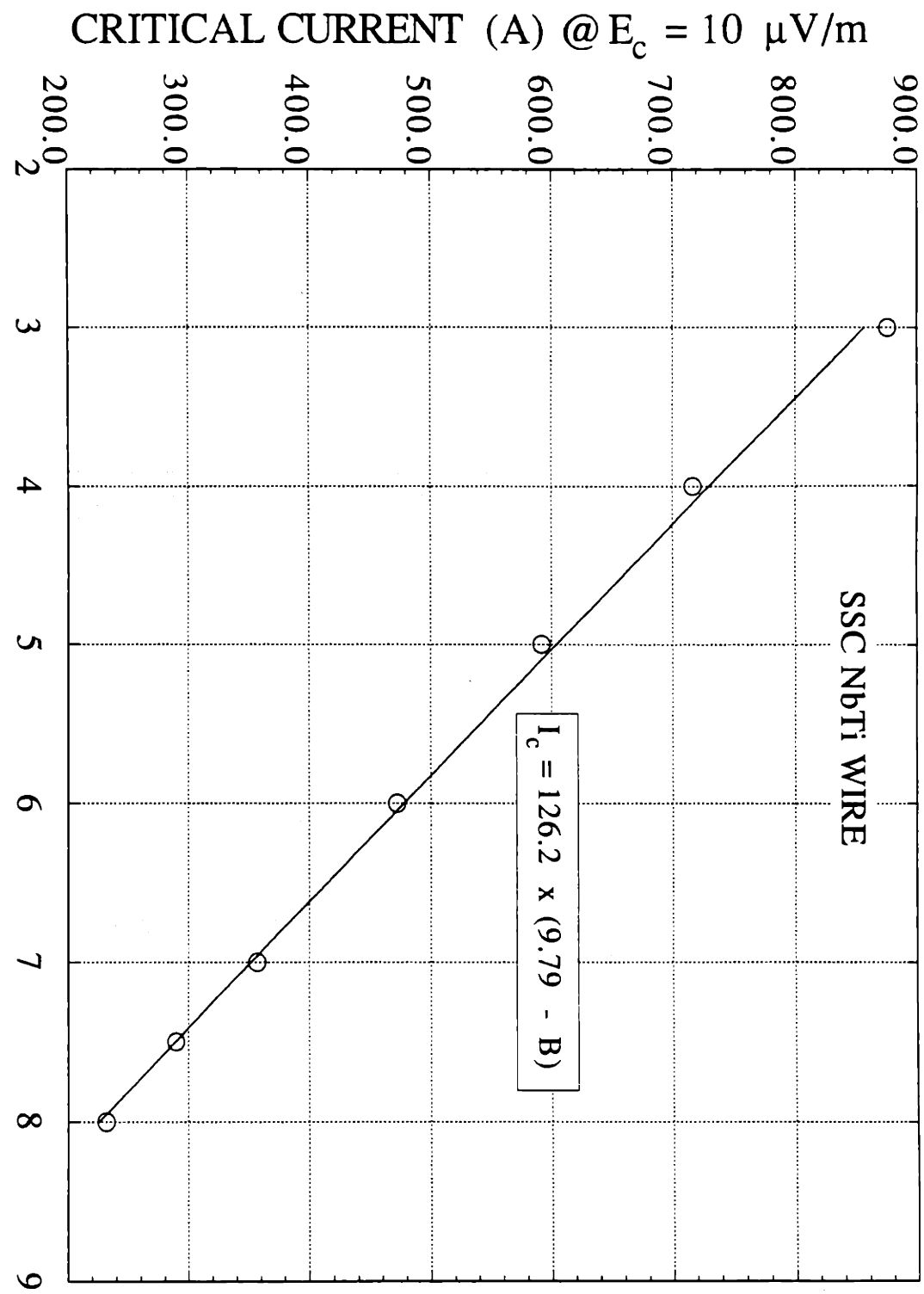

Fig. 5.2 Critical current profile of the SSC NbTi wire manufactured by Supercon.

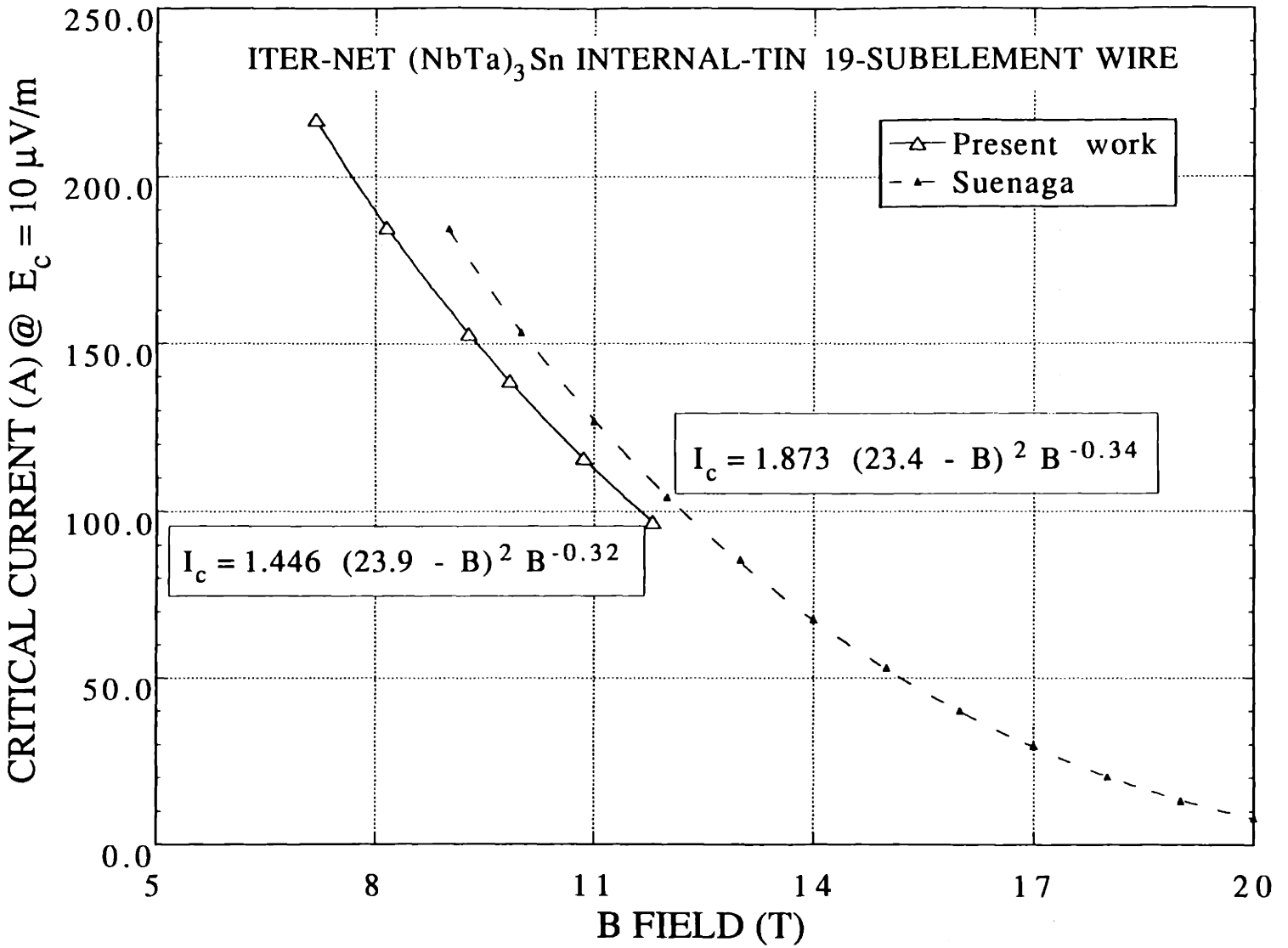

Fig. 5.3 Critical current profile of the ITER-NET $(NbTa)_3Sn$ internal-tin 19-subelement wire manufactured by IGC.

against the length reduction on the outer windings, which relatively reduces the compressive stress placed on the filaments by the matrix material. A composite wire with less compressive stress is expected to have a higher critical current. Therefore, the thermal compatibility between the mandrel and the test wire should not be the source causing a lower critical current. As reported by the manufacturer (Ref. 5.3), inconsistent critical currents have been measured in different segments of a same wire. The discrepancy shown in Fig. 5.3 is possibly caused by either partial filament breakage or non-uniform filament cross section (sausaging) along the length of the wire during the manufacturing process.

Fig. 5.4 shows the comparison of critical current profiles of two US-DPC MJR wires, CRe1116a and Cre1084, with the averaged profile. The averaged critical current profile is the test result of 14 randomly-selected US-DPC MJR wires measured by Takayasu, et al. (Ref. 5.4) The previous tests were performed with the apparatus designed specifically for critical current measurement. The wires were tested in a background field generated by a low-noise DC superconducting magnet. The averaged experimental critical current profile is considered to be highly reliable. The critical currents measured in the present work from the AC-loss test wires wound on the MACOR sample holder have good agreement with the averaged profile in the field range between 3 T and 12 T. The discrepancy is less than 5%.

Table 5.5 summarizes the best-fitted constants C_{SC}^*, B_{c2}^*, p, and q applied to the Eqs. (3.2c) and (3.6b) for the superconductor filament region in these three wires, which will be applied in the loss calculations.

Table 5.5 Parameters of critical current density profiles for AC-loss test wires

Parameter	NbTi SSC wire	Nb_3Sn internal-tin ITER-NET wire	Nb_3Sn MJR US-DPC wire
C_{SC}^* (A / m^2-SC / T^{p+q-1})	5.83 x 10^8	2.408 x 10^7	4.845 x 10^7
B_{c2}^* (T)	9.79	22.14	22.135
p	1	0.5	0.5
q	1	1.5	2

V.3 CONSTITUENT AC LOSSES

As described in Section II.4.2, the importance of the field screening in a composite wire caused by the coupling current depends on the ratio of $\tau_w \dot{B}_e$ and the penetration field of the multifilamentary zone of the composite wire, $B_{p,MF}$. When the field changing rate is

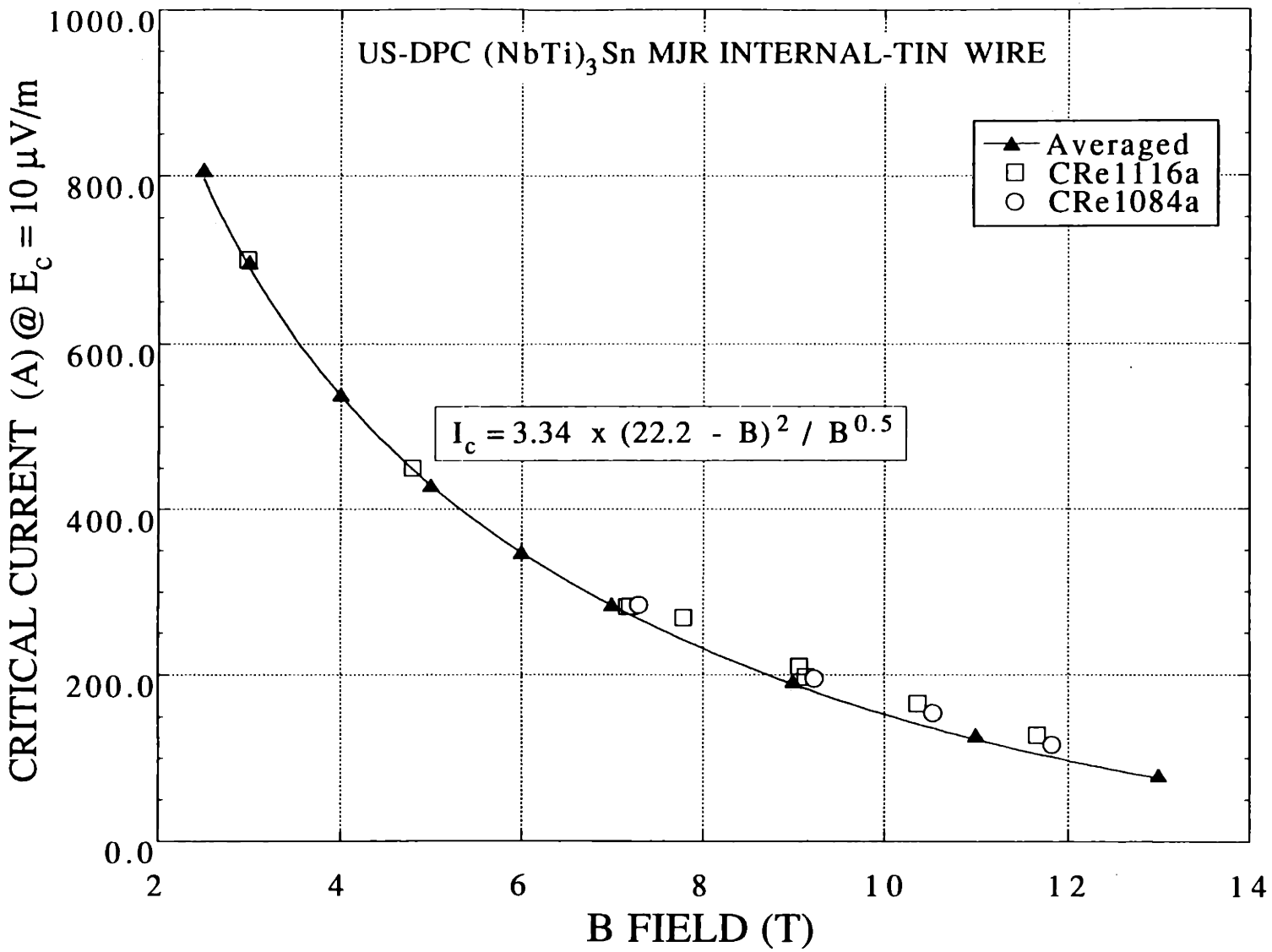

Fig. 5.4 Critical current profile of the US-DPC $(NbTi)_3Sn$ internal-tin modified jelly-roll (MJR) wire manufactured by TWCA.

relatively slow, the field screening can be neglected. The total AC loss is calculated as the linear sum of the filament hysteresis loss, the coupling loss, and the additional loss due to the transport current if it is applied. Before the model calculation of the AC losses for the test wires, it is important to find out whether the simple linear summation of different losses is applicable in the applied external field conditions.

Table 5.6 $\max\{\tau_w\}$ and $\min\{B_{p,MF}\}$ of test wires

Wire	$\max\{\tau_w\}$ (s)	$\min\{B_{p,MF}\}$ (T)
NbTi SSC wire	0.001	0.89 @ 8 T
Nb_3Sn internal-tin ITER-NET wire	0.0003	0.21 @ 12 T
Nb_3Sn MJR US-DPC wire	0.0008	0.57 @ 12 T

In order to cover the overall test range, the comparison between $\tau_w\dot{B}_e$ and $B_{p,MF}$ will be made by using the $\max\{\tau_w\} \times \max\{\dot{B}_e\}$ and the $\min\{B_{p,MF}\}$ for both ramp field and ripple field tests. If the $\max\{\tau_w\} \times \max\{\dot{B}_e\}$ remains much smaller than the $\min\{B_{p,MF}\}$, linear summation for the total loss can be used as a good estimation. If this is not the case, much more complicated non-linear analysis will be needed.

As seen in Table 5.6, for each of the test wire, the calculated $\max\{\tau_w\}$ is 1 ms or less, and the $\min\{B_{p,MF}\}$ is greater than 0.2 T. With the $\max\{\dot{B}_e\} \leq 1.5$ T/s for the background magnetic field, the $\max\{\tau_w\} \times \max\{\dot{B}_e\}$ is about two order of magnitude less than the $\min\{B_{p,MF}\}$. Therefore, for all the field conditions and in all the test wires, the field screening can be neglected, and the total loss is simply the linear sum of all the constituent losses.

V.4 AC LOSSES: TEST RESULTS AND COMPARISONS

All the experimentally measured AC losses are shown in this section. Based on the availability of the test wires, more test results of the US-DPC MJR wires will be found. The AC losses in the ramp field tests without transport current are shown in Figs. 5.6 to 5.13. In the ramp field condition, additional losses due to the transport currents are plotted in Figs. 5.14 to 5.23. Losses in the ripple field tests are plotted in Figs. 5.24 to 5.26 for different types of test wires.

Because of the use of the constant flow-rate feedback control system (Chapter IV), the heater power was continuously adjusted all the time by the flow-rate signal. The flow-rate signal which is sensitive to the perturbation of the liquid helium bath, fluctuated at a small amplitude with respect to the preset reference value. When the recording time was set to a limited number of field cycles, the heater power averaged over the recording time may deviate by a small amount from the preset value. Fig. 5.5 shows the fluctuation of the heater power. The root-mean-squared deviation is estimated as 1.63 mW which is considered as the range of the experimental error for the experiment results.

The analytical results are plotted in all the figures containing the test results. The purpose of the comparison is to identity whether the AC-loss mechanisms of different wires can be properly described by the existing loss models. Analytical parametric study is not the purpose of this research. Therefore, in some model calculations, adjustment to some of the applied parameters such as the lower field critical current density, the effective filament diameter, the effective transverse resistivity, etc. could result in a better fit to the experimental result, is not performed. Instead of using physical filament size, the effective filament size extracted from the experimental result will be used to calculate a more realistic hysteresis loss. The analysis is started with estimating the effective filament diameter from the extrapolated hysteresis loss of each conductor.

To verify the present experimental system, some of the extrapolated hysteresis loss are compared with the test results obtained by another author independently (Ref. 5.5). Due to the uniqueness of the present test conditions, the experimental results available for comparison are limited to those in slowly ramped field. At higher time-rate of field variation, the comparisons can only be made between the test results and the analytical results.

V.4.1 Ramp Field Test Without Transport Current

V.4.1.1 Benchmark Comparison of Experimental Hysteresis Losses

In order to verify the present experimental system, it is important to compare the test results measured in this work with those using different method. Since only the calorimetric method has been developed to measure the AC losses in the present work, experimental data for similar conductors measured by the magnetization method were provided by Goldfarb (Ref. 5.5) at the National Institute of Science and Technology

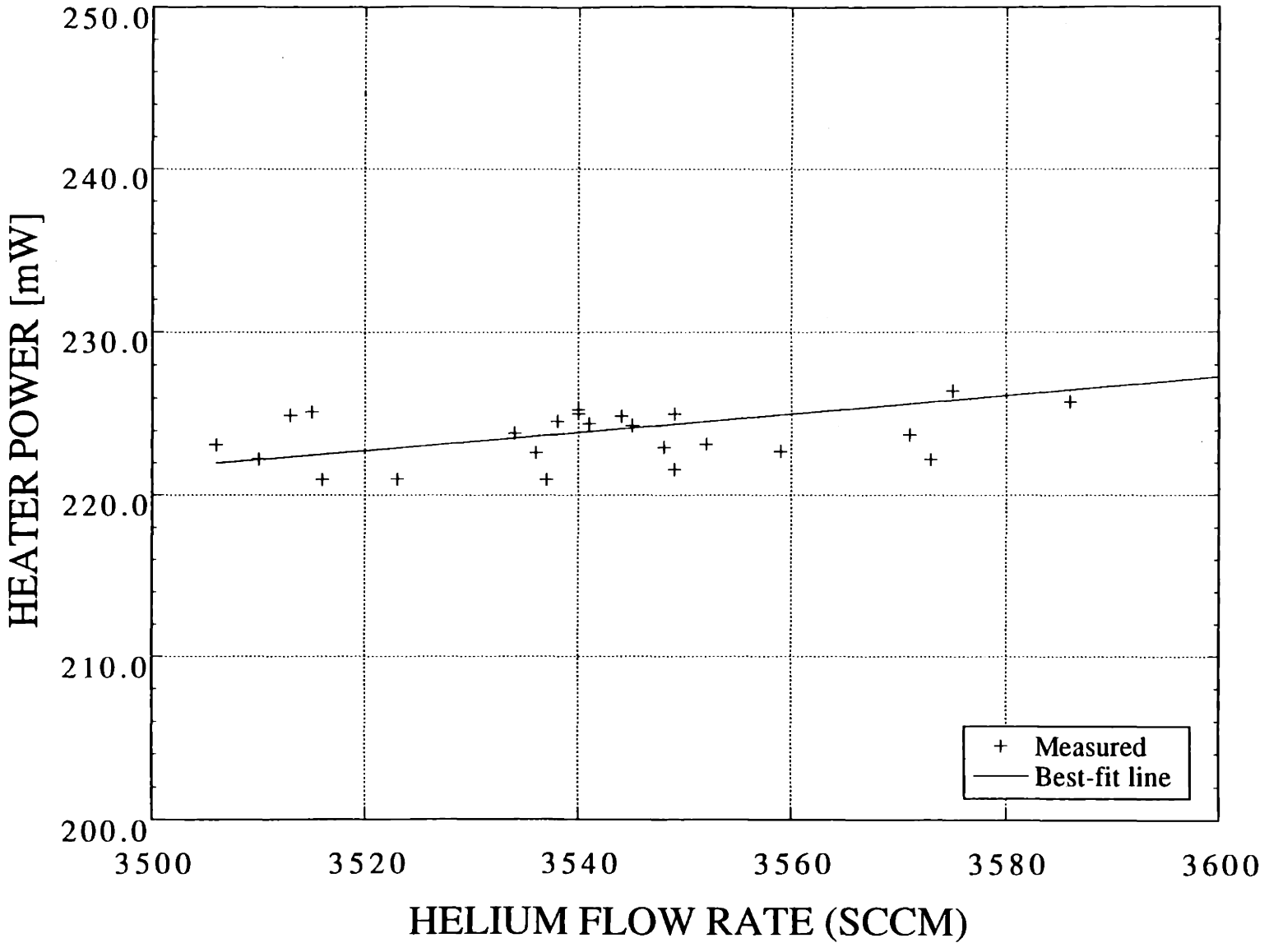

Fig. 5.5 Fluctuation of the heater power. The averaged error is estimated as 1.63 mW.

(NIST) and by the TWCA (Ref. 5.6). However, only the hysteresis losses at very slow field variation are available for comparison. The original AC-loss data obtained from the magnetization method were measured in a full cycle field variation between +3 T and -3 T. By comparing the magnetization areas enclosed by the full and half cycle field variations, the loss in the 0 - 3 T - 0 field variation applied in the calorimetric measurement is estimated to be 42.6% of the full cycle loss. The hysteresis losses of three US-DPC MJR wires measured with different methods are listed in Table 5.7. The magnetization data listed in the table have been converted into half cycle loss for purpose of comparison.

Table 5.7 Comparison of hysteresis losses of the MJR wires measured by different experimental methods

Wire	Magnetization Method (mJ/cm^3-wire/cycle)	Calorimetric Method (mJ/cm^3-wire/cycle)
CRe1076AB	80.9	~ 83
CRe1106B2A	98	~ 100
CRe1116A	89.5	~ 89

The hysteresis losses in all three conductors are in reasonably good agreement. Since the hysteresis loss using the calorimetric method is obtained by extrapolating the total loss to the region of slow time-rate of field change, the experimental error is about ±15%.

V.4.1.2. Effective Filament Diameter

As described in Chapter IV, the effective filament size is obtained from the measured hysteresis loss. Since the calorimetric method measures the total AC losses of the test wire averaged over one cycle of field variation, the hysteresis loss is approximated by extrapolating the total loss profile to zero ramp rate at a given range of field variation. Using the semi-empirical field-dependent critical current density formula, the effective filament diameter is then evaluated with Eq. (3.35).

Fig. 5.6 shows the loss distributions of all three types of test wires as a function of the field ramp rate at large ranges of field variation, 9 T for Nb_3Sn and 7.5 T for NbTi composites. The extrapolated hysteresis losses, the effective filament diameter, and the physical filament diameter for each type of the wire are listed in Table 5.8. The reason for extrapolating the loss profile with a large field variation is to reduce the error in estimating the effective filament diameter caused by the extrapolated lower field critical current. As

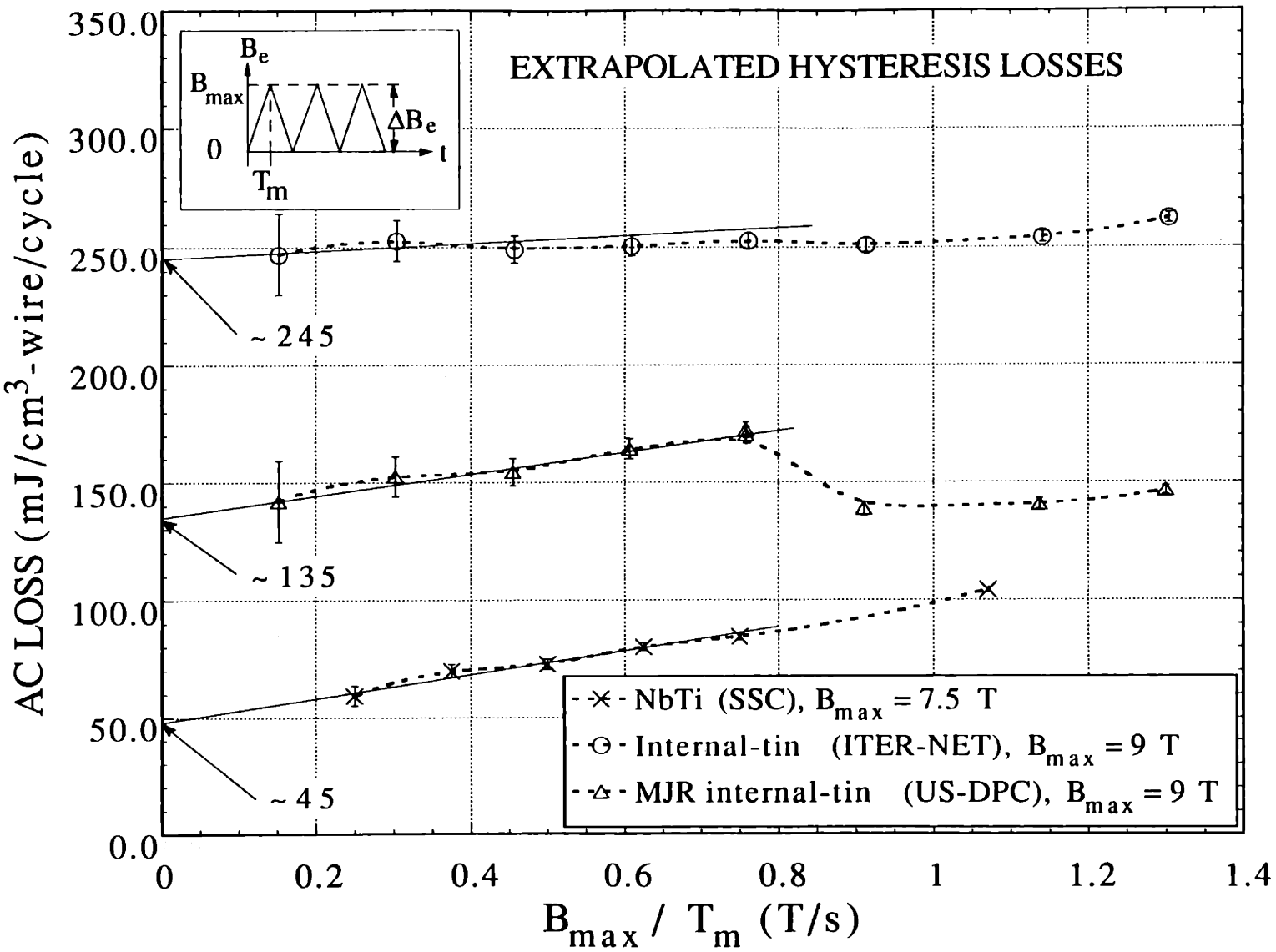

Fig. 5.6 Hysteresis losses extrapolated from the ramp field test for all three types of samples.

described in Chapter III, filament bridging and proximity effect are the possible reasons of the large effective filament sizes for the Nb_3Sn and NbTi composite wires, respectively.

Table 5.8 Extrapolated hysteresis loss, effective and physical filament sizes

Wire	Hysteresis Loss (mJ/cm^3-Wire/cycle)	Effective Filament Diameter (μm)	Physical Filament Diameter (μm)
NbTi SSC wire	~ 45	~ 14	6
Nb_3Sn internal-tin ITER-NET wire	~ 245	~ 23	~ 3*
Nb_3Sn MJR US-DPC wire†	~ 135	~ 19	~ 5*

* When forming the Nb_3Sn, the growth of the Nb filament by ~ 35% of volume fraction has been accounted. † From a single wire CRe1084 with B_{max} = 9 T.

Three Nb_3Sn MJR wires, with similar construction but drawn from different billets, were tested in ramp field condition at different ranges of field variation. All the test results are plotted against the ramp rate as shown in Fig. 5.7. The averaged extrapolated hysteresis losses are approximately 85, 100, 120, and 135 mJ/cm^3-wire/cycle at the ranges of field variation of 3, 4.5, 7, and 9 T, respectively. As seen in Fig. 5.8, the analytical hysteresis-loss distribution has the best-fit to the experimental results between 3 T and 9 T if the effective filament diameter of 21.8 μm is chose in the calculation. The d_{eff} = 21.8 μm for the best-fit line is consistent with d_{eff} = 19 μm calculated from the hysteresis loss at B_{max} = 9 T. It is important to notice that the good agreements between the calculated and the measured hysteresis losses are found not only at large but also at small field variations. The consistently good agreement indirectly proves that the semi-empirical field-dependent critical current formula applied in the model calculation for MJR wire has properly predicted the lower field (say < 2.5 T) critical current distribution.

V.4.1.3 Comparison with Analytical Results

V.4.1.3.1 Ramp-rate Dependence

The measured and calculated AC losses plotted against the field changing rates for three types of conductors are shown in Figs. 5.9 to 5.11. As seen in Figs. 5.9 and 5.10, the calculated total AC losses using existing AC-loss model, agree well with the measured results for NbTi and the internal-tin wire. In the NbTi composite wire (Fig. 5.9), the model calculation shows that hysteresis loss is the dominant loss mechanism in the lower ramp rate region. Coupling loss increases monotonically and overrides hysteresis loss at a

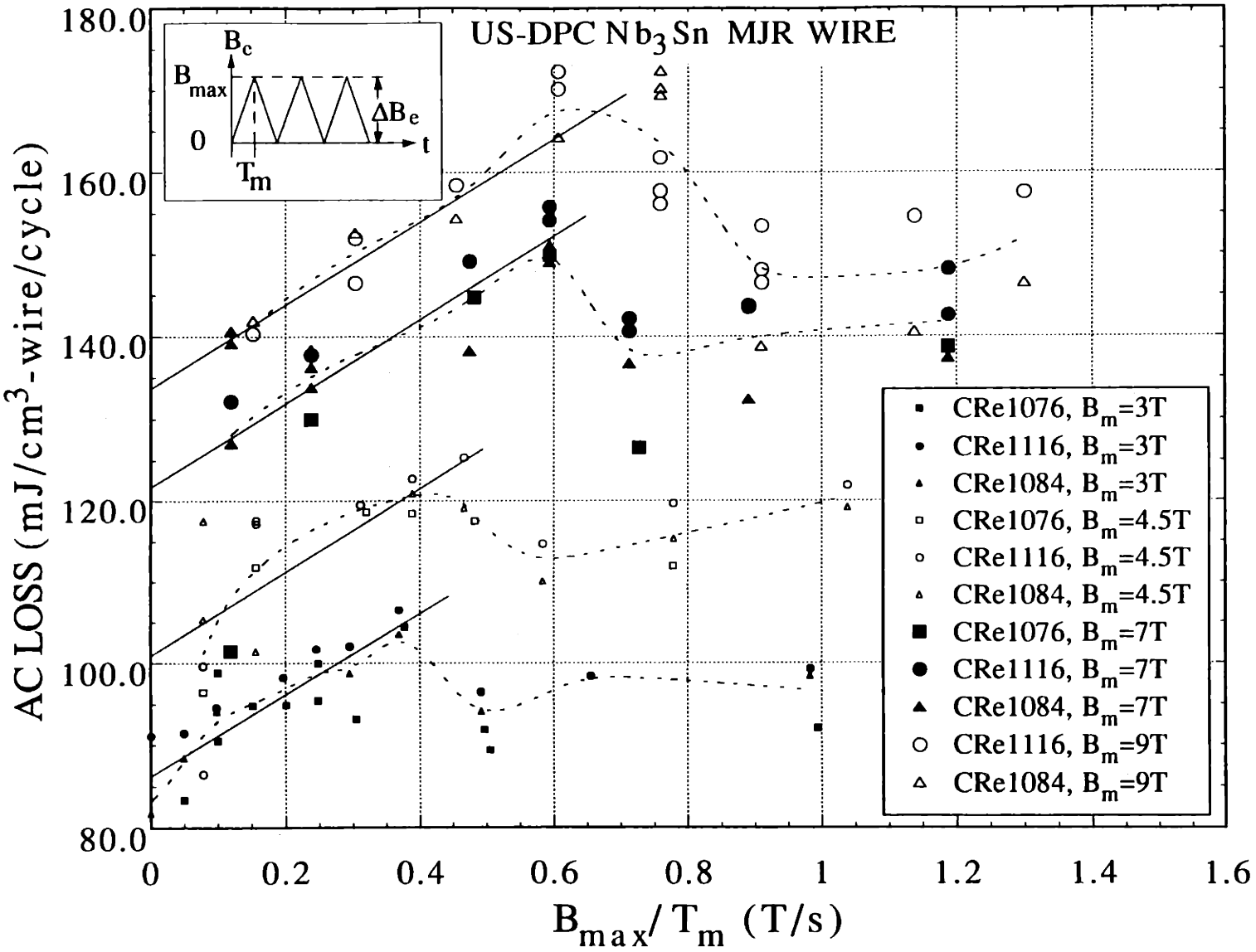

Fig. 5.7 Extrapolated hysteresis losses from different US-DPC MJR wires at various B_{max}.

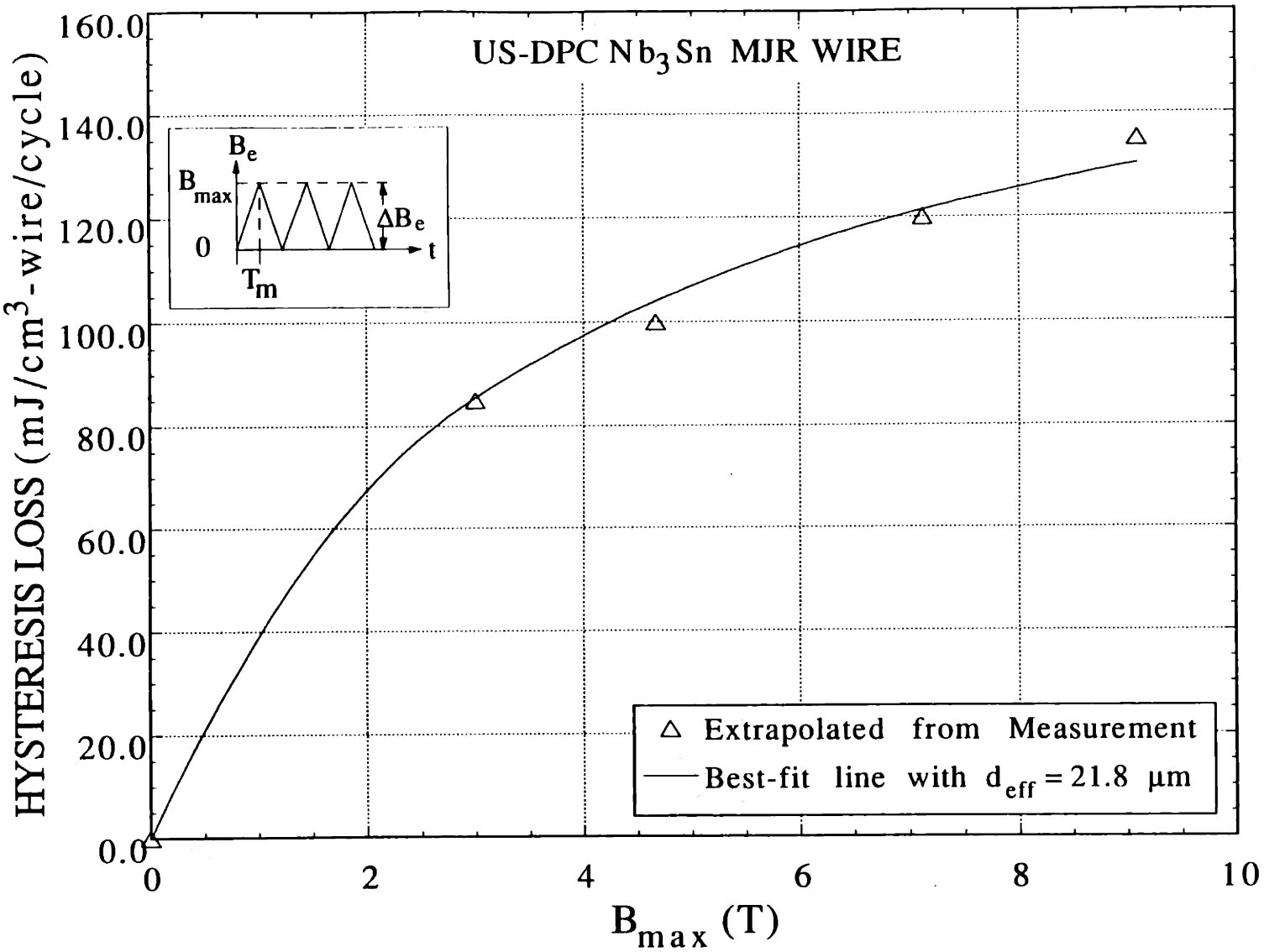

Fig. 5.8 Comparison of extrapolated experimental hysteresis losses with the calculated results for a MJR wire (CRe1084). The best-fit line of the hysteresis loss is obtained by using $d_{eff} = 21.8$ μm.

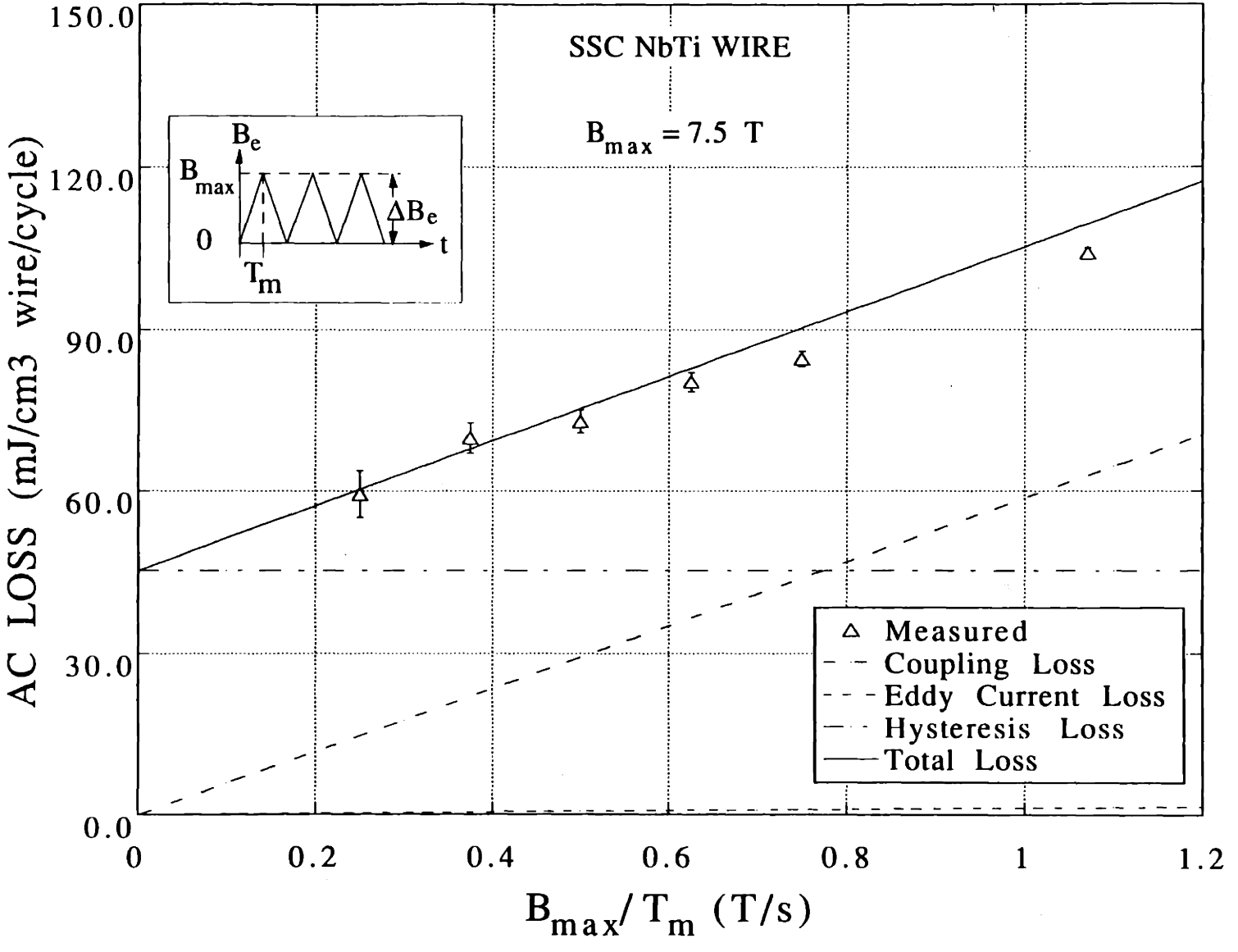

Fig. 5.9 Comparison of measured and calculated AC losses of a NbTi wire as a function of ramp rate in ramp field conditions. The solid lines are calculated results.

ramp rate above about 0.8 T/s. The large coupling loss is caused by the use of pure copper for all the normal material in the central core, the filament zone matrix, and the outer cladding. As compared with the NbTi composite wire, the internal-tin composite wire has a very low coupling loss for all the ramp rates applied in the measurement, which is shown in Fig. 5.10. The reason for the low coupling loss is due to the forming of bronze in the filament zone matrix, which has a resistivity about an order of magnitude higher than the copper. Moreover, between the filament zone and the copper outer cladding, there are bronze and tantalum layers with thicknesses which can not be neglected. Since these boundary layers are more resistive than both the bronze in the filament zone and the copper in the outer cladding, only a small amount of coupling current can flow out of multifilamentary zone and into copper cladding. Therefore, even though the internal-tin wire has a thick copper outer cladding, the coupling loss remains low.

A new AC-loss characteristics in the US-DPC MJR wire was revealed experimentally in the present work. As seen in Fig. 5.11, for each B_{max}, the measured loss profile as a function of the ramp rate has a local maximum at a slow time-rate of field variation. The hump occurs at a higher ramp rate as the range of the field variation increases. As has been discussed in Section V.3, in the field and ramp rate ranges applied in this research, $\tau_w \dot{B}_e << B_{p,MF}$ is true for all the test wires and the field screening due to the saturation layer should not occur. From Chapters II and III, when the field screening effect can be neglected and the given field variation is larger than the penetration field of the superconducting filament, the hysteresis loss should remain a constant, and the coupling loss increases with the ramp rate. The occurrence of the ramp-rate dependent local maximum loss of the MJR wire contradicts the analytical prediction by the existing AC-loss models. Such a phenomenon has never been observed experimentally or discussed analytically for a single-strand.

By using a single value for the field-independent effective filament diameter, the hysteresis loss of the MJR wire as shown in Fig. 5.8 seems to be properly simulated by the existing model. The occurrence of the local maximum loss at such a low ramp rate is likely caused by some new coupling and field screening mechanisms which have not been included in the existing AC-loss models. The shifting of the maximum loss at different B_{max} seems to be dependent on the magnitude of the applied field. A new model developed in this work, which will be discussed in Chapter VI, provides a possible explanation for the occurrence of the local maximum loss at low ramp rate in the MJR wire.

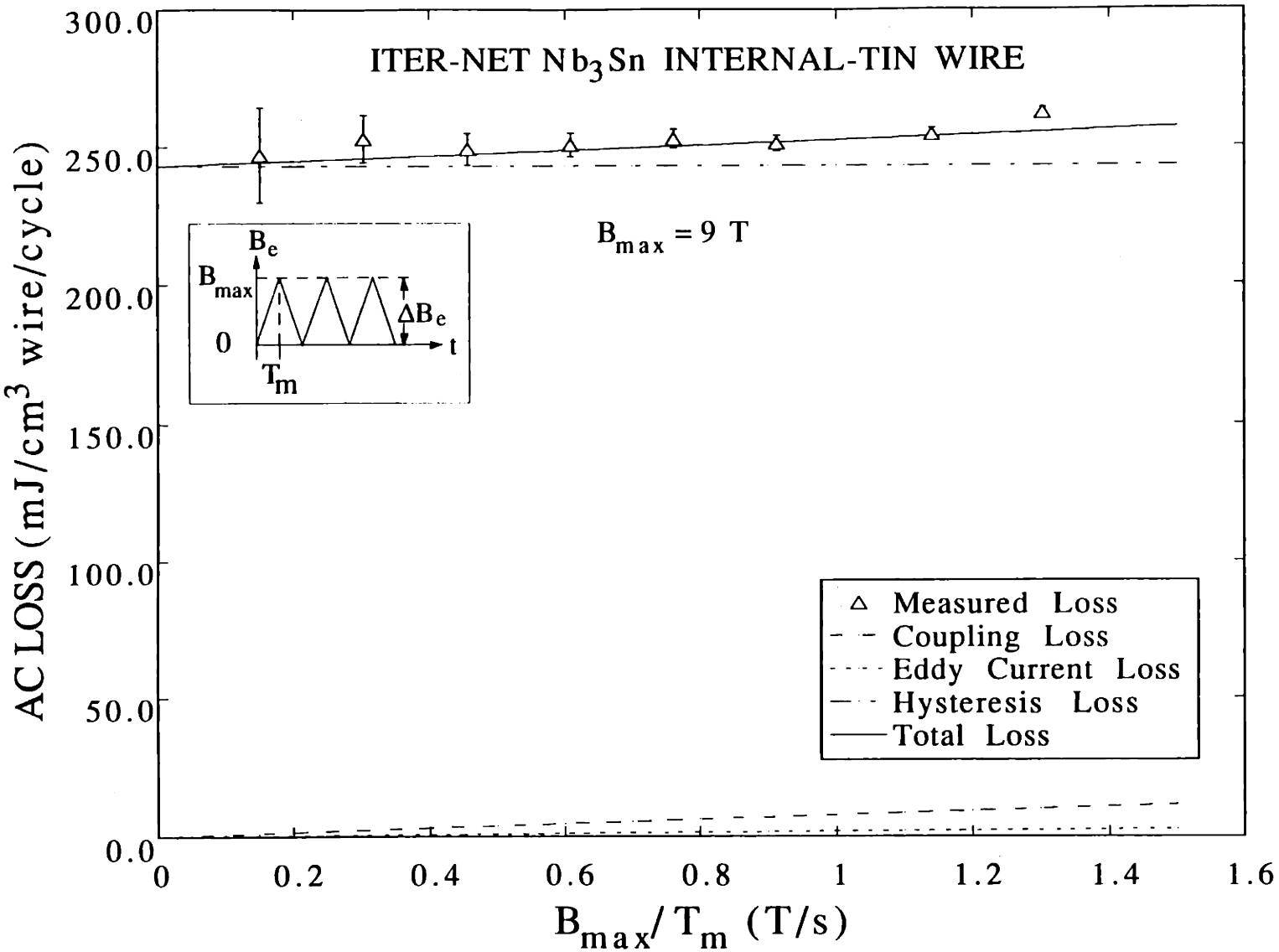

Fig. 5.10 Comparison of measured and calculated AC losses of a Nb_3Sn internal-tin wire as a function of ramp rate in ramp field conditions. The lines are calculated results.

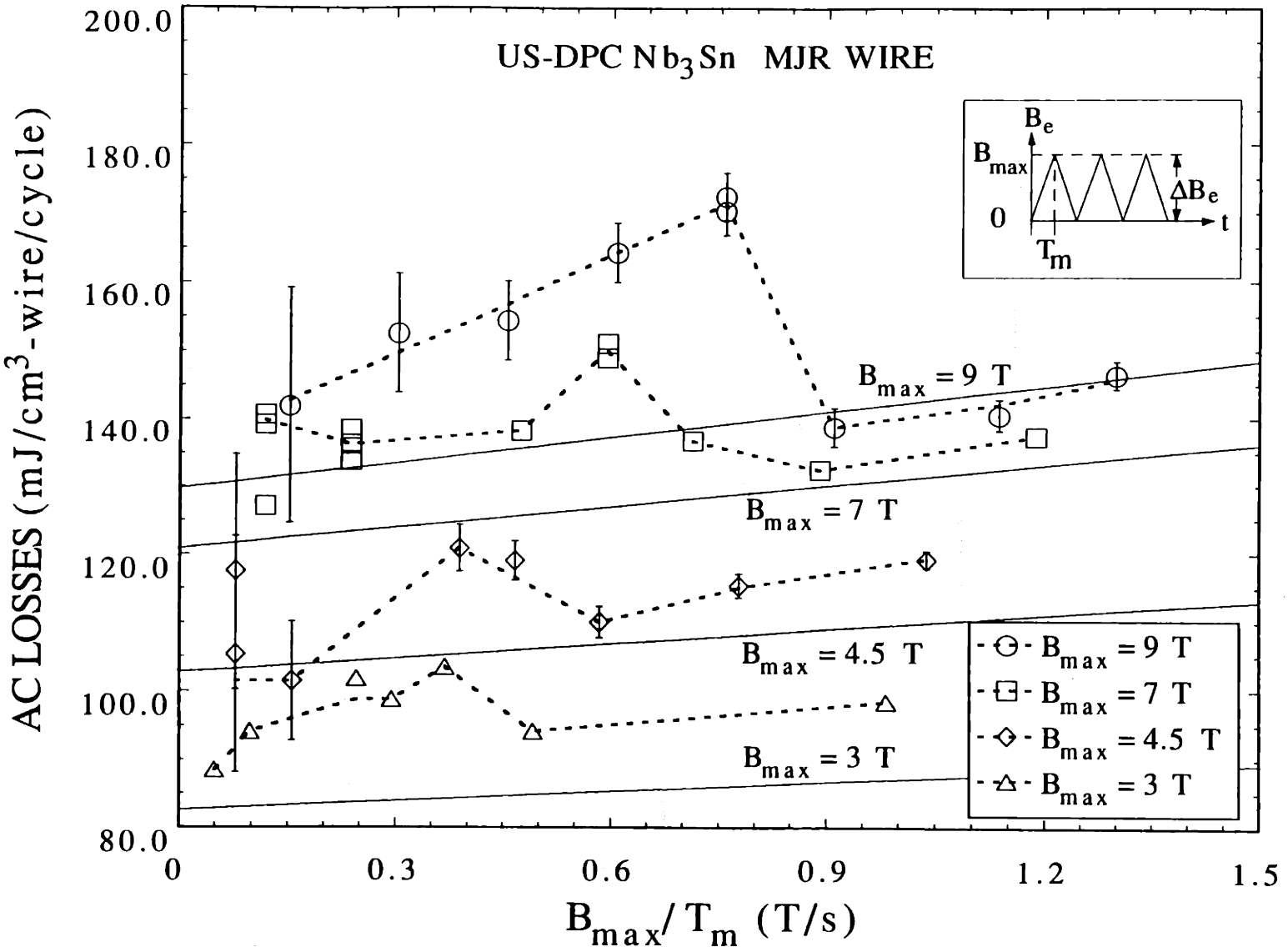

Fig. 5.11 AC losses of a Nb_3Sn MJR wire (CRe1084) in ramp field conditions. Dashed lines show the trends of the test results; solid lines are the calculated results using existing AC-loss models.

V.4.1.3.2 Field Dependence

Measurements of the AC loss as a function of the range of the field variation were performed on the internal-tin and the MJR wires. The test results are shown in Figs. 5.12 to 5.14. The internal-tin wire was tested at a given rise-time of T_m = 12 s. Fig. 5.12 shows that the calculated total losses agree better with the test results at a higher B_{max} and under-estimate the losses by about 30% at B_{max} = 4.5 T. From the model calculations, the major contribution to the total loss of the internal-tin wire in the applied field conditions is the hysteresis loss. With the effective filament size estimated at B_{max} = 9 T in Fig. 5.6, it is not surprising to have a better agreement at a higher B_{max}. As the field variation becomes smaller, the contribution of the lower field critical current density to the hysteresis loss becomes more important. In general, the slope of the critical current profile as a function of the applied field becomes steeper as the applied field is lowered. The lower field critical current is usually under-estimated when it is extrapolated from the high field values (Chapter III). The loss integration of the magnetization loop in the lower field region is consequently under-estimated. This explains why the deviation of the calculated hysteresis loss becomes larger as the B_{max} decreases. As the peak value of the field variation (4.5 T) is below the lowest field (5 T) at which the critical current was measured on this wire, the calculated loss depending on the extrapolated critical current density will be less reliable. The comparison of the loss in the internal-tin wire as a function of B_{max} is an example elucidating the importance of the lower field critical current in the AC-loss calculation.

Measured and calculated AC losses for MJR wire as a function of the maximum field variation are plotted in Fig. 5.13 for different rise-times. At T_m = 60 s, when the hysteresis loss dominates, the calculated total loss has good agreement with the experimental result. Both experimental results at T_m = 10 s and 12 s are higher than the model predictions by about 15%. The experimental results show that the AC losses at T_m = 12 s are consistently higher than those at T_m = 10 s, which is just opposite to the model prediction and has never been found in a conventional composite wire. Also, not predicted by the existing loss models is the saturation of the experimental loss at B_{max} = 9 T when the rise-time was set to 10 s. Since all these discrepancies are ramp-time dependent, they are again likely caused by non-conventional coupling and field screening mechanisms as mentioned in Section V.4.1.3.1.

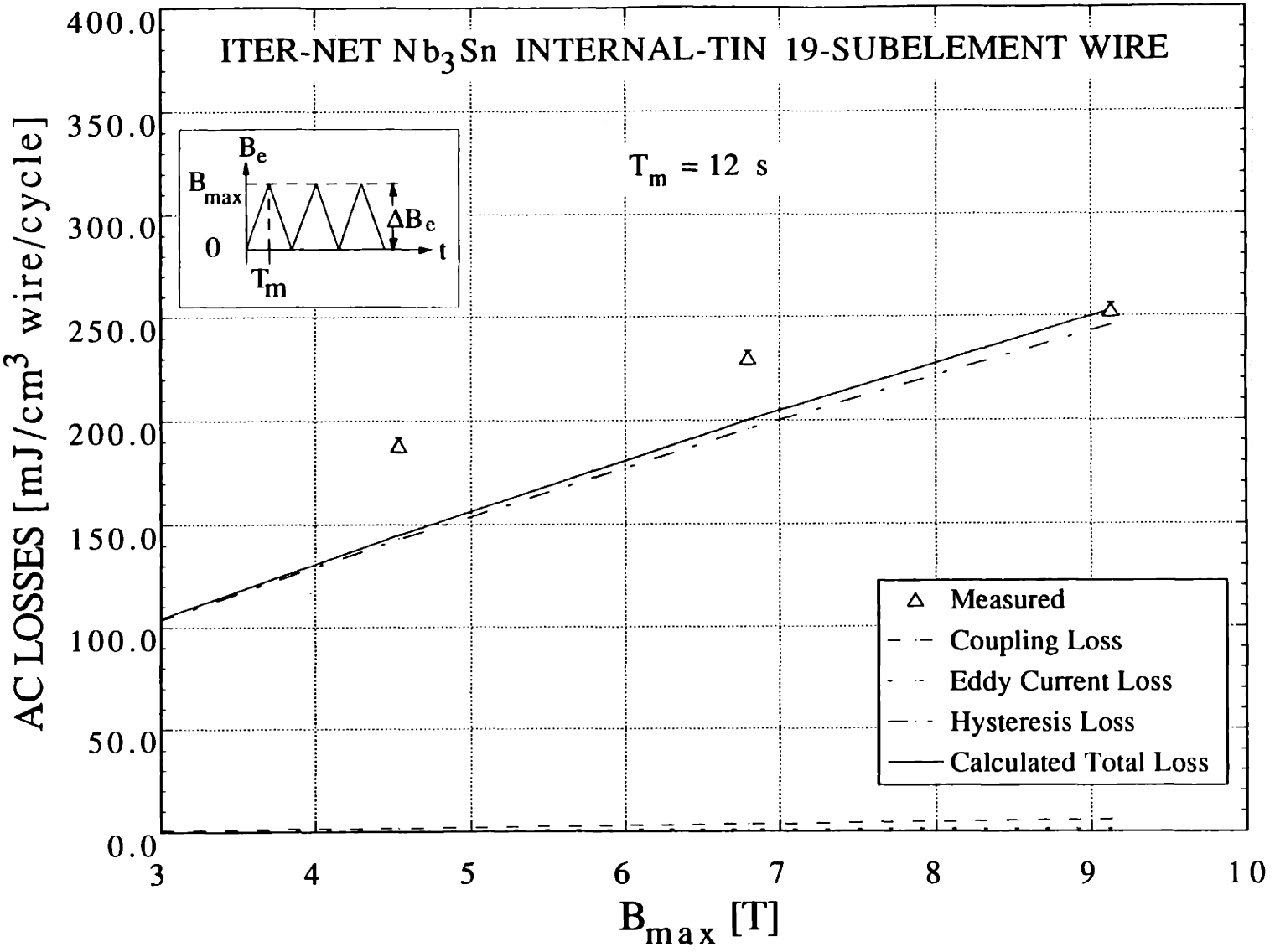

Fig. 5.12 Comparison of measured and calculated AC losses of a Nb_3Sn internal-tin wire as a function of B_{max} in ramp field conditions. The symbols are measured results; the lines are calculated results.

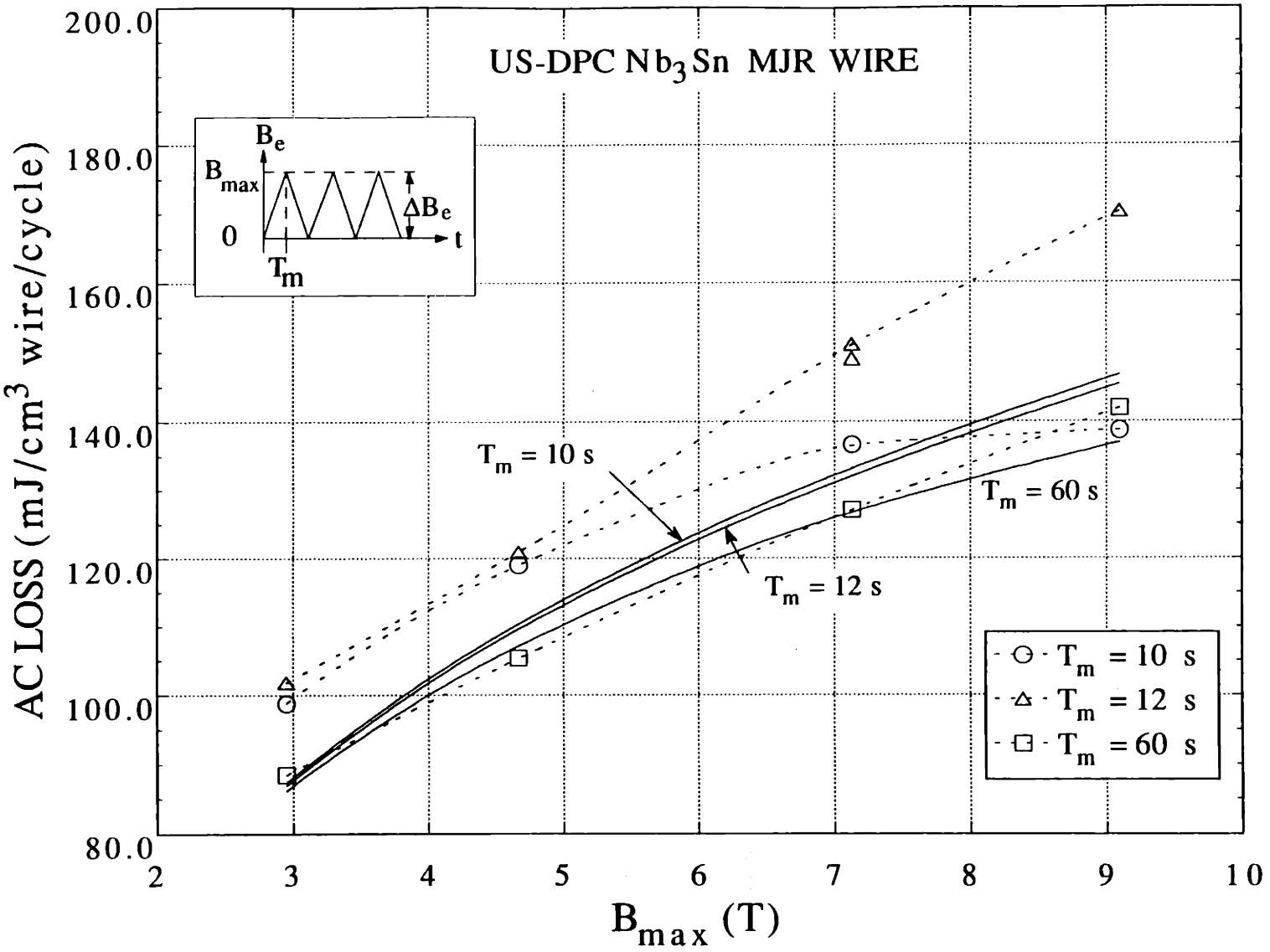

Fig. 5.13 AC losses of a Nb_3Sn MJR sample in a cyclic ramp field as a function of maximum external field. Dashed lines show the trends of the experimental results. Solid lines are calculated results.

V.4.2 Ramp Field Test With Transport Current

Additional losses due to the transport currents were tested under ramp field condition for different wires. At a given rise-time and given range of field variation, the loss profiles were measured as a function of the transport current. When an AC transport current synchronized with the field ramping was applied, the peak transport current $I_{AC,max}$ was used as the variable for the loss profile.

It is clear that existing loss models based on 1-D critical state model is not appropriate to simulate the large field variation conditions applied in the present experiment. However, for comparison purpose, analytical results are still plotted on the same figure with the measured loss profiles as a function of transport current. For the convenience of finding the proportional constant α in Eqs. 2.106 and 2.108, the test results are plotted as $Q(I)/Q(0)$ vs. $(I/I_c)^2$. By definition in existing loss model, I_c is a constant critical current evaluated at $B_{mean} = (B_{max} + B_{min}) / 2$. The α is simply the slope of the profile. The absolute value of the additional loss due to transport current is thus $\alpha\, Q(0)\, (I/I_c)^2$. From existing analysis, $\alpha = 1$ for DC current and $\alpha = 0.33$ for AC current.

The AC-loss profile of a current-carrying wire was also measured as a function of the time-rate of field ramping at a given range of field variation and given DC or synchronized AC transport current. In the existing model, the additional loss due to the transport current is considered as a hysteretic type of loss in a bulk superconductor, and is consequently time-independent.

V.4.2.1 Transport Current Dependence

The NbTi wire carrying transport current was tested with the $B_{max} = 7.5$ T and the $T_m =$ 10 s. The applied DC or maximum AC transport currents were varied between 50% and 95% of the DC critical current at 7.5 T. The later was measured as 290 A at 10 μV/m criteria. In order to compare with existing model, the transport currents are normalized with $I_c(B_{mean})$. As estimated from Fig. 5.2, $I_c(3.75T) \sim 750$ A. The test results plotted in Fig. 5.14 show that the experimental $\alpha \sim 0.33$ for both DC and AC currents.

The additional loss of the current-carrying internal-tin wire at $B_{max} = 9$ T and $T_m = 12$ s was measured with the transport current varied between 50% and 95% of the DC critical current at 9 T which is 253 A at 10 μV/m criteria. The transport currents are normalized

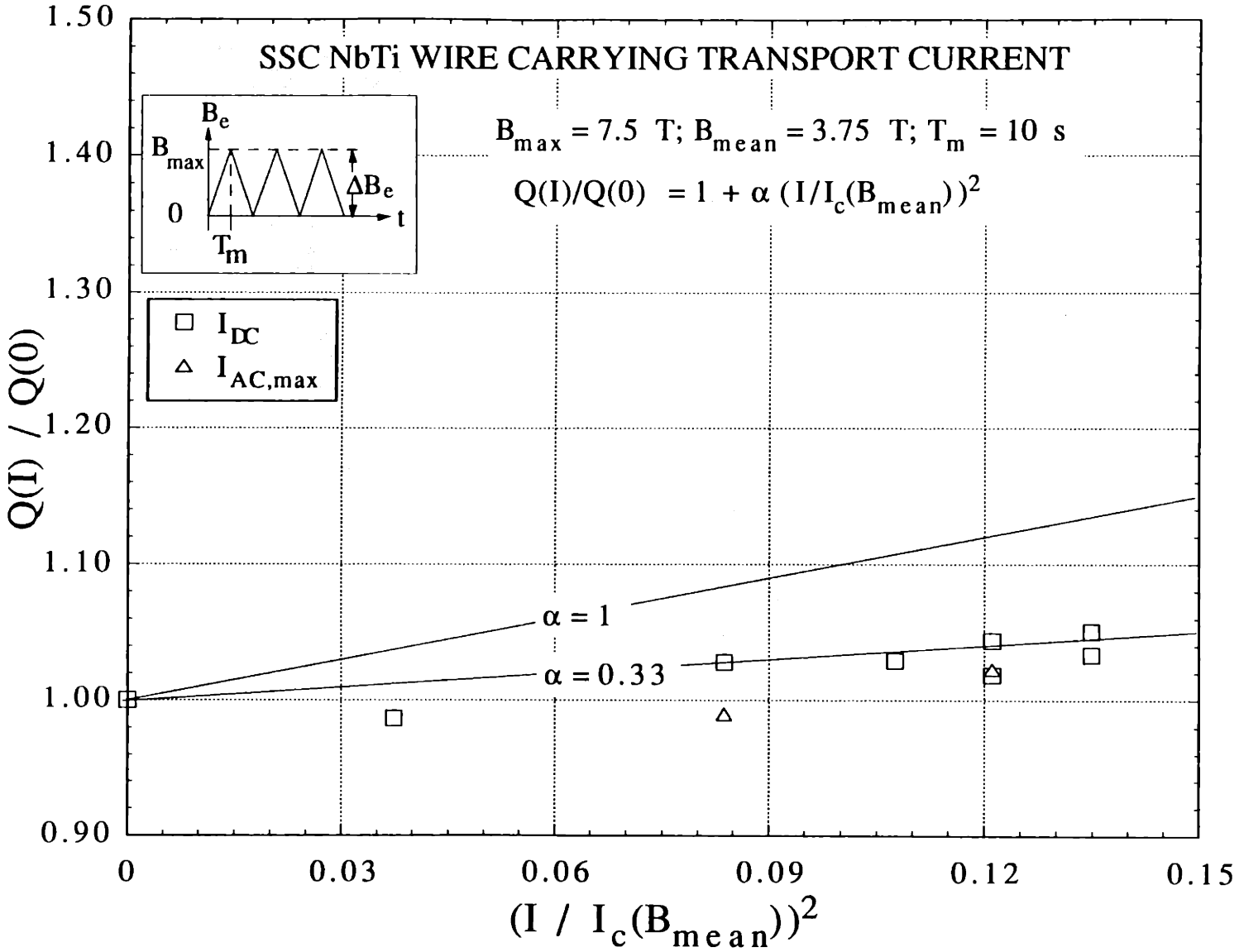

Fig. 5.14 Increment of AC loss as a function of AC or DC transport current for a NbTi wire in a ramp field condition. I_c ~ 750 A (DC) at 3.75 T.

with $I_c(4.5T) \sim 336$ A as estimated from Fig. 5.3. Fig. 5.15 shows that the experimental α value are close to the line of $\alpha = 0.33$ for both DC and AC currents.

The loss profiles of the MJR wire carrying a transport current were performed with $B_{max} = 9$ T and $T_m = 12$ s, 30 s , and 60 s. The transport currents were varied between 25% and 95% of the DC critical current at 9 T which is 196 A at 10 μV/m criteria. Single-point losses with the wire carrying 95% of I_c at 9 T were also measured at $T_m = 7$ s, 15 s, and 20 s. Again, all transport currents are normalized with $I_c(4.5T) \sim 493$ A as estimated from Fig. 5.4. Fig. 5.16 shows that the experimental α values are close to $\alpha = 1$ line wen either DC or AC current is applied under the background field condition of $B_{max} = 9$ T and $T_m = 12$ s. In the case of test wire carrying DC current, as shown in Fig. 5.17, the experimental α values of all the normalized losses are above the line of $\alpha = 1$. As seen in Fig. 5.18, when the conductor carries an AC transport current less than 95% of the DC critical current at 9 T, most of the additional losses have an α value above unity. Exceptions are found when the conductor is carrying a low AC current and varied at a fast rise-time of 10 s.

General conclusions drawn from above test results are: (1) existing AC-loss analysis for additional loss caused by transport currents can not be applied to the large-amplitude ramp field conditions, and (2) the additional losses of a composite superconductor carrying a DC or an AC current are about the same when $I_{DC} = I_{AC,max}$ and the field changing rate is not nearly static. The first conclusion is expected. The second conclusion can not be explained by existing loss model even when a field-dependent critical current is applied to re-derive the model. The AC-loss mechanism of a composite superconductor carrying large transport current in a large cyclic field must be re-examined.

V.4.2.2 Ramp-rate Dependent

The absolute and the normalized AC losses of all three types of conductors as a function of the field ramp rate are plotted in Figs 5.19 to 5.24. The dimensionless loss in the current-carrying strand at a given B_{max} and B_{max}/T_m is normalized by the current-free loss at the same background field condition.

The NbTi wire was tested with $B_{max} = 7.5$ T and I_{DC} or $I_{AC,max}$ set to 90% of the DC critical current at 7.5 T. As seen in Fig. 5.19, the largest difference between the loss in the NbTi wire carrying DC transport current and that in current-free condition is found at

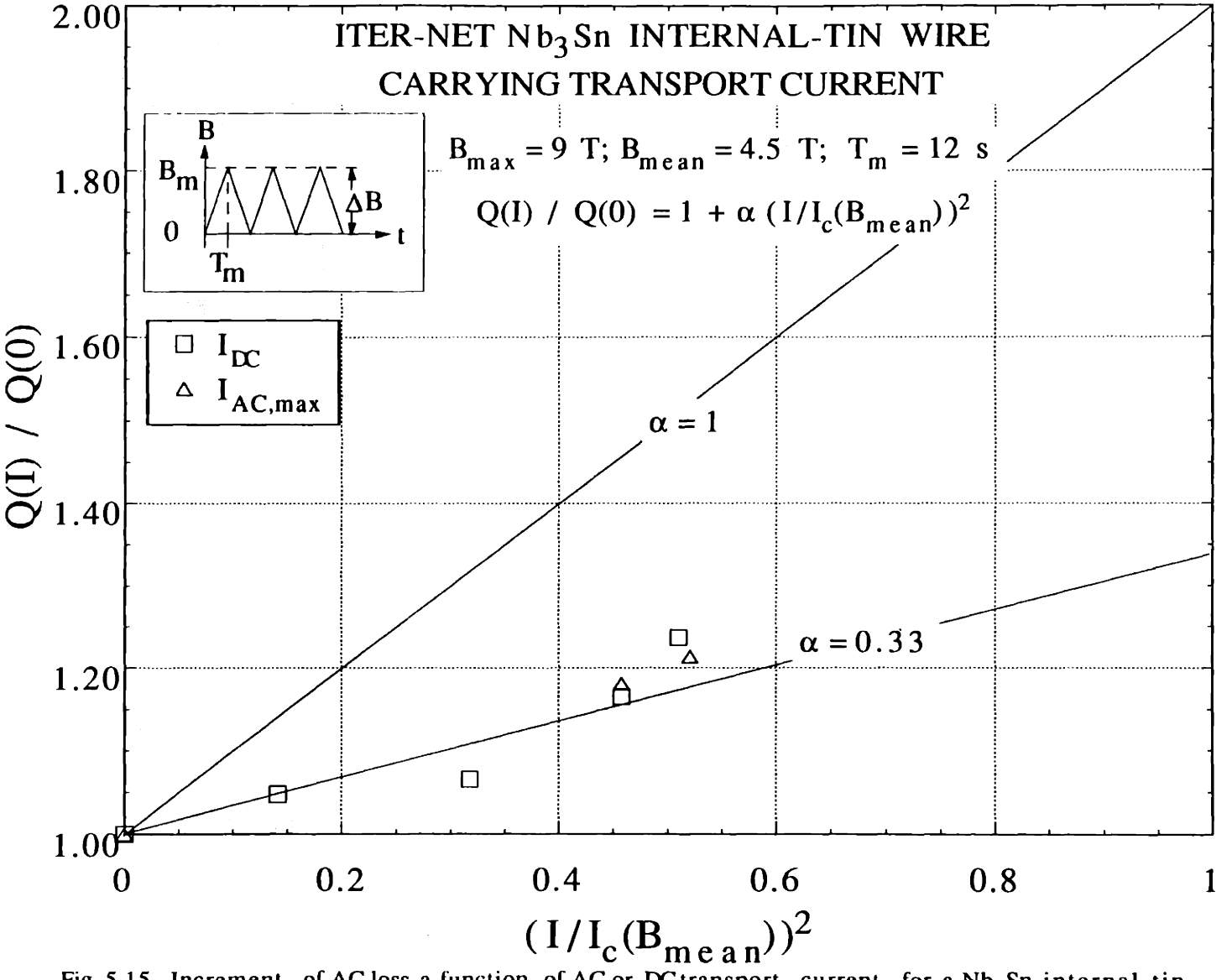

Fig. 5.15 Increment of AC loss a function of AC or DC transport current for a Nb_3Sn internal-tin wire in a ramp field condition. $I_c \sim 336$ A (DC) at 4.5 T.

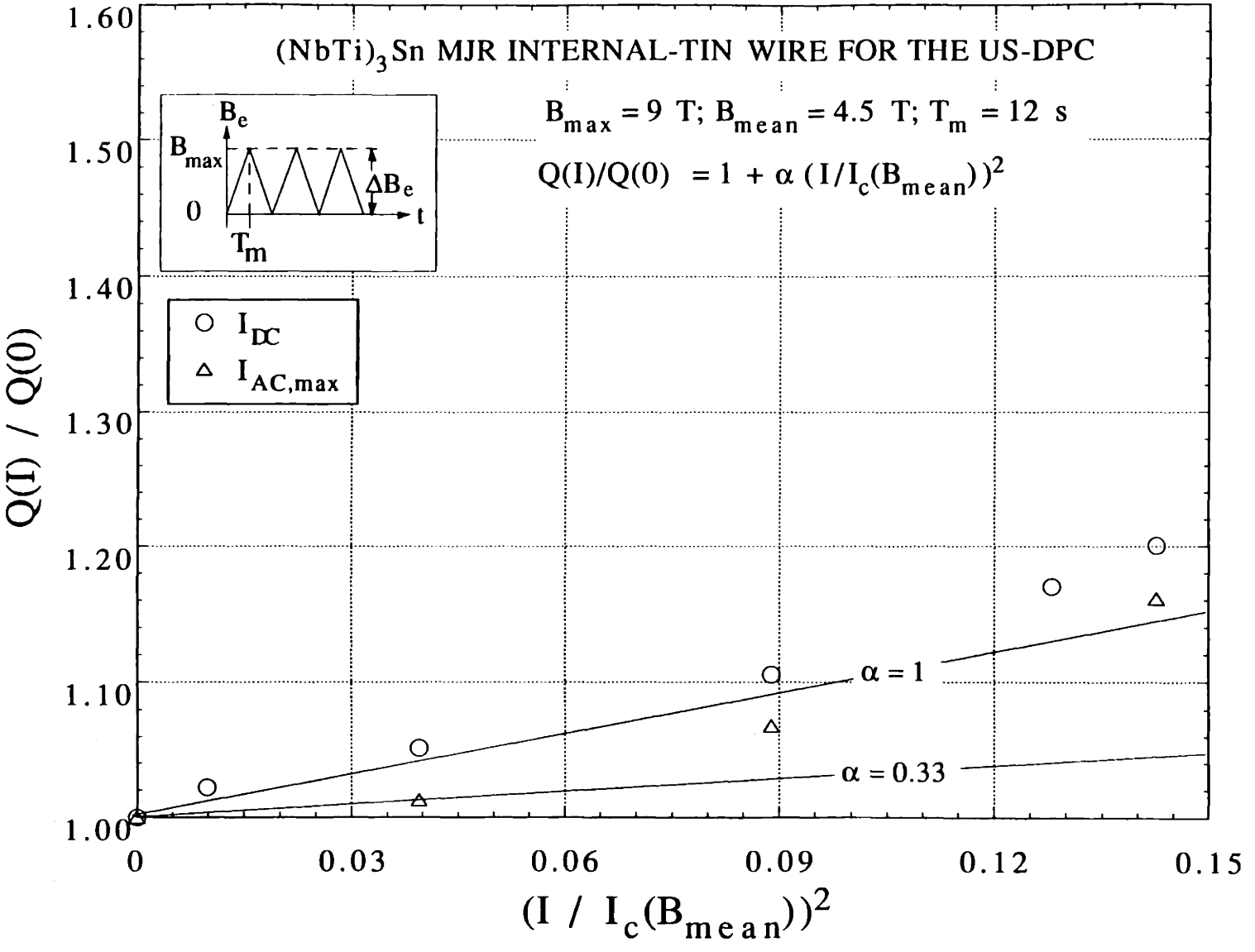

Fig. 5.16 Increment of AC loss as a function of DC or AC transport currents for a Nb_3Sn MJR wire (CRe1084) in ramp field condition. $I_c \sim 493$ A at 4.5 T.

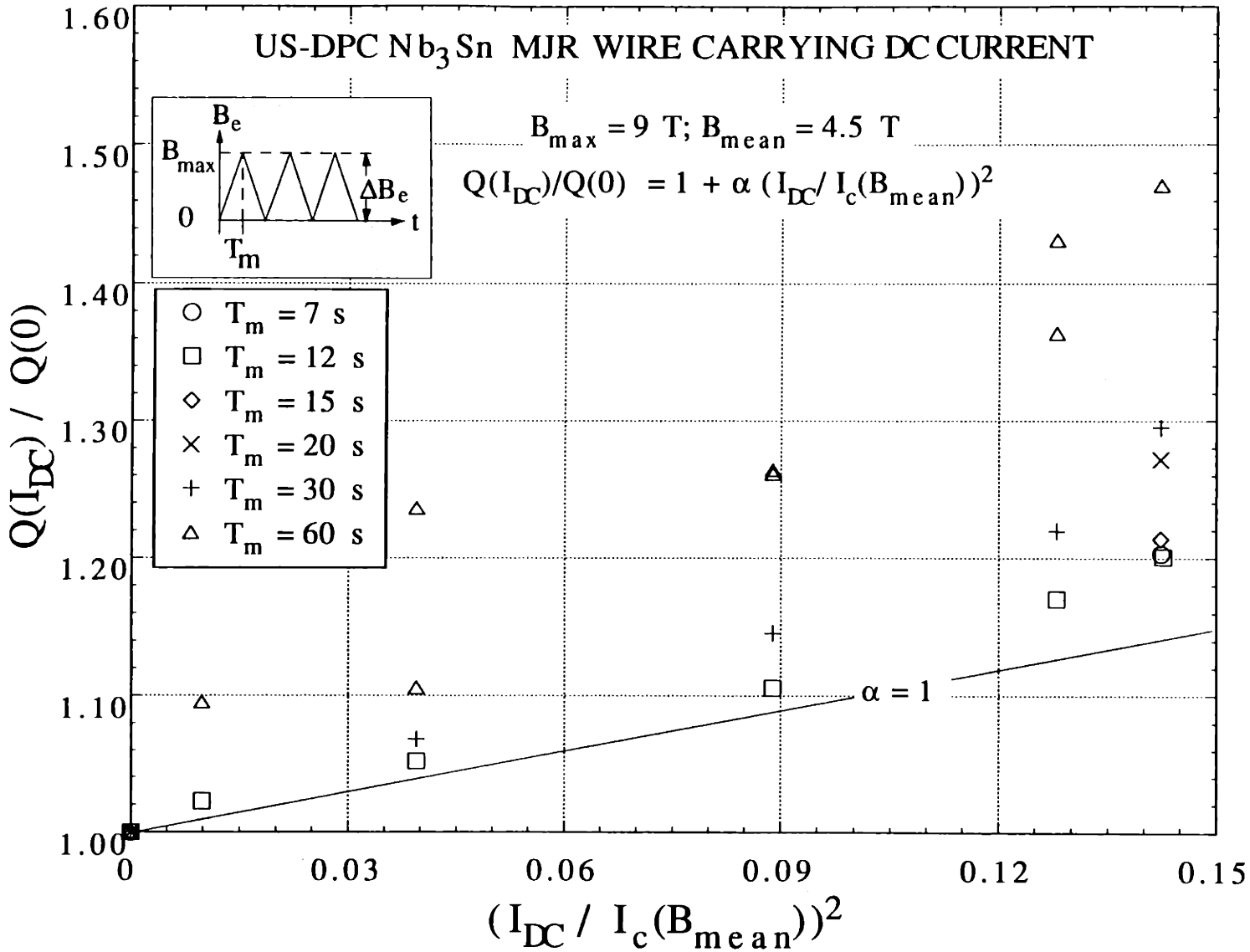

Fig. 5.17 Increment of AC loss as a function of DC transport current for a Nb_3Sn MJR wire (CRe1084) in ramp field conditions. $I_c \sim 493$ A at 4.5 T.

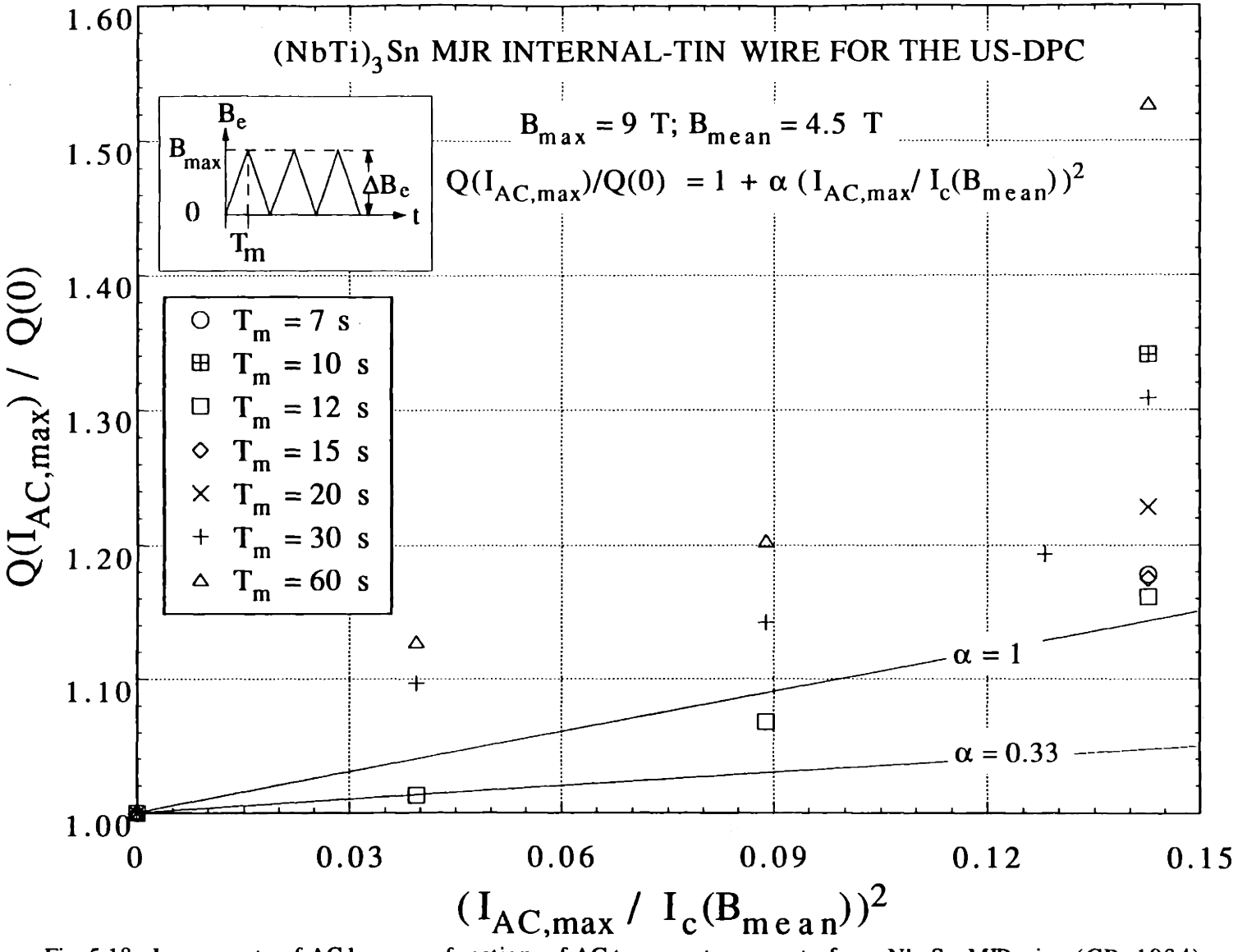

Fig. 5.18 Increment of AC loss as a function of AC transport current for a Nb_3Sn MJR wire (CRe1084) in ramp field condition. $I_c \sim 493$ A at 4.5 T.

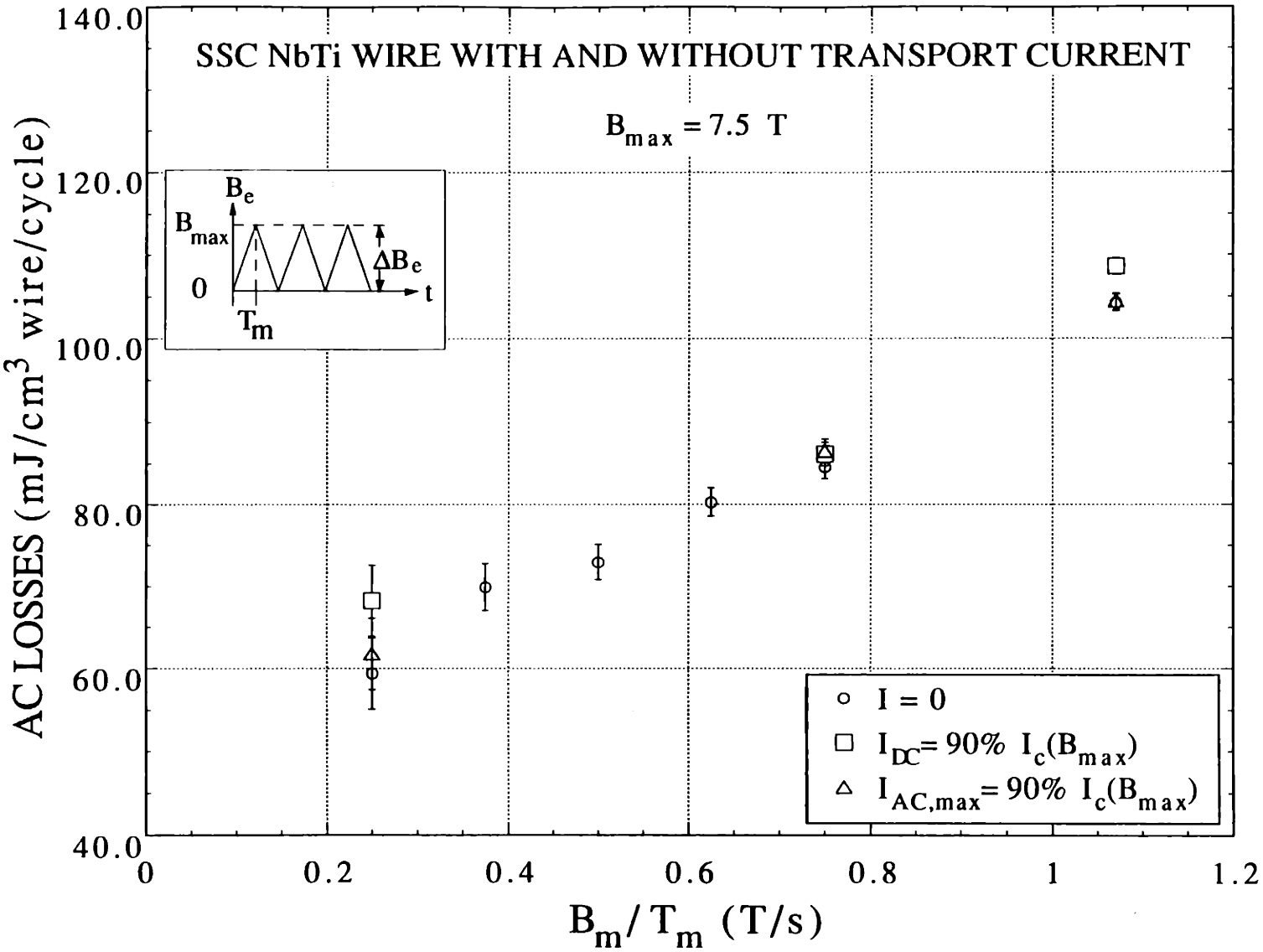

Fig. 5.19 AC loss as a function of ramp rate for a SSC NbTi wire with and without transport currents in a ramp field condition. I_c=290 A (DC) at 7.5 T with 10 μV/m criteria.

B_{max}/T_m = 0.25 T/s. The difference is merely beyond the range of the experimental error. As seen in Fig. 5.20, as the ramp rate decreases, the fraction of the loss increment caused by the DC transport current increases to about 17% of the Q(0). However, at the same field ramp rate, the AC transport current causes less than 5% increment of the AC loss.

In both internal-tin and MJR Nb_3Sn wires, the additional loss caused by the transport current is more significant than that in the NbTi wire. The internal-tin wire was tested in a cyclic ramp field with B_{max} = 9 T and 90% of the critical current at 9 T. As seen in Fig. 5.21, at the ramp rate of 0.3 T/s, the loss increment is about 40% of the loss in the current-free wire, and the total loss with transport current at this slow ramp rate is larger than those at higher ramp rates. At B_{max}/T_m = 0.75 and 1.3 T/s, the additional losses due to both DC and AC transport currents become lower but not as insignificant as in the case of NbTi. It is important to notice that the total losses of the wire carrying both DC and synchronized AC transport currents are similar not only in their trends as a function of ramp rate but also in their absolute values. The normalized losses plotted in Fig. 5.22 show that the fraction of the additional loss decreases from 40% to 10% as the ramp rate increases from 0.3 T/s to 1.3 T/s at given B_{max} and I_{DC} or $I_{AC,max}$. When extrapolating the normalized loss to zero ramp rate, the Q(I)/Q(0) ratio is approximately 1.8 for both DC and synchronized AC currents.

The test results of two MJR wires carrying transport currents are shown in Fig. 5.23. Both wires were tested with I_{DC} or $I_{AC,max}$ set to 95% of the critical current at 9 T and B_{max} = 9 T. The current-carrying loss distribution of the wires follows the trend of the current-free loss profile in the higher ramp rate regime. At ramp rates less than 0.45 T/s, the additional loss increases as the ramp rate becomes smaller. Similar to the internal-tin wire, the total loss with transport current at 0.15 T/s is larger than those at higher ramp rates, even though the current-free conductor at this ramp rate has the lowest loss. Again, the additional losses caused by either DC or synchronized AC transport currents have similar values in the range of the applied ramp rates. Fig. 5.24 shows the distribution of the normalized losses. The normalized additional loss decreases from ~ 55% at 0.15 T/s to ~ 20% at ramp rates ~ 0.45 T/s and saturates at ~ 20% when the ramp rate is further increased. Similarly, extrapolating the normalized loss down to zero ramp rate, both normalized losses by DC and synchronized AC currents approach ~ 1.7.

Conclusions from this part of test results for all three types of wire are: (1) the additional losses due to both DC and synchronized AC currents have similar values at various field

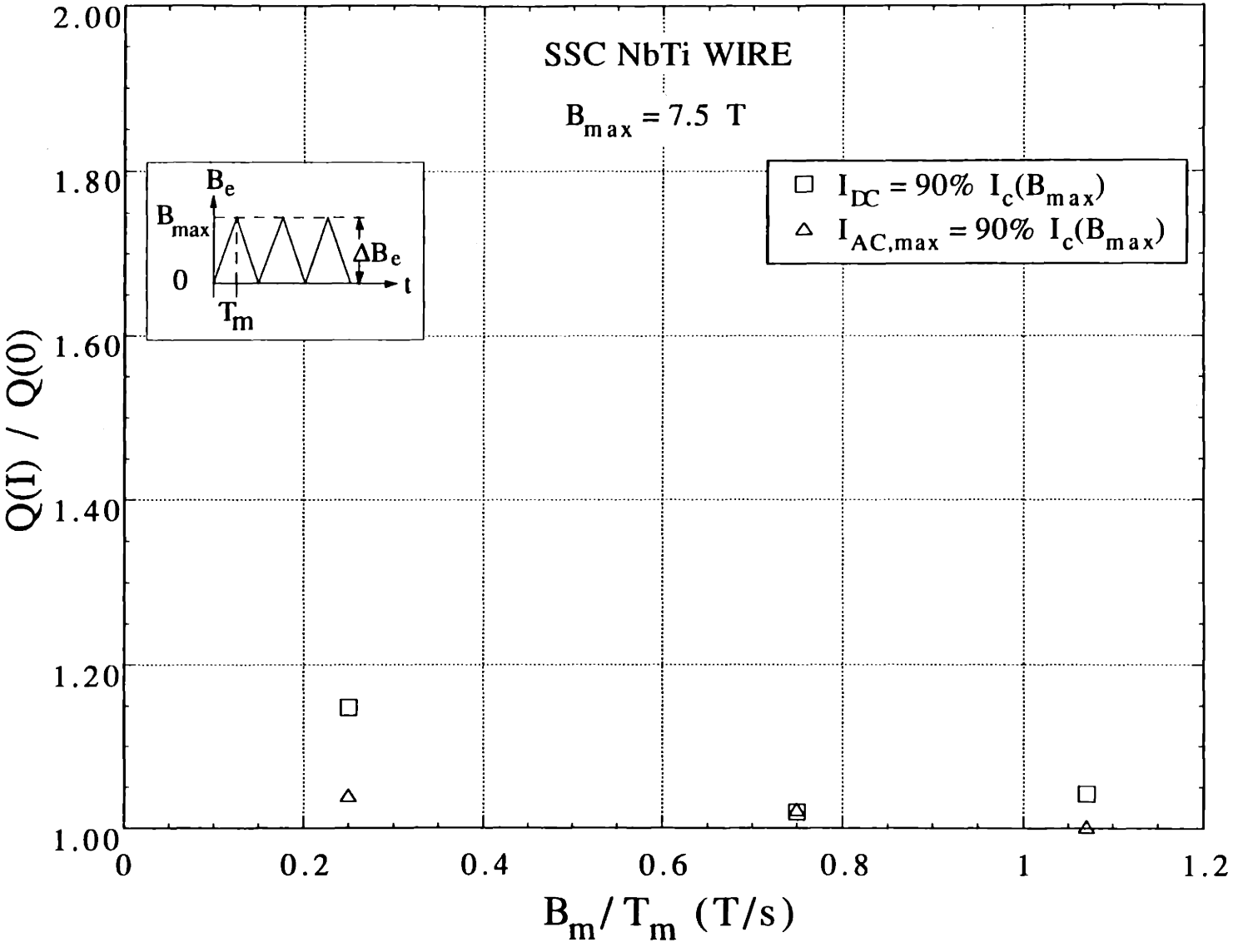

Fig. 5.20 Additional AC loss due to the transport current as a function of ramp rate for a SSC NbTi wire. I_c=290 A (DC) at 7.5 T with 10 μV/m criteria.

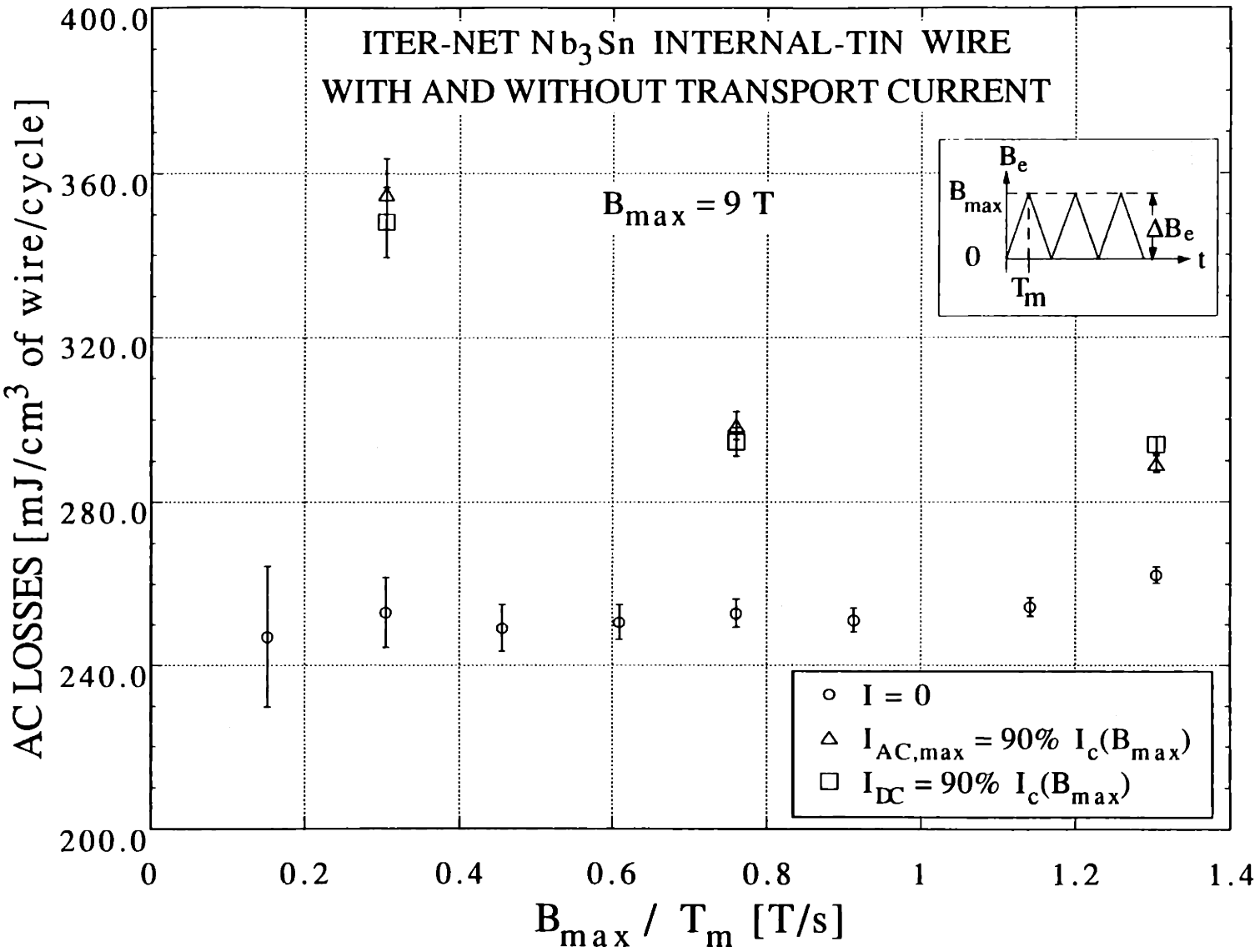

Fig. 5.21 AC losses as a function of ramp rate for ITER-NET Nb_3Sn internal-tin wire with and without transport current. $I_c = 253$ A (DC) at 9 T with 10 μV/m criteria.

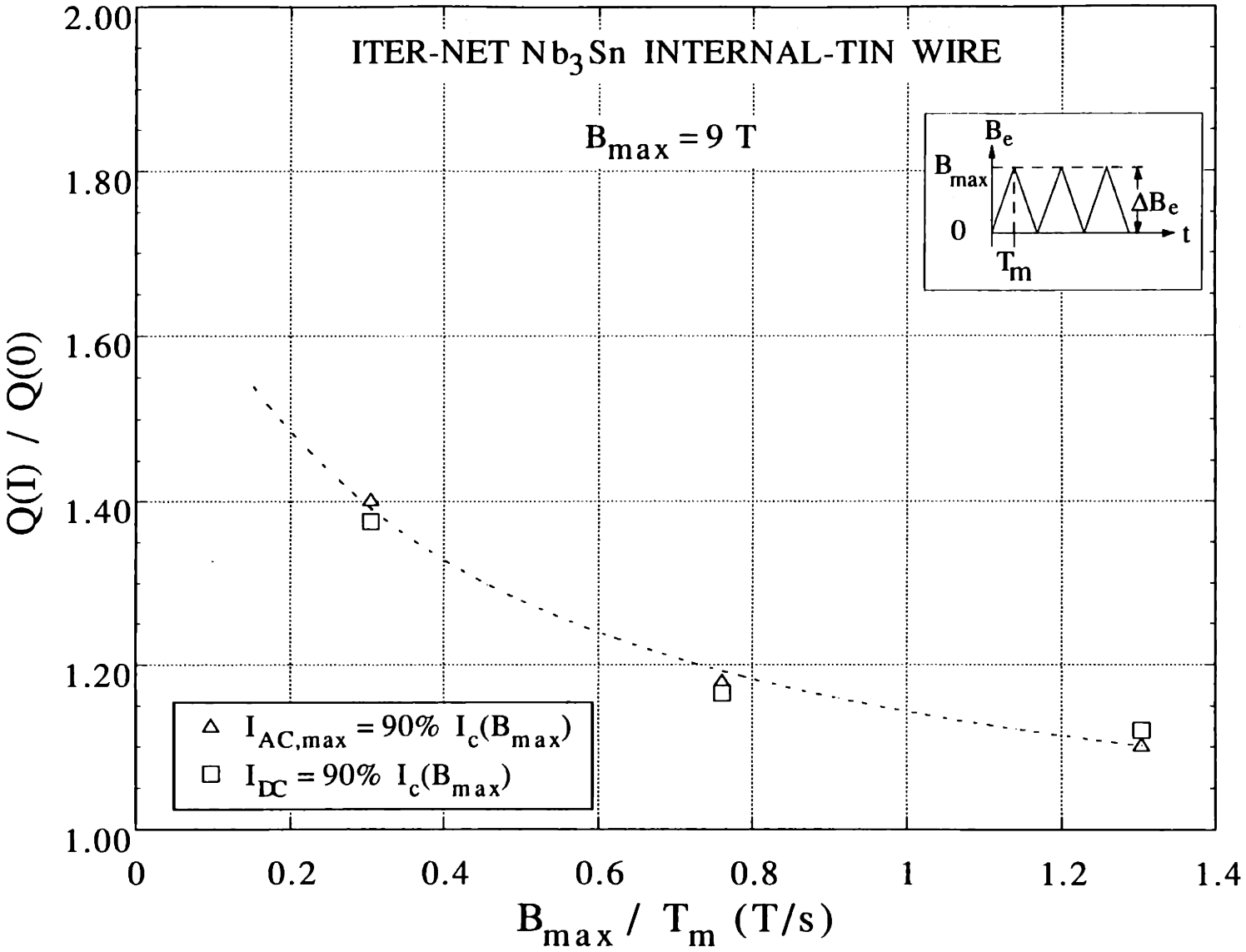

Fig. 5.22 Additional AC losses due to transport current as a function of ramp rate for internal-tin wire. I_c = 253 A (DC) at 9 T with 10 μV/m criteria. Dashed line shows the trend of test result.

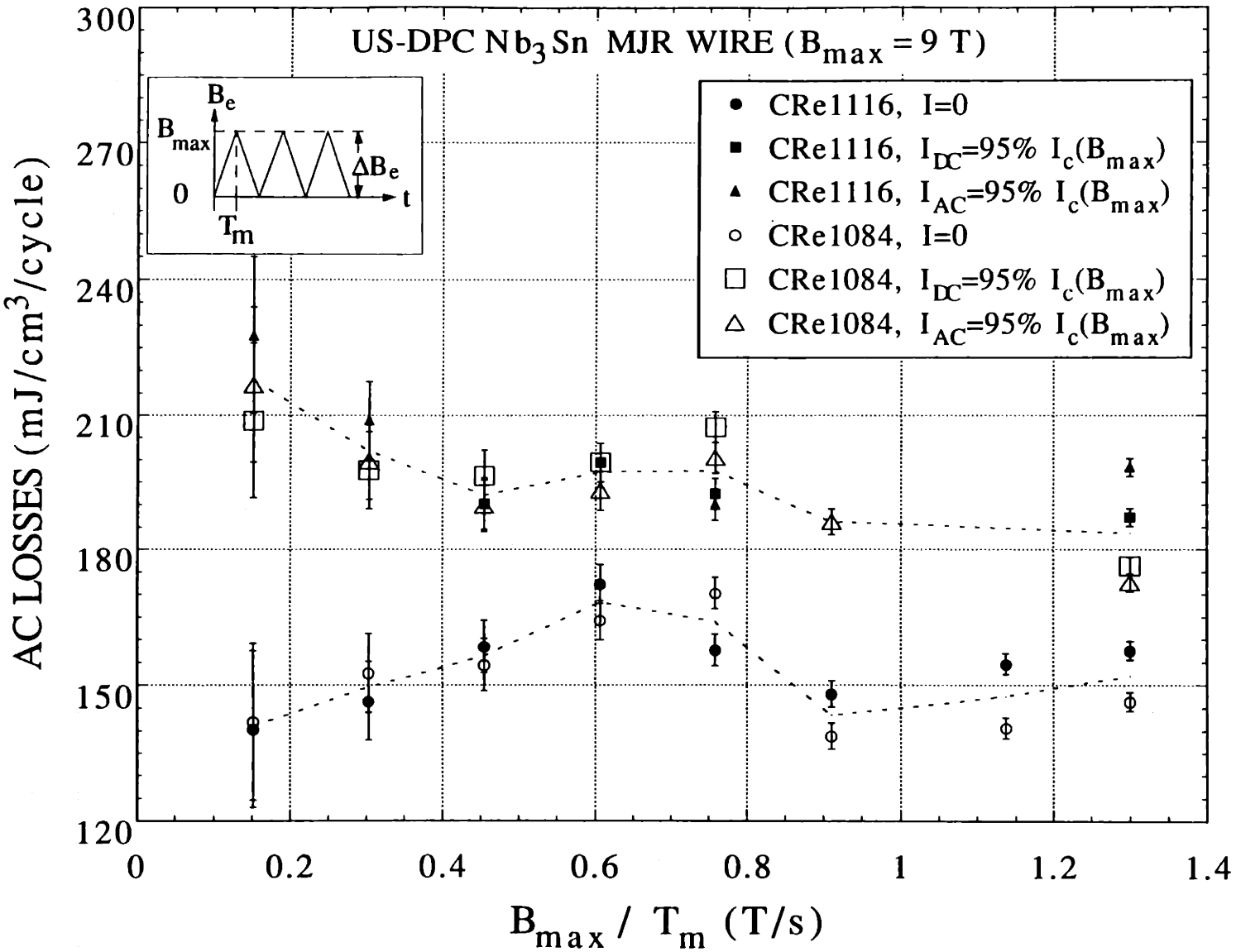

Fig. 5.23 AC losses as a function of ramp rate for US-DPC Nb_3Sn MJR wires with and without transport current. I_c = 210 A (DC) for CRe1116 and 196 A (DC) for CRe1084 at 9 T with 10 μV/m criteria.

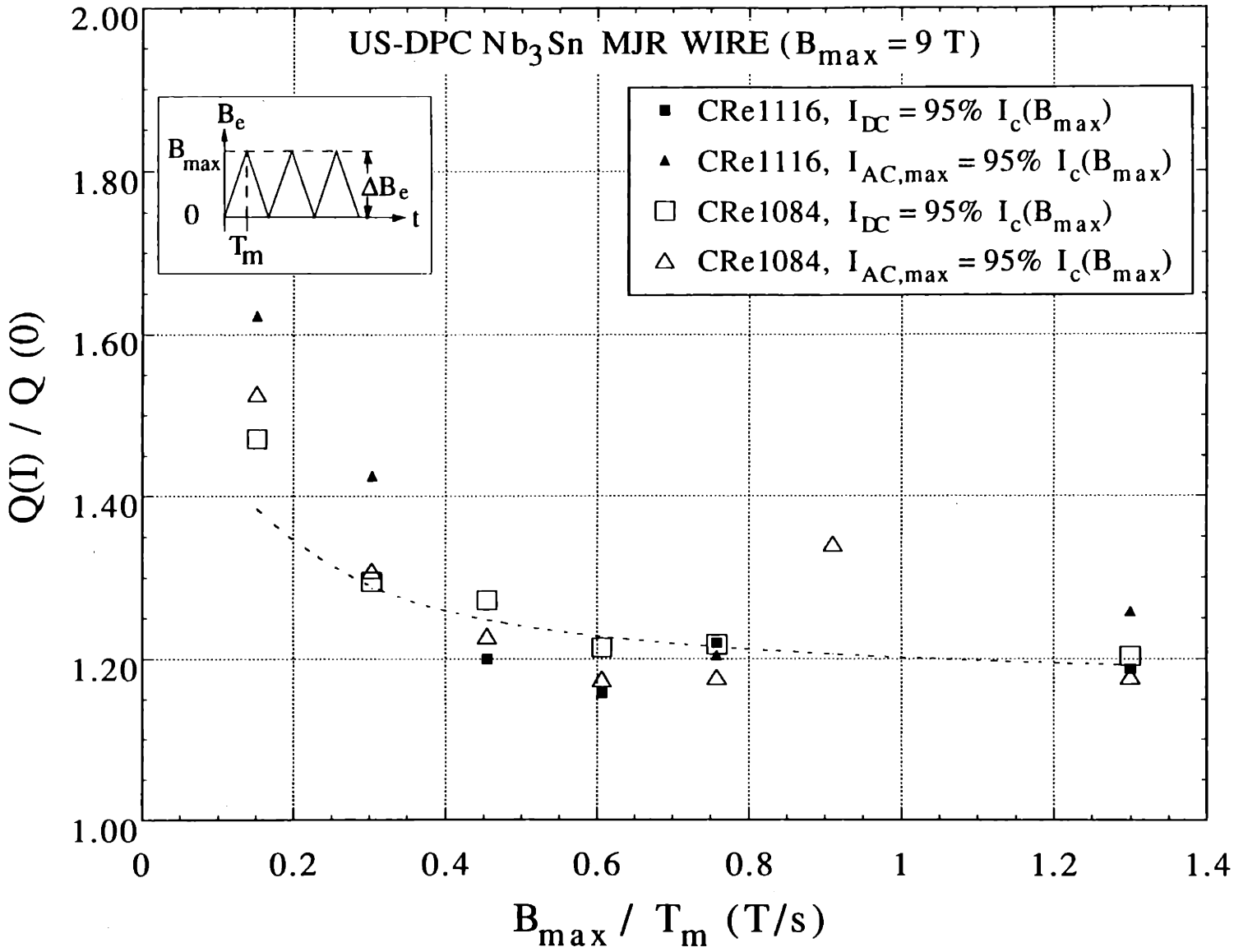

Fig. 5.24 Additional AC loss due to transport current as a function of ramp rate for US-DPC Nb_3Sn MJR wires. I_c = 210 A (DC) for CRe1116 and 196 A (DC) for CRe1084 at 9 T with 10 μV/m criteria. Dashed line shows the trend of test results.

changing rate, and (2) the total loss in a current-carrying composite superconductor can be higher at a slow field variation than at a fast changing field. The second conclusion is in contradiction to the generally accepted concept that high time-rate of field variation generates high AC losses. So far, an analytical model explaining the ramp-rate dependent loss of a current-carrying single-strand has not been found in the literature survey.

V.4.3 Ripple Field Test Without Transport Current

The measured losses in ripple field tests along with the calculated results using existing models are plotted against the DC bias field in Figs. 5.25 to 5.27. In all the experimental results, a maximum loss can be found in the range of the tested bias fields. The maximum loss is contributed by the hysteresis loss. As discussed in Section III.3, at a given ΔB, the hysteresis loss is inversely proportional to the penetration field of the filament $\Delta B_p(B_{DC})$ when $\Delta B_p(B_{DC}) \geq \Delta B$, and is proportional to the $\Delta B_p(B_{DC})$ when $\Delta B_p(B_{DC}) < \Delta B$. The $\Delta B_p(B_{DC})$ is proportional to the critical current density which decreases with the increase of the B_{DC}. Starting with small bias field, where the $\Delta B_p(B_{DC})$ is larger than the ΔB, the hysteresis loss increases with the bias field. As the bias field becomes large enough that $\Delta B > \Delta B_p(B_{DC})$, the dependence of the loss on the bias field is reversed. Thus, the maximum loss is found at the bias field where $\Delta B = \Delta B_p(B_{DC})$.

In the calculated losses for all three types of conductors, the hysteresis loss and the coupling loss are of the same order of magnitude. Error in the model calculation is thus complicated by the uncertainties contributed from both types of losses: the effective filament diameter and the low field critical current density in the hysteresis-loss calculation, and the effective transverse resistivity in the coupling-loss calculation. The error in estimating the effective transverse resistivity changes the level of the loss since the applied ripple frequency is fixed at 7.5 Hz. The uncertainties in the critical current profile and the effective filament diameter affect the calculated B_{DC} for the maximum loss. Also, when a small amplitude ripple is superimposed on a large DC bias field, the critical state model is applied to calculate the hysteresis loss. Any error in the critical current density profile will directly appear in the calculated hysteresis loss.

Fig. 5.25 shows the loss dependence on the bias field for the NbTi wire. Although the critical current of the NbTi wire was measured down to 3 T, the maximum ripple field loss is found experimentally at $B_{DC} \sim 1$ T. Extrapolated critical current is used in the hysteresis-loss calculation in this regime. The hysteresis loss calculation predicts a small

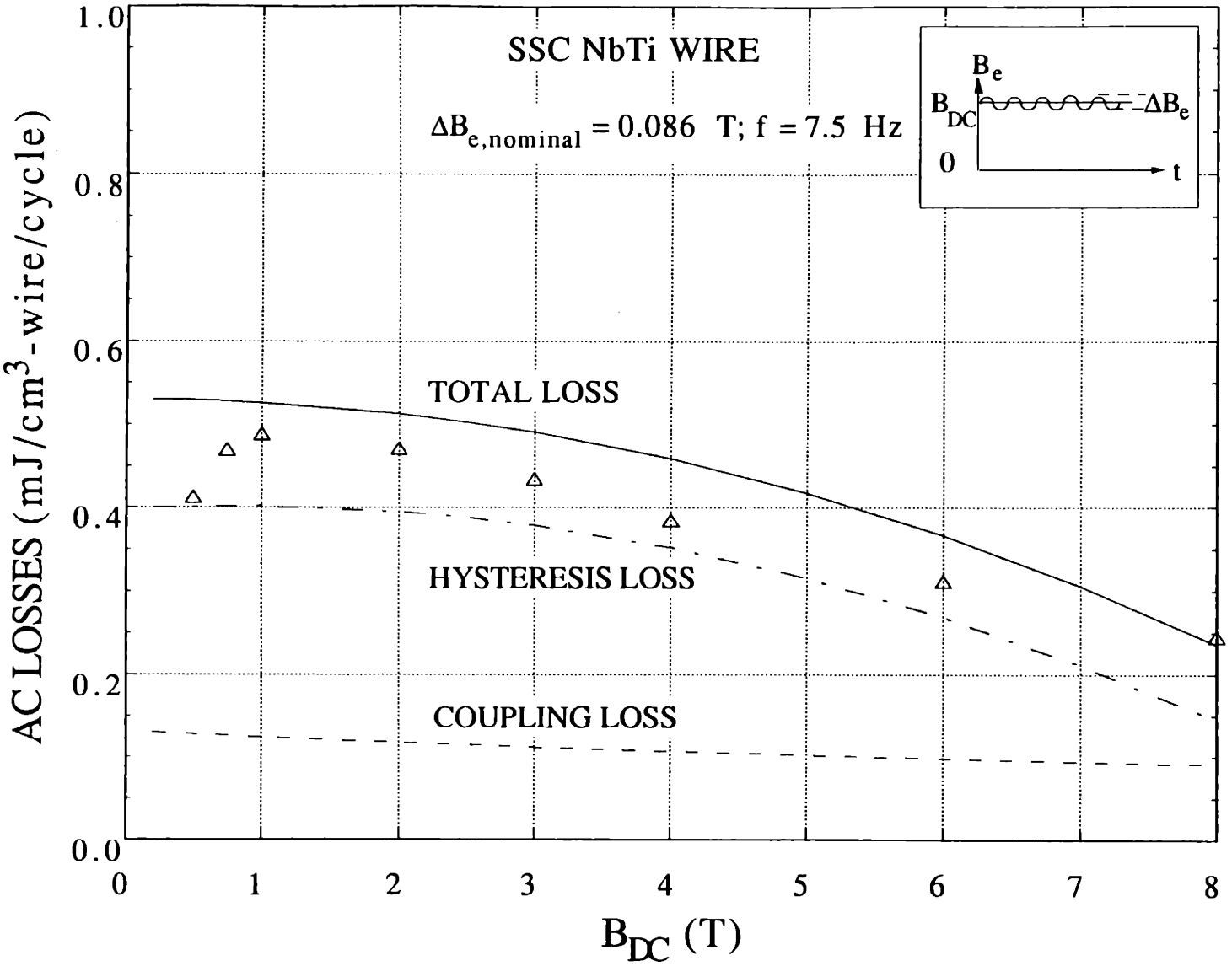

Fig. 5.25 Ripple field losses of a NbTi SSC wire as a function of DC bias field. The symbols are experimental results and the lines are calculated results.

maximum at ~ 0.7 T. However, no maximum is found in the total loss profile since the peak in the hysteresis loss is smeared by the decreasing trend of the coupling loss. The empirical critical current formula is apparently not correctly describing the lower field critical current. The calculated total loss is about 10% higher than the experimental results in the region with higher bias field, which is probably caused by the error in estimating the transverse resistivity. The calculated coupling time constant at B_{DC} = 0 T is about 1 ms.

A similar discussion is applied to the test results of the internal-tin wire as shown in Fig. 5.26. Moreover, a consistently large discrepancy in the loss levels between the measured and the calculated results throughout the range of the applied bias field can be observed. A possible explanation for the large discrepancy is that due to the limitation of the available instruments in controlling and identifying the ripple field amplitude, a consistent instrumentation error in setting the ripple field variation may have occurred. By assuming a ripple field with the amplitude lowered by 30%, the calculated loss profile becomes less than 25% greater than the experimental result, but the bias field at which the maximum loss occurs will also be shifted from B_{DC} ~ 6 T to ~ 8 T. The coupling time constant is calculated as ~ 0.3 ms at B_{DC} = 0 T.

As proven experimentally in the ramp field test, the MJR wire has a good empirical formula for the field-dependent critical current profile. Keeping all the parameters the same as those used in the ramp field loss calculation, Fig. 5.27 shows that the calculated total loss profile is in good agreement with the test result even in the lower field regime. The coupling time constant is calculated as ~ 0.8 ms at B_{DC} = 0 T and ~ 0.6 ms at B_{DC} = 12 T. The maximum loss is found at B_{DC} ~ 4 T both analytically and experimentally.

V.5 SUMMARY AND FURTHER DISCUSSION

The purpose of this chapter is to provide the experimental results of the field-dependent critical currents as well as measured AC losses for different conductors in various background field and current conditions. Analytical results calculated from existing loss models are also presented for purpose of comparison. The major conclusions of this chapter are stated here. Comparisons of the experimental results with the existing model calculations not only justify the experimental setup in the higher ramp rate regime but also reveal the insufficiency of these models in predicting the AC-loss properties in the MJR wire. From the test results, the fraction of the additional loss of a current-carrying

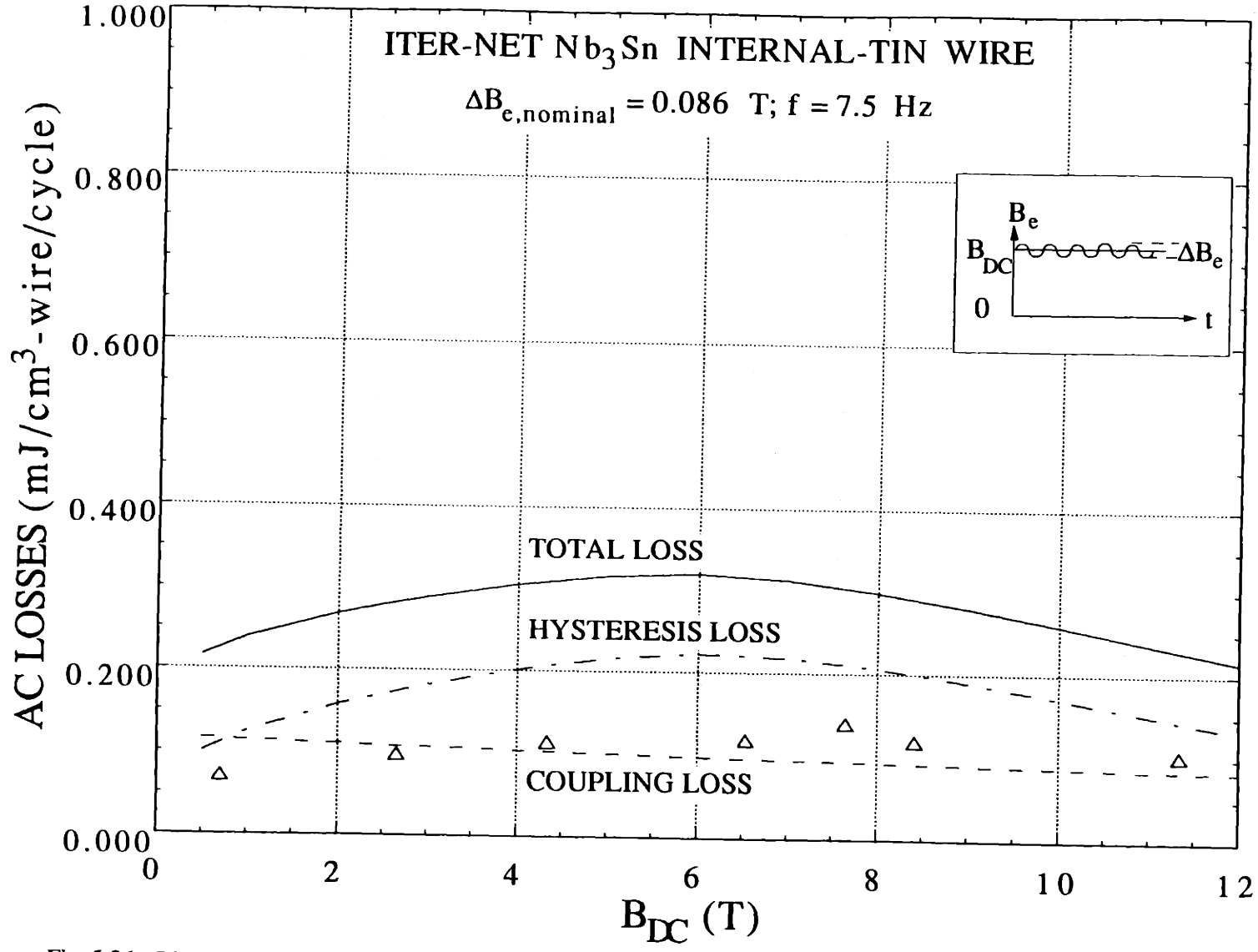

Fig. 5.26 Ripple field losses of Nb_3Sn internal-tin wire as a function of DC bias field. The symbols are the experimental results and the lines are the calculated values.

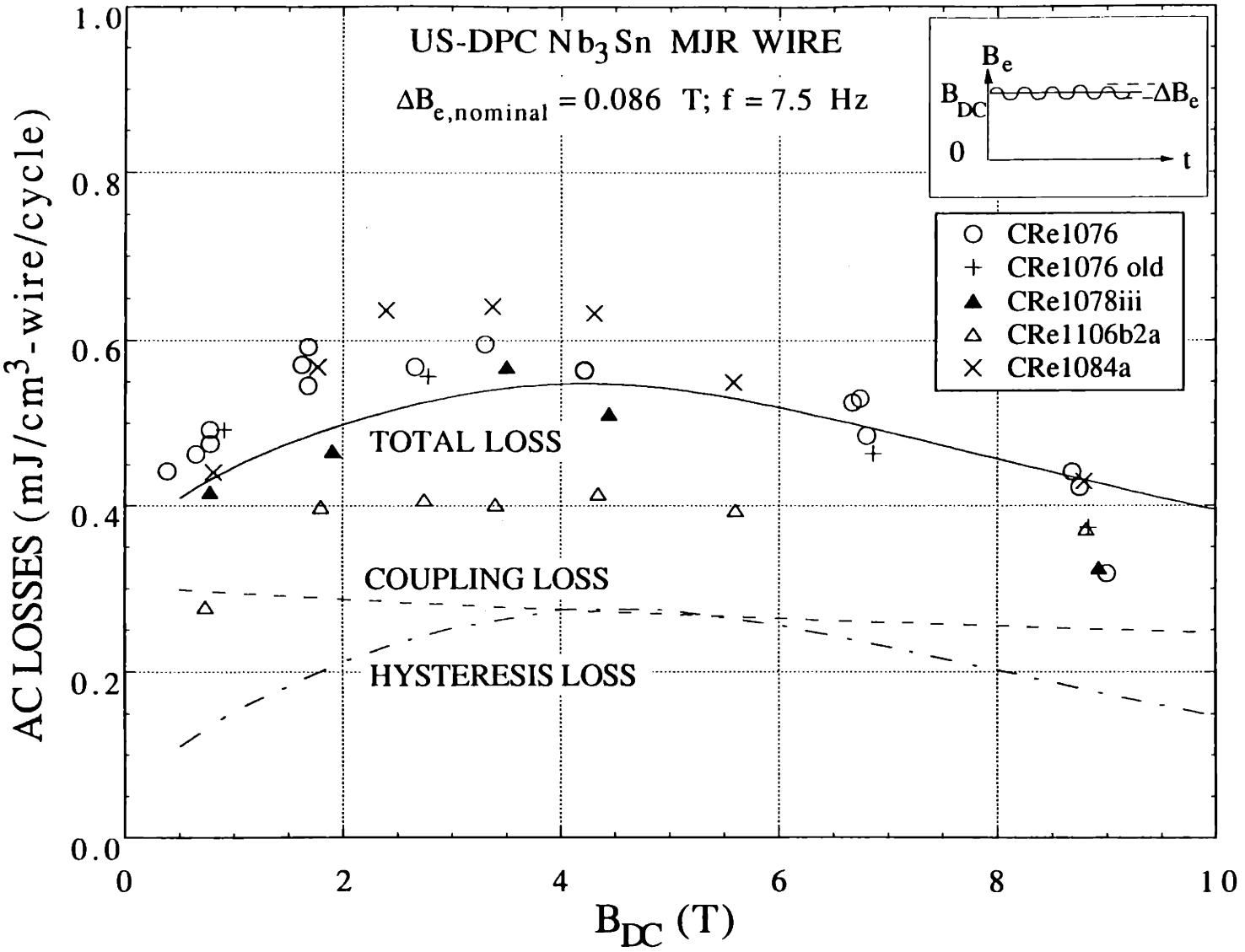

Fig. 5.27 Ripple field losses of Nb_3Sn MJR internal-tin wires as a function of DC bias field. The symbols are experimental results and the lines are calculated results.

composite single-strand in ramp field condition decreases from unity at zero ramp rate and saturates at a low value as the ramp rate increases. The additional loss of a current-carrying superconductor predicted in the existing model can not be applied when the field variation is far from static. An analytical model explicitly describing this loss mechanism has not been found. As has been found in several comparisons, a reliable lower field critical current density profile is of great importance in improving the accuracy of the model calculation. In addition to the transport current method, alternative methods measuring the lower field critical currents should be considered. Summaries and inter-comparisons among test results are discussed in the following.

Critical currents of all three types of wire were measured using the same sample coil for AC-loss test (Figs. 5.2 to 5.4). The constants for the empirical critical current densities are listed in Table 5.5 The critical currents of the MJR wires measured in the present work have good agreement with the averaged profile in the field range between 3 T and 12 T. The latter was obtained independently from 14 randomly-selected US-DPC MJR wires. The good agreement proves that the sample winding method applied in the present work does not degrade the superconducting property of the single strand. The critical currents of the internal-tin wire measured in this work are consistently lower than those by Suenaga. The inconsistency is probably caused by the variation of the wire quality along the axial direction.

The hysteresis losses of three MJR wires extrapolated from the calorimetric measurement agree with those measured by the magnetization method performed independently by Goldfarb at NIST (Table 5.7). This justifies the reliability of the present experimental system operated in the regime of slow field variation where hysteresis loss is the dominant loss mechanism.

Based on the existing AC-loss model, a crude calculation (Table 5.6) shows that the field screening should not occur in all the wires at any range and time-rate of field variation applied in the present work. The total AC loss is thus the linear sum of the hysteresis loss, the coupling loss, and the additional loss due to the transport current if it is applied.

In the ramp field test, the AC losses of all three types of conductors are plotted as a function of the field ramp rate or the maximum applied field (Figs. 5.6 to 5.13). Comparisons of the AC-loss test results with the calculation based on the existing AC-loss models show reasonable agreements in NbTi and internal-tin wires. Some discrepancies

are caused by three major uncertainties applied in the model calculations: the field-dependent critical current especially in the lower field regime, the effective filament diameter, and the transverse resistivity.

In the MJR wire, when the loss is plotted against the ramp rate for each given peak field, a local maximum loss is found in the slow field variation range. According to the existing AC-loss models, a maximum loss may be caused by the field screening mechanism at some high ramp rate. The expected ramp rate of having significant field screening in the MJR wire is estimated to be about two orders of magnitude higher than what is found in the test results. The occurrence of the local maximum loss at slow ramp rate has never been experimentally observed or analytically discussed. A new inter-bundle coupling model derived in Chapter VI provides a possible explanation to this newly found phenomenon.

The AC losses of the current-carrying wires are plotted in Figs. 5.14 to 5.24. When the loss is plotted as a function of either transport current or ramp rate, the test results of the current-carrying wires in ramp field conditions show that the additional losses caused by both DC and synchronized AC transport currents have similar values when $I_{DC} = I_{AC,max}$. When the AC loss of the current-carrying wire is normalized with the current-free loss at the same ramp rate, additional losses caused by transport current becomes ramp-rate dependent. For the current-carrying Nb_3Sn internal-tin wires, the extrapolated Q(I)/Q(0) ratio at zero ramp rate approaches ~ 1.8 which is close to the prediction in the existing model. At a higher ramp rate, the Q(I)/Q(0) ratio becomes smaller. The trend of the ramp-rate dependent Q(I)/Q(0) ratio of NbTi wire is similar to those of Nb_3Sn wires. In the MJR wires, it is clear that the Q(I)/Q(0) ratio approaches ~ 1.2 and saturates at ramp rates higher than 0.45 T/s after decreasing from ~ 1.7 at zero ramp rate. Analysis of the AC loss of a current-carrying composite wire is complicated by the non-linear interaction of the transport current, the coupling current, and the saturated layer in the multifilamentary zone. It is not clear whether this problem has been solved numerically. However, similar test results as well as analytical loss models have not been found in the literature.

Analysis of the ripple field AC losses in the present work is difficult due to similar loss level of different AC-loss mechanisms. All the uncertainties in various losses have overlapping contributions to the error in the total loss calculation. A best combination of parameters for the model calculation could be found with numerical parametric study. However, this is not the purpose of this thesis work.

In both NbTi and internal-tin wires (Figs. 5.25 and 5.26), a common discrepancy is found in the lower bias field regime due to insufficient information of the lower field critical current. As demonstrated in the ramp field test, the extrapolated hysteresis loss profile as a function of maximum applied field provides an indirect way to check the goodness of the field-dependent critical current profile since the loss is the integration of the critical current density with respect to the applied AC field. On the other hand, since the hysteresis loss calculation for the ripple field test is based on the critical state model, the loss is directly proportional to the critical current density at the applied DC bias field. Ripple field tests at a lower bias field provides another possible way to check the lower field critical current density if other types of losses can be properly characterized from high bias field loss data. When calculating the critical current density from the hysteresis loss, the effective filament diameter plays an important role. If the effective filament diameter can be calculated from ripple field loss measured at a high bias field, the ramp field loss can thus be calculated with the information from ripple field test and high field critical currents. It is important to notice that the critical current density extracted from AC loss is the averaged value which is almost not affected by the local defects of the filaments and is generally higher than that determined by using the transport current method. It will be an interesting future topic to examine whether this is a practical method to reduce the effect of the uncertainty in the low field critical currents on the loss calculations.

For the MJR wire in the ripple field (Fig. 5.27), with all the parameters the same as those used in calculating the ramp field loss, the calculated total loss profile is in good agreement with the test result even in the lower field regime. The major reason of the good agreement is due to the accurate field-dependent critical density profile especially in the lower field regime. However, such good agreement in the ripple field test is inconsistent with the large discrepancy found in the ramp field test using the same MJR wire. The loss mechanism which causes the local maximum loss in the ramp field test seems to be insignificant in the ripple field test. Since the applied background fields in these two types of tests are different in their wave-forms, amplitude, and frequency range, it is difficult to draw any other significant conclusion by simply comparing these two experimental results. As shown in the next chapter, in the MJR type of wire, the ramp-rate dependent loss mechanism causing a local maximum loss in the slow ramp rate regime diminishes as the rise-time decreases. The new model seems to be appropriate in explaining why different results are found in different frequency regimes.

V.6 REFERENCES

5.1 Reisner, D, private communication.

5.2 Suenaga, M., private communication.

5.3 Gregory, E., private communication.

5.4 Takayasu, M., et al., 'Critical currents of Nb_3Sn wires for the US-DPC coil,' IEEE Trans. on Magnetics, Vol. 27, No. 2, 1991, p. 1767.

5.5 Goldfarb, R., private communication.

5.6 Smathers, D., private communication.

CHAPTER VI

INTER-BUNDLE COUPLING EFFECT ON THE AC LOSSES OF A DOUBLE-STACKED COMPOSITE WIRE

VI.1 INTRODUCTION

Calculated AC-loss results using existing hysteresis-loss and coupling-loss formulae have been compared with the test data in Chapter V. When the total loss is plotted against the field ramp rate, the experimental loss profiles of the NbTi and internal-tin test wires have good agreements with model calculations. However, the MJR wire shows a local maximum at a slow field changing rate which is not predicted in the existing AC-loss models. In this chapter a new AC-loss model taking into account the saturation of the filament bundle walls caused by strong local inter-bundle coupling currents in the inner multifilament region is proposed to provide a possible explanation for such a phenomenon.

VI.2 DOUBLE-STACKING WITH INDIVIDUAL TIN-DIFFUSION BARRIER

In order to understand the special loss profile of MJR, the construction of the MJR wire is compared with the other two conductors. As observed in Fig. 4.6, the NbTi wire has a very uniform filament distribution in the multifilamentary zone (Fig. 4.6(a)). Two types of internal-tin Nb_3Sn wires as shown in Figs. 4.6(b) and 4.6(c), which are manufactured with double-stacking technique for reducing the distortion of the filaments. The filaments are clustered in each bundle rather than uniformly distributed over the wire as in the NbTi wire. In order to make a continuous long length wire, ductile material in addition to those needed for making superconductor filaments, is required inside the multifilamentary zone. Both NbTi and MJR wires explicitly include a large copper core in the center, while the internal-tin wire has several sub-divided normal cores distributed in the wire which will be discussed in more detail in the following comparison of the construction of these two Nb_3Sn composite wires.

In the internal-tin wire as seen in Fig. 4.6(b), a thick tantalum layer, adopted as a global tin diffusion barrier, clearly separates the multifilamentary zone from the external copper cladding. The global diffusion barrier encircles all the filamentary bundles and the matrix material. Each bundle has a tin core in the center surrounded by the multifilamentary zone. Every three filament bundles are arranged in the most compact form as a unit. The sub-divided normal cores are distributed among the three-bundle units as seen in Fig. 4.6(b). After heat treatment, the tin core in each bundle and all the Cu within the diffusion barrier becomes bronze. The external cladding remains pure copper. The cross sectional uniformity of the tin content in the bronze is affected by the positions of the tin cores and the Nb filaments. However, the variation of the electric resistivity of the matrix material enclosed by the diffusion barrier is not expected to be significant.

In the MJR internal-tin wire (Fig. 4.6(c)), all the filament bundles are arranged in a most compact array with the central bundle replaced by a copper core. Each bundle has a multifilamentary zone containing a tin core, and wrapped by an individual diffusion barrier made of vanadium. After heat treatment, the central normal core of the wire, the external cladding, and the inter-bundle matrix remain pure copper. The difference in inter-bundle and intra-bundle resistivities of a MJR wire can be of an order of magnitude which is much more dramatic as compared to that of an internal-tin wire using a global diffusion barrier.

As a summary of the above comparison, the MJR wire is different from the NbTi wire in the filament distribution and the intra-bundle matrix resistivity, and is different from the internal-tin wire in the resistivity of the inter-bundle matrix material and the arrangement of the bundles (closest packing in MJR). The comparison suggests that the occurrence of the local maximum in the ramp-rate dependent loss profiles of the MJR wire, as found in Fig. 5.11, may result from the synthetic effects of filament clustering, low inter-bundle matrix resistivity, and small inter-bundle spacing.

VI.3 INTER-BUNDLE COUPLING LOSSES

In the conventional coupling loss analysis, the effective transverse resistivity in the multifilament region is mostly averaged over different matrix materials, even when a wire has a double stacking construction (Ref. 6.1). A homogenization process is valid when the variation of the electric resistivity in the multifilamentary zone is insignificant. As shown in

Chapter V, the homogenization process applied to the analysis of the coupling losses in the internal-tin wire with a global tin-diffusion barrier made a good comparison to the experimental results since the resistivities in the bundle core, the intra- and inter-bundle matrix are at least of the same order of magnitude. However, when it is applied to the MJR wire, the averaging process takes account of the volume fractions of various matrix materials but excludes the interaction of the synthetic effects as discussed above.

VI.3.1 Assumptions

In an early article, Walters (Ref. 6.2) performed an analysis regarding the coupling currents in a multi-slab system. The critical field changing-rate $\dot{B}_c$ was characterized by the saturation of the outer-most slab, similar to what has been discussed in Section II.3.2.3. Walters also pointed out that when the thickness of the superconductor slab is larger than the spacing between the superconductors, the critical field changing-rate needs to be modified by a size effect. The previous analysis can not be applied to the MJR single-strand configuration, but the latter argument is an important starting point to the present new model development.

From the photomicrograph of the cross sectional construction of the MJR wire as shown in Fig. 6.1(a), all the filament bundles are highly distorted. In the present work, for the convenience of analyzing the inter-bundle interaction, each bundle is idealized into a hexagonal cross section which is the original geometry of the bundle in a billet before it is drawn down to a wire. Fig. 6.1(b) shows that all the filament bundles are assumed to be arranged in a close-packed array. These two assumptions: hexagonal bundle cross section and close-packed bundle array, are very important in simplifying the inter-bundle coupling analysis.

The present analysis started with Walters' multi-slab analysis by assuming that in the inner multifilament region the inter-bundle spacing w is small compared with the filament bundle wall thickness 2a (Fig. 6.2(a)). The outer regions of the multifilament slabs which are really the inner regions of two neighboring bundles, are electrically isolated from their original bundles. This is a rare but reasonable assumption if the intra-bundle matrix resistivity is much higher than that of the inter-bundle which is exactly the case in a MJR wire. Also, for simplicity, the thin diffusion barrier at the outer edge of each bundle is neglected. As a first approach to this particular problem, the coupling currents due to remote slabs and bundles are ignored at the present stage.

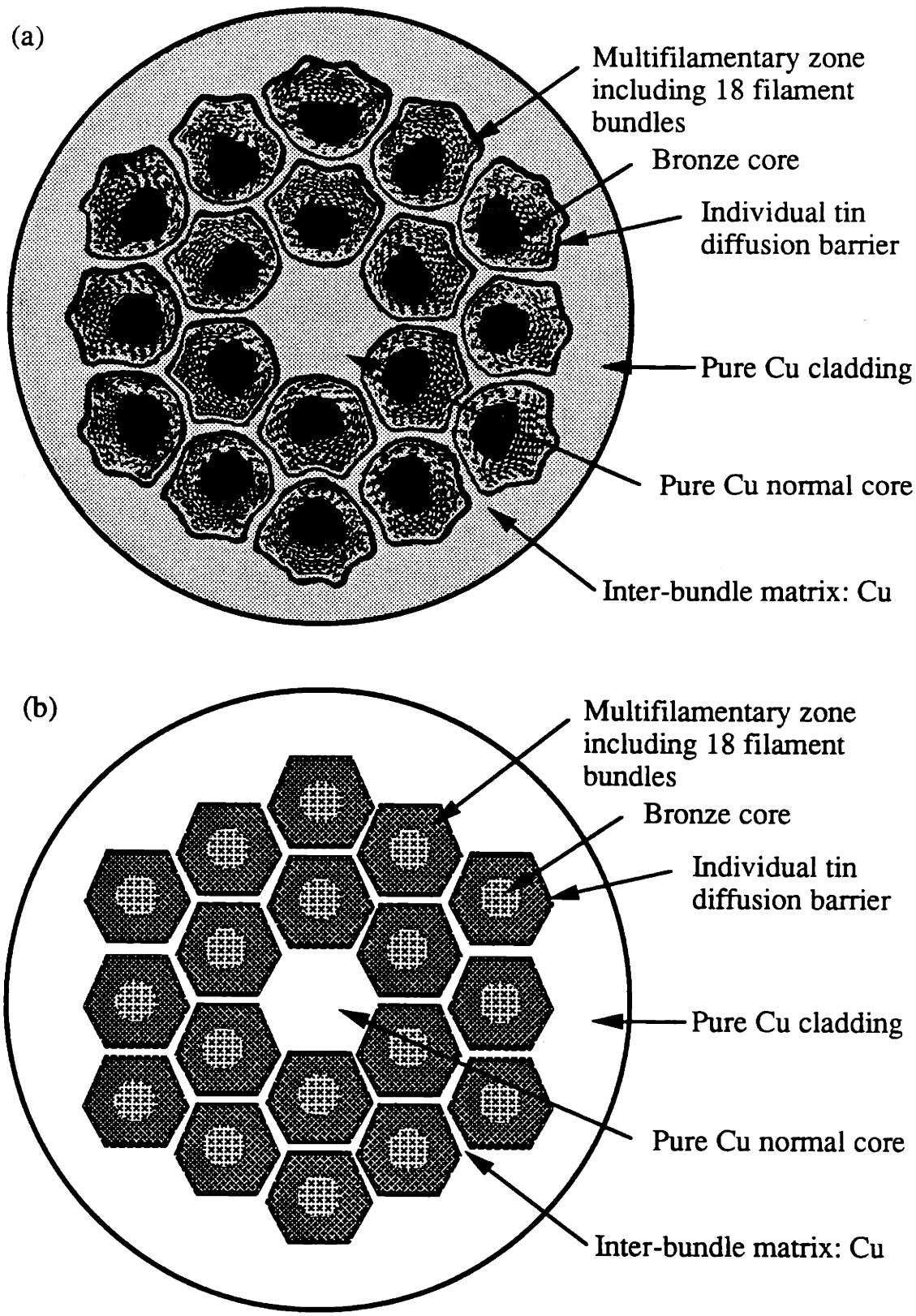

Fig. 6.1 (a) Cross sectional microphotograph of a MJR wire with individual tin diffusion barrier; (b) Schematic of an idealized cross sectional construction of a MJR wire with hexagonal multifilamentary bundles.

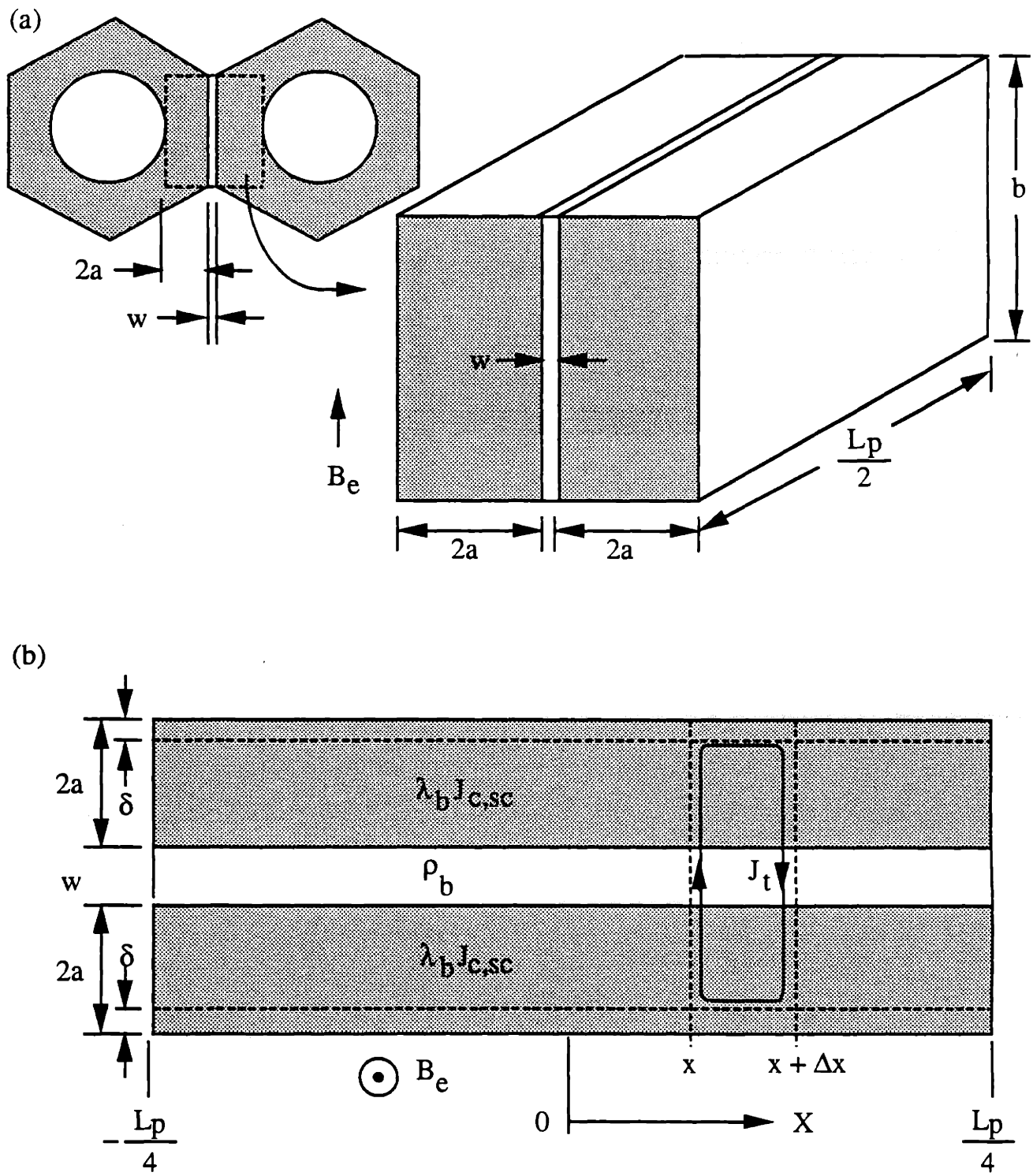

Fig. 6.2 Slab model for inter-bundle coupling loss. Each filament bundle wall with a thickness of 2a, a height of b, and a length of Lp/2 is detached from its original bundle under the assumptions that the inter-bundle resitivity is much smaller than the intra-bundle resistivity, and the inter-bundle spacing w << 2a.

As seen in Fig. 6.2(b), the filament bundle wall is taken as a superconducting slab of thickness 2a with a critical current density of $\lambda_b J_{c,SC}$, where λ_b is the local volume fraction of the filaments in the bundle wall, and $J_{c,SC}$ is the critical current density of the superconducting filament. The inter-bundle normal slab has a thickness of w and an electric resistivity of ρ_b. The slab system is considered to be electrically segmented into half of the twist pitch, $L_p/2$, to account for the bundle twisting.

A large external cyclic ramp field B_e is applied parallel to the wider side of the slabs which has a height of b. Considering the large amplitudes of the time-varying field, the $\lambda_b J_{c,SC}$ and ρ_b are assumed to be dependent on the applied field. For simplicity, in the following derivation the applied-field dependence of both parameters will not be specified until it is needed. Inside the multifilament slab, the critical state model is assumed for the instantaneous spatial distribution of the $\lambda_b J_{c,SC}$. In the ramped field condition, $d(B_e - B)/dt \sim \tau\, d\dot{B}/dt \sim 0$ is approximately true in the low frequency range for the present work. The approximation of $\dot{B} \approx \dot{B}_e$ will be applied.

VI.3.2 Inter-bundle Coupling Currents

By applying Faraday's law to the small area surrounded by the loop between x and x + Δx as shown in Fig. 6.2(b), the relationship between the transverse coupling current density J_t in the normal slab and the time-varying field $\dot{B}$ can be expressed as

$$\frac{dJ_t(x)}{dx} = \dot{B}\,\frac{4a + w - 2\delta}{\rho_b\, w} \tag{6.1}$$

where δ is the thickness of the saturation layer. The coupling current density in the normal slab at x is obtained by integrating Eq. (6.1) with the boundary condition $J_t(L_p/4) = 0$ which is given as

$$J_t(x) = \dot{B}\,\frac{4a + w - 2\delta}{\rho_b\, w}\left(\frac{L_p}{4} - x\right)$$

The net total coupling current in the normal slab in half of the slab length is obtained by integrating $\Delta I_t(x) = b\,\Delta x\, J_t(x)$ from 0 to $L_p/4$ with $I_t(0) = 0$, which is

$$I_t\left(\frac{L_p}{4}\right) = b\,\dot{B}\,\frac{4a + w - 2\delta}{2\,\rho_b\,w}\left(\frac{L_p}{4}\right)^2 \tag{6.2}$$

The supercurrent flowing in the saturation layer, or the screening current is given as

$$I_s = \lambda_b\, J_{c,SC}\, b\, \delta.$$

By conservation of total current, the net total coupling current equals the screening current which leads to the most important relationship,

$$\lambda_b\, J_{c,SC}\, \delta = \dot{B}\,\frac{4a + w - 2\delta}{2\,\rho_b\,w}\left(\frac{L_p}{4}\right)^2 \tag{6.3}$$

Eq. (6.3) includes all the key parameters determining the saturation of the multifilament slabs.

VI.3.3 Effective Coupling Time Constant

The shielding field, B_s, induced by the screening current in the saturation layer, is expressed as $B_e - B = B_s = \mu_0 K_s$, where K_s is the linear screening current density defined as $\lambda_b J_{c,SC}\delta$ which is the left-hand-side expression of Eq. (6.3). Thus,

$$B_e - B = \tau_b \dot{B}\,\frac{\pi^2(4a + w - 2\delta)}{8\,w} \tag{6.4}$$

with

$$\tau_b \equiv \frac{\mu_0}{\rho_b}\left(\frac{L_p}{2\pi}\right)^2$$

is the coupling time-constant of a slab system with an equivalent twist pitch of L_p, which has a normal slab with a resistivity of ρ_b sandwiched by two multifilamentary superconducting slabs. By including the ratio of the geometric parameters, the effective resistivity $\rho_{b,eff}$ and the related effective time constant $\tau_{b,eff}$ of the sandwich system can be further defined as

$$\rho_{b,eff} \equiv \rho_b \frac{8\,w}{\pi^2 (4a + w - 2\delta)} \quad \text{and} \quad \tau_{b,eff} \equiv \tau_b \frac{\pi^2 (4a + w - 2\delta)}{8\,w} \tag{6.5}$$

In a slowly changing field, $\delta \rightarrow 0$ and Eq. (6.5) becomes

$$\rho_{b,eff} \approx \rho_b \frac{8\,w}{\pi^2 (4a + w)} \quad \text{and} \quad \tau_{b,eff} \approx \tau_b \frac{\pi^2 (4a + w)}{8\,w}, \quad \text{for slow field variation} \tag{6.6}$$

As seen in Eq. (6.6), in the case of $w << 2a$, $\rho_{b,eff} \sim w\rho_b / 5a$ and $\tau_{b,eff} \sim 5a\tau_b / w$. Depending on the wire design, the ratio of 5a / w can make $\tau_{b,eff}$ more than an order of magnitude larger than τ_b. This magnified effective inter-bundle coupling time constant is the major mechanism causing the peak of inter-bundle coupling loss shifted to a lower frequency (Ref. 6.3). Remember that such shift occurs only if the following two conditions are satisfied simultaneously: (1) the inter-bundle matrix resistivity is much lower than that of intra-bundle; and (2) the inter-bundle spacing is much smaller than the bundle wall thickness.

At higher field changing rate, the multifilament slabs are saturated by the local coupling currents, that is $\delta \rightarrow 2a$, Eq. (6.5) is reduced to

$$\rho_{b,eff} \approx \rho_b \frac{8}{\pi^2} \approx \rho_b \quad \text{and} \quad \tau_{b,eff} \approx \tau_b \frac{\pi^2}{8} \approx \tau_b, \qquad \text{for fast field variation} \tag{6.7}$$

and the geometric effect is no longer important as in the case of slow field variation.

VI.3.4 Saturation Field

For the condition of $w << 2a$, Eq. (6.4) is approximated as

$$B_e - B \approx \tau_b \dot{B} \frac{\pi^2 a}{2\,w} \left(1 - \frac{\delta}{2a}\right) \tag{6.8}$$

From Eq. (6.3) with the penetration field of the multifilamentary superconducting slab expressed as

$$B_{pb} = \mu_0 \lambda_b J_{c,SC} ,$$

the ratio of the saturation layer thickness to the filament bundle wall thickness is given as

$$\frac{\delta}{2a} \approx \frac{\frac{\tau_b \dot{B}}{B_{pb}}}{\frac{\tau_b \dot{B}}{B_{pb}} + \frac{4w}{\pi^2 a}} \qquad \text{for } w << 2a \tag{6.9}$$

Substituting δ in Eq. (6.9) into Eq. (6.8), the non-linear differential equation can not be solved analytically. However, for the extreme cases of slow and fast field variations, Eq. (6.8) can be linearized as (Ref. 6.4)

$$B_e - B \approx \tau_b \dot{B}_e \frac{\pi^2 a}{2w} \qquad \text{for slow field variation: } \frac{\tau_b \dot{B}_e}{B_{pb}} << \frac{4w}{\pi^2 a} \tag{6.10}$$

$$B_e - B \approx 2B_{pb} \qquad \text{for fast field variation: } \frac{\tau_b \dot{B}_e}{B_{pb}} >> \frac{4w}{\pi^2 a} \tag{6.11}$$

The approximation of $\dot{B} \approx \dot{B}_e$ has been applied on the right hand side of the Eq. (6.10) for the case of slow field variation.

The saturation field, B_{sat}, at which the multifilamentary slabs are saturated by the coupling current passing through the normal slab is obtained by solving

$$\frac{\tau_b(B_{sat})\,\dot{B}_e}{B_{pb}(B_{sat})} \approx \frac{4w}{\pi^2 a} \quad \text{or} \quad \rho_b(B_{sat})\, J_{c,SC}(B_{sat}) \approx \frac{L_p^2\, \dot{B}_e}{16\, w\, \lambda_b} \tag{6.12}$$

Depending on the complexity of the expressions for $\rho_b(B_{sat})$ and $J_{c,SC}(B_{sat})$, Eq. (6.12) is sometimes solved iteratively. It is important to know that the B_{sat} is physically meaningful only if the solution falls in the range between the first and the second critical fields of the superconductor material in the filament bundle, i.e., $B_{c1} < B_{sat} < B_{c2}$. For practical application, $B_{c1} \approx 10^{-2}$ T and $B_{c2} \approx B_{c2}^*$ found from the critical current density profile as discussed in Chapter III, are applied in the present work.

VI.3.5 Magnetization and Losses

Magnetizations of the inter-bundle matrix due to the inter-bundle coupling currents are simply the right-hand-side of Eqs. (6.10) and (6.11), which are

$$- \mu_0 M_{cb1} \approx - B_{pb} \frac{\delta}{a} \quad \text{for} \frac{\tau_b \dot{B}_e}{B_{pb}} \leq \frac{4w}{\pi^2 a} \tag{6.13}$$

$$- \mu_0 M_{cb2} \approx - 2B_{pb} \quad \text{for} \frac{\tau_b \dot{B}_e}{B_{pb}} > \frac{4w}{\pi^2 a} \tag{6.14}$$

where the constraints to the applicable ranges have been relaxed for the convenience of loss calculations. Similar linearization approximation was applied in the early works of conventional penetration loss analysis by Ogasawara et al. (Refs. 6.4 and 6.5). In the slow field variation limit, the expression on the right hand side of Eq. (6.13) reduces to that of Eq. (6.10).

For a cyclic changing field, the magnetization loss is

$$Q = - 2 \int_{B_{min}}^{B_{max}} M(B_e)\, dB_e \tag{6.15}$$

By using Eq. (6.13) before the saturation layer become significant, the loss in the normal slab affected by a uni-directional cyclic field ramped as B_{min} - B_{max} - B_{min}, is expressed as

$$Q_{cb1} = \frac{2}{\mu_0} \int_{B_{min}}^{B_1} B_{pb}(B_e) \frac{\delta(B_e)}{a} dB_e \quad \text{for } B_e \leq B_{sat} \tag{6.16}$$

where $B_1 = B_{sat}$ if $B_{sat} \leq B_{max}$, and $B_1 = B_{max}$ if $B_{sat} > B_{max}$. After full saturation, from Eq. (6.14),

$$Q_{cb2} = \frac{4}{\mu_0} \int_{B_2}^{B_{max}} B_{pb}(B_e)\, dB_e \qquad \text{for } B_e > B_{sat} \tag{6.17}$$

where $B_2 = B_{min}$ if $B_{sat} \le B_{min}$, and $B_2 = B_{sat}$ if $B_{sat} > B_{min}$. In the range of field variation, the magnetization loss due to the inter-bundle coupling currents is $Q_{cb} = Q_{cb1} + Q_{cb2}$.

Magnetization of the superconductor filament in the inter-bundle coupling dominant region remains the same as Eq. (3.26), only it is scaled down by a volume fraction of non-saturated region (Ref. 6.4), which is expressed as

$$- \mu_0 M_{hb1} \approx \frac{2}{3} B_p \left(1 - \frac{\delta}{2a}\right) \qquad \text{for } \frac{\tau_b \dot{B}_e}{B_{pb}} \le \frac{4w}{\pi^2 a} \tag{6.18}$$

where the instantaneous penetration field of a cylindrical superconductor filament with a radius of r_f is defined the same as that in Chapter III,

$$B_p \equiv \frac{2}{\pi} \mu_0 J_{c,SC} r_f.$$

After the multifilamentary slabs are fully saturated,

$$- \mu_0 M_{hb2} = 0 \qquad \text{for } \frac{\tau_b \dot{B}_e}{B_{pb}} > \frac{4w}{\pi^2 a} \tag{6.19}$$

For an applied field much higher than the first penetration field of the filament in cyclic field variation ΔB_{p0} (Eq. 3.25), the hysteresis loss is approximated as

$$Q_{hb1} \approx \frac{4}{3\mu_0} \int_{B_{min}}^{B_1} B_p(B_e) \left(1 - \frac{\delta(B_e)}{2a}\right) dB_e \qquad \text{for } B_e \le B_{sat} \tag{6.20}$$

and

$$Q_{hb2} = 0 \qquad \text{for } B_e > B_{sat}. \tag{6.21}$$

VI.4 TOTAL AC LOSS

The hysteresis loss, Q_h, in the regions not affected by the inter-bundle coupling currents is calculated with Eq. (3.27),

$$Q_h \approx -2\int_{B_{min}}^{B_{max}} M(B)\,dB = \frac{8}{3\pi} r_f \int_{B_{min}}^{B_{max}} J_{c,SC}(B)\,dB \quad (J / m^3 \text{ superconductor}) \tag{3.27}$$

which is similar to Eq. (6.20), with $B_1 = B_{max}$ and $\delta = 0$. For a wire with close packing construction, only the outer-most bundle walls of external filament bundles are not affected by the inter-bundle coupling currents. This is dramatically different from the conventional saturation of a composite multifilamentary wire (Section II.4) in which the saturation always starts from the outer-most boundary of the filamentary zone.

When a center normal core is adopted in a wire, the filaments in the inner-most bundle walls next to the center core are surrounded by regions with strong inter-bundle coupling currents. Therefore, the field applied to the inner-most filament layer is similarly screened and Eq. (6.20) is also applied to this inner region as well.

The coupling currents crossing the whole cross sectional area are induced by the filaments in the outer-most unsaturated bundle walls. The loss power due to inter-filament coupling currents is calculated from the extended Turck's formulae for a composite wire with 5-zone (or 5-layer) construction as derived in Section II.3.3,

$$P_c = \frac{\dot{B}_e^2 L_p^2}{(2\pi)^2}\left(\frac{R_{MFo}}{R_3}\right)^2 \left| \frac{k}{\rho_t(B_e)} + \frac{l}{\rho_i(B_e)} + \frac{m(B_e)}{\rho_1(B_e)} + \frac{n(B_e)}{\rho_2(B_e)} + \frac{s(B_e)}{\rho_3(B_e)} \right| \quad (W / m^3 \text{ wire}) \tag{2.63}$$

Eq. (2.63) is valid when $\tau_w(B_e)\,\dot{B}_e << B_{p,MF}(B_e) << B_e$, where $B_{p,MF}(B_e)$ and $\tau_w(B_e)$ are defined in Eqs. (2.49) and (2.65), respectively. Since the coupling currents induced by the filaments in the non-saturated layer pass through the whole multifilamentary zone including the region saturated by the inter-bundle coupling currents, homogenized effective transverse resistivity $\rho_t(B_e)$ as discussed in Subsection II.3.2.2 is applied in Eq. (2.63). The filament coupling loss is thus

$$Q_c = 2\int_0^{T_m} P_c\,dt = 2\frac{T_m}{\Delta B}\int_{B_{min}}^{B_{max}} P_c(B_e)\,dB_e \quad (J / m^3 \text{ wire}) \tag{6.22}$$

for a cyclic ramp field with a constant ramp rate of $\dot{B}_e = (B_{max} - B_{min}) / T_m$, where T_m is the rise-time of the external field. Since the coupling currents are flowing in the conventional way between the filaments within the non-saturated multifilamentary region, the loss is scaled down by the fraction of the non-saturated region in the multifilamentary zone, $f_{\text{non-sat in MF zone}}$.

The conventional eddy current loss power in each layer external to the multifilamentary zone is given as (Ref. 6.6),

$$P_{e,i}(B_e) \approx \frac{\dot{B}_e^2}{4}\frac{1}{\rho_i(B_e)}\frac{R_i^4 - R_{i-1}^4}{R_i^2} \quad (W / m^3 \text{ clad}) \qquad \text{for } i = 1 \text{ to } 3$$

and the eddy current loss in each layer becomes

$$Q_{e,i} = 2\frac{T_m}{\Delta B}\int_{B_{min}}^{B_{max}} P_{e,i}(B_e)\,dB_e \quad (J / m^3 \text{ resistive layer / cycle}) \qquad \text{for } i = 1 \text{ to } 3 \tag{6.23}$$

The total loss Q_{total} is the sum of Q_h from Eq. (3.27), Q_c from Eqs. (2.63) and (6.22) for the non-saturated region, the losses in Eqs. (6.16), (6.17), and (6.20) for the saturated region, and the eddy current losses $Q_{e,i}$'s in Eq. (6.23). Each term is weighed by the proper volume fraction depending on the material (matrix materials or superconductor) and the loss mechanism (inter-bundle coupling or unsaturated regions). Thus,

$$Q_{total} = Q_h \times f_h + Q_c \times f_c + Q_{hb} \times f_{hb} + Q_{cb} \times f_{cb} + \sum_i Q_{e,i} \times f_{e,i} \tag{6.24}$$

where $f_h = f_{\text{SC in wire}} \times f_{\text{non-sat in MF zone}}$

$f_c = 1 - f_{\text{SC in wire}}$

$f_{hb} = f_{\text{SC in wire}} \times (1 - f_{\text{non-sat in MF zone}})$

$f_{cb} = f_{\text{inter-bundle matrix in wire}}$

$f_{e,i} = f_{\text{resistive layer i in wire}}$

In the present MJR wire construction, the $f_{\text{non-sat in MF zone}}$ is approximated as the ratio of the total volume of the outer-most bundle walls to that of the overall bundle walls. Also, the $f_{\text{inter-bundle matrix in wire}}$ is approximated as the ratio of the volume of the inter-bundle matrix enclosed in the outer-most bundle walls to that of the overall resistive material in the wire.

VI.5 INTER-BUNDLE COUPLING EFFECT ON THE AC LOSSES OF MJR WIRE

By using the test wire specifications listed in Tables 5.3 and 5.4, the calculated loss results plotted against the field ramp rate for the MJR wire based on the proposed model are shown in Fig. 6.3 for 0 - 9 T - 0 ramped field. The inter-bundle coupling loss Q_{cb}, although weighted by a small volume fraction, apparently causes a local maximum to the total loss profile at a low field ramping rate. After the occurrence of the maximum inter-bundle coupling loss (Q_{cb}), both the coupling loss and the hysteresis loss (Q_{hb}) in the inter-bundle coupling dominant region decrease as the ramp rate increases, which causes a dip in the total loss profile. At even higher ramp rates, the filament coupling loss Q_c dominates all other losses, and the total loss increases monotonically. The trend of the analytical total loss profile as a function of ramp rate agree with that of the experimental results.

Fig. 6.4 shows the calculated AC-loss profiles as a function of the ramp rate at different ranges of field variation. The local maximum loss is located at a higher ramp rate as the range of the field variation decreases. Compared with the experimental profiles as shown in Fig. 5.7, the measured local maximum loss shifts to a lower ramp rate as the range of the field variation decreases which is just opposite to the model calculation. Also, the measured maximum losses are lower than the calculated values by about 20% at field variation less than 9 T. The reason for this discrepancy is not clear. It could be due to the lack of the coupling between a bundle wall and the remote array of walls or bundles. Further study of this problem should be a future research subject.

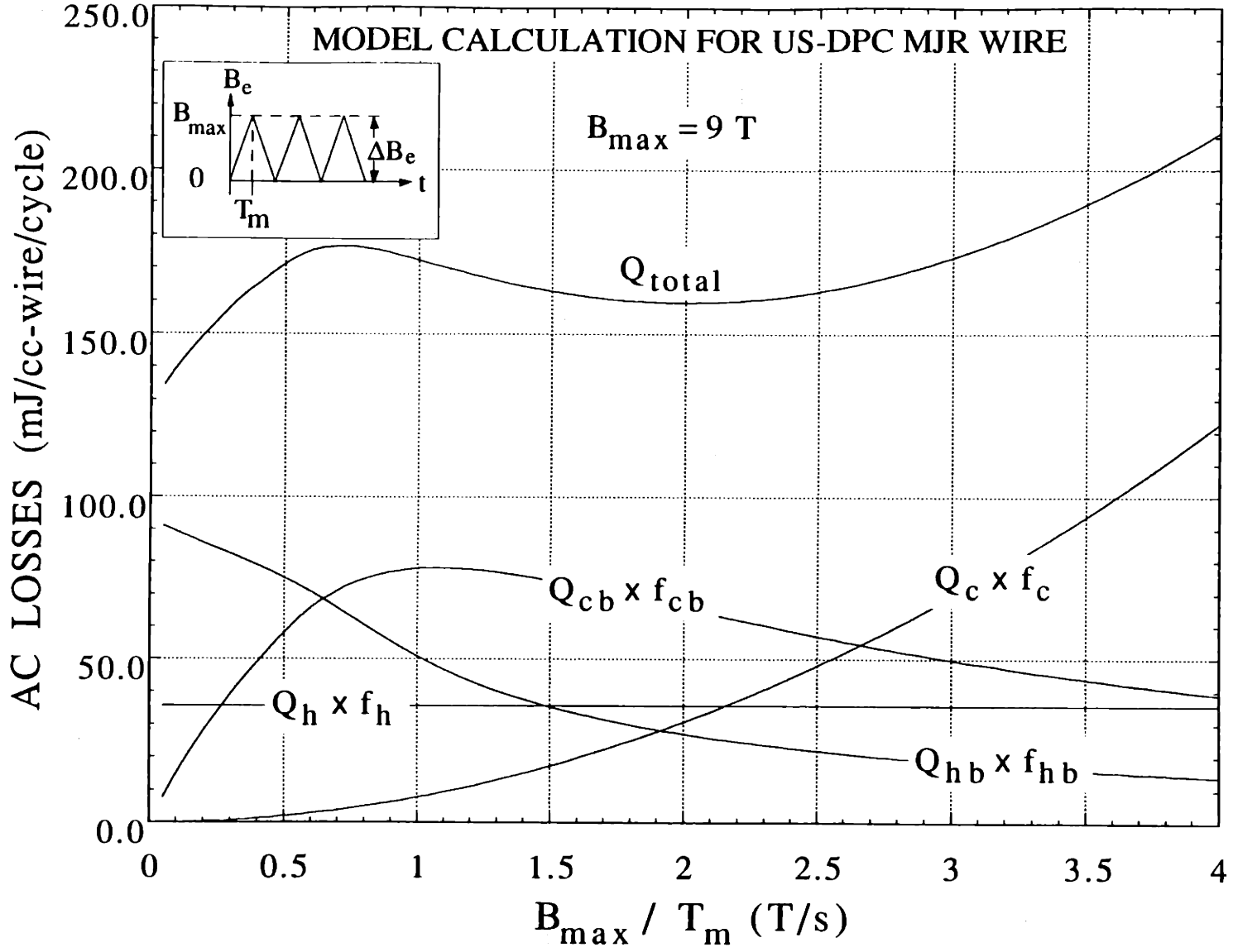

Fig. 6.3 Analytical AC-loss profiles including inter-bundle coupling effect, as a function of field ramp rate for the US-DPC MJR wire at $B_{max} = 9$ T.

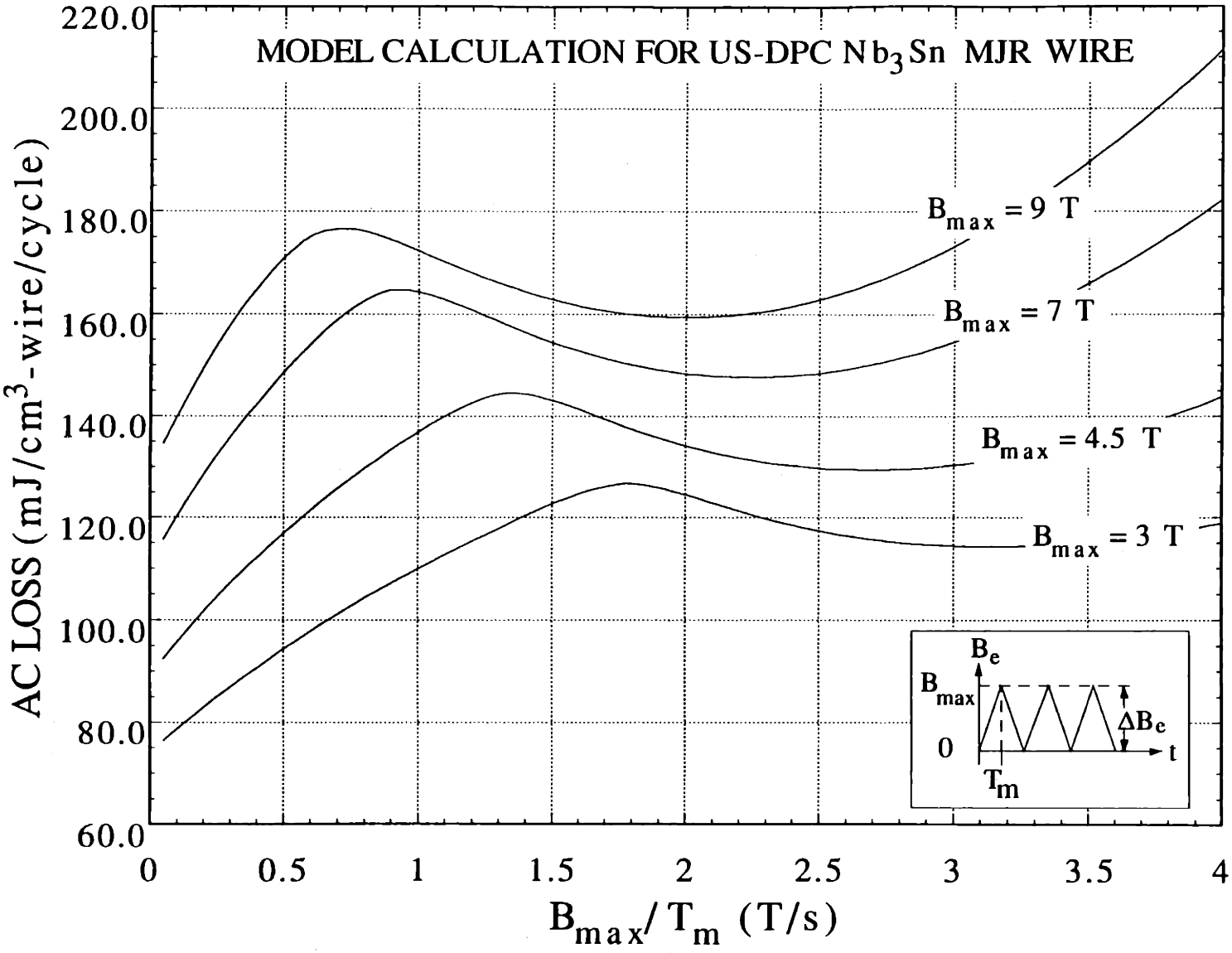

Fig. 6.4 Analytical AC-loss profiles including inter-bundle coupling effect, as a function of field ramp rate for the US-DPC MJR wire at different ranges of field variation.

VI.6 CONCLUSION

A local maximum at slow field variation was found in the AC-loss profile versus field ramp rate for the MJR wire which is different from those of the other two test wires, and is not predicted by the existing AC-loss models. The proposed inter-bundle coupling loss model is the first analytical model attempting to understand the loss mechanism causing the local maximum loss at a slow ramp rate. From the inter-bundle coupling effect, when the inter-bundle matrix resistivity is much lower than that of the intra-bundle, and the inter-bundle spacing is much smaller than the bundle wall thickness, the inter-bundle coupling time constant at a slow field variation is found to be magnified by a geometric effect. The magnification effect go to the inter-bundle coupling time constant diminishes at a higher ramp rate. With the proposed model and estimated MJR configuration, the calculated total AC-loss profile has a trend similar to that found from measurement. However, the local maximum loss in the calculation shifts to a higher ramp rate as the range of the field variation is reduced which is opposite to the trend from measurement. Also, the calculated local maximum losses are about 20% higher than those by measurement. Although having these discrepancies, the proposed inter-bundle coupling loss model is able to explain the local maximum loss in the slow ramp rate regime and to simulate the trend of the loss profile as a function of the ramp rate.

VI.7 REFERENCES

6.1 Turck, B., 'Effective transverse resistivity in multifilamentary superconducting composite,' ICEC 9 - ICMC, Kobe, Japan, May 11-14, 1982.

6.2 Walters, C.R., 'Stability and flux penetration in multifilament systems,' Paper II in 'Experimental and theoretical studies of filamentary superconducting composite,' Superconducting Magnet Group, Rutherford Laboratory, Chilton, Berks, RPP/A 73, November, 1969.

6.3 Kwasnitza, K., 'Scaling law for the AC losses of multifilaments superconductors,' Cryogenics, 1977, p. 616.

6.4 Ogasawara, T., et al., 'Transient field losses in multifilamentary composite conductors carrying dc transport currents,' Cryogenics, 1980, p. 216.

6.5 Ogasawara, T., et al., 'Transient field losses in multifilamentary composite conductors carrying transport currents,' IEEE Trans. on Magnetics, MAG-17, No. 1, 1981, p. 967.

6.6 Ito, D., Koisumi, M., Hamajima, T., Nakane, F., 'The influence of filament bundle location on coupling losses in superconducting composites. Part I: mixed matrix conductor,' Cryogenics, 1983, p. 643.

CHAPTER VII

ANALYSIS OF AC LOSSES IN THE US-DEMONSTRATION POLOIDAL COIL

VII.1 US-DEMONSTRATION POLOIDAL COIL (US-DPC)

The US-Demonstration Poloidal Coil (US-DPC) is a mid-size prototype ohmic heating coil designed as a development step in pulsed superconducting magnet technology. It was designed and built by the Superconducting Magnet Development Group at MIT and tested at the Japan Atomic Energy Research Institute (JAERI) in late 1990 (Ref. 7.1). The US-DPC consists of three double-pancake coils connected electrically in series. Each double pancake is wound with 150 m cable-in-conduit conductor (CICC), and has 33 turns with an inner winding diameter of 1 m and an outer diameter of 1.8 m. The cable is made of 225 strands of chrome-plated MJR internal-tin wire. Fig. 7.1 shows the schematic cross sectional view of the US-DPC cable enclosed in an Incoloy-908 double jacket. The Incoloy-908 was developed by MIT (Ref. 7.2) to satisfy the requirements of a sheathing alloy with a coefficient of thermal expansion closely matching that of Nb_3Sn (Ref. 7.3).

Fig. 7.2 shows the configuration of the Demonstration Poloidal Coil Test Facility at the JAERI (Ref. 7.1). The US-DPC was sandwiched by two background NbTi coils, DPC-U1 and DPC-U2. During the test, the US-DPC was energized either as a single coil or in series with the background coils. The US-DPC was cooled down to a temperature of about 4.5 K after the whole test facility was enclosed by a vacuum chamber which was surrounded with a liquid nitrogen layer. The test condition of the US-DPC was thus nearly adiabatic.

The goals of the US-DPC experiment were (Ref. 7.1): (1) Evaluation of the manufacturing process in terms of coil performance; (2) AC operation to 10 T at 10 T/s; (3) Evaluation of a dual-flow cooling scheme. The first goal was fully accomplished. The coil was able to operate in the DC mode to a peak field of 8 T in series with background coils. No detectable defect in the conduit or degradation of the conductor performance was found.

CROSS SECTIONAL VIEW OF THE US-DPC CONDUCTOR

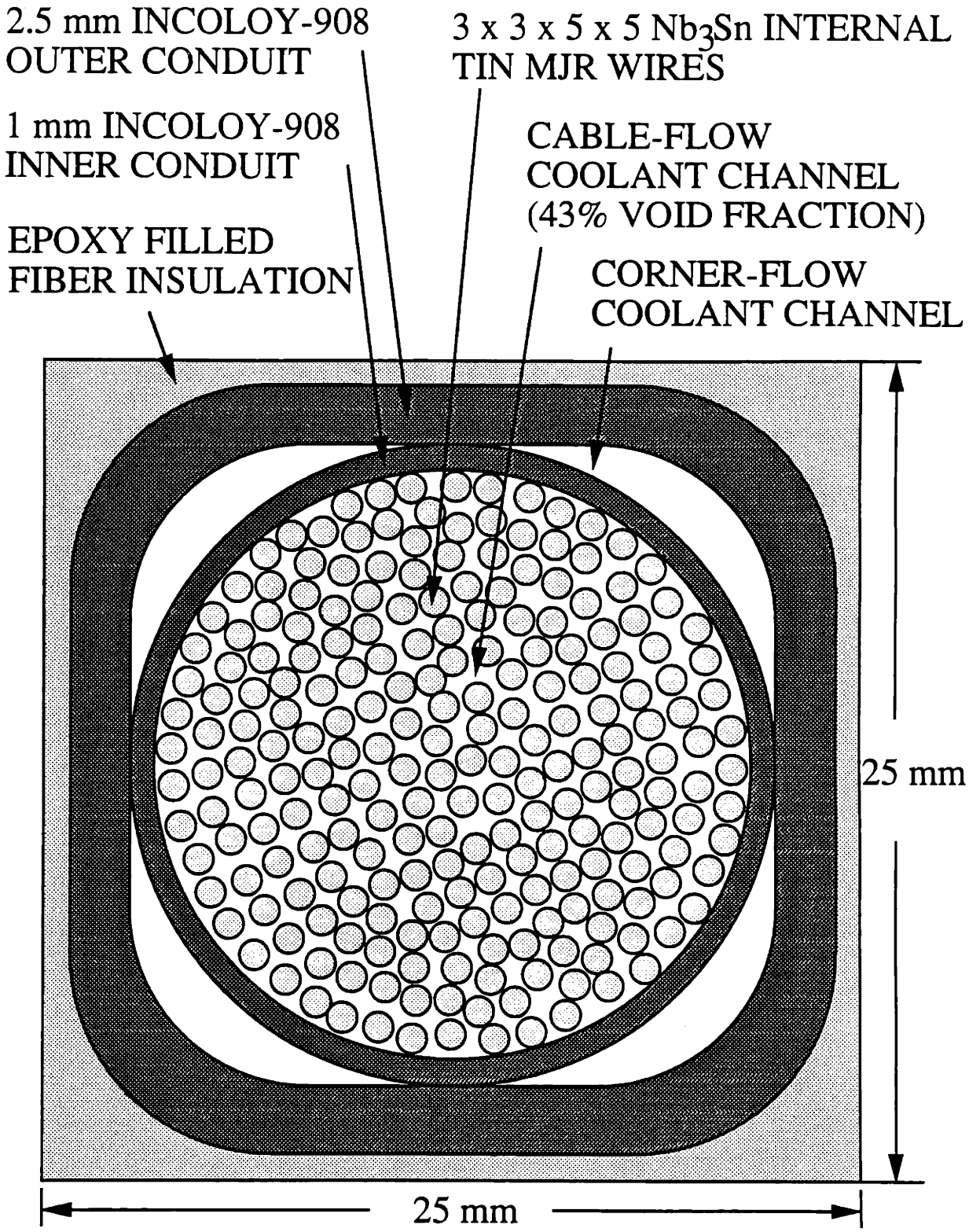

Fig. 7.1 Cross sectional view of the US-DPC cable-in-conduit conductor

DEMONSTRATION POLOIDAL COIL TEST FACILITY

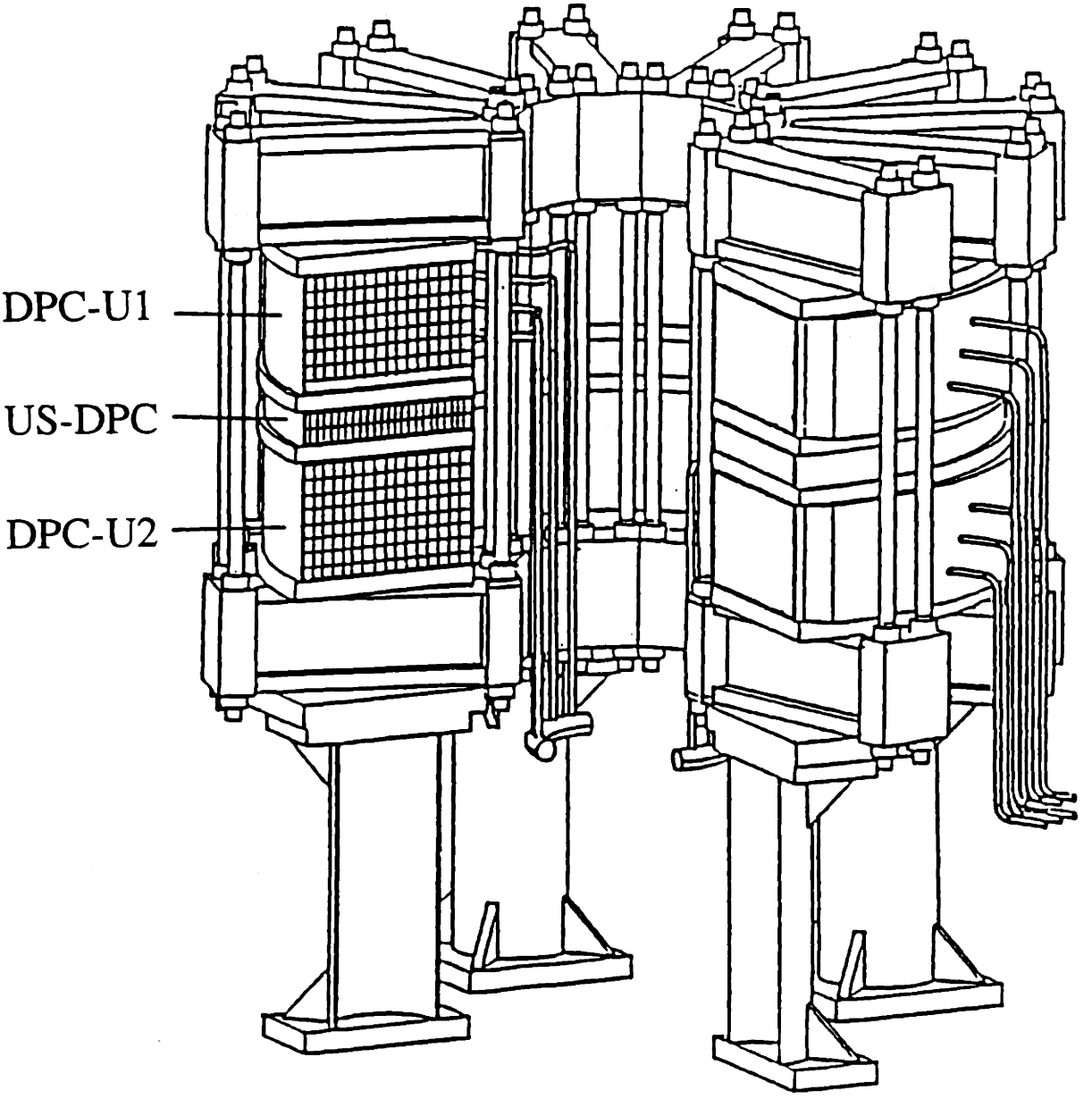

Fig. 7.2 Configuration of the Demonstration Poloidal Coil Test Facility at JAERI, Japan.

The Incoloy 908 conduit was proven to be compatible with the Nb_3Sn superconducting cable from the evidence that the critical current density in the US-DPC was consistent with that of a single strand (Ref. 7.4). One goal of the AC operation was to measure the AC losses in the US-DPC cable due to large simultaneously ramped field and current. The increment of the AC losses due to the cabling process was a major question to be answered. Another goal was to test the limits of the AC operation of the US-DPC. The design goal of 10 T at 10 T/s was ambitious for a large scale superconducting magnet such as the US-DPC. This goal was not achieved because of an unexpected ramp-rate limitation in the US-DPC coil. Operation from 0 T to 7 T at 7 T/s and 0 T to 3.8 T at 19 T/s was achieved. The third goal, evaluation of the dual flow cooling scheme, was abandoned during the experiment in order to allow more experimental time to study the ramp-rate limitation.

The distribution of the transverse time-changing field along the radial direction of the double-pancake winding as well as the field-dependent critical current density profile of the cable were obtained from the measurements in the US-DPC experiment (Ref. 7.1). The three double-pancake coils in the US-DPC were labeled as Coil A, B, and C. Each of Coil A and C had a helium-cooled current lead connected with the bus bar. Coil B was sandwiched by Coils A and C. It had more instrumentation and was better isolated from the possible Joule heating from the current leads. The AC loss analysis was concentrated on this specific coil. The specification of Coil B is listed in Table 7.1.

The purpose of this chapter is to understand the AC-loss characteristics of the full-size US-DPC cable as measured during the test program. Single-strand test results in various forms are compared with those of the cable to identify the difference in AC-loss behavior of the cable in addition to those in the constituent wires. Since the range of the available background field in the single-strand test is quite different from that applied in the US-DPC experiment (Fig. 7.3), the analysis has to be done through analytic calculations as discussed in Chapters II and III. The crucial AC-loss parameters in the strand and the US-DPC, i.e., the effective filament diameters for the hysteresis losses and the effective transverse resistivities for the coupling losses, are calculated for comparisons.

A practical scheme which predicts the AC losses in a full-size cable by using the laboratory-scale experimental results and the analytical formulae developed in this research, can be converted from the comparison process applied in this chapter. This prediction method for the AC losses of a full-size cable will be described in details.

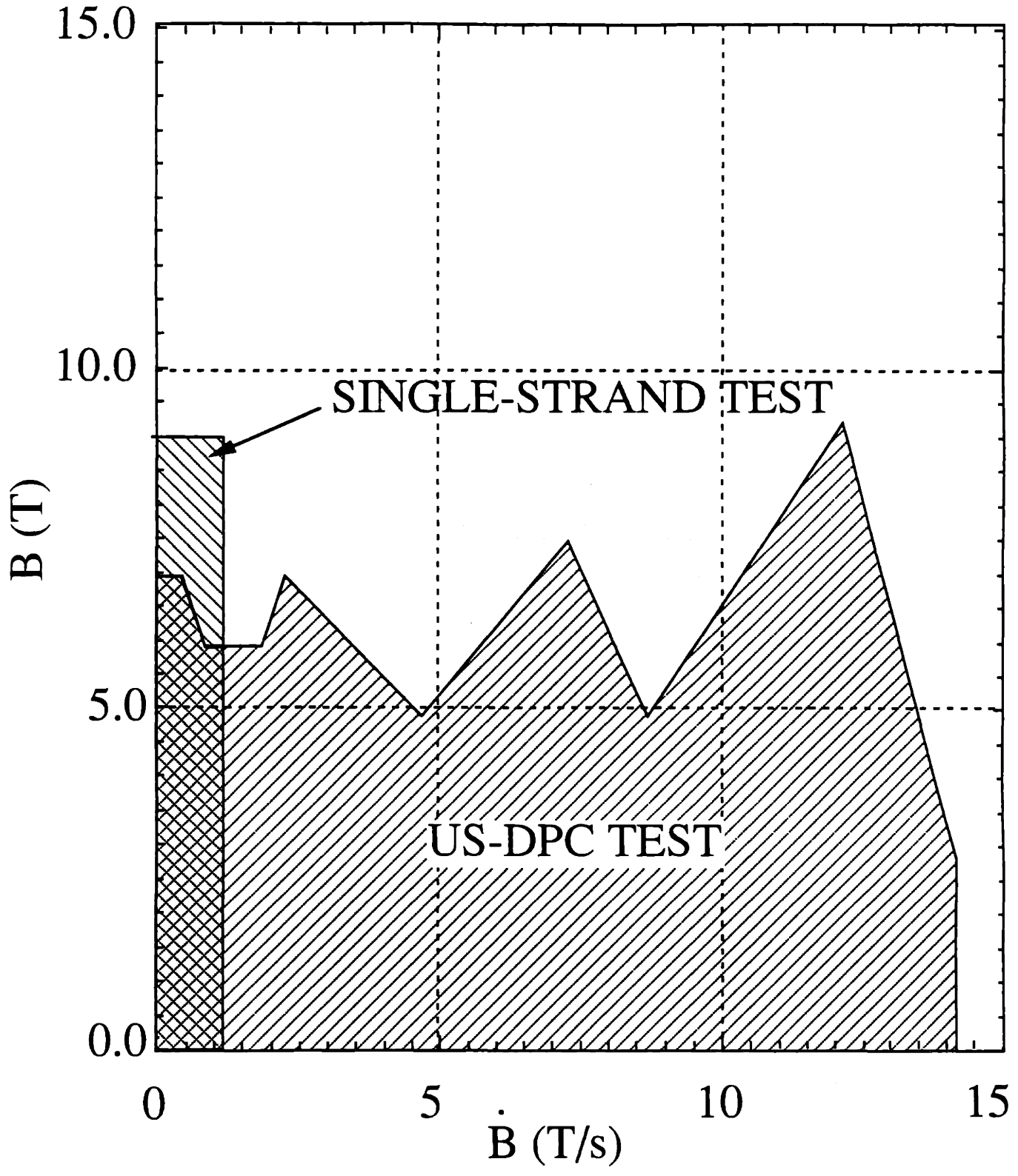

Fig. 7.3 Comparison of the field conditions in the US-DPC test (Ref. 7.1) and the single-strand test.

Table 7.1 Specification of the US-DPC Coil (Ref. 7.1)

Superconductor	MJR Nb_3Sn composite
Conduit	Incoloy-908
Coil winding	Double Pancake
Number of turns	33
Inner diameter	1.0 m
Outer diameter	1.8 m
Length	150 m
Load line (single US-DPC)	0.190 T/kA
Load line (series mode)	0.307 T/kA
Fraction of wires in cable space	57%
Cable channel cross sectional area	193.0 mm^2
Cable cross sectional area	108.6 mm^2
Number of strands	225
Cable pattern	3 x 3 x 5 x 5
Strand pitch	12.7 mm
Triplet pitch	51 mm
3 x 3 pitch	102 mm
3 x 3 x 5 pitch	203 mm
3 x 3 x 5 x 5 pitch	305 mm

VII.2 US-DPC EXPERIMENT

VII.2.1 Transverse Field Distribution Along the Conductor

Fig. 7.4 shows the calculated transverse field distribution on the mid-plane of the coil B as a function of the radius when the US-DPC is charged with a maximum current of 30 kA in the single coil mode (Ref. 7.1). Unlike the uniform background transverse field applied in the laboratory-scale experiment, the transverse field distribution is a highly non-uniform function of the radius of the pancake. The maximum field at the inner edge of the crossover turn is approximately 5.66 T at 30 kA. The minimum field was only 5% to 9% of the maximum value in the same pancake winding. The transverse field distribution in

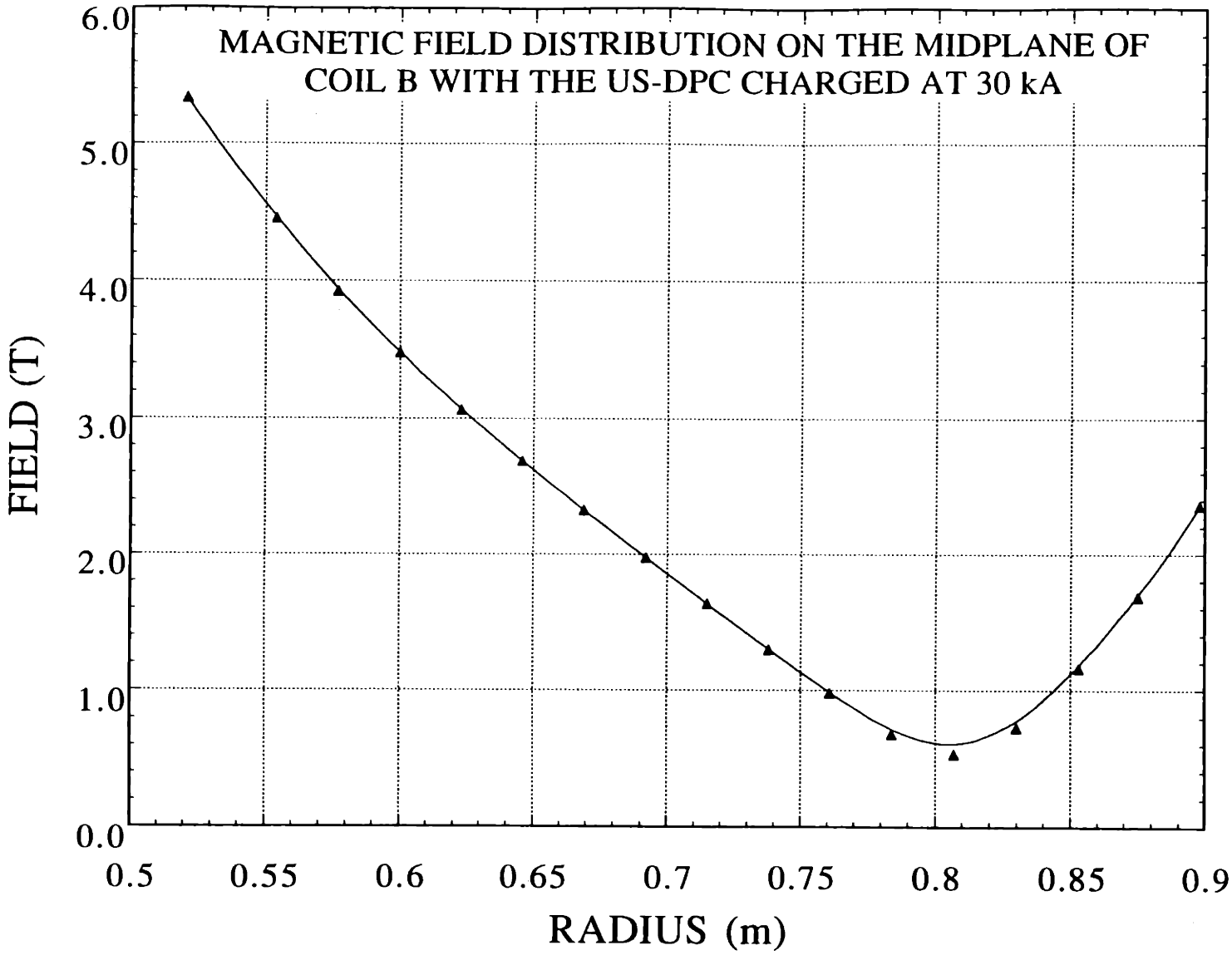

Fig. 7.4 Magnetic field distribution as a function of the radius on the midplane of the Coil B with the US-DPC energized at 30 kA in single coil mode.

each turn of the coil was considered to be uniform for purposes of AC-loss calculation. The magnitude of the field is linearly proportional to the applied current.

VII.2.2 Critical Current Density

The critical current measurement of the US-DPC was performed by both the transport current method and by the current-sharing temperature method (Ref. 7.4). The transport current method was applied at higher fields (> 3.5 T) at elevated helium temperatures. Lower field (down to about 1.9 T) critical currents were measured by the current-sharing temperature method. The transport current measurements were performed at different fixed helium inlet temperatures depending on the field level. The US-DPC was charged up slowly until a resistive voltage was measured in a length of the inner-most turn of the coil B. To measured the current-sharing temperature, the US-DPC was charged up and held at a fixed current, followed by raising the helium temperature until a resistive voltage at the same location was observed. In the overlapping test region, results from these two methods were consistent. The test results were further converted into the critical current at 4.2 K by using Eq. (3.1) (Ref. 7.4) which is a semi-empirical formula based partly on the flux-pinning theory. Eq. (3.1) is restated here as

$$J_c(b, t, \varepsilon) = C(\varepsilon)\ \{B_{c2}(T,\varepsilon)\}^{-1/2}\ (1-t^2)^2\ b^{-1/2}\ (1-b)^2\ \ (A/m^2 \text{ of non-Cu}) \qquad (7.1)$$

where

ε = uniaxial strain

$C(\varepsilon) = C_0(1-a\,|\varepsilon|^u)^{1/2}\ \ (A\ T^{1/2}\ m^{-2})$

C_0 = a coefficient independent of field, temperature, and strain $(A\ T^{1/2}\ m^{-2})$

$B_{c2}(t, \varepsilon) = B_{c20}(\varepsilon)\ (1-t^2)\{1 - 0.31\ t^2\ (1 - 1.77\ \ln t)\}\ \ (T)$

$B_{c20}(\varepsilon) = B_{c20m}(1-a\,|\varepsilon|^u)\ \ (T)$

$t = T/T_{c0}(\varepsilon)$

$b = B/B_{c2}(t, \varepsilon)$

$T_{c0}(\varepsilon) = T_{c0m}(1-a\,|\varepsilon|^u)^{1/w}\ \ (K)$

$a = 900$ for $\varepsilon < 0$, 1200 for $\varepsilon > 0$

$u = 1.7$

$w = 3$

With the first three fitting parameters fixed at $B_{c20m} = 27.5$ T, $T_{c0m} = 16$ K, and $C_0 = 8.8 \times 10^9$ A $T^{1/2}$ m^{-2}, Takayasu et al. (Ref. 7.4) found that Eq. (7.1) has the best fit to the

critical current data with T = 4.5 K and ε = -0.001 for the US-DPC conductor, and with T = 4.2 K and ε = -0.0036 for the MJR single-wire tests.

Another critical current density formula can be obtained by fitting the critical current data measured in single-wire barrel tests. The purely empirical exponential formula is given as

$$J_c'(B) = 5.972 \times 10^9 \, e^{-0.2162\,B} \quad [A/m^2 \text{ of non-Cu}] \quad \text{for } 2.5\ T \le B \le 15\ T \qquad (7.2)$$

As shown in Fig. 7.5, both Eqs. (7.1) and (7.2) have good fit to the measured critical currents in the field range between 2.5 T and 15 T. Only a small inconsistency is observed in the region between 2.5 T and 6 T. The exponential form slightly under-estimates the critical current at 2.5 T. However, in the field range below 2.5 T, the deviation of the extrapolated critical current distributions of these two formulae becomes significant as the field decreases.

The purpose of showing a second critical current formula Eq. (7.2) for the same experimental data set is to demonstrate how the lower field critical current dominates all other effects in evaluating the effective filament diameters. Both Eqs (7.1) and (7.2) will be applied in Section VII.3.2.2 to calculate the effective filament diameters from the hysteresis losses measured in the single-strand and US-DPC experiments.

VII.2.3 AC-loss Experiment

In the US-DPC experiment, a total of 232 current ramps (shots) were made in AC mode. Among the AC shots, 51 quenches were identifiable. The current applied to the US-DPC in each shot was either single or multiple pulses. Trapezoidal and triangular pulses were the major wave-forms applied in the experiment. The current rise-time varied from 0.5 s (0 kA to 30 kA) to 14 s (0 kA to 34 kA).

The AC loss in the US-DPC was measured with adiabatic calorimetric method. On each double-pancake, the coolant inlet and outlet pressures, mass flow rates, and temperatures were continuously monitored. All three parameters changed each time the coil was energized. However, the transient times of the helium flow-rate and the pressure at the helium outlet were on the order of few seconds which was short compared with ~ 200 s of the temperature transient. Therefore, it was a good assumption to consider the US-DPC as

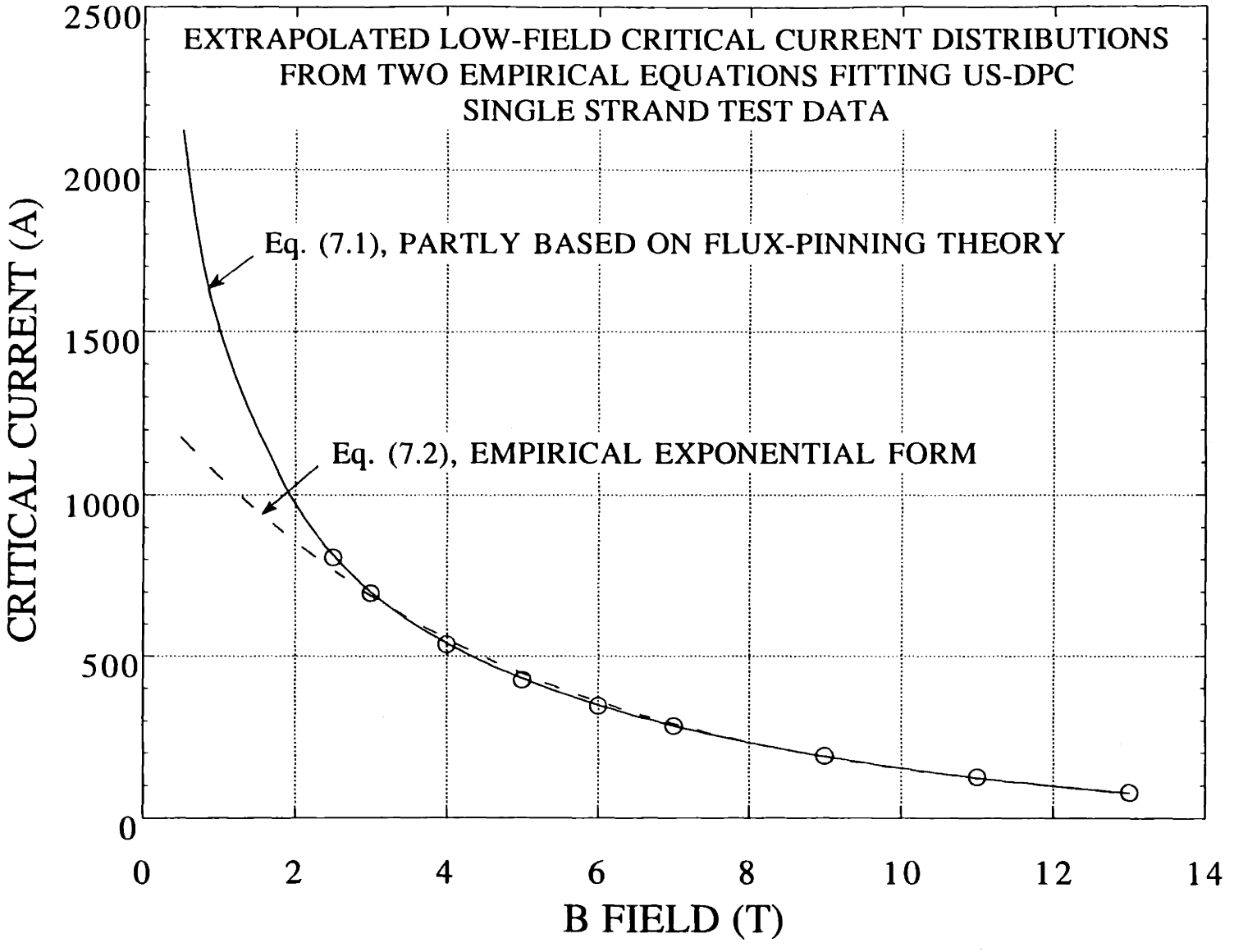

Fig. 7.5 Deviation of the extrapolated low-field critical current distributions of two formulae fitting the same set of US-DPC MJR single strand test data.

an adiabatic system. The AC loss was then calculated by the time-integral of the helium enthalpy change which depends on the helium temperatures at inlet and outlet.

VII.3 AC-LOSS ANALYSIS

VII.3.1 Introduction

Although the US-DPC was tested with transport current, the ratio of the transport current to the critical current was less than 40% in the highest field region. From single-wire AC loss measurements shown in Chapter V, the additional loss due to the transport current was expected to be less than 5% and thus was neglected in the present analysis. With the field and ramp rate conditions applied in the US-DPC experiment, the inter-strand coupling currents flowing in a cable made of bare composite wires which have copper-to-copper contacts, would be large enough to induce significant field screening in the cable (Ref. 7.5). However, the US-DPC cable was made of chrome-plated strands, and the inter-strand coupling current was reduced by the chrome layer (Ref. 7.6) and the field screening becomes negligible. This statement is verified by calculation of the effective coupling time constant in the cable in Section VII.3.3.2. The loss analysis is thus simplified to calculate only the hysteresis and coupling losses in the sum of the individual strands.

The Incoloy-908 is ferromagnetic with a low hysteresis loss of 4.1 mJ/cm^3/cycle in $\pm$ 1 T field-sweep which is at least one order of magnitude less than that of MJR superconducting wire. The electrical resistivity of Incoloy-908 is about two orders of magnitude higher than the copper in the composite wire. The eddy current loss in the conduit can be neglected. Thus, as a first order estimation, all the loss in the US-DPC will be considered as generated by the superconducting cable only.

VII.3.2 Effective Filament Diameter of the US-DPC

VII.3.2.1 Analytical Model

To evaluate the effective filament diameter from the measured loss results of Coil B, Eq. (3.35) calculating the d_{eff} of a single-strand from the experimental hysteresis loss in non-copper materials $[Q_{h,nonCu}]_{expt}$, which is given as

$$d_{eff} = 2\, r_{f,eff} \approx \frac{[Q_{h,nonCu}]_{expt}}{\frac{4}{3\pi}\int_{B_{min}}^{B_{max}} \frac{I_c(B)}{A\, f_{nonCu}}\, dB} \quad (m) \tag{3.35}$$

must be modified for the non-uniform transverse field distribution in the radial direction of the coil. The integration of the critical current density over the applied field is calculated turn-by-turn. The total loss is the sum of the losses in all the turns of the double pancake. By substituting Eq. (7.1) into Eq. (3.35) and setting B_{min} = 0 T, the expression of the effective filament diameter of a N turn cable is given by

$$d_{eff} = \frac{\underline{[Q_{h,ramp}]_{expt}\,(J/m^3\ wire/cycle)}}{f_{nonCu}} \quad (m) \tag{7.3}$$
$$\frac{4}{3\pi}\sum_{n=1}^{N}\frac{V_n}{V_{tot}}\left[C(\varepsilon)\, B_{c2}^{0.5}(t,\varepsilon)(1-t^2)^2\left(2b_{max,n}^{0.5} - \frac{4}{3}b_{max,n}^{1.5} + \frac{2}{5}b_{max,n}\right)\right]$$

where f_{nonCu} is the volume fraction of the non-copper material in the composite wire, $b_{max,n} = B_{max,n}/B_{c2}(t,\varepsilon)$ is the dimensionless maximum field in the nth turn of the pancake winding, V_n is the volume of the superconducting cable in the nth turn, and V_{tot} is the total volume of the superconducting cable in the double pancake.

Similarly, substituting the second critical current formula Eq. (7.2) into Eq. (3.35), the effective filament diameter d'_{eff} is given as

$$d'_{eff} = \frac{\underline{[Q_{h,ramp}]_{expt}\,(J/m^3\ wire/cycle)}}{f_{nonCu}} \quad (m) \tag{7.4}$$
$$\frac{4}{3\pi}\sum_{n=1}^{N}\frac{V_n}{V_{tot}}\left[2.76\times10^{10}\left(1 - e^{-0.2162\, B_{max}}\right)\right]$$

VII.3.2.2 Effective Filament Diameter

In Fig. 7.6, the AC losses of the Coil B in single-trapezoidal pulse fields are plotted against the ramp rate with the maximum applied current as a parameter. The experimental hysteresis losses of Coil B are estimated by extrapolating the best-fit line for each maximum current to zero ramp rate. Fig. 7.7 shows the distribution of the extrapolated hysteresis loss as a function of maximum applied field.

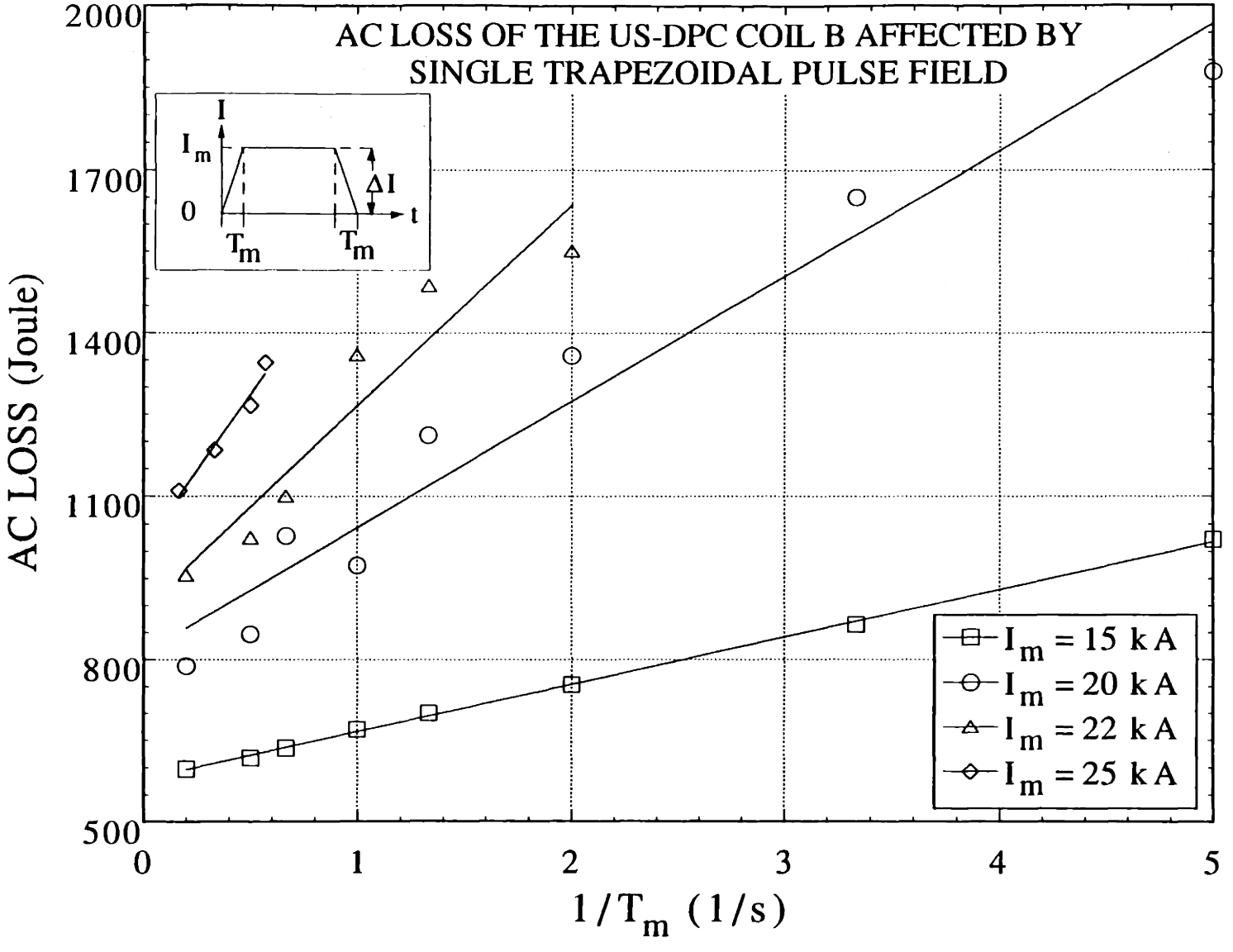

Fig. 7.6 Measured AC losses of US-DPC Coil B in single trapezoidal pulse fields. The hysteresis losses at different applied currents are obtained by extrapolating the best-fit lines to $1/T_m \sim 0$ (1/s).

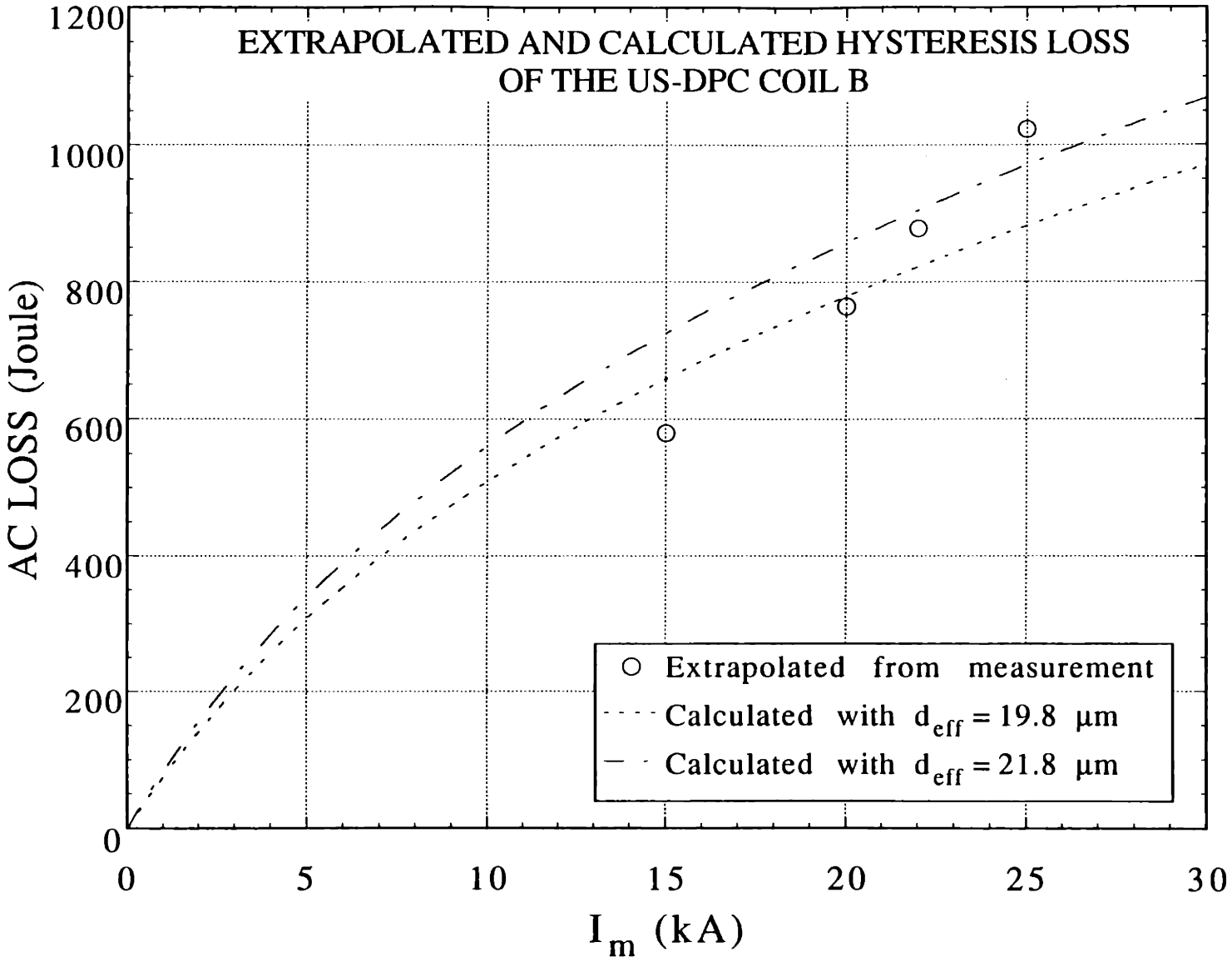

Fig. 7.7 Comparison of the extrapolated and calculated hysteresis losses in the US-DPC Coil B. d_{eff} = 21.8 μm is from the single-wire test, and d_{eff} = 19.8 μm is from the US-DPC test.

By using Eq. (7.3), the averaged d_{eff} of the US-DPC hysteresis loss is found as 19.8 μm. The variation is about 30%, with a maximum of 23 μm for 25 kA ramp and a minimum of 17.5 μm for 15 kA ramp. The d_{eff} in the single-strand test has been shown in Section V.4.1.2 as 21.8 μm with a variation of about 10%. Calculated hysteresis losses with these two best-fit d_{eff}'s are also shown in Fig. 7.7 for comparison. As a first-order comparison, these effective filament diameters from two experiments with very different configuration and field conditions are in reasonable agreement.

Fig. 7.7 also shows the inconsistency in the trends of the current (also field) dependent distributions of the extrapolated and the calculated hysteresis losses. The source of the inconsistency is not clear at this stage. A possible explanation is that the lower field shielding effect by the conduit material has not been included in the loss calculation. The Incoloy-908 is a ferromagnetic material which saturates at a field about 1 T. At a field lower than the saturation field of Incoloy-908, the superconducting cable inside the conduit will not be affected by the field generated from other turns. Since the transverse field distribution along the conductor is non-uniform in the double pancake winding, part of the coil volume experiences only a few percent of the peak field. When the applied current is lowered, the volume of the coil in a lower field regime (say < 1 T) is increased. When the current applied to the US-DPC is 15 kA, about 2/3 of the Coil B volume is below 1 T. This is a likely explanation of the steeper loss distribution of the experimental hysteresis loss than that by calculation when the loss is plotted against the applied current. Experimental verification of the field shielding effect by the Incoloy-908 conduit should be a future research subject.

In addition to the consistent d_{eff} calculated from the hysteresis losses measured in the US-DPC and the single-strand tests, it is important to know the sensitivity of the d_{eff} to various variables. As seen in Eq. (7.3), the d_{eff} is affected by the critical current profile which is a function of field, temperature, and strain. In the following few paragraphs, the sensitivity of the d_{eff} will first be examined by perturbing the temperature and strain conditions. The d'_{eff} calculated with the second critical current formula Eq. (7.2) which is inconsistent with the first formula Eq. (7.1) only in the low-field regime, will be compared with that in the reference case for the purpose of examining the low-field critical current effect on the d_{eff}.

The sensitivity of the effective filament diameter evaluated with Eq. (7.3) due to the variations of the temperature and the strain are examined by perturbing the temperature between 4.2 K and 4.5 K and the strain between -0.0036 and -0.001. The reference case for measuring the critical current are T = 4.5 K and e = -0.001 for the US-DPC test and T = 4.2 K and e = -0.0036 for the single-strand test. The reference d_{eff}'s are listed in Table 7.2 as cases 1 and 2. The perturbed d_{eff}'s are listed as cases 3 to 5. The d_{eff} shown in case 3 is calculated using the hysteresis loss from the US-DPC test and the critical current profile of the single-strand. Comparing cases 1 and 3, the perturbed d_{eff} deviates from the reference value by less than 10%. The hysteresis loss (and the d_{eff}) calculation by using the J_c model from Eq. (7.1) is not sensitive to the temperature and strain effects in the ranges applied to the present study.

Table 7.2 Comparisons of effective filament diameters

Case	Experiment	J_c model	Applied T [K]	Applied ε [%]	d_{eff} (μm)
1	US-DPC (Reference)	$J_c(b, t, \varepsilon)$	4.5	-0.1	19.8
2	Single Wire (Reference)	$J_c(b, t, \varepsilon)$	4.2	-0.36	21.8
3	US-DPC	$J_c(b, t, \varepsilon)$	4.2	-0.36	20.1
4	US-DPC	$J_c(b, t, \varepsilon)$	4.5	-0.36	20.4
5	US-DPC	$J_c(b, t, \varepsilon)$	4.2	-0.1	19.4
6	US-DPC	$J'_c(B)$	4.2	----	38
7	Single Wire	$J'_c(B)$	4.2	----	28

As mentioned before, both Eqs. (7.1) and (7.2) have good fitting to the measured single-strand critical current profile within the range where the test data are available. According to the above comparison of cases 1 and 3 in Table 7.2, the d'_{eff} calculated with Eq. (7.4) using $J'_c(B)$ in Eq. (7.2), should similarly give a consistent result for both the US-DPC and the single-strand test. The effective filament diameters of both the US-DPC and the single-wire are re-calculated by using Eq. (7.4) and the calculated results are listed as cases 6 and 7 in Table 7.2.

With the exponential formula $J_c'(B)$, the d_{eff} is estimated as 38 μm for the US-DPC, and 28 μm for the single-wire. In contrast to the good agreement in cases 1 and 2, the inconsistency of the d_{eff} in cases 6 and 7, for the similar composite wire applied in different experiments is as large as 30%. The d_{eff} = 38 μm for the US-DPC agrees with the preliminary estimation of 45 μm by JAERI (Ref. 7.7) who used another critical current

fitting formula in exponential form. The ~ 35% disagreement in the d_{eff}'s in cases 2 and 7 is apparently caused by the difference in the J_c distributions in the low-field (< 2.5 T) region as mentioned above. An under-estimation of the low-field critical current distribution in Eq. (7.2) causes a smaller loss integration, and consequently a larger d_{eff} value in case 7.

The inconsistency in effective filament diameters evaluated in cases 6 and 7 can be explained from the field condition applied in the US-DPC. Due to the non-uniform field distribution along the conductor, ~ 30% (if I_m = 25 kA) to ~ 60% (if I_m = 15 kA) of the US-DPC cable volume is affected by a field always lower than 1 T. The under-estimation of the low-field J_c becomes more apparent to the d_{eff} evaluation for the US-DPC than for the single wire. This is the major reason why the d_{eff} in case 6 is so much higher than that in case 7 when the same J_c model was applied.

From the above comparisons for the US-DPC and single-strand experiments, one may conclude that the low-field critical current distribution is more important than the temperature and the strain effects in determining the hysteresis loss or the effective filament diameter when the other quantity is known. Low-field critical current profile must be confirmed experimentally when it is adopted to calculated the AC losses in a superconducting magnet built for ramp field application.

VII.3.3 Coupling Time Constant of the US-DPC

The major contribution to the AC loss in a cable made of bare composite wire is the inter-strand coupling loss which can be more than one order of magnitude higher than the total loss in a single strand (Refs. 7.5, 7.6, and 7.8). The analytical solution of the coupling time constant of a cable is complicated by the interaction of several factors such as the true value of the transverse resistivity of the composite wire in the cable, different twist pitches at different cabling stages, uncertainties in the inter-strand contact resistivity affected by the surface condition, the cable compaction, and the Lorentz force. (Refs. 7.6 to 7.8). So far, the effective coupling time constant of a cable has to be found experimentally. A general analytical model calculating inter-strand coupling loss applicable to most of the experimental results has not been fully developed.

In the case of the US-DPC, the cable was made of chrome-plated composite wires. The contact resistivity between wires is assumed to be high enough to impede most of the inter-

strand coupling currents (Ref. 7.6). Based on this assumption and the frequency range of the US-DPC operation, the field screening effect in the cable will be neglected for now. This approximation will be verified once the effective coupling time constant in the cable is computed. Since the chrome layer is not a perfect electric insulator, inter-strand coupling current is still expected. Order of magnitude evaluation of this additional loss is one of the major subjects of this subsection.

Again, due to the different background field conditions applied in the single-strand and the US-DPC experiments, comparison of the losses will first be performed on the basis of an effective coupling time constant. At a low frequency of field variation where the field screening is negligible, the coupling loss is proportional to the coupling time constant (Eq. 3.66). If no other source of dissipation after the hysteresis and the coupling losses are accounted for in these test results, the increment of the coupling time constant will be the contribution from the cabling process.

Only a few of the US-DPC measurements were made when the coil was charged with a small amplitude sinusoidal AC current superimposed on the flat-top of a trapezoidal AC current. The AC-loss results in these ripple field tests were used to calculate the coupling time constant and compared with that of a single-strand. The hysteresis loss in the ripple field test can not be extracted experimentally as in the ramp field test. Hysteresis loss in a ripple field was thus estimated analytically by applying the already characterized effective filament diameter.

The effective coupling time constant calculated from the losses of the US-DPC is a lumped parameter since the coupling time constant of the cable in the double pancake winding is affected by the non-uniform field distribution. From the single-strand calculation, the variation of the intra-strand coupling time constant caused by the change of the magnetoresistivity is about 10% for the field range between 0 T and 12 T. The variation of the magnetoresistivity affected by the DC bias fields in different turns of the double pancake will be neglected since the uncertainties in estimating both inter- and intra-strand transverse resistivities may be even larger.

The hysteresis losses of the US-DPC in single trapezoidal ramp field condition have been estimated by extrapolating the ramp rate dependent total loss profiles down to zero ramp rate. From the same set of test results, the coupling loss is obtained by subtracting the extrapolated hysteresis loss from the total loss. Single-strand coupling loss calculated

for the US-DPC field condition will be multiplied by the number of wires in the cable and compared with the experimental results. The purpose is to identify any significant AC-loss behavior in the cable in addition to those measured in the single-strand tests.

VII.3.3.1 Analytical Models

A composite superconductor is affected by a transverse ripple field superimposed on a DC bias field defined as

$$B_e(t) = B_{DC} + \frac{\Delta B_e}{2} \sin \omega t \tag{7.5}$$

where ω is the angular frequency, ΔB_e is the peak-to-peak value of the applied sinusoidal ripple field, and B_{DC} is the DC bias field in the same direction as the ripple field. The coupling loss per cycle of a superconductor wire is obtained by integrating the loss power function Eq. (2.65) over the period of the field variation. The Eq. (2.65) is restated here as

$$P_c = 2 \frac{\tau_w(B_e) \dot{B}_e^2}{\mu_0} \quad (W / m^3 \text{ wire}) \tag{2.65}$$

where $\tau_w(B_e)$ is the coupling time constant of a single-strand as a function of external field B_e. The coupling loss for a single-wire is integrated over one field cycle as

$$Q_{c,ripple} = \frac{\Delta B_e^2}{2\mu_0} \frac{\pi \omega \tau_w(B_{DC})}{1 + \omega^2 \tau_w^2(B_{DC})} \quad (J / m^3 \text{ wire / cycle}) \tag{7.6}$$

For self-sufficiency , the hysteresis loss of a cylindrical superconductor in a small cyclic field condition, based on the critical state model, is restated here as

$$Q_h = \frac{\Delta B^2}{2\mu_0} \left[\frac{4}{3} \frac{\Delta B}{\Delta B_p(B_{DC})} - \frac{2}{3} \left(\frac{\Delta B}{\Delta B_p(B_{DC})} \right)^2 \right] \qquad \text{for } \Delta B \le \Delta B_p(B_{DC}) \tag{3.12}$$

$$Q_p = \frac{\Delta B_p^2(B_{DC})}{3\mu_0} \qquad \text{at } \Delta B = \Delta B_p(B_{DC}) \tag{3.13}$$

and

$$Q_h = \frac{2\Delta B_p^2(B_{DC})}{3\mu_0}\left[\frac{\Delta B}{\Delta B_p(B_{DC})} - \frac{1}{2}\right] \qquad \text{for } \Delta B > \Delta B_p(B_{DC}) \qquad (3.14)$$

where

$$\Delta B_p(B_{DC}) = \frac{4}{\pi}\mu_0 J_{c,SC}(B_{DC})\, r_f \qquad (3.10)$$

and $\Delta B \approx \Delta B_e$ for the US-DPC frequency range.

A similar set of equations is used to calculate the effective coupling time constant of the US-DPC cable. Since the total loss is obtained experimentally and the calculated hysteresis loss is not affected by the cabling process (unless the field screening is present), the coupling loss of the cable is expressed as

$$\sum_{n=1}^{N} \{Q_{c,ripple,n}\, V_n\} = [Q_{tot}]_{expt}\, V_{tot} - \sum_{n=1}^{N} \left\{\frac{[Q_{h,n}]_{calc}}{f_{SC\ in\ wire}} V_n\right\} \qquad (7.7)$$

where $[Q_{tot}]_{expt}$ is the experimental total loss and V_n is the volume of the composite wires in turn n of Coil B. $Q_{h,n}$ is the hysteresis loss per unit volume of the superconductor in turn n of Coil B which is modified from Eqs. (3.12) and (3.13) as

$$Q_{h,n} = \frac{\Delta B_{e,n}^2}{2\mu_0}\left[\frac{4}{3}\frac{\Delta B_{e,n}}{\Delta B_p(B_{DC,n})} - \frac{2}{3}\left(\frac{\Delta B_{e,n}}{\Delta B_p(B_{DC,n})}\right)^2\right] \qquad \text{for } \Delta B_{e,n} \le \Delta B_p(B_{DC,n}) \quad (7.8)$$

and

$$Q_{h,n} = \frac{2\Delta B_p^2(B_{DC,n})}{3\mu_0}\left[\frac{\Delta B_{e,n}}{\Delta B_p(B_{DC,n})} - \frac{1}{2}\right] \qquad \text{for } \Delta B_{e,n} > \Delta B_p(B_{DC,n}) \quad (7.9)$$

with

$$\Delta B_p(B_{DC,n}) = \frac{2}{\pi}\mu_0 J_{c,SC}(B_{DC,n})\, d_{eff} \qquad (7.10)$$

where the effective filament diameter d_{eff} has been estimated in Subsection VII.3.2.2. The coupling loss in turn n of the Coil B is estimated as

$$Q_{c,ripple,n} = \frac{\Delta B_{e,n}^2}{2\mu_0} \frac{\pi\omega\tau_{eff}}{1 + \omega^2\tau_{eff}^2} \tag{7.11}$$

The effective coupling time constant τ_{eff} of the cable in the Coil B is the lumped parameter to be determined from the ripple field test.

In the case of a trapezoidal pulse, only the time-varying part of the field causes AC losses. The external field can be considered as a triangular field with the same rise-time and down-time T_m, and $|\dot{B}_{e,n}| = (B_{max,n} - B_{min,n}) / T_m$. When the field variation is large, for example on the order of Tesla, the magnetic effect to the matrix material should be accounted. The coupling time constant changes instantaneously with the external field, which is no longer a single value as in the case of ripple field. Substituting the linear field pattern and the field-dependent matrix resistivity into Eq. (2.65) for turn n in Coil B and integrating over a field cycle, the expression for the total coupling loss in Coil B affected by the triangular AC field is thus written as

$$\sum_{n=1}^{N} Q_{c,ramp,n} V_n = \sum_{n=1}^{N} 2\left(\frac{L_p}{2\pi}\right)^2 \frac{B_{max,n} - B_{min,n}}{\beta T_m} \ln\left[\frac{\frac{\rho_{0,RT}}{RRR} + \beta B_{max,n}}{\frac{\rho_{0,RT}}{RRR} + \beta B_{min,n}}\right] V_n \quad (J / cycle) \tag{7.12}$$

The total coupling loss in the Coil B affected by a ramp field can be obtained by subtracting the extrapolated hysteresis loss from the total loss for each maximum applied field.

VII.3.3.2 Effective Coupling Time Constant and Coupling Loss

Three of the US-DPC test results (shots 205 to 207) of Coil B are used to evaluate the effective coupling time constants. All were single-trapezoidal pulses ramped up from 0 kA to 20 kA in 1 s, followed by a flat-top of 13 s, then ramped down to 0 kA in 1 s. In the latter two shots, a 6.5 Hz sinusoidal wave-form field was superimposed on the flat-top for 11 s with a peak-to-peak current value of 600 A and 1400 A for shot 206 and 207, respectively. The coupling loss due to the sinusoidal ripple is obtained by subtracting the total loss of shot 205 from that of shot 206 or 207. With the measured total loss and

calculated hysteresis loss of coil B in the ripple field test, the effective coupling time constants of the US-DPC Coil B are estimated with Eqs. (7.7) to (7.11).

Fig. 7.8 shows the non-uniform radial distributions of the transverse ripple and DC bias fields. The ripple field was generated by a 600 A current ripple. Both fields are transverse to the cable and parallel to each other. The τ_{eff}'s of Coil B in those two ripple field conditions are listed in Table 7.3 as cases 1 and 2. The radial distributions of the calculated hysteresis and coupling losses for case 1 are shown in Fig. 7.9. To verify the present computational scheme, the τ_{eff}'s of the single-wire CRe1116, tested in uniform background field, and evaluated by the same method from the coupling losses, are also shown in the same Table as cases 3 and 4. The τ_{eff} in case 5 is estimated analytically by applying a multi-layer construction model (II.3.3) to the MJR wire.

Table 7.3 Comparison of effective coupling time constants obtained in ripple field tests

No	Specimen	Ripple Field	f (Hz)	Bias Field	$[Q_{tot}]_{expt}$ (J/cycle)	$[Q_h]_{calc}$ (J/cycle)	$Q_{c,ripple}$ (J/cycle)	τ_{eff} (ms)
1	Coil B	ΔI = 0.6 kA	6.5	20 kA	4.11	0.86	3.25	1.18
2	Coil B	ΔI = 1.4 kA	6.5	20 kA	37.38	5.77	31.61	2.12
3	CRe1116	ΔB= 0.086 T	7.5	3.37 T	0.0091	0.0037	0.0054	0.88
4	CRe1116	ΔB= 0.086 T	7.5	4.30 T	0.0090	0.0039	0.0051	0.82
5	MJR Wire	ΔB= 0.086 T	7.5	0 T	Analytical Calculation			~ 0.85

Comparing the coupling time constants of the single wire in cases 3 to 5, the effective values evaluated using the method discussed in this subsection are in good agreement with the analytical prediction. Comparing cases 1 and 2 with case 5, the effective coupling time constant of the US-DPC Coil B is larger than that of the single-strand by a factor of 1.4 and 2.5, respectively. When the Coil B is operated at a similar frequency as the single-strand, the small increment of the effective coupling time constant in the Coil B provides a strong evidence that the chrome-plating on the wire effectively reduces most of the inter-strand coupling currents.

The two effective coupling time constants of Coil B in cases 1 and 2 are inconsistent. With limited ripple test results, it is difficult to judge whether the loss in case 1 was under-estimated or the loss in case 2 was affected by an additional heat source such as Joule heating due to a recovered quench. More information may be obtained from the

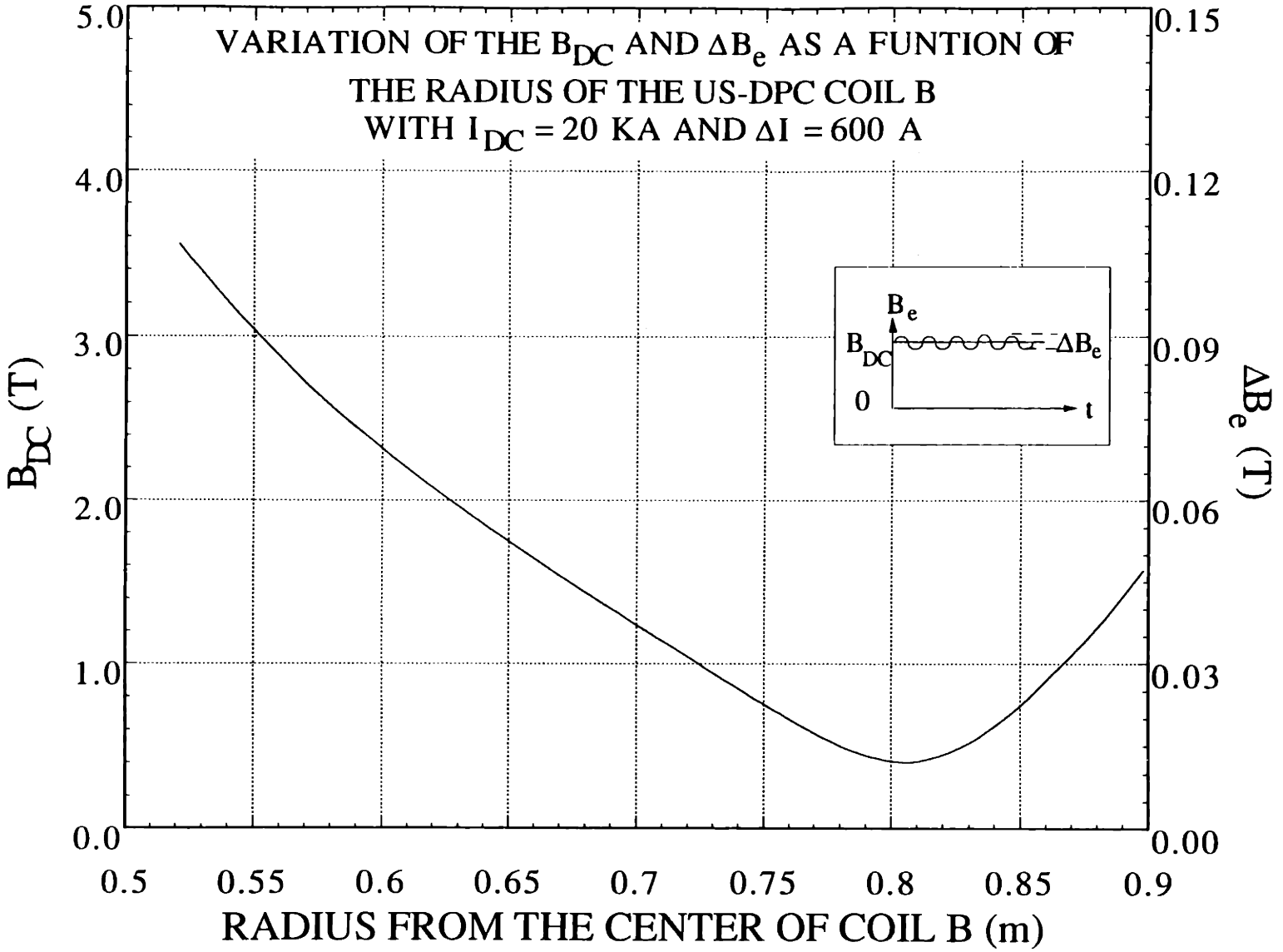

Fig. 7.8 Variation of the DC bias field and the peak-peak field as a function of the radius of the US-DPC Coil B when I_{DC} = 20 kA and ΔI = 600 A ripple is applied.

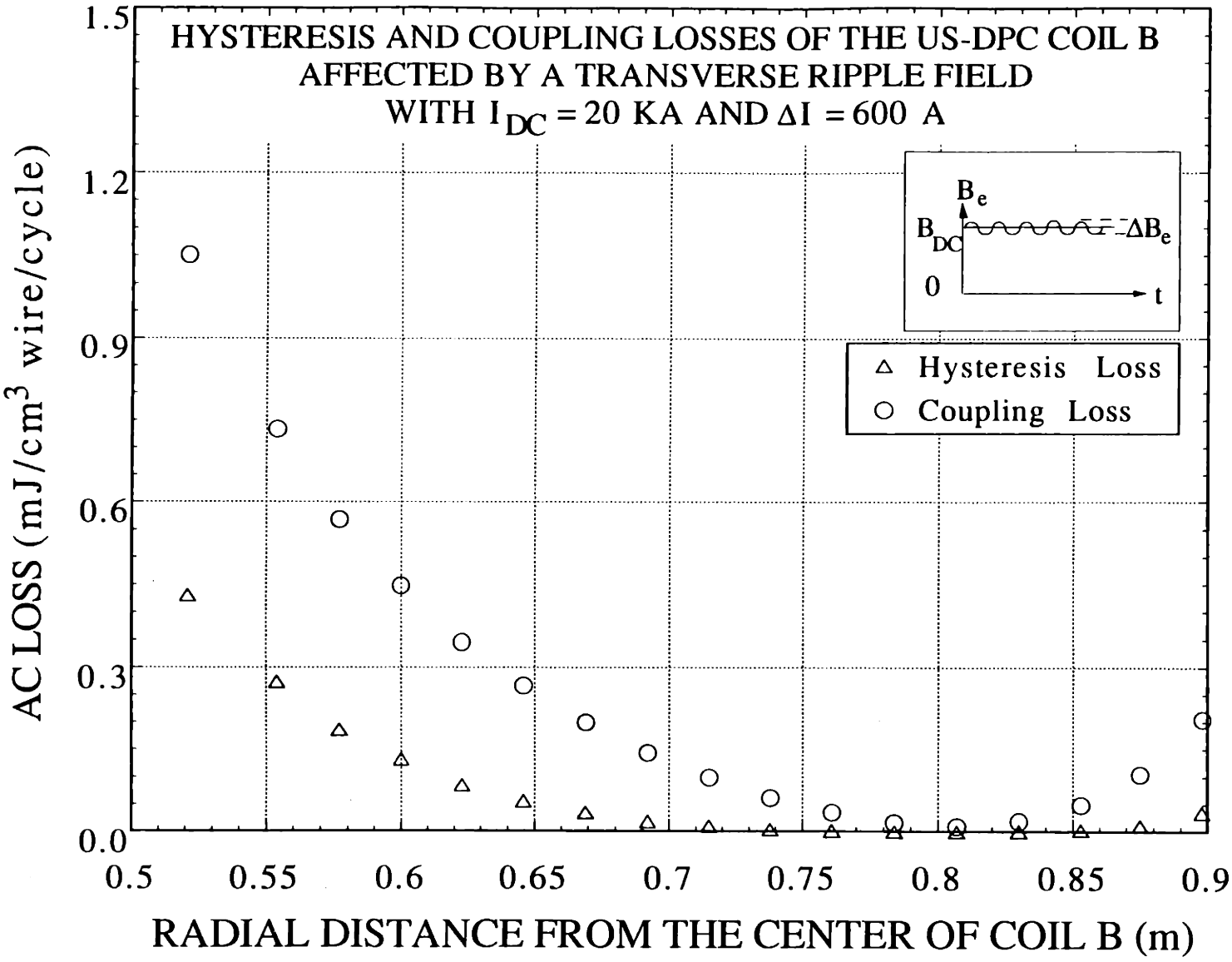

Fig. 7.9 Calculated hysteresis and coupling losses in each turn of the US-DPC Coil B affected by a ripple field generated by I_{DC} = 20 kA and ΔI = 600 A.

comparison of the measured coupling losses of the Coil B with the analytical results of single-wire for the trapezoidal ramp field condition.

The experimental coupling losses of Coil B in the single trapezoidal pulse field tests as shown in Fig. 7.10 are obtained by subtracting the extrapolated hysteresis losses from the total losses. Applying the same US-DPC field conditions to the calculation, the analytical coupling losses of 225 single-strands are also plotted in the same figure as solid lines. Since the additional inter-strand coupling loss is not in the single-strand loss calculation, it is not surprising that the coupling loss profiles of single-strands are lower than those of Coil B. As seen in Fig. 7.10, the above description is true when the current applied to the Coil B is greater than 15 kA. Moreover, the coupling losses in the cable are less than 50% higher than that in 225 single-strands which is consistent with case 1 in Table 7.3 in the ripple field analysis. This indicates that the loss result of case 2 in ripple field test is very likely affected by some extra heat source.

When the current applied to the US-DPC is 15 kA, the coupling loss in the cable is consistently lower than that in the single-strands. This is consistent with what has been shown in Fig. 7.6 in the analysis of the hysteresis loss and effective filament diameter. The same explanation of field shielding effect in the cable due to the magnetization of the Incoloy-908 conduit can be applied here as well.

The presumption of negligible field screening effect caused by the inter-strand coupling currents in the Coil B can be verified by extending the criteria of penetration loss for a single-strand (Section III.4) to a cable. In a single-strand, the importance of field screening effect is judged by comparing the magnitudes of the screening field $\tau\dot{B}_e$ caused by the coupling currents with that of the penetration field of the multifilamentary zone $B_{p,MF}$. The field screening effect is neglected if $\tau\dot{B}_e << B_{p,MF}$. In analogy to the single-strand, the penetration field of the cable is defined as

$$B_{p,cable}(B_{DC}) \equiv \frac{1}{\pi}\mu_0 J_{c,SC}(B_{DC}) f_{SC\ in\ wire} f_{wire\ in\ cable} D_{cable} \qquad (7.13)$$

where $f_{wire\ in\ cable}$ is the fraction of the wires in the cable space (Table 7.1) and D_{cable} is the equivalent diameter of the US-DPC cable, which is defined as

$$\frac{\pi}{4} D_{cable}^2 \equiv \text{cable channel cross sectional area}$$

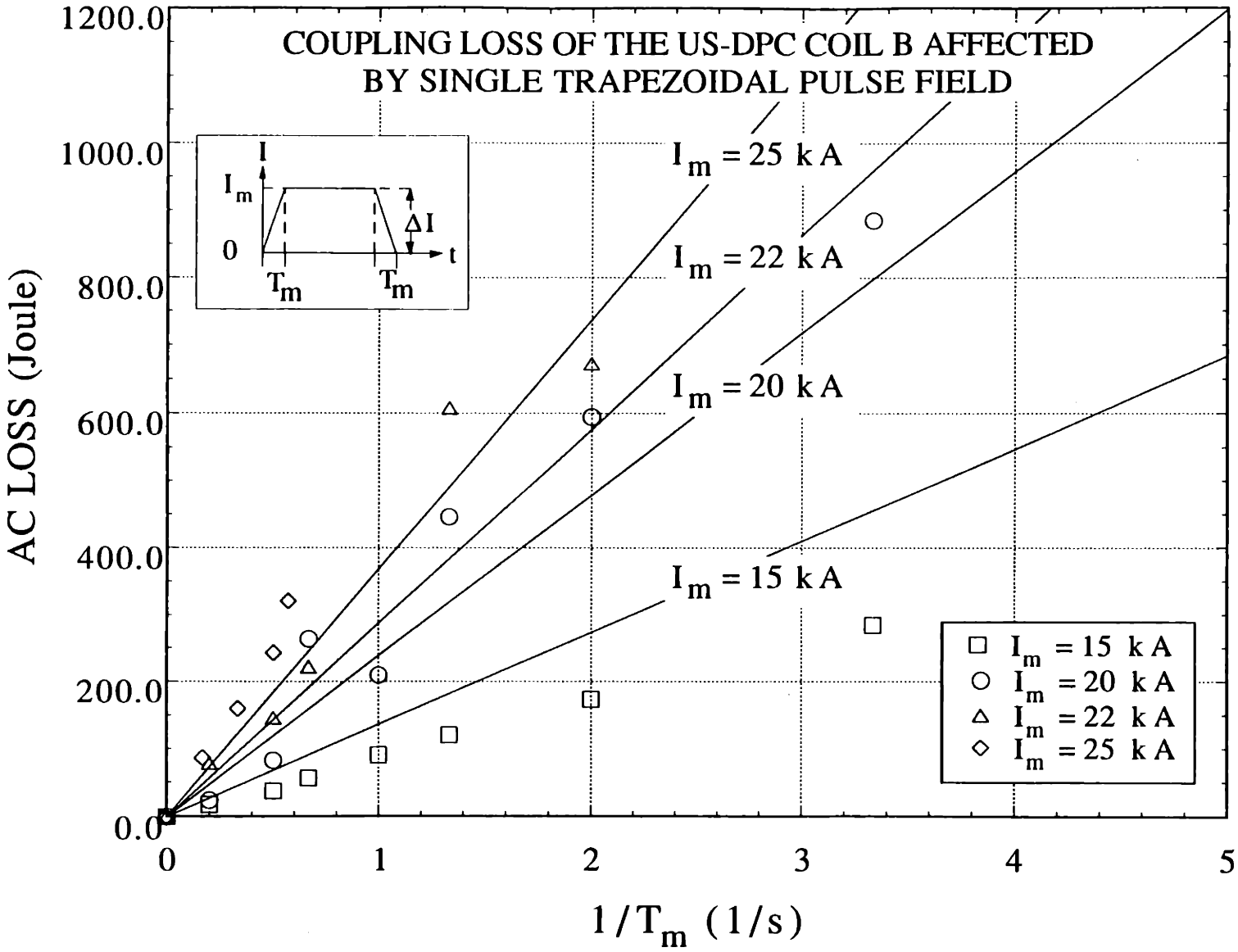

Fig. 7.10 Comparisons of measured (symbols) and calculated (lines) coupling losses in the US-DPC Coil B affected by single trapezoidal pulse fields.

The field screening effect in a cable is negligible if

$$\tau_{eff}\dot{B}_e << B_{p,cable} \tag{7.14}$$

By setting the B_{DC} at high field (say 9 T) to cover the full range of the US-DPC operation, the critical current density of superconductor $J_{c,SC}$ is estimated as 4.03×10^9 A / m^2 SC. The $f_{SC\ in\ wire}$, $f_{wire\ in\ cable}$, and D_{cable} is estimated as 0.105, 0.57, and 1.87×10^{-2} m, respectively. The penetration field of the cable at 9 T is thus $B_{p,cable}(9\ T) \sim 1.86$ T. From the measurement, $\tau_{eff} < 2.5$ ms for the US-DPC cable, even if $\dot{B}_e$ is as large as 75 T / s at 9 T which is far beyond the field range in the US-DPC operation, the screening field in the cable $\tau_{eff}\dot{B}_e$ (~ 0.187 T) remains an order of magnitude lower than the penetration field. The saturated region and the field screening in the cable is therefore negligible as presumed in the beginning of this analysis.

VII.4 A PREDICTION SCHEME FOR AC LOSSES IN A FULL-SIZE CABLE

With the success of the US-DPC experiment, the CICC type of superconducting coil with chrome-plated Nb_3Sn cable and Incoloy-908 conduit has become a leading candidate for the magnet system in the International Thermonuclear Experimental Reactor (ITER) project (Refs. 7.9 and 7.10) which is currently in design phase. The design scenario of the ohmic heating coil operation starts with a sharp ramp down of 2 T/s at 14 T, followed by 0.3 T/s ramp from 13 T to -12 T for ~ 70 s, and then a even slower ramp down from -12 T to - 14 T in about 250 s. Fig. 7.11 illustrates the ranges of the fields and field changing rates for the ITER ohmic heating coil, the US-DPC experiment, and the laboratory-scale experiment. It is clear that the field condition applied in the laboratory-scale test does not match those in the large-scale superconducting magnets. However, reliable prediction of the AC losses is one of the most important requirement in designing a large superconducting magnet (Ref. 7.10). The purpose of this section is to provide a practical prediction method based on the full spectrum of this thesis work.

From the good agreements in comparing the AC-loss parameters calculated from the test results of the US-DPC and single-strand, the comparison process can be converted into a scheme which provides reliable prediction of the AC losses of a full-size cable by using the laboratory-scale experimental results and the analytical formulae developed in this research.

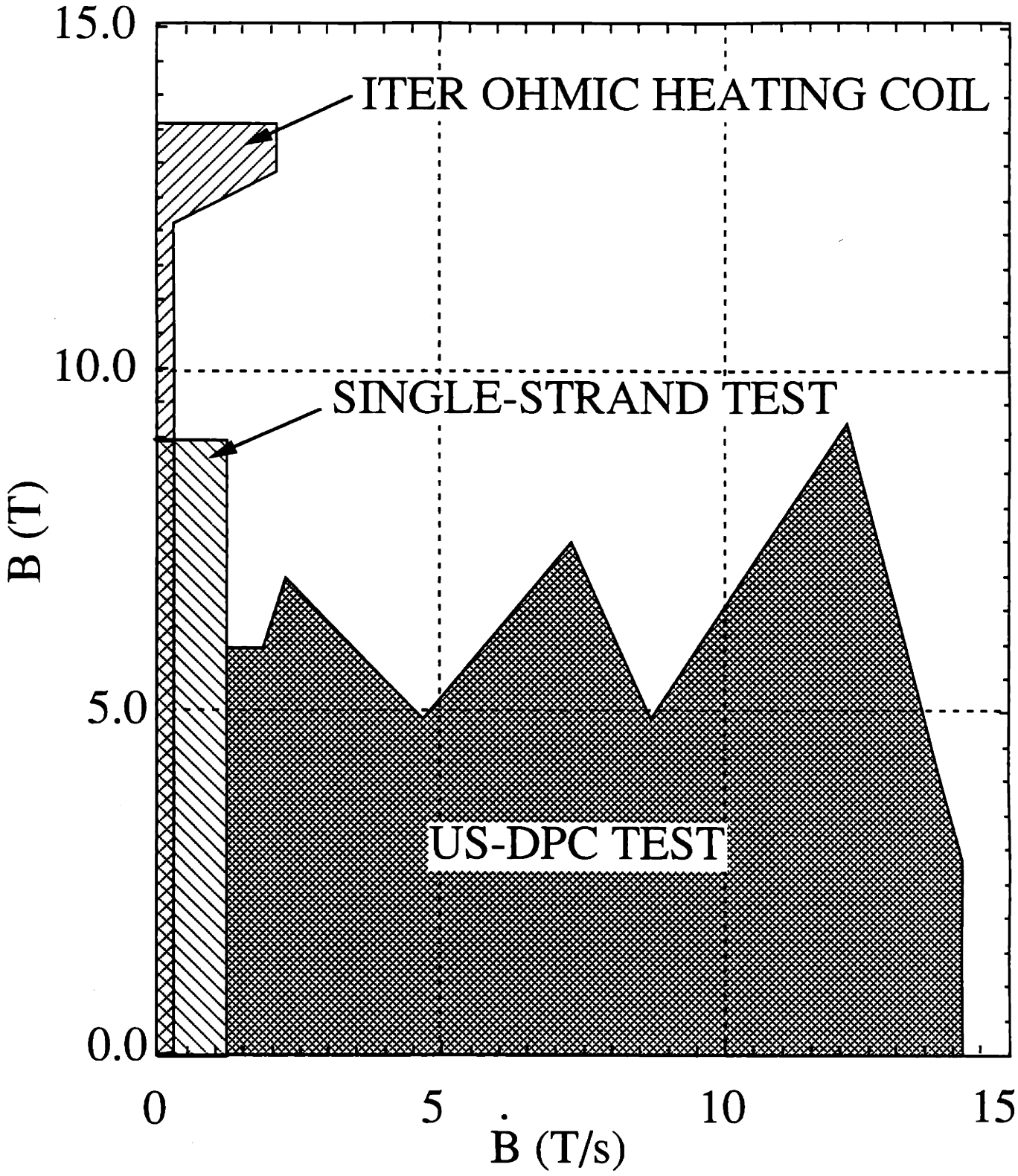

Fig. 7.11 Comparison of the field conditions in the US-DPC test (Ref. 7.1), the single-strand test, and the ITER ohmic heating coil design (Ref. 7.10).

The good agreements in comparing the d_{eff} for hysteresis loss and the τ_{eff} for the coupling loss in the US-DPC and the single-strand experiments, are achieved because:

1) low inter-strand coupling current are due to the consistently good quality control in manufacturing the chrome-plated Nb_3Sn superconducting wire and cable;
(2) low or no degradation in the critical current of the full-size cable was found due to the compatible thermomechanical properties between the superconducting cable and the Incoloy 908 conduit over the temperature range between 4.2 K and ~ 1000 K;
(3) accurate field-dependent critical current densities were measured in both the large coil and single-strand experiments over the full-range of the applied field conditions;
(4) low additional loss was caused by the transport current as evaluated from the single-strand experiments.

Within the constraints of the above mentioned conditions, prediction scheme of AC losses in a full-size cable for a large-scale pulse magnet, is summarized as follows:

(1) Measuring $J_c(B_e)$ of the candidate wire: The single-strand critical current measurement using transport current method should cover the full range of the field variation to be applied in the full-size cable, if it is possible (Section V.2).
(2) Obtaining analytical $J_c(B_e)$: Eqs. (3.1) to (3.3) for Nb_3Sn composite wire can be applied to fit the single-strand experimental data. When the low-field critical current can not be measured, the extrapolated critical current profile should be confirmed with the experimental AC-loss data as discussed in Section V.5.
(3) Evaluating d_{eff} of the candidate wire: The d_{eff} of the candidate composite wire can be estimated from the extrapolated hysteresis losses in the laboratory-scale single-strand ramp field test as demonstrated in Section V.4.1. The variation of the external field applied in the single-strand ramp field test should be within the range where the field dependent critical current can be accurately measured. For simplicity, the range of the field variation should also be larger than the the penetration field of the superconducting filament.
(4) Evaluating τ_{eff} of the candidate wire: The τ_{eff} of the candidate composite wire can be evaluated from the single-strand ripple field test as demonstrated in Section V.4.3. With the d_{eff} evaluated from the ramp field test results in step (3), and the $J_c(B_e)$ profile estimated in steps (1) and (2), the coupling loss in the ripple field test can be separated from the total loss as demonstrated in Sections VII.3.3.1 and VII.3.3.2. If the full-size cable is designed for large field variation, the field-dependent effective resistivity of the matrix materials $\rho_{eff}(B_e)$ is needed. A ρ_{eff}, averaged over the range

of the field variation, can be estimated from Eq. (2.56) with the known τ_{eff}. The magnetoresistivity in the ρ_{eff} can be scaled with Eq. (2.47).

(5) Evaluating hysteresis loss of the full-size cable: When the d_{eff} is known from step (3), the hysteresis loss of a full-size cable can be estimated from Eq. (7.3) and Eqs. (7.7) to (7.10) for ramp field and ripple field condition, respectively.

(6) Evaluating coupling loss of the full-size cable: When the τ_{eff} or the $\rho_{eff}(B_e)$ is known from step (4), the coupling loss of a full-size cable can be estimated from Eq. (7.12) and Eq. (7.11) for ramp field and ripple field condition, respectively.

(7) Evaluating additional loss caused by the transport current: The additional loss caused by the transport current depends on the design value of the full size cable, which should be justified by the laboratory-scale experiment as demonstrated in Section V.4.2, if it is possible. If the experimental information is not available, the scaling laws of these loss increments in the full-size cable, as reviewed in Eq. (2.107) for DC current and Eq. (2.108) for AC current, should be used with a great care.

(8) Calculating total loss: If the condition of low inter-strand coupling current is satisfied, the total loss is the linear sum of the losses evaluated in steps (5) to (7).

Again, the constraints of applying the above prediction scheme to evaluate the AC losses in a full-size Nb_3Sn cable are (1) low inter-strand coupling current and (2) low or no degradation of the critical current due to any work beyond the level of the single-strand.

Prediction of AC losses in a full-size cable by using the laboratory-scale experimental results and the analytical formulae developed in this research, is the most practical application of this thesis work.

VII.5 SUMMARY

The purpose of this chapter is to understand AC-loss characteristics of the full-size US-DPC cable. In order to identify AC-loss behavior in a cable, comparisons of experimental AC losses between the US-DPC and the single-strand were performed through model calculations. The key parameters in judging AC losses, the effective filament diameter d_{eff} for hysteresis loss and the effective coupling time constant τ_{eff} for coupling loss in a strand and the US-DPC Coil B, are the major vehicles for comparing test results from two different experiments. Possible sources causing discrepancies found in the comparisons are discussed. Improvement in the AC-loss modeling and future experimental work are

suggested. A practical method, which predicts AC losses in a full-size cable by using laboratory-scale experimental results and analytical formulae developed in this research, has been converted from the comparison process developed in this chapter.

AC-loss analysis of the US-DPC cable was simplified to calculate the hysteresis and coupling losses based on the presumption that the field screening effect induced by the inter-strand coupling currents in the cable was effectively reduced by the chrome-plating on the composite strands. This presumption was verified later when the effective coupling time constant of the cable became available. Although the US-DPC was tested with transport current, the ratio of the transport current to the critical current was relatively small, and so, the additional loss due to the transport current was neglected in the analysis.

Analytical AC-loss models for single-strand were modified for the non-uniform field condition applied in the US-DPC experiment. Within the test range, a consistent effective filament diameter of ~ 20 μm was calculated from the single-strand losses as well as the cable losses. However, the trends of the the peak-field dependent distributions of the extrapolated and the calculated hysteresis losses were not consistent. The source of the discrepancy is not clear at this stage. A possible explanation is the low field shielding effect on the superconducting cable caused by the magnetization of the ferromagnetic Incoloy 908 conduit. Experimental verification is suggested.

A sensitivity study on the effective filament diameter was performed by changing the temperature and the strain state in the semi-empirical critical current formula which is based partly on the flux pinning theory. The hysteresis loss was found insensitive to the perturbations of the temperature and the strain in the ranges of interest ($0\ T \le B_e \le 9\ T$, $4.2\ K \le T \le 4.5\ K$, and $-0.36\ \% \le \varepsilon \le -0.1\ \%$). An alternative best-fit field-dependent critical current formula which has a low extrapolated J_c profile in the low-field region ($B_e < 2.5$ T), was applied to calculate the effective filament diameters. Due to the underestimation of the low-field critical current, the effective filament diameters of both the single-strand and the US-DPC cable calculated by using the alternative critical current formula are larger than those by using the primary formula. With the alternative critical current formula, the effective filament diameter of the US-DPC is found to be higher than that of the single-strand by ~ 30%. The inconsistency results from the effect of a low critical current in the low-field region combined with the large volume of the superconducting cable in the low field region in the US-DPC double-pancake winding. The loss integral in the US-DPC is

underestimated more than that in the single-strand, and therefore a larger effective filament diameter is obtained from the US-DPC test results.

For a superconducting magnet for ramp field applications such as the US-DPC or a future ITER ohmic heating coils, the field variation must pass through the low field region. The low-field critical current distribution is the most important factor in determining the hysteresis loss or the effective filament diameter. Since a best-fit critical current formula in the high field region does not guarantee a correct profile in the low field region, the field-dependent critical current formula adopted in the loss calculation must be confirmed experimentally over the full current spectrum.

Effective coupling time constants evaluated from the test results of both the single-strand and the US-DPC Coil B were compared with the analytical values. The comparison scheme was validated by the consistent single-strand coupling time constant value of ~ 0.85 ms evaluated from the test results and the analytical model. Comparing the effective coupling time constant of the Coil B with that of a single-strand, the increment of the coupling time constant in Coil B due to the cabling process was found to be about 30%. This concludes that the chrome-plating on the constituent wires in the US-DPC cable is effective in reducing the inter-strand coupling currents. Using the effective coupling time constant of the US-DPC cable, the field screening effect in the cable due to inter-strand coupling currents was identified to be negligible which confirmed the presumption adopted in this analysis.

A practical method for predicting AC losses of a full-size cable has been developed based on the good agreements in comparing AC-loss parameters calculated from the test results of the US-DPC and single-strand. The prediction scheme has been converted from the comparison process using the laboratory-scale experimental results and the analytical formulae developed in this research. The ability to predict AC losses in a full-size cable from laboratory-scale experimental results is the most important application of this thesis work.

VII.6 REFERENCES

7.1 Painter, T.A., et al. 'Test Data from the US-Demonstration Poloidal Coil Experiment', PFC/RR-92-1, also DOE/ER/54110-1, Plasma Fusion Center, Massachusetts Institute of Technology, January 1992.

7.2 Morra, M.M., et al., 'Incoloy 9XA, a new low coefficient of thermal expansion sheathing alloy for use in ICCS magnets', presented at ICMC, June 1987.

7.3 Steeves, M.M., Hoenig, M.O., Cyders, C.J., 'Effects of Incoloy 903 and tantalum conduits on critical current in Nb_3Sn cable-in-conduit conductors,' Adv. Cryo. Eng., Vol. 30, 1984, p. 883.

7.4 Takayasu, M., et al., 'Critical currents of Nb_3Sn wires of the US-DPC coil,' Adv. Cryo. Eng., Vol. 38, 1992, p. 619.

7.5 Gung, C.Y., 'AC losses of a multi-stage cable with copper-to-copper inter-strand contacts affected by a transverse fast sinusoidal ripple field superposed to a DC bias field', PFC Report, Massachusetts Institute of Technology, 1992.

7.6 Mower, T.M., and Iwasa, Y.,'AC losses in multifilamentary composite superconducting strands and cables,' Adv. Cryo. Eng., No. 32, 1986, p. 771.

7.7 Superconducting Magnet Laboratory, JAERI, 'Review of US-DPC experiment', presented in Proceedings of US-DPC Test Results Workshop, April 16-17, 1991, MIT Plasma Fusion Center, Cambridge, Massachusetts

7.8 Ciazynski, D., et al., 'AC losses and current distribution in 40 kA NbTi and Nb_3Sn conductors for NET/ITER,' presented in ASC'92, Chicago.

7.9 Conn, R.W., Chuyanov, V.A., Inoue, N., and Sweetman, D.R., 'The International Thermonuclear Experimental Reactor,' Sci. American, April, 1992, p. 103.

7.10 *ITER MAGNET SYSTEM*-Concept and Design Activity, International Atomic Energy Agency, Vienna 1990.

CHAPTER VIII

SUMMARY AND CONCLUSIONS

VIII.1 SUMMARY OF THE THESIS WORK

The present thesis research contains five major contributions to the development of superconductors for high-current ramp-field applications:

(1) modification of the existing hysteresis-loss and coupling-loss models to simulate respectively the magnetic field conditions and the test wire construction applied in this thesis research;

(2) design and construction of a reliable and versatile laboratory-scale cryogenic experimental system for isothermal calorimetric measurement of energy dissipation (AC loss) in a current-carrying composite superconducting wire affected by a time-changing field with a large field variation;

(3) performance of calorimetric measurements of the AC losses in three types of superconducting wire with the current and field conditions simulating those of high-current pulse magnets. All three wires are candidate superconductors for advanced superconducting magnet applications.

(4) development of a new analytical AC-loss model explaining the occurrence of a local maximum in the ramp-rate dependent experimental AC-loss profile of the MJR wire;

(5) development of a computational methodology for comparing the AC losses of the US-DPC with those of constituent single-strand and an AC-loss prediction scheme applicable to other pulsed field magnets for fusion applications.

VIII.2 MODIFICATION OF THE EXISTING AC-LOSS MODELS

Existing AC-loss models including hysteresis loss, coupling loss, penetration loss, and additional loss due to transport current, have been examined. This review determined that existing hysteresis-loss models must be modified for the current and field condition for

pulse magnets, and existing coupling-loss model should be extended for the wire constructions used in the present work.

Existing hysteresis-loss analyses based on the critical state model in 2-D cylindrical geometry have been modified for two types of field variation which are of interest to the present work: (1) a small sinusoidal wave-form field superimposed on various large DC bias fields, and (2) a unidirectional large-amplitude triangular cyclic field. In both cases, the hysteresis loss depends strongly on the field-dependent critical current density which now has been taken into account by the work of this thesis. The final forms of the hysteresis losses are given in Eqs. 3.10 to 3.14 and 3.27 to 3.29. The effective filament diameter d_{eff} calculated from experimental hysteresis losses in large field variation are expressed in Eqs. 3.33 and 3.35.

The cross sectional constructions of most composite wires can be approximated with multi-layer configurations. In order to have a single coupling-loss model covering all the wire constructions applied in this thesis work, existing analysis for a 4-layer configuration has been generalized for a 5-layer structure. The expressions of the modified coupling-loss power density are given in Eqs. (2.63) to (2.66).

VIII.3 EXPERIMENTAL APPARATUS

A new laboratory-scale isothermal calorimetric system for measuring AC losses of a composite superconducting wire has been designed and constructed as part of this thesis work. The purposes of building this new measurement apparatus were as follows:

(1) to measure the absolute values of total AC losses;
(2) to evaluate specific loss components;
(3) to provide AC-loss characteristics of a current-carrying US-DPC wire affected by a large-amplitude ramp field prior to the US-DPC experiment;
(4) to estimate the d_{eff} and t_{eff} for analytical AC-loss calculations;
(5) to compare the AC losses between single-strand and US-DPC cable.

The present calorimetric system has been designed to be free from two major sources of disturbance affecting the accuracy of AC-loss calorimetric measurement: (1) spontaneous thermoacoustic resonance, and (2) the field-dependent noise caused by the boil-off helium gas leaks in the high field region. The low efficiency of the calorimetric measurement,

which is the greatest disadvantage of this method, has been largely improved by coupling the calorimetric system with a constant flow-rate control electronic feedback system and a computer data acquisition system.

The unique feature of the present experimental system is the capability of measuring AC losses of a brittle Nb_3Sn composite superconducting wire carrying a high DC or a background field synchronized AC current (up to 95% of critical current) in a ramp field with large field variation (up to ~ 1.5 T/s at 0 - 9 T - 0 sweep). The latter experiment simulating the operation of a superconducting wire in a large-scale high-amplitude pulse magnet has never been performed in other laboratory-scale measurements.

VIII.4 SINGLE-STRAND AC-LOSS MEASUREMENTS AND COMPARISONS

Three important types of wire for major large-scale high-current ramp-field magnet applications have been tested, namely: a NbTi wire for Superconducting Super Collider, a Nb_3Sn internal-tin prototype wire for the ITER model ohmic heating coil, and the Nb_3Sn modified-jelly-roll (MJR) internal-tin wires for the US-DPC. The following conclusions have been drawn from the comparison between the measured AC losses and the calculated results using the modified AC-loss models.

(1) Good agreement has been found in benchmark comparisons between experimental hysteresis losses measured in the present work and results from independent magnetization measurements. This validates the present experimental system in the very low time-rate of field variation ($\leq$ 0.05 T/s)

(2) Good agreement has been found between the analytical AC losses and the test results from the first two current-free test wires. This justifies the experimental system in the region with higher time-rate of field variation ($\geq$ 0.05 T/s).

(3) The measured ramp-rate dependent AC-loss profiles of the MJR wire indicates a local maximum in a low ramp-rate regime (~0.2 T/s to ~ 0.6 T/s) which is not predicted by the existing models and has never been observed or discussed before. A new model has been developed to provide a quantitative explanation of this measurement result.

(4) A primary goal of testing AC losses of a current-carrying composite wire was to identify the importance of the additional loss caused by the transport current in the ramp rate region applied to the US-DPC experiment. The single-strand test results showed that the increment of the loss is less than 5% of the total loss of a current-free sample

and can be neglected. With the improvement of the experimental data base, the experimental results show that when a DC or an AC current is applied to a composite superconductor under ramp field condition, the additional AC losses caused by transport current are similar if $I_{DC} = I_{AC,max}$. This test result is not predicted by existing model, even when the field-dependent critical current density is taken into account. More future effort is required to explain these test results.

(5) Dependence of the additional loss by transport current on the field changing rate is another important new result. The test results reveal that the total loss of a composite wire carrying a large DC or AC current may have a higher loss in a slowly ramped field than that in a fast changing field. This conclusion is in contradiction to the generally accepted concept that high time-rate of field variation generates high AC losses. These new AC-loss properties of a current-carrying composite wire, which have been experimentally identified in all three types of wire, may lead to a new area for future analytical work.

(6) By comparing the calculated results with those from measurements, the importance of the low-field critical current density profile to the hysteresis-loss calculation has been demonstrated in both ramp field test and ripple field test at a low DC bias field. The low-field critical current density profile extrapolated from the high-field region has been till now, a widely adopted procedure for loss calculation. The results of this thesis demonstrate that this procedure should only be applied with experimental justification.

VIII.5 INTER-BUNDLE COUPLING LOSS MODEL

The experimental results have shown a local maximum in the ramp rate dependent AC-loss profile in the MJR wires. This thesis proposes an inter-bundle coupling loss model as a first analytical model attempting to understand this result. In the new model, when (1) the inter-bundle matrix resistivity is much lower than that of the intra-bundle, and (2) the inter-bundle spacing is much smaller than the bundle wall thickness, the inter-bundle coupling time constant at a slow field variation is found to be magnified by a geometric effect. The consequent high inter-bundle coupling currents saturate the superconducting filaments in the bundle wall at a ramp rate at least one order lower than predicted by the existing models. The proposed inter-bundle coupling loss model has succeeded in explaining the occurrence of the local maximum loss in the slow ramp rate regime and simulating the trend of the loss profile as a function of the ramp rate.

For practical application, the present inter-bundle coupling model requires more future work since the calculated results show that the local maximum loss shifts to a higher ramp rate as the range of the field variation is reduced which is inconsistent with the trend from the measurement. Also, the calculated local maximum losses are about 20% higher than those by the measurement. Further development of the AC-loss model based on the present inter-bundle coupling analysis is important in not only improving the prediction of the AC-loss behavior of the MJR type of wire but also providing an analytical basis for the design and optimization of a composite superconducting wire with a similar wire construction.

VIII.6 AC LOSSES OF THE US-DPC

The AC losses of the Coil B in the US-DPC have been analyzed based on the assumptions of low inter-strand coupling loss due to the chrome-plating on each wire in the cable and low additional loss caused by the low transport current. The former assumption was confirmed by the cable coupling time constant. The second assumption was based on the single-strand test results.

Due to the different field conditions in the US-DPC and the single-strand experiments, comparisons of the losses are based on the d_{eff} for hysteresis and τ_{eff} for coupling loss. Both of the d_{eff} (~ 20 μm) and the τ_{eff} (~ 1 ms) evaluated from the full-size US-DPC cable loss have been found to be in good agreement with those calculated from the laboratory-scale single-strand test results. Considering the complicated field condition as well as the thermomechanical stress and Lorentz forces applied to the cable in the US-DPC, this good agreement is considered significant. The good agreement in both AC-loss parameters was achieved because:

(1) low inter-strand coupling current are due to the consistently good quality control in manufacturing the chrome-plated Nb_3Sn superconducting wire and cable;
(2) low or no degradation in the critical current of the full-size cable was found due to the compatible thermomechanical properties between the superconducting cable and the Incoloy 908 conduit over the temperature range between 4.2 K and ~ 1000 K;
(3) accurate field-dependent critical current densities were measured in both the large coil and single-strand experiments over the full-range of the applied field conditions;
(4) low additional loss caused by the transport current was known from single-strand experiments.

From the success of the US-DPC experiment, the CICC type of superconducting coil with chrome-plated Nb_3Sn cable and Incoloy-908 conduit has become a leading candidate for the ITER magnet system (Refs. 8.1 and 8.2). A reliable prediction of AC losses is one of the most important requirements in the magnet design stage. Within the constraints of the above mentioned conditions, a prediction method for AC losses in a full-size cable has been developed out of the process applied in the loss comparison. The practical scheme uses the formulae applied in this work with required parameters d_{eff}, τ_{eff}, and full range $J_c(B)$ evaluated from the laboratory-scale single-strand experiments as has been demonstrated in this thesis work. The prediction scheme for the AC losses of a full-size cable is the most important application of this thesis work.

VIII.7 RECOMMENDED FUTURE WORK

Future research subjects based on this thesis study can be summarized as follows:

(1) perform magnetization measurements in the present calorimetric system for a better understanding of instantaneous loss behavior in the test sample;

(2) expand the capacity of the present calorimetric system for testing conductors beyond the level of a single-strand, such as a multi-strand cable;

(3) develop a more reliable method in characterizing low-field critical current density profile for hysteresis-loss or effective filament diameter calculation;

(4) improve the present version of inter-bundle coupling model by including remote bundle coupling in the analysis;

(5) re-investigate AC-loss mechanism of a current-carrying superconducting wire affected by an AC field with large field variation;

(6) characterize the field shielding effect on a superconducting cable due to the magnetization of the ferromagnetic Incoloy-908 conduit.

VIII.8 REFERENCES

8.1 Steeves, M.M., et al., 'Applicability of the US-DPC to the ITER model poloidal coil,' 1991 IEEE 14th Symposium on Fusion Engineering, 1991, p. 459.

8.2 Minervini, J.V., et al., 'Preliminary design of a U.S. ITER model poloidal coil,' 1991 IEEE 14th Symposium on Fusion Engineering, 1991, p. 478.

APPENDIX A

DETAIL OF AC-LOSS SAMPLE WINDING

A.1 PARTS

1) 1 35 m (120 ft) of superconducting wire, wire size should not be too much different from 0.031″.

$$\pi \times 3'' \times 63 \text{ (outer coil)} + \pi \times 2.5'' \times 74 \text{ (inner coil)}$$
$$+ 36'' \text{ current lead} \times 2 + \sim 36'' \text{ of spare length}$$
$$\approx 1283'' \approx 107 \text{ ft} \Rightarrow \text{cut } 120 \text{ ft}$$

NOTE: The length for the leads may be changed, depending on the heat treatment setup.

2) 1 threaded thin wall G-10 tube (Fig. A.1).

3) 1 MACOR tube with both sides threaded (Fig. A.1).

4) 3 1/4″ stainless bolts, L ~ 1″, with matching nuts and washers. The tail end of the bolt needs two flat surfaces for the convenience of drilling a hole for a cutter pin to go through (as seen in the sketch). All metallic surface must be oxidized to prevent sintering.

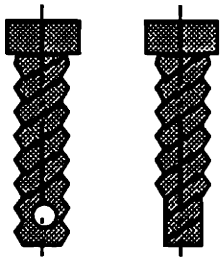

5) 3 stainless steel cutter pins (oxidized), L ~ 1.5″

6) 2 stainless steel rods or tubes, 1/4″ OD, L ~ 2 ft (oxidized).

7) 6 stainless steel rods or tubes, 1/4″ OD ,L ~ 6″ (oxidized).

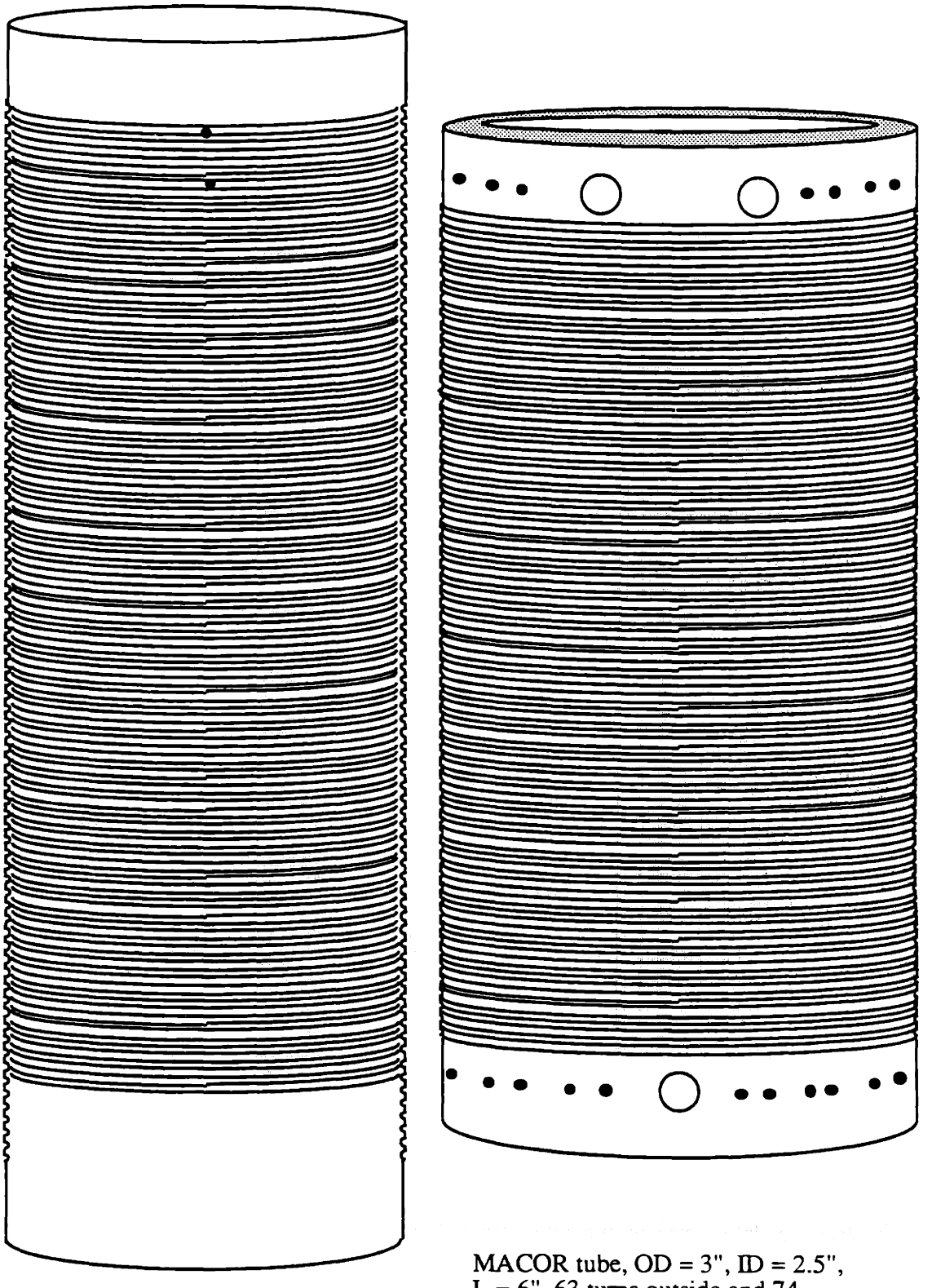

Thin shell G-10 tube, OD ~2.5"

MACOR tube, OD = 3", ID = 2.5", L = 6", 63 turns outside and 74 turns inside

Fig. A.1 Schematic of threaded thin shell G-10 tube and MACOR tube for sample winding.

8) 2 alumina tubes, ID ~ 0.03", OD ~ 0.05", L ~ 2"

9) 2 quartz tubes, ID ~ 0.04", OD ~ 0.08", L ~ 2 ft.

10) stainless steel wire (gauge 13), and wire cutter

11) scotch tape

12) alcohol and cleaning cloth

13) thin nylon gloves

14) soapy water (or snoop)

A.2 PROCEDURE

NOTE: Do not make any unnecessary sharp bends or twists to the wire throughout the procedure.

NOTE: Be sure you are skillful in doing step (15) before you start to work on the real sample wire.

1) Measure 120 ft of the wire and cut from the spool (NO SHARP BENDING).
2) Wipe the wire with alcohol and cloth about 3 times. If the wire is very dirty, use the ultrasonic cleaning machine. **NOTE:** Do not hold the wire too tight during the cleaning since the wire can easily be stretched.
3) Fix the free end of the wire to the hole on the G-10 tube (as shown in the following sketch).

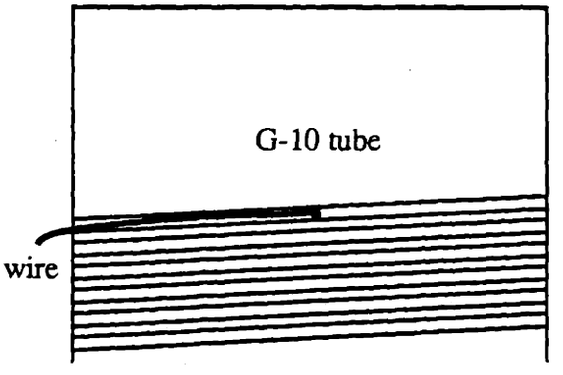

Pass a small segment of wire through the small hole, make a sharp bend inside the tube, and align the wire in the groove.

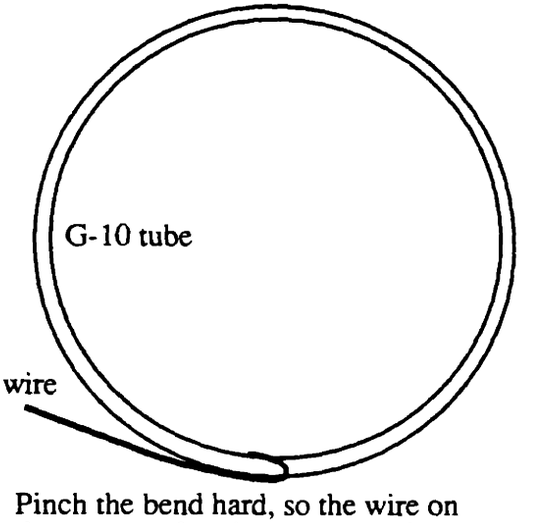

Pinch the bend hard, so the wire on the outer surface is very smooth

4) Fix a rod or a screw driver on a vice, use it as a spool holder.
5) Wind the wire to the G-10 tube until about 3/4" above the lowest thread on the G-10. Be sure the wire is in the groove throughout the length. **NOTE:** No loose winding, no heavy stress to the wire.
6) Tape the wire to the G-10 tube at lower end (only temporary holding, do not bend the wire)
7) Apply soapy water or snoop to the inner groves of the MACOR for reducing the friction between the wire and the machined MACOR surface (see next step). **NOTE:** The next step can be done with water or without any lubricant if you are skillful.
8) Rotate the bottom end (single-hole end) of the MACOR tube onto the top end (where the winding begins) of the G-10 tube (Fig. A.2). If the rotation is difficult, it may comes from the following problems:
    (i) The wire diameter is too much larger than 0.031".
    (ii) The top fixture of the wire on the G-10 tube is bulging.
    (iii) Some turns of the wire on the G-10 tube may be loose.
9) Allow 4 to 5 ft of the wire above the inner upper-most groove of the MACOR for the current-lead.use (i.e. about 4 to 5 turns free from the inner MACOR groove).
10) Remove the top fixture of the wire on the G-10, let the wire spring out, and tape the wire to the top edge of the MACOR.
11) Remove the bottom tape on the G-10. Keep the bottom of the G-10 tube on the table all the time, then let the wire spring out. **NOTE:** Do not let the extra turns slip out of the bottom of the G-10 tube. Since the superconducting wire is always twisted, the residual stress tends to flip each turn by some angle. Few run-away turns tend to form a spherical surface which can hardly be undone without making extra sharp bends.
12) 'Theoretically', the wire should already have been transferred from the G-10 to the inner threads on the MACOR.
13) Rewind the extra length back to the spool very carefully (rotate the spool and the G-10 at the same time, then tape the wire to the spool.
14) Rotate the G-10 tube out (downward). **NOTE:** Depending on the wire diameter, sometimes the G-10 tube can be withdrawn directly when it has been rotated about half way out.

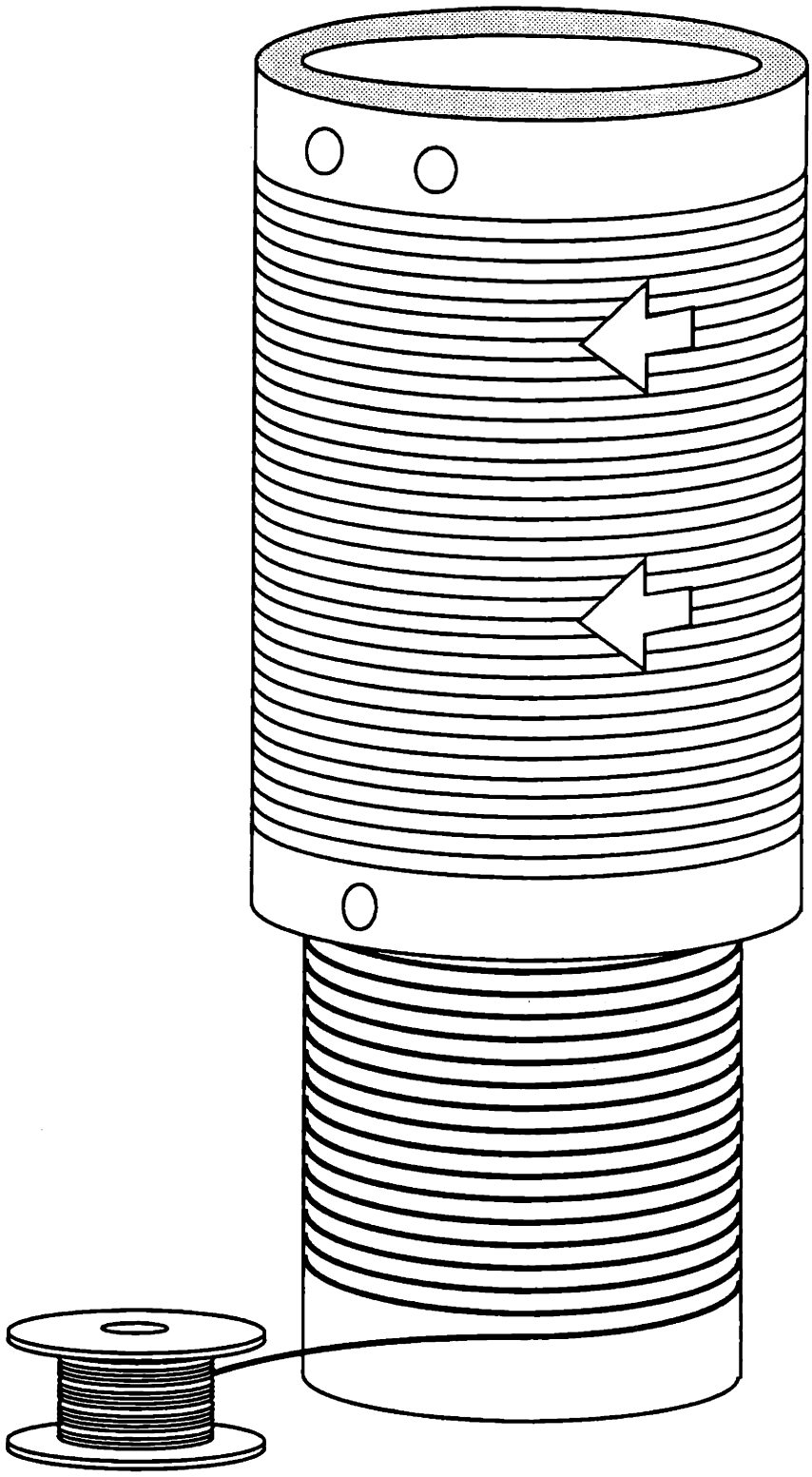

Fig. A.2 Mounting of the inner coil to the MACOR sample holder.

15) Manipulate the upper half of the turns so the wire is tightly loaded into the grooves on the inner surface of the MACOR tube:

NOTE: THIS IS THE MOST DIFFICULT PROCEDURE!! SOME PRACTICE IS NECESSARY BEFORE THE REAL TEST WIRE IS USED.

(i) DO NOT PUSH loose turns in the inner coil to one side of the wall.

(ii) Starting from the mid-plane of the MACOR. Touch the turns near the mid-plane of the inner coil with one finger from each hand. Use the friction between your finger tips and the wires to rotate the turns at a small amount in the direction that expands the radius of the turns (clock-wise when you see from the top of the MACOR).

NOTE: As the radii of the lower turns (near the mid-plane) are expanded, they are taking some length from the upper turns. The radii of the upper turns are reduced, and the upper turns are likely to come out of the grooves. The consequence of run-away turns would be the same as what has been mentioned in step (11). Any turn comes out of the groove must be returned to its original position immediately, then rotate the turns above it so it will expand slightly (Don't rotate too much unless those turns below it have been fixed). You must do the rotation throughout the length between the mid-plane and the top groove by only a small amount each time at each location.

(iii) Repeat the small rotation throughout the length several times until all the turns are tightly sitting in the groove. DO NOT permanently fix the upper-most turn yet.

(iv) Visually examine the inner winding when you think you have finished the rotation. When a light is shed into the inner winding, the loose turns reflect more light. Try to improve them if you can.

16) As shown in the following sketch and Fig. A.2, fix the wire to the MACOR with the stainless steel bolts, nuts, and washers. All the surfaces must be oxidized before heat treatment.

17) Turn the MACOR upside down without forcing the wire to twist. Manipulate the lower half of the turns as above mentioned, then fix the bottom end with stainless steel bolts.

18) Wind the outer coil from bottom-side up.

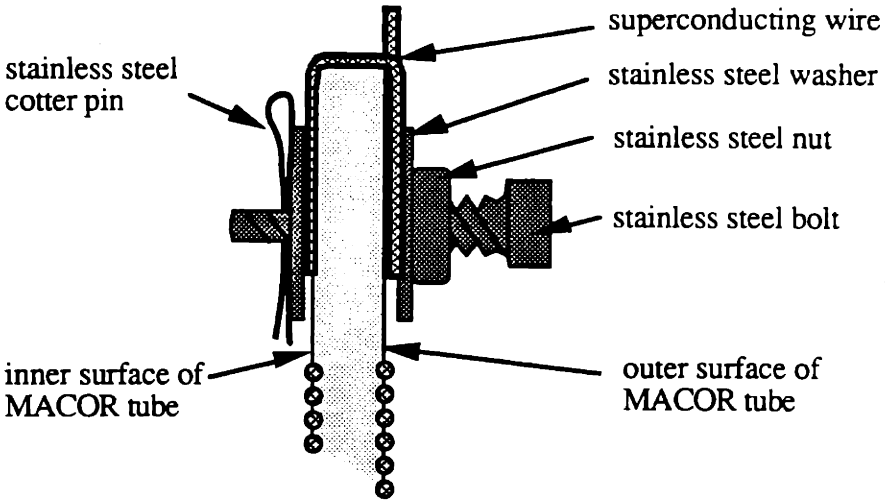

19) Fix the wire to the upper end of the MACOR with the stainless steel bolts, nuts, and washers (all with oxidized surface).

20) Allow 4 to 5 ft length of the wire for another current lead.

21) Flush the wire with lukewarm water thoroughly. It is important to remove the soap completely before the heat treatment. **NOTE:** Do not heat treat a wet wire.

22) Use stainless steel wires to tightly hold those six 6˝-long stainless steel rods or tubes (oxidized) to the surface of the inner coil (Fig. A.3).

23) Use stainless steel wires to fix those two 2 ft-long stainless steel rods or tubes (oxidized) to the surface of the outer coil. Keep them between the two upper bolts on the MACOR (they are used for holding the current leads) (Fig. A.3).

24) Pass each lead through a short alumina tube. Push the alumina tube to the end of the lead (on top of the bolt) (Fig. A.3).

25) Starting from 3˝ above the bolts, make a very shallow U-bend on each lead (Fig. A.3).

26) Pass each lead through a quartz tube. Keep the quartz tube slightly above the bend (Fig. A.3).

27) Fix the quartz tubes to the long stainless steel tubes or rods with stainless steel wires (Fig. A.2) **NOTE:** The quartz tubes can easily be broken if the stainless steel wires are too tight. However, if the stainless steel wires are loose, the quartz tubes may slip down onto the U-bend and break the heat-treated current lead at the bending segment.

28) Fuse (spot weld) the end of each current lead. The wire is ready for heat treatment.

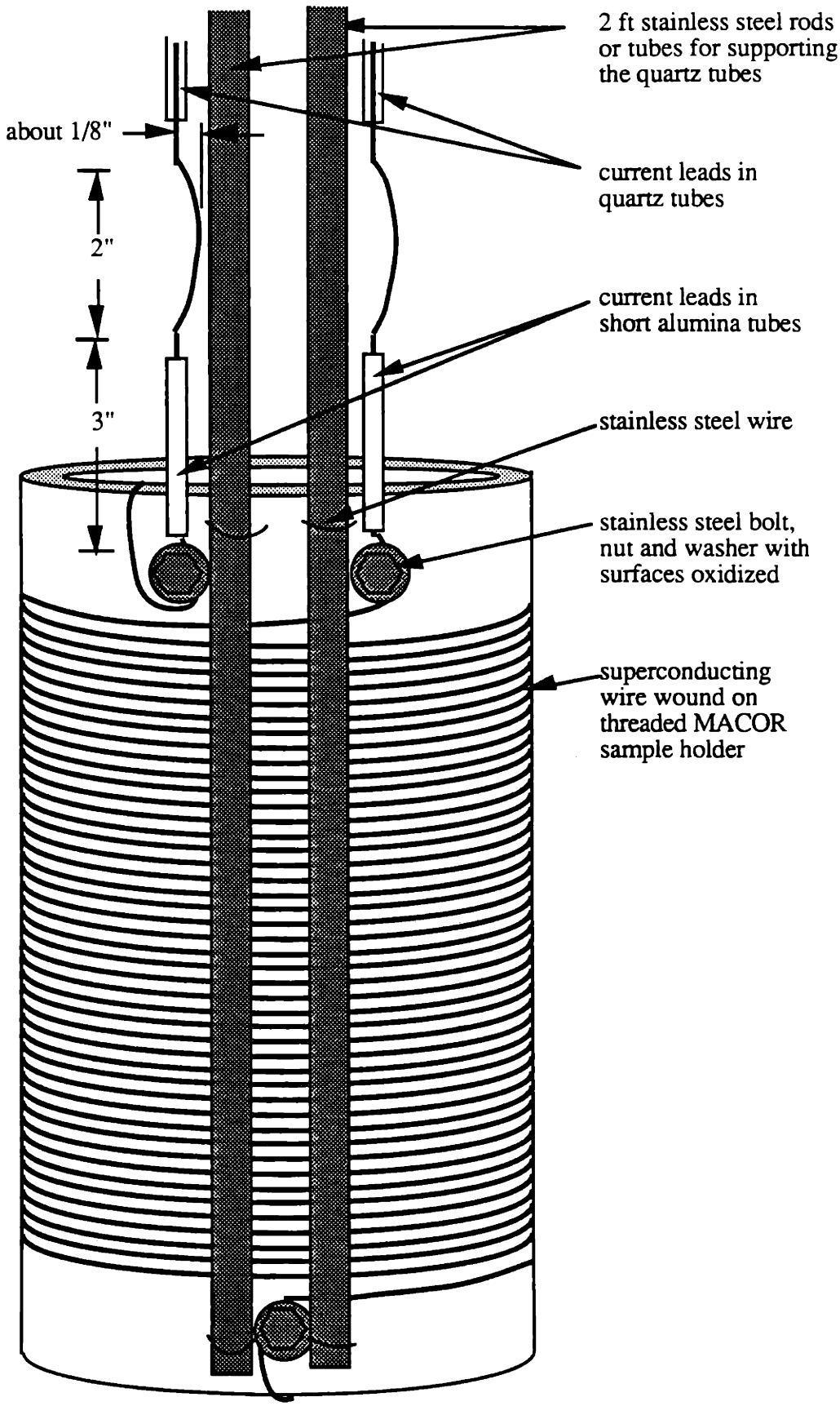

Fig. A.3 Reinforcement of AC-loss sample before heat treatment.